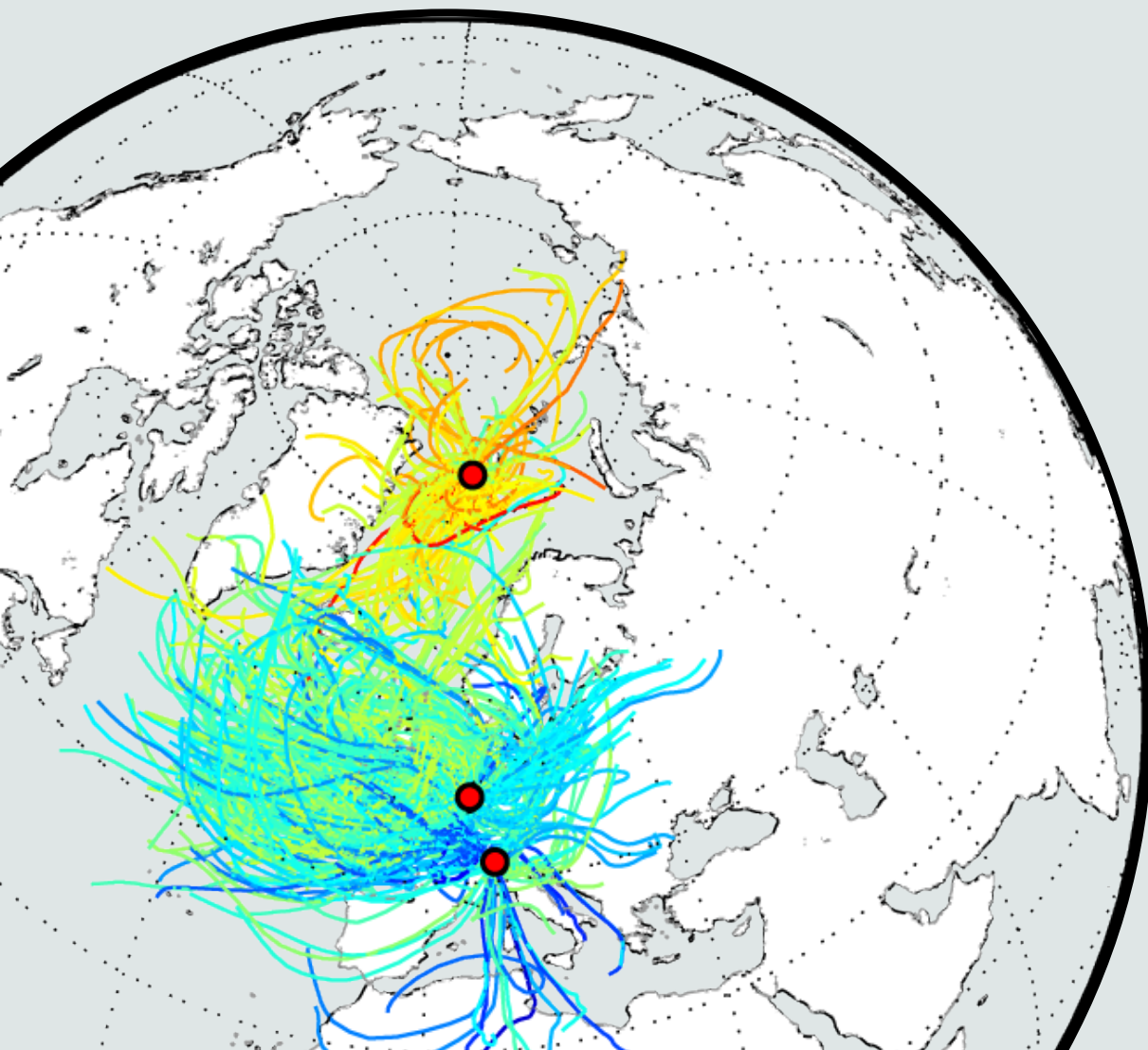


Diss. ETH No. 19659

# Effects of relative humidity on aerosol light scattering

Paul Christoph Zieger





Diss. ETH No. 19659

# **Effects of relative humidity on aerosol light scattering**

A dissertation submitted to  
ETH ZÜRICH

for the degree of  
Doctor of Sciences

presented by  
PAUL CHRISTOPH ZIEGER  
Dipl. Physiker, Freie Universität Berlin  
born 29 September 1978  
citizen of Germany

accepted on the recommendation of  
Prof. Dr. Thomas Peter, examiner  
Prof. Dr. Urs Baltensperger, co-examiner  
Prof. Dr. Gerrit de Leeuw, co-examiner  
Dr. Ernest Weingartner, co-examiner

2011





# Contents

<b>1</b>	<b>Introduction</b>	<b>1</b>
1.1	Atmospheric aerosols . . . . .	1
1.2	How aerosols effect the Earth's climate . . . . .	3
1.2.1	Aerosol direct effect . . . . .	4
1.2.2	Aerosol indirect effects . . . . .	6
1.2.3	Effects of relative humidity on aerosol light scattering . . . . .	7
1.3	Motivation and overview of the thesis . . . . .	9
<b>2</b>	<b>The physical basis</b>	<b>11</b>
2.1	Water uptake by aerosol particles . . . . .	11
2.2	Atmospheric absorption and scattering of solar radiation . . . . .	15
2.2.1	Rayleigh theory . . . . .	17
2.2.2	Mie theory . . . . .	17
2.2.3	Main aerosol optical properties . . . . .	20
2.2.4	Modeling the effect of relative humidity on the aerosol optical properties . . . . .	21
<b>3</b>	<b>Measured and predicted aerosol light scattering enhancement factors at the high alpine site Jungfraujoch</b>	<b>23</b>
3.1	Introduction . . . . .	24
3.2	Experimental . . . . .	25
3.2.1	Measurement site . . . . .	25
3.2.2	Instruments . . . . .	25
3.2.3	Mie calculations to predict $f(\text{RH})$ . . . . .	29
3.3	Results and discussion . . . . .	30
3.3.1	Measured $f(\text{RH})$ . . . . .	30
3.3.2	Prediction of $f(\text{RH})$ . . . . .	35

3.3.3	RH dependence of derived climate relevant properties . . . . .	38
3.4	Summary and conclusions . . . . .	42
<b>4</b>	<b>Effects of relative humidity on aerosol light scattering in the Arctic</b>	<b>45</b>
4.1	Introduction . . . . .	46
4.2	Experimental . . . . .	47
4.2.1	Humidified and dry nephelometer . . . . .	47
4.2.2	Measurement of the aerosol size distribution . . . . .	48
4.2.3	Measurement of the aerosol light absorption . . . . .	49
4.2.4	Aerosol filter sampling and analysis . . . . .	49
4.2.5	Comparison of dry nephelometer measurements . . . . .	50
4.2.6	Inlet systems . . . . .	50
4.3	Model description . . . . .	51
4.3.1	Forward calculation . . . . .	52
4.3.2	Backward calculation – retrieval of the apparent hygroscopic growth factor . . . . .	52
4.4	Simulation of a passive sea salt tracer . . . . .	52
4.4.1	Dispersion model . . . . .	53
4.4.2	Emission calculation . . . . .	53
4.5	Results . . . . .	53
4.5.1	Parametrization of $f(\text{RH})$ . . . . .	57
4.5.2	Deliquescence caused by sea salt . . . . .	59
4.5.3	Compensating effects of size and hygroscopicity . . . . .	59
4.5.4	Impact of $f(\text{RH})$ on climate relevant parameters . . . . .	64
4.5.5	Predicting $f(\text{RH})$ . . . . .	65
4.6	Conclusions . . . . .	66
<b>5</b>	<b>Comparison of ambient aerosol extinction coefficients obtained from in-situ, MAX-DOAS and LIDAR measurements at Cabauw</b>	<b>69</b>
5.1	Introduction . . . . .	70
5.2	The Cabauw site and the CINDI campaign . . . . .	72
5.3	Experimental . . . . .	72
5.3.1	In-situ measurements . . . . .	73
5.3.2	MAX-DOAS measurements . . . . .	77
5.3.3	Lidar measurements . . . . .	78

5.4	Results	80
5.4.1	WetNeph analysis	81
5.4.2	Factors influencing $f(\text{RH})$ at Cabauw	82
5.4.3	Closure study	83
5.4.4	Comparison to remote sensing data	88
5.5	Conclusions	96
<b>6</b>	<b>Comparison and conclusions</b>	<b>99</b>
6.1	Scattering enhancement at three European sites	99
6.1.1	Measurements	100
6.1.2	Closure studies	101
6.2	Comparison to OPAC	104
6.3	Conclusions	111
6.4	Outlook	112
	<b>List of abbreviations</b>	<b>117</b>
	<b>Bibliography</b>	<b>119</b>
	<b>Acknowledgements</b>	<b>135</b>
	<b>Curriculum vitae</b>	<b>137</b>



# Abstract

Atmospheric aerosols, which are defined as solid or liquid particles suspended in the air, are tiny and mostly not visible to our eyes. Nevertheless, they have an immense impact on our health and on our global climate as well. Anthropogenic emissions of greenhouse gases, like carbon dioxide or methane, and anthropogenic emissions of particulate matter have changed the Earth's climate. Aerosols scatter and absorb solar radiation and by doing so they directly influence the Earth's radiation budget. In addition, anthropogenic aerosol particles also modify cloud properties, causing e.g. brighter clouds with longer lifetimes and changed precipitation behavior. The net effect of anthropogenic aerosols on the Earth's climate is a cooling one, in contrast to the greenhouse gases which are characterized by a warming effect. However, the *Intergovernmental Panel on Climate Change* concludes in his last assessment report that the high uncertainty in the net radiative forcing of all main climate agents (greenhouse gases, aerosols, surface changes, and natural forcings) is mainly dominated by the high uncertainty in the aerosol radiative forcing. This is mainly caused by the high temporal, spatial, and compositional variability of the aerosol and the poorly understood and quantified aerosol effects. Since aerosol particles can take up water, they can change in size and chemical composition depending on the ambient relative humidity (RH). This directly influences the aerosol radiative forcing because the aerosol optical properties will change with varying RH.

Therefore, long-term in-situ measurements of aerosol optical and microphysical properties are usually performed at standardized dry conditions to avoid the RH-effect when quantifying and characterizing the main aerosol properties. This is especially important for the aerosol light scattering coefficient  $\sigma_{\text{sp}}(\lambda)$  which strongly depends on RH ( $\lambda$  denotes the wavelength). These dry measured values significantly differ from the ambient and thus climate relevant ones. The knowledge of this RH effect is therefore of crucial importance for climate forcing calculations. In addition, it is also needed for the comparison or validation of remote sensing with in-situ measurements.

The key parameter to describe the influence of RH on the aerosol light scattering is the scattering enhancement factor  $f(\text{RH}, \lambda)$  which is defined as the aerosol scattering coefficient  $\sigma_{\text{sp}}(\text{RH}, \lambda)$  at a certain RH divided by the dry  $\sigma_{\text{sp}}(\text{dry}, \lambda)$ . The magnitude of the scattering enhancement depends on the size and the chemical composition of the aerosol. The scattering enhancement can e.g. be measured by using a humidified nephelometer. It can also be calculated via Mie theory using e.g. the measured size distribution, hygroscopic growth, and chemical composition as input.

In this thesis, the influence of relative humidity on the aerosol light scattering has been investigated using measurements and model studies from three European sites. These were selected according to the specific aerosol type typically encountered at the site. At the Jungfraujoch, located in the Swiss

Alps at 3,580 m a.s.l., mainly free tropospheric aerosol with injections from the planetary boundary layer and long-range transported mineral dust was studied using data of a one-month intensive field campaign carried out in May 2008. At the Zeppelin station in Ny-Ålesund, located in Spitsbergen at 78.5°N and 475 m a.s.l. in the Arctic, mainly clean Arctic aerosol with influence of sea salt transported up to the measurement site was measured within July and October 2008. At last, the influence of RH on the aerosol light scattering was investigated at Cabauw, located in a rural area in the Netherlands, using results from a comprehensive field campaign carried out during 4 months in summer and fall 2009. Here, a large variety of aerosol types were encountered, ranging from continental, urban to maritime clean and polluted aerosol.

At these three sites, the  $f(\text{RH})$  varied between approx. 1.3 to 6.6 (at RH=85 % and at  $\lambda=550$  nm). The lowest values of  $f(\text{RH})$  were observed for long-range transported Saharan dust at the Jungfraujoch and for polluted aerosol encountered at Cabauw, while the largest values of  $f(\text{RH})$  were measured for clean maritime and Arctic aerosol at Ny-Ålesund. The relative contributions of the accumulation to coarse mode and its chemical composition determined the magnitude of  $f(\text{RH})$ . At the Jungfraujoch, the coarse mode was most probably attributed to non-hygroscopic mineral dust whereas at Cabauw and Ny-Ålesund it was dominated by hygroscopic sea salt. Sea salt was not observed at the Jungfraujoch, which explains the absence of hysteresis effects of the hygroscopic growth that were observed at the other two sites. The accumulation mode was dominated either by low-hygroscopic organic substances, non-hygroscopic black carbon, or by hygroscopic inorganic salts. The interdependence between size and hygroscopicity can lead to compensation effects of  $f(\text{RH})$  as observed at Ny-Ålesund and explained by model calculations. Both, the size and the chemical composition, are important to predict  $f(\text{RH})$ .

The importance of the scattering enhancement for the validation of remote-sensing with in-situ measurements is shown. The ambient aerosol extinction coefficients measured in-situ were compared to MAX-DOAS (multi-axis differential optical absorption spectroscopy) and LIDAR (light detection and ranging) measurements. Both are remote sensing techniques used to retrieve aerosol extinction profiles besides other atmospheric parameters. The correlations between both remote sensing techniques and the in-situ measurements were good. However, the MAX-DOAS retrieval showed a systematic difference for most of the cases depending on the MAX-DOAS retrieval algorithm applied. Best agreement between MAX-DOAS and in-situ was achieved for low aerosol optical depths and low planetary boundary layer heights. These are important findings especially for the novel MAX-DOAS profiling techniques. The agreement between LIDAR and in-situ measurements was generally better but the extinction coefficient had to be extrapolated to ground using the measured backscatter signal.

The results obtained here were also compared to a widely used aerosol optical database (OPAC) that is used in many different fields of atmospheric research. It was found that the measurement results obtained here differ from the values predicted by OPAC. Although different reasons were brought forward, these differences could also point towards the need for a revision concerning the hygroscopic growth as currently implemented in the OPAC database.

# Zusammenfassung

Atmosphärische Aerosole sind feste oder flüssige in der Luft schwebende Teilchen, die allgemein auch als Feinstaub bekannt sind. Zwar sind sie klein und kaum sichtbar für unser Auge, können jedoch einen negativen Einfluss auf unsere Gesundheit und das Klima unserer Erde haben. Menschlich verursachte Emissionen von Treibhausgasen, wie z.B. Kohlendioxid oder Methan, aber auch die Emissionen von Aerosolen haben unser Erdklima nachweislich verändert. Anthropogene - also menschlich verursachte - Aerosole streuen und absorbieren zusätzlich solare Strahlung und beeinflussen damit direkt den Strahlungshaushalt der Erde. Zusätzlich beeinflussen sie auch die Wolkenbildung, denn anthropogene Aerosole ändern die Strahlungseigenschaften, aber auch die Lebensdauer und Niederschlagseigenschaften der Wolken. Im Gegensatz zu Treibhausgasen bewirken die Aerosole einen negativen Strahlungsantrieb, d.h. sie haben einen kühlenden Einfluss auf unser Klima, da sie vermehrt Strahlung zurück in den Weltraum streuen. Der *Zwischenstaatliche Ausschuss für Klimaänderungen* (IPCC) der Vereinten Nationen hält in seinem letzten Bericht fest, dass die Unsicherheiten im Gesamtstrahlungsantrieb aller wichtigen Klimakomponenten (also Treibhausgase, Aerosole, Änderungen der Erdoberfläche, sowie natürliche Quellen) von den grossen Unsicherheiten des Strahlungsantriebs der Aerosole dominiert werden. Dies ist überwiegend auf die unterschiedlichen zeitlichen und räumlichen Skalen aber auch auf die grosse Vielfalt in deren Zusammensetzung zurückzuführen. Im Allgemeinen sind die verschiedenen Aerosolprozesse noch wenig verstanden. Da Aerosole auch Wasser aufnehmen können, ist ihre Grösse und chemische Zusammensetzung abhängig von der relativen Luftfeuchte (RH). Dies hat wiederum einen direkten Einfluss auf die optischen Eigenschaften der Aerosole und damit auch auf ihren direkten Strahlungsantrieb.

Langzeitmessungen von optischen und mikrophysikalischen Aerosoleigenschaften werden aufgrund des Feuchteeffektes meist unter trockenen Bedingungen durchgeführt. Besonders der Lichtstreuoeffizient des Aerosols  $\sigma_{sp}(\lambda)$  als Funktion der Wellenlänge  $\lambda$  ist stark von der RH abhängig und wird daher bei Langzeitmessungen immer trocken gemessen. Die Abhängigkeit von  $\sigma_{sp}(\lambda)$  gegenüber RH ist jedoch wichtig, um den tatsächlichen Aussenwert zu bestimmen, der wiederum für eine genaue Berechnung des Strahlungsantriebes nötig ist. Zudem ist das Wissen über die RH-Abhängigkeit von  $\sigma_{sp}(\lambda)$  wichtig für den Vergleich von Fernerkundungsmethoden mit in-situ Messungen (Punktmessungen).

Der Feuchtefaktor der Lichtstreuung  $f(RH, \lambda)$  ist einer der Hauptgrössen bei der Bestimmung des RH-Einflusses auf den Streukoeffizienten. Er ist definiert als der Aerosolstreuoeffizient  $\sigma_{sp}(RH, \lambda)$  gemessen bei einer bestimmten Feuchte, dividiert durch den trockenen Aerosolstreuoeffizienten  $\sigma_{sp}(dry, \lambda)$ . Die Grösse von  $f(RH, \lambda)$  hängt hauptsächlich von der Grössenverteilung und der chemi-

schen Zusammensetzung des Aerosols ab.  $f(\text{RH}, \lambda)$  kann u.a. mit einem feuchtereguliertem Nephelometer gemessen oder auch mittels Mie-Theorie berechnet werden.

Im Rahmen dieser Arbeit wurde der Einfluss der relativen Feuchte auf die Lichtstreuung des Aerosols für Messungen an drei europäischen Standorten untersucht. Die Stationen wurden gemäss des Aerosoltyps ausgewählt, welcher dort überwiegend vorzufinden ist. Zuerst wurden Messungen vom Jungfraujoch, welches auf 3580 m (ü.d.M.) in den Schweizer Alpen liegt, analysiert. Dort wurde überwiegend Aerosol aus der freien Troposphäre und vereinzelt weittransportierter Wüstenstaub gemessen. In Ny-Ålesund, das auf Spitzbergen in der Arktis liegt, wurde hauptsächlich sehr sauberes, arktisches Aerosol und Seesalz beobachtet. In Cabauw, das in einer ländlichen Gegend in den Niederlanden liegt, wurde, während einer umfangreichen viermonatigen Messkampagne im Sommer und Herbst 2009, eine grosse Vielfalt verschiedenster Aerosoltypen gemessen. Diese reichten von sauberem Seesalz bis hin zu verschmutztem Aerosol, welches aus den verschiedensten Industrie- und Siedlungsgebieten bis nach Cabauw transportiert wurde.

Der gemessene Feuchtefaktor  $f(\text{RH}, \lambda)$  variierte an den drei Standorten zwischen ca. 1.3 und 6.6 (bei  $\text{RH}=85\%$  und  $\lambda = 550 \text{ nm}$ ). Die kleinsten Werte von  $f(\text{RH}, \lambda)$  wurden bei fern-transportiertem Wüstenstaub am Jungfraujoch und bei stark verschmutztem Aerosol in Cabauw gemessen, während sauberes arktisches und reines Seesalz in Cabauw oder in Ny-Ålesund mit den höchsten Werten von  $f(\text{RH}, \lambda)$  ausgezeichnet war. Die relativen Beiträge aus den unterschiedlichen Moden der Grössenverteilung und ihre chemische Zusammensetzung bestimmten die Grösse von  $f(\text{RH}, \lambda)$ . Auf dem Jungfraujoch wurden Partikel mit Durchmesser grösser als ca.  $1 \mu\text{m}$  hauptsächlich durch nicht-hygrokopischen Mineralstaub bestimmt, während sie in Ny-Ålesund und Cabauw überwiegend aus sehr hygrokopischen Seesalz bestanden. Auf dem Jungfraujoch wurde kein Seesalz beobachtet und daher wurde auch keine Hysterese in den gemessenen Feuchtefaktoren beobachtet. Partikel kleiner als ca.  $1 \mu\text{m}$  waren entweder durch nicht-hygrokopischen Russ, schwach-hygrokopisches organisches Material oder hygrokopische anorganische Salze bestimmt. Durch die Nichtlinearität der Mie-Streuung kann es zu kompensierenden Effekten zwischen Grösse und chemischer Mischung kommen, was in Ny-Ålesund auch tatsächlich beobachtet wurde. Für eine genaue Vorhersage von  $f(\text{RH}, \lambda)$  ist deshalb die Kenntnis der Grössenverteilung und der chemischen Zusammensetzung unabdingbar.

Im Rahmen dieser Arbeit war es möglich, die in-situ gemessenen Extinktionskoeffizienten auf Ausserbedingungen zurückzurechnen und mit Messungen von zwei verschiedenen Fernerkundungsmethoden zu vergleichen. MAX-DOAS (multi axis differential absorption spectroscopy) und LIDAR (light detection and ranging) ermöglichen die Ableitung von Höhenprofilen des Aerosolextinktionskoeffizienten. Für den überwiegenden Teil des Messdaten zeigte sich ein systematischer Unterschied zwischen MAX-DOAS und den in-situ Messungen, während es nur bei geringer Grenzschichthöhe und geringer aerosoloptischer Tiefe zu einer Übereinstimmung kam. Der Vergleich von LIDAR und in-situ Daten ist komplizierter, da der Extinktionskoeffizient vom LIDAR erst ab einer gewissen Höhe abgeleitet werden kann. Allerdings konnte mit einer Extrapolationsmethode eine verbesserte Übereinstimmung zwischen LIDAR und in-situ Messungen im Vergleich zu MAX-DOAS erreicht werden.

Die hier durchgeführten Messungen wurden zudem mit Modelldaten verglichen. Es zeigte sich, dass die Messungen zu den Daten der OPAC Datenbank nicht übereinstimmten, was wahrscheinlich auf die implementierten Wachstumsfaktoren zurückzuführen ist.



## Chapter 1

# Introduction

Since aerosols are a major player governing the Earth's climate, influence the visibility, and also have an adverse health effects on humans, their properties and processes are an important field of scientific study. This thesis deals with the water uptake of aerosols, which directly influences all the different aerosol properties and processes. Here, the focus is set on the influence of the water uptake on aerosol light scattering, which is needed to better constrain the impact of aerosols in the Earth's radiative budget.

An overview on the main sources, sinks, processes, and properties of aerosols will be given in Sect. 1.1. This will be followed by a discussion on the effect of aerosols on the Earth's climate and how water uptake plays its part in influencing the radiative properties (Sect. 1.2). A short overview on the motivation and on the investigated sites is given in Sect. 1.3.

### 1.1 Atmospheric aerosols

An *aerosol* is technically defined as a suspension of liquid or solid particles in a gas (Seinfeld and Pandis, 2006). They originate from different sources, are exposed to different kinds of processes in the atmosphere, and are removed from it by various sinks. Their atmospheric lifetime of a few days to a few weeks is relatively short, compared to the one of greenhouse gases with lifetimes that range up to several years or even centuries. The combination of specific sources and short lifetimes of aerosols explains their highly non-uniform distribution around the globe.

The size of aerosol particles ranges from a few nanometers to several hundreds of micrometers. In general, the aerosol size distribution is characterized by different size modes, which are specific concerning their sources, their different transformation and removal processes. Figure 1.1 shows a schematic three modal surface size distribution with an overview on the relevant processes and example images of typical aerosol particles found in these modes (adapted from Whitby and Cantrell, 1976; Seinfeld and Pandis, 2006; Heintzenberg et al., 2003). The first and fundamental separation is made between the *fine mode* (particle diameter  $D < 2.5 \mu\text{m}$ ) and the *coarse mode* ( $D > 2.5 \mu\text{m}$ ). The main removal process of the coarse mode is sedimentation due to their larger size and mass, which is usually accompanied by short residence times in the atmosphere. A further separation of the fine mode is done by defining the *nucleation mode* for very small particles with approx.  $D < 10 \text{ nm}$  that are freshly nucleated

particles. This is being followed by the *Aitken mode* for particles between approx.  $10\text{ nm} < D < 0.1\ \mu\text{m}$  and by defining the *accumulation mode* for particles between  $0.1 < D < 2.5\ \mu\text{m}$ . The nucleation mode is characterized by a high number concentration of particles that mainly originate from gas-to-particle conversion of hot vapors (e.g. from combustion processes) and are lost through coagulation to the accumulation mode. In this transient mode, the particles accumulate (low efficiency in particle removal) either from coagulated particles from the nucleation mode or they are exposed through growth by condensation of vapors on existing particles. Here, the main removal mechanism is rain-out (in-cloud scavenging, e.g. by forming cloud droplets) or washout (collision with rain droplets or snow flakes).

When describing the sources of atmospheric aerosol, one has to first differentiate between natural and anthropogenic, and also between primary (emitted directly into the atmosphere) and secondary particles (formed in the atmosphere through gas-to-particle conversion). The main natural source of primary particles is sea salt, which is emitted from the oceans by evaporated sea spray. Mineral dust, originating from arid and semi-arid regions of the world, is the second important contributor of natural primary particles. Volcanic dust and biogenic particles (e.g. pollen or other plant material) are further natural primary particles that are emitted. All these natural primary particles are mainly found in the coarse mode of the aerosol size distribution (see Fig. 1.1). Typically natural sources of secondary aerosol are the biosphere (e.g. the oceans) and volcanoes that emit sulfur e.g. in form of dimethyl sulfide (DMS) and sulfur dioxide into the atmosphere which can be oxidized to sulfate and form new particles. The biosphere can also emit volatile organic compounds (VOC) that can be oxidized and are able to form new particles. Anthropogenic emissions of primary particles include industrial dust, black carbon from (incomplete) combustion and organic material. Secondary aerosol sources of anthropogenic origin include sulfates from  $\text{SO}_2$  emissions, biomass burning, organics from anthropogenic VOC's, ammonia emissions, and nitrates from nitrogen oxides. These can e.g. be emitted through domestic heating using coal or wood, from industrial plants, from vehicle emissions, from agricultural activities, or from large forest fires. Although the global emissions are dominated by the natural sources (Seinfeld and Pandis (2006) give an estimate of 3100 Tg/year), they are mainly related to contributions from the coarse mode, while the emissions from anthropogenic sources (Seinfeld and Pandis (2006) estimate 450 Tg/year) are mainly contributions from the fine mode (with correspondingly higher number concentrations).

Anthropogenic emissions of aerosol particles have many effects on the environment. These are for example linked with adverse health effects on humans, since particles can enter the human respiratory and cardiovascular system, where they may cause damage on cells and organs. Several studies (e.g., Laden et al., 2006; Pope III and Dockery, 2006; Pope III et al., 2002; Dockery et al., 1993) and also historic reviews (e.g., Brimblecombe, 1987, on air pollution during medieval times and on the great London smog in 1952) have shown the relationship between air pollution and an increased rate of mortality.

Visibility degradation is another example on the impact of air pollution on the environment (e.g., Malm et al., 1994; Charlson, 1969). In a particle-free atmosphere the best visibility is approximately 296 km at sea level (Seinfeld and Pandis, 2006) which then is only limited by the Rayleigh scattering of air molecules. The visibility can be downgraded under the presence of aerosols (causing additional scattering and absorption of light) to a few kilometers or even to a few hundreds of meters e.g. in very polluted cities. Also the water uptake ability of the aerosol has a major influence on the visibility. This

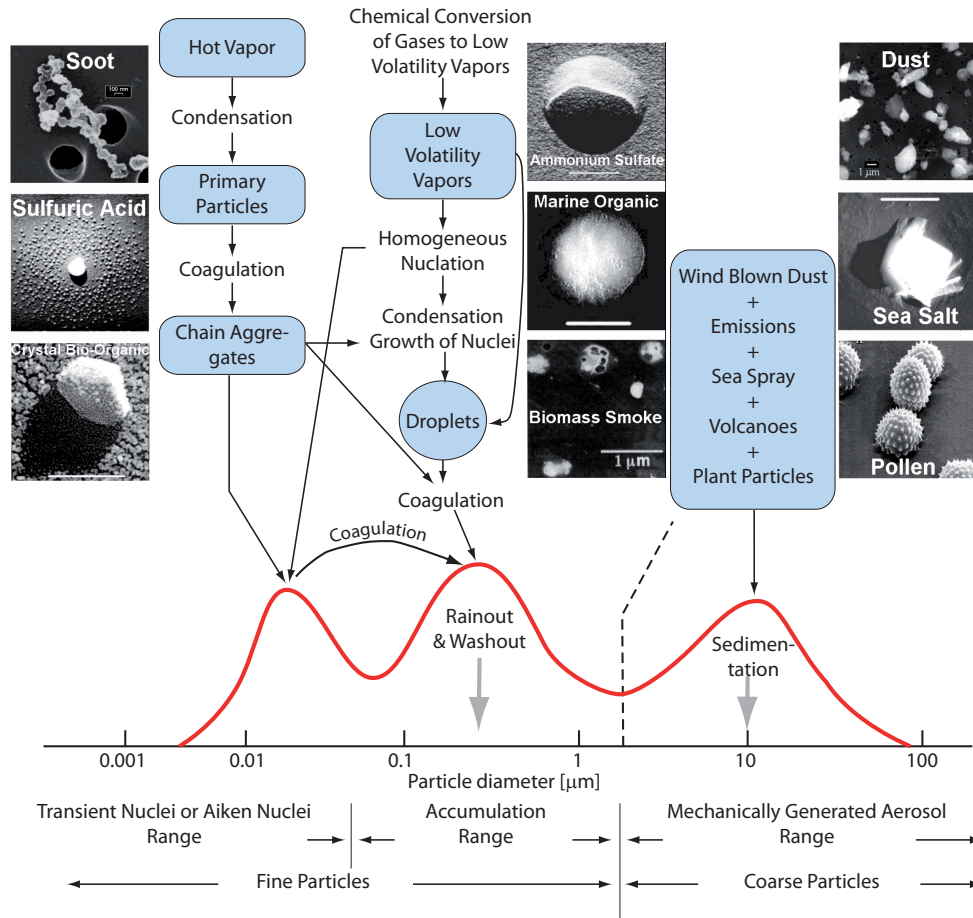


Figure 1.1: Principal modes, sources, and particle formation and removal mechanisms shown for an idealized aerosol surface size distribution (adapted from Whitby and Cantrell, 1976; Seinfeld and Pandis, 2006). Shown are also example images of single aerosol particles (taken from Heintzenberg et al., 2003).

can e.g. be nicely observed during Foehn wind conditions at the downwind site of high mountains when visibility is increased due to the reduced scattering of (dry) aerosol particles.

## 1.2 How aerosols effect the Earth's climate

Since the industrial revolution the atmospheric concentrations of greenhouse gases, like carbon dioxide ( $\text{CO}_2$ ), methane ( $\text{CH}_4$ ), nitrous oxide ( $\text{N}_2\text{O}$ ) or halocarbons (like chlorofluorocarbons (CFC's) used in refrigerators) and of anthropogenic aerosol particles have increased and with this humans have contributed to climate change. Greenhouse gases and aerosols affect our climate by altering the incoming solar radiation (shortwave) and outgoing infrared (longwave) radiation that are part of the Earth's energy balance (IPCC, 2007).

The *radiative forcing*  $\Delta F$  is commonly used to compare the magnitude of different anthropogenic and natural agents causing climate change. It is usually defined as the stratospherically adjusted radiative flux change (in units  $\text{Wm}^{-2}$ ) evaluated at the tropopause (IPCC, 2007). One can also define  $\Delta F$  at

the top of the atmosphere (TOA) or at surface level (see e.g., Ramanathan et al., 2001). The radiative forcing is linearly related to the mean equilibrium surface temperature (Seinfeld and Pandis, 2006). A positive sign of  $\Delta F$  indicates a global mean surface warming, while a negative sign indicates a cooling effect.

Figure 1.2 from the current *Intergovernmental Panel on Climate Change Fourth Assessment Report* (IPCC, 2007) summarizes the main components that contribute to the radiative forcing of climate change compared with pre-industrial times (~1750) and today (2005). The greenhouse gases have a warming effect (positive  $\Delta F$ ), with CO<sub>2</sub> as the largest contributor, followed by CH<sub>4</sub>, N<sub>2</sub>O, halocarbons, and tropospheric ozone. The level of scientific understanding is assumed to be medium to high (which is also reflected in smaller uncertainties in Fig. 1.2). Aerosols in contrast are showing a negative radiative forcing (a cooling effect). This is on the one hand caused by the *direct effect* of aerosols, because aerosols additionally scatter and absorb short- and longwave radiation, and on the other hand caused by *indirect effects*, because aerosols modify the microphysical and radiative properties of clouds (Schwartz, 1996). Here, the level of scientific understanding of the total aerosol effect is rather low to medium (also reflected in the larger uncertainties). The main reason for these large uncertainties is the high spatial and temporal variability of aerosols and their indirect effects. These large uncertainties in the total aerosol effect also propagate when combining all anthropogenic radiative forcing effects, which in total is estimated to be  $+1.6 [-1.0, +0.8] \text{ Wm}^{-2}$  (the values in brackets give the 90% upper and lower confidence range). Figure 1.2 also includes the radiative forcing caused by changes in the surface albedo (surface reflectance), which has been caused by human induced changes in land (agriculture, forest clearance, etc.) and ice cover (e.g. darker and reduced ice shields). Besides anthropogenic forcings also natural forcings exist. This can e.g. be changes in the solar radiation or by volcanic eruptions that emit sulphate aerosol into the stratosphere causing a negative forcing. However, these natural forcings are very small compared to the anthropogenic ones since the start of the industrial era. As a result, IPCC (2007) emphasizes that the anthropogenic radiative forcing is much more important for current climate change than the natural forcings. The quantification of the radiative forcing and of other climate influences of aerosols is of high priority for relating historical climate change to increasing greenhouse gases and determining the Earth's climate sensitivity (Ghan and Schwartz, 2007).

### 1.2.1 Aerosol direct effect

As mentioned above, anthropogenic aerosol particles additionally scatter and absorb solar and terrestrial radiation. This leads to an increased reflection of solar radiation back to space (=increased surface albedo) and will lead mostly to a cooling but under certain conditions also to a warming of the surface. This effect is called the direct effect of aerosols. The effect of anthropogenic aerosols on outgoing longwave radiation is relatively minor (except for desert dust, see e.g., Ramanathan et al., 2001). The magnitude of the direct aerosol radiative forcing depends mainly on the aerosol composition (refractive index), its size distribution and concentration, and on the surface albedo (or reflectance) below the aerosol. Since aerosol particles can take up water and change their size and chemical composition, the effect on the incident radiation also strongly depends on the relative humidity, which is the main subject of the work.

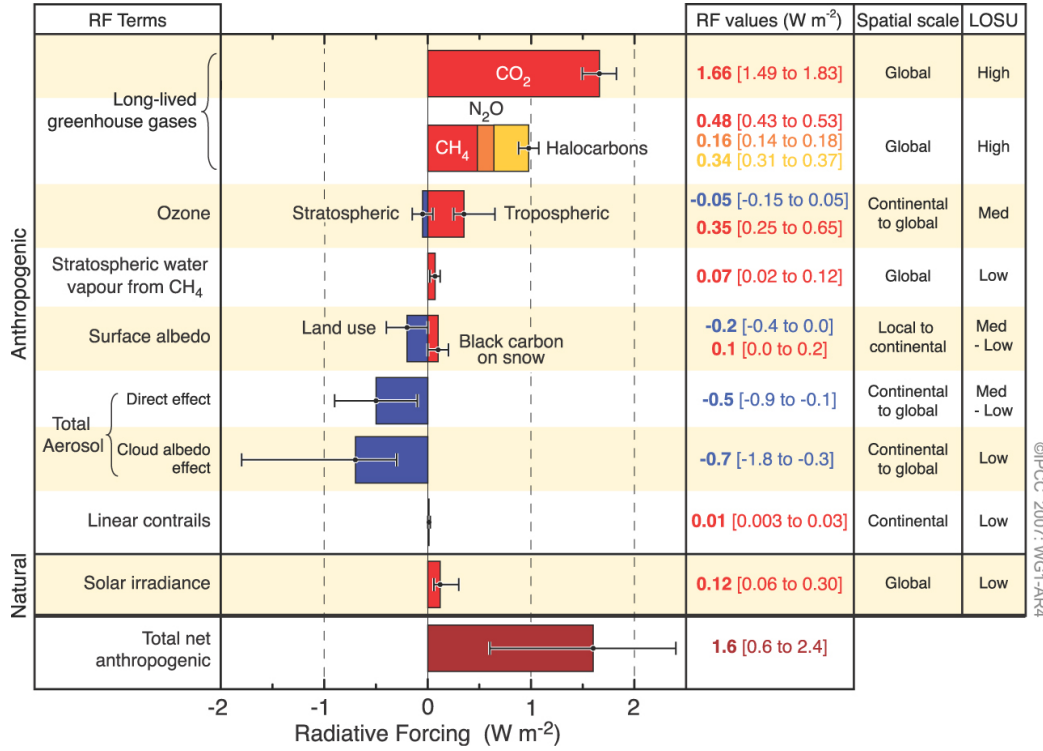


Figure 1.2: Summary of the principle components to the radiative forcing of climate change. These radiative forcing values are given for the year 2005 relative to the start of the industrialization (~1750). The error bars indicate the uncertainty of the respective forcing. Given are also the spatial scale and the level of scientific understanding (LOSU). The figure is taken from IPCC (2007).

Several theoretical equations or model studies have retrieved equations to estimate the direct radiative forcing of aerosols (e.g., Charlson et al., 1991, 1992; Schwartz, 1996; Haywood and Shine, 1995, 1997; Liou, 2002; Seinfeld and Pandis, 2006). Haywood and Shine (1995), for example, give for the TOA radiative forcing<sup>1</sup> of an optically thin partially absorbing aerosol layer the following equation:

$$\Delta F \approx -\tilde{D}S_0T_{\text{at}}^2(1 - A_c)\omega_0\bar{\beta}\tau_a \left( (1 - R_s)^2 - \frac{2R_s}{\bar{\beta}} \left( \frac{1}{\omega_0} - 1 \right) \right), \quad (1.1)$$

where  $\tilde{D}$  is the fractional day length,  $S_0$  the solar constant (direct solar irradiance at the top of the atmosphere),  $T_{\text{at}}$  the atmospheric transmission (caused by air molecules),  $A_c$  the fractional cloud amount,  $\omega_0$  the spectrally weighted single scattering albedo (fraction of scattered to total extinction, see Eq. 2.33),  $\bar{\beta}$  the spectrally weighted backscattered fraction (fraction of upward scattered light relative to the local horizon),  $\tau_a$  the spectrally weighted aerosol optical depth (see Eq. 2.30), and  $R_s$  the surface reflectance (fraction of incoming radiation reflected by the surface).

Equation 1.1 might produce a negative (cooling) or positive (warming) value for the radiative forcing, depending on the critical single scattering albedo  $\omega_0^{\text{crit}}$  (which follows from Eq. 1.1 if  $\Delta F = 0$ ):

<sup>1</sup>The direct radiative forcing due to tropospheric aerosols is (in contrast to greenhouse gases)  $\Delta F$  most frequently derived at TOA instead at the tropopause (as defined above) because radiative transfer calculations have shown that the differences are negligible (Haywood and Shine, 1997; IPCC, 2007).

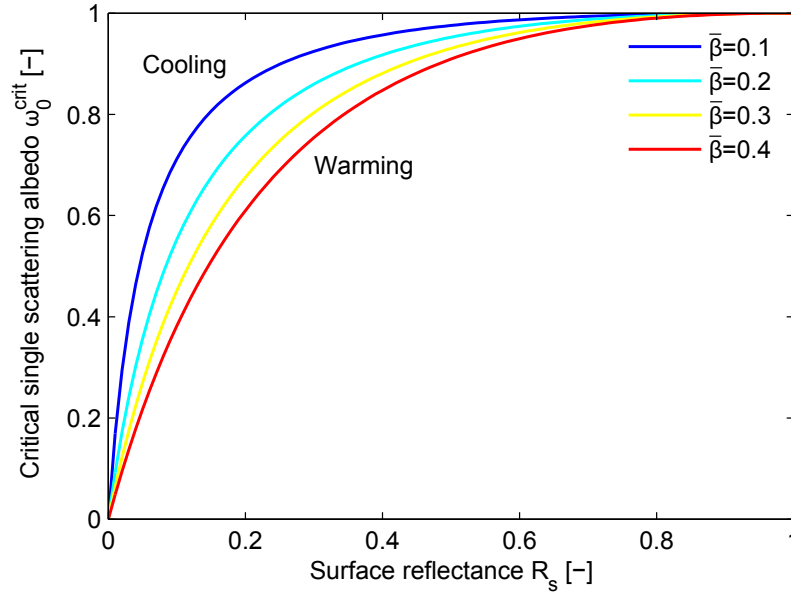


Figure 1.3: The critical single scattering albedo  $\omega_0^{\text{crit}}$  (at which the aerosol radiative forcing changes sign) as a function of surface reflectance  $R_s$  and the backscatter fraction  $\bar{\beta}$ . Figure adapted from Haywood and Shine (1995).

$$\omega_0^{\text{crit}} = \frac{2R_s}{\bar{\beta}(1-R_s)^2 + 2R_s}. \quad (1.2)$$

The critical single scattering albedo versus surface reflectance for different upscatter fractions is shown in Fig. 1.3. As can be seen, the warming or cooling effect depends besides the aerosol upscatter fraction, which is determined mainly by the aerosol size but as well as by the composition (refractive index), also on the surface properties below the aerosol. Dark aerosol (e.g. soot) over bright surfaces (e.g. snow) will lead to a warming effect (positive forcing), while brighter aerosol (e.g. mineral dust) over dark surfaces (e.g. oceans) will lead to a cooling effect (negative forcing) because more incident light is scattered back to space compared to the same surface without the specific aerosol layer.

### 1.2.2 Aerosol indirect effects

Aerosol particles are needed to form clouds, since they serve as a cloud and ice condensation nuclei (see Sect. 2.1). Anthropogenic emissions lead to an increase in particle number concentration with different sizes and different chemical compositions. This changes the ability of the aerosol particle to act as a cloud condensation nuclei and this has a major influence on the cloud radiative properties, their lifetime and the total amount of clouds. Different effects are being distinguished:

The *cloud albedo effect* (Lohmann and Feichter, 2005) - which is also called the *first indirect effect* (Ramaswamy et al., 2001) or the *Twomey effect* (Twomey, 1977) - describes the effect that an increase in particle number concentration (with a fixed liquid water content) will lead to an increase in cloud droplet number with smaller diameters, which will lead to a brighter cloud. The brighter cloud will lead to an increase in the reflection of solar radiation and thus will lead to a climate cooling. This effect is considered to be a direct radiative forcing (IPCC, 2007) and is estimated to be  $-0.7\text{Wm}^{-2}$  on a global

average and contributes to the total anthropogenic radiative forcing with the largest uncertainty (see Fig. 1.2).

The *cloud lifetime effect* (Lohmann and Feichter, 2005) - which is also called the *second indirect effect* or *Albrecht effect* (Ramaswamy et al., 2001) - summarizes different microphysically induced effects on the cloud liquid water content, its lifetime and height. Smaller and more cloud droplets may lead on the one hand to a brighter cloud, but on the other hand also to a cloud with a reduced precipitation efficiency. This suppression of precipitation in a polluted cloud will cause an increase in cloud life time and in turn to an increase in the amount of clouds (Ramanathan et al., 2001), which eventually will lead to further reflection of solar radiation and a cooling effect.

The absorption of solar (shortwave) radiation will be followed by a heating of the aerosol which will decrease the RH in the surrounding and thus may result in an evaporation of the cloud droplet. This heating can also change the stability of the troposphere and thus may suppress convection. This *semi-direct effect* (Lohmann and Feichter, 2005) can lead to a reduced cloud cover and thereby to a positive radiative forcing. Both, the *cloud life time effect* and the *semi-direct effect* are not considered as a radiative forcing (IPCC, 2007), because feedback mechanisms occur (e.g. the hydrological cycle has been altered).

In addition, there are several further effects on clouds due to anthropogenic pollution (see e.g., Lohmann and Feichter, 2005, for further details), which are not discussed here.

### 1.2.3 Effects of relative humidity on aerosol light scattering

All of the aerosol parameters governing the direct aerosol radiative forcing in Eq. 1.1 depend on the relative humidity (RH), since aerosol particles can take up water and with this change their size and chemical composition. This has a direct influence on their optical properties and therefore also on the direct radiative forcing. The scattering enhancement factor  $f(\text{RH}, \lambda)$  is the key parameter that describes the RH-dependency of the aerosol light scattering and is defined as:

$$f(\text{RH}, \lambda) = \frac{\sigma_{\text{sp}}(\text{RH}, \lambda)}{\sigma_{\text{sp}}(\text{RH}_{\text{dry}}, \lambda)}, \quad (1.3)$$

where  $\sigma_{\text{sp}}(\text{RH}, \lambda)$  is the scattering coefficient at a certain RH and wavelength  $\lambda$  and  $\sigma_{\text{sp}}(\text{RH}_{\text{dry}}, \lambda)$  is the corresponding dry scattering coefficient (for a definition of  $\sigma_{\text{sp}}$  see Sect. 2.2).  $f(\text{RH}, \lambda)$  will increase with increasing RH and will be  $\geq 1$ , if the particles do not experience significant restructuring when taking up water. It depends on the size and on the chemical composition of the particle, because both parameters determine the scattering properties and its ability to take up water.

As an example, Fig. 1.4 shows  $f(\text{RH}, \lambda)$  for different inorganic salts and for a typical organic substance calculated via Mie theory (see Sect. 2.2.2) at a fixed RH of 85% (assuming a single lognormal size distribution with a width of 1.8). It can be seen, that both the size and the chemical composition matter when determining the scattering enhancement. The chemical composition is important for the refractive index, and even more important for the actual hygroscopic growth of the particle (see Sect. 2.1). Sodium chloride is one of the most hygroscopic salts and therefore shows the largest values of  $f(\text{RH}, \lambda)$ , e.g. a lognormal distribution of pure NaCl particle with a mode diameter of 100 nm will

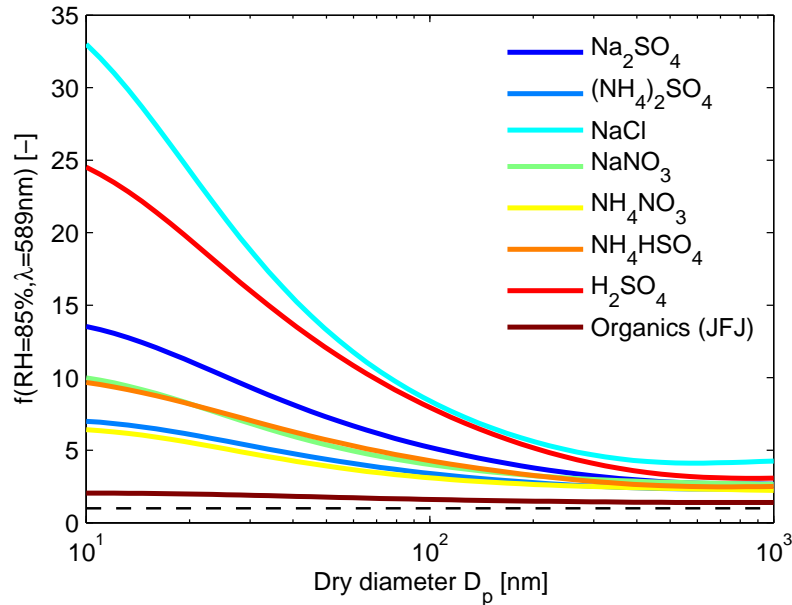


Figure 1.4: The scattering enhancement  $f(\text{RH})$  at  $\text{RH}=80\%$  and  $\lambda=589\text{ nm}$  vs. dry particle diameter calculated for different inorganic salts (see legend) and for organics (typically found at the Jungfraujoch, JFJ). The hygroscopic growth factors were taken from Topping et al. (2005); Sjogren et al. (2008) and the refractive index from Seinfeld and Pandis (2006); Nessler et al. (2005a).

scatter at 85 % RH approximately eight times more compared to dry conditions.

In the atmosphere, aerosol particles will always be encountered as mixtures with varying microphysical properties. To illustrate the possible magnitude of  $f(\text{RH}, \lambda)$  with RH, Fig. 1.5 shows  $f(\text{RH}, \lambda)$  for different aerosol types, which have been calculated via Mie theory using the widely used OPAC database (Hess et al., 1998, OPAC: Optical Properties of Aerosol and Clouds)<sup>2</sup> for typical aerosol types as proposed therein. It can be seen that the maritime and Arctic aerosol types exhibit the largest values of  $f(\text{RH}, \lambda)$ , since their composition is dominated by hygroscopic components like sea salt. Continental and urban aerosols typically contain less- or non-hygroscopic substances (like organics or soot) and are therefore characterized by a reduced  $f(\text{RH}, \lambda)$ . Desert aerosol mainly consists of non-hygroscopic mineral dust and has therefore the lowest values of  $f(\text{RH}, \lambda)$ .

There is also an RH enhancement of the aerosol light absorption, however, the scattering enhancement is clearly the dominant part, especially concerning the single scattering albedo and the aerosol extinction coefficient (see Sect. 2.2), where the contribution of the absorption is negligible (Nessler et al., 2005b). As seen from the direct aerosol radiative forcing (Eq. 1.1), an increase in RH will lead to an increase in the aerosol optical depth and in the single scattering albedo, but will lead to a decrease in the upscatter fraction (larger particles scatter more into the forward direction). Overall, the first two factors are prevailing and this will lead to a decrease (remind the negative sign) of the radiative forcing and therefore to a larger cooling effect, if the RH is increased, while the surface reflectance and the (hygroscopic) aerosol type are assumed to stay unchanged (see also Sect. 3.3.3).

The influence of RH on the aerosol light scattering can be measured using humidified nephelome-

<sup>2</sup>A detailed discussion on the OPAC database with a focus on the implemented hygroscopic growth and a comparison to the measurement results of  $f(\text{RH}, \lambda)$  obtained here will follow in Chapt. 6.



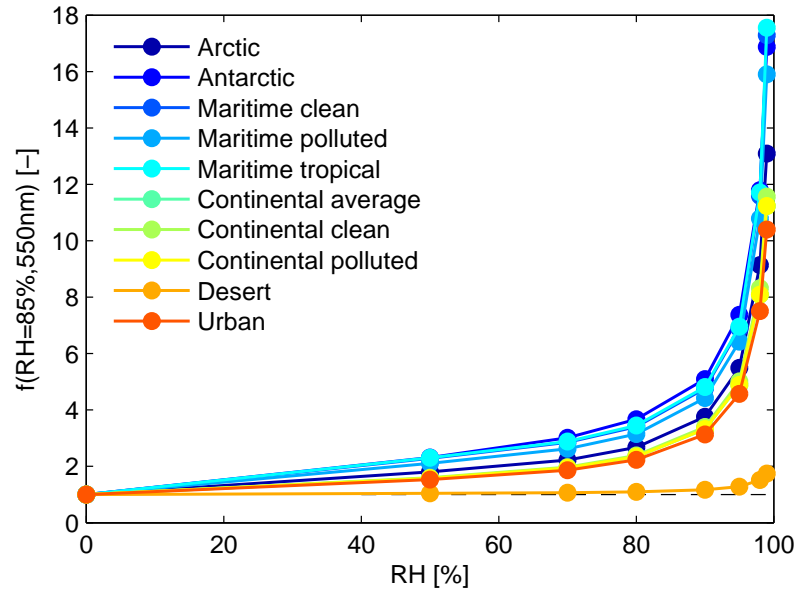


Figure 1.5: The scattering enhancement  $f(\text{RH})$  calculated at  $\lambda=550$  nm for different model aerosol types. The OPAC data used here is given only at eight discrete relative humidities (Hess et al., 1998).

ters. An overview on the historical development and on the different kind of techniques is given in Fierz (2010). Within this thesis, measurements of a newly developed humidified nephelometer (WetNeph) were used. The WetNeph was installed and characterized within the PhD work of Rahel Fierz-Schmidhauser. A brief description will follow in Sect. 3.2.2. A full technical description and comparison of mono-disperse salt measurements to model calculations can be found in Fierz-Schmidhauser et al. (2010).

### 1.3 Motivation and overview of the thesis

The knowledge of the scattering enhancement is important for several reasons. First of all, long-term measurements of physical and optical properties of aerosols are often performed at dry conditions in order to keep measurements comparable (e.g.  $\text{RH} < 30\text{--}40\%$  as recommended by WMO/GAW, 2003). These dry measurements differ from the ambient values, which are the climate relevant ones and are eventually needed to determine the aerosol direct radiative forcing. In addition, the knowledge of the RH-dependency is also needed for the comparison of ground-based measurements with other optical aerosol measurements (e.g. with LIDAR, MAX-DOAS or satellite retrieval), as will be shown in Chapt. 5. Furthermore, the RH effect is also important for the correction of satellite retrievals (e.g., Remer et al., 2005), or for the general use to improve climate models (e.g., Textor et al., 2006; Ghan and Schwartz, 2007; Chin et al., 2009).

The influence of relative humidity on aerosol light scattering was studied using measurement data from three intensive field campaigns carried out different European sites. Here, the focus was set on three sites<sup>3</sup>:

<sup>3</sup>As already mentioned, this work was related to the PhD thesis of Rahel Fierz-Schmidhauser (Fierz, 2010). Within her work, measurements and model studies were also performed at other sites, e.g. at the Black Forest in Germany (Fierz-

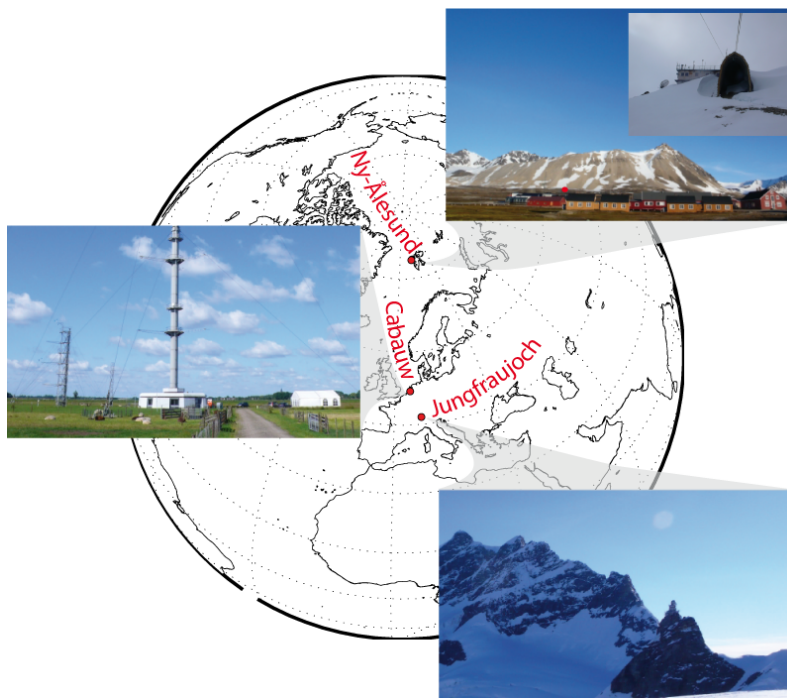


Figure 1.6: Overview on the investigated sites. The Jungfraujoch station is located in the Swiss Alps at 3580 m a.s.l. The measurements in the high Arctic were carried out at Ny-Ålesund, Spitsbergen. The instruments were installed at the Zeppelin station at an altitude of 475 m a.s.l. (see little photograph). Cabauw is located in the Netherlands. The inlet was at approx. 60 m a.s.l. while the in-situ instruments were located in the basement of the tower.

1. Jungfraujoch, mainly free tropospheric aerosol with injections from the planetary boundary layer and long-range transported mineral dust, see Chapt. 3.
2. Ny-Ålesund, mainly clean Arctic aerosol with influence of sea salt transported up to the measurement site, see Chapt. 4.
3. Cabauw, large variety of aerosol types encountered, ranging from continental, urban to maritime aerosol, see Chapt. 5.

An overview on the location and a picture of each site is seen in Fig. 1.6. The measurements were carried out at certain periods of the year (see Tab. 6.1 in Chapt. 6) and are at most only representative for these time periods and locations. However, the complexity of the observed aerosol (in terms of composition and variability) increased from Jungfraujoch to Ny-Ålesund and Cabauw. The results of all sites are finally discussed and compared to model data in Chapt. 6, which will end with some general conclusions and an outlook. The physical basis of this thesis is explained in Chapt. 2.

---

Schmidhauser et al., 2010) and at Mace Head, Ireland (Fierz-Schmidhauser et al., 2010a), where the author of this thesis partly contributed as well.

## Chapter 2

# The physical basis

### 2.1 Water uptake by aerosol particles

The water uptake by aerosol particles below water vapor saturation is usually described by the *hygroscopic growth factor*  $g(\text{RH})$  which is defined as

$$g(\text{RH}) = \frac{D_{\text{wet}}(\text{RH})}{D_{\text{dry}}}, \quad (2.1)$$

where  $D_{\text{dry}}$  is the dry particle diameter and  $D_{\text{wet}}(\text{RH})$  the diameter at a specific RH. The hygroscopic growth as a function of RH is described by Köhler theory (Köhler, 1936). Numerous textbooks cover the Köhler theory in detail (e.g., Seinfeld and Pandis, 2006; Pruppacher and Klett, 2010, where this chapter is partly based on). Here, only a brief description is being given. The relative humidity RH is defined as the vapor pressure  $e$  divided by the saturation vapor pressure  $e_0$  of water (at a certain temperature and over a flat surface), which can also be called the saturation ratio  $S$ :

$$\frac{\text{RH}}{100\%} = S = \frac{e}{e_0}. \quad (2.2)$$

Two effects have to be accounted for when determining the equilibrium RH above an aerosol droplet:

1. the Raoult's law (solute effect)
2. the Kelvin effect (curvature effect).

*Raoult's law* (or solute effect) states that the equilibrium vapor pressure  $e_{\text{sol}}$  over an aqueous solution (assuming a flat surface and an ideal solution without interaction between solvent and solution) is always lower than  $e_0$  and is a linear function of the solute concentration:

$$\frac{e_{\text{sol}}}{e_0} = \chi_w \quad \text{with} \quad \chi_w = \frac{n_w}{n_w + n_{\text{sol}}}, \quad (2.3)$$

where  $\chi_w$  is the mole fraction of water, which is calculated by taking the number of moles of water molecules  $n_w$  and solute molecules  $n_s$ , respectively.

For non-ideal solutions, the Raoult's law is modified by introducing the water activity coefficient  $\gamma_w$  in Eq. 2.3 (*modified Raoult's law*):

$$\frac{e_{\text{sol}}}{e_0} = \chi_w \gamma_w = a_w. \quad (2.4)$$

$\gamma_w$  is a function of substance, temperature, and the mole fractions of all solute substances in solution. The product of  $\chi_w \gamma_w$  is called *water activity*  $a_w$ .

The *Kelvin effect* (or curvature effect) states that the equilibrium vapor pressure over a curved surface  $e_K$  always exceeds the vapor pressure compared to the vapor pressure of the same solution with a flat surface. This is expressed by the *Kelvin equation*:

$$S_{\text{Kelvin}} = \frac{e_K}{e_0} = \exp\left(\frac{4\sigma_{\text{sol}}M_w}{RT\rho_w D}\right), \quad (2.5)$$

where  $\sigma_{\text{sol}}$  is the surface tension of the solution,  $M_w$  the molecular weight of water,  $\rho_w$  the density of water,  $R$  the ideal gas constant,  $T$  the temperature, and  $D$  the particle diameter.

According to Köhler theory, the saturation ratio  $S$  (or RH) relates to the droplet diameter  $D$  for an aqueous solution as follows:

$$S = \frac{e_d}{e_0} = a_w S_{\text{Kelvin}} = a_w \exp\left(\frac{4\sigma_{\text{sol}}M_w}{RT\rho_w D}\right), \quad (2.6)$$

which is a combination of the modified Raoult's law (Eq. 2.4) and the Kelvin equation (Eq. 2.5).

For dilute solutions, Eq. 2.6 can be approximated by:

$$\ln(S) = \ln\left(\frac{e_d}{e_0}\right) = \underbrace{\frac{A}{D}}_{\text{Kelvin}} - \underbrace{\frac{B}{D^3}}_{\text{Raoult}} \quad (2.7)$$

with  $A = \frac{4M_w\sigma_w}{RT\rho_w}$      $B = \frac{6n_{\text{sol}}M_w}{\pi\rho_w}$ ,

where the surface tension of the solute is approximated by the one of water ( $\sigma_w$ ). An example Köhler curve (calculated using Eq. 2.7) is shown in Fig. 2.1 for a NaCl particle with a dry size of  $D=50$  nm (and taking  $\sigma_w=0.072$  Jm<sup>-2</sup> at  $T=298$  K from Seinfeld and Pandis, 2006). The contributions of the Kelvin ( $S$  always above 1) and the Raoult effect ( $S$  always below 1) are shown separately. The Köhler curve shows a maximum at a certain diameter, which is called the *critical diameter*  $D_{\text{crit}}$ . The maximum is called *critical supersaturation ratio*  $S_{\text{crit}}$ . The Kelvin effect is the clearly dominant factor for larger droplets, while the Raoult effect is dominant for very small particles in relation to their dry size. On the rising part of the Köhler curve ( $D < D_{\text{crit}}$ ), droplets are in a stable equilibrium with their environment (Seinfeld and Pandis, 2006). This means that - at a fixed  $S$  - the droplet will stay at its original equilibrium state if it experiences small perturbations caused e.g. by the gain or loss of few water molecules. On the descending part of the Köhler curve ( $D > D_{\text{crit}}$ ), small perturbations, e.g. through additional water molecules, will lead to a larger size with a decreased equilibrium vapor pressure and with this, more water will condense on the droplet which will grow even further. Perturbations that result in a loss of

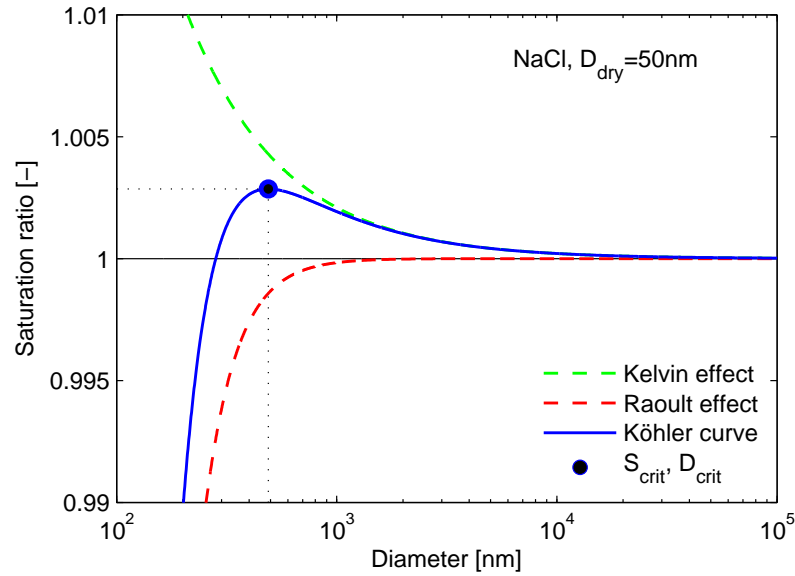


Figure 2.1: Köhler curve (Saturation ratio vs. particle diameter) of a sodium chloride (NaCl) particle with a dry size of  $D_{\text{dry}} = 50 \text{ nm}$  (at  $T = 298 \text{ K}$ ). The contributions of the Raoult effect (red curve) and the Kelvin effect (green curve) are shown. The critical saturation ratio  $S_{\text{crit}}$  and the corresponding critical diameter  $D_{\text{crit}}$  are indicated (blue bullet).

water molecules will lead to additional evaporation. A pure water droplet would evaporate completely, but if the droplet is a solution, it will (due to the Raoult effect) only evaporate until it reaches the diameter that corresponds to the stable equilibrium state on the ascending branch of the Köhler curve. Therefore, the droplets larger than the critical diameter are in unstable equilibrium states. Particles beyond the critical supersaturation ratio are considered to be cloud droplets (or activated particles).

The Kelvin effect is also responsible for the fact that the critical diameter decreases with decreasing dry particle size, while the critical supersaturation increases (for the same substance). This is also the reason why the hygroscopic growth factor decreases for smaller (dry) particles.

The hygroscopic growth described by Köhler theory is restricted to liquid particles. Inorganic and also some organic compounds can also form solid particles (crystals) at low RH. The state (liquid or crystal) has to be included when describing the hygroscopic growth. If the particle is dry and solid (e.g. a single NaCl crystal) it will start taking up water at a defined RH, called the deliquescence relative humidity (DRH). This sudden water uptake occurs at the RH where the Gibbs free energy of the wet particle becomes lower than the one of the dry particle. The droplet will take up water if the RH is further increased to maintain thermodynamic equilibrium (now the droplet follows the Köhler curve). The droplet will evaporate water if the RH is decreased. The phase transition from liquid to solid (crystallization) however does not occur at the DRH, the droplet rather stays supersaturated until it crystallizes at the efflorescence relative humidity (ERH). This can be explained by nucleation kinetics: the water needs to evaporate from the supersaturated droplet and a crystal needs to be formed through nucleation at a critical supersaturation. This hysteresis phenomenon is shown in Fig. 2.2 where the hygroscopic growth factor  $g(\text{RH})$  (see Eq. 2.1) for a NaCl particle (dry size  $D_{\text{dry}} = 100 \text{ nm}$ ) is shown. The DRH of a substance can be significantly lower or even fully suppressed if it is mixed with other components (e.g., Ming and Russell, 2001; Seinfeld and Pandis, 2006). The ERH may be at a larger RH

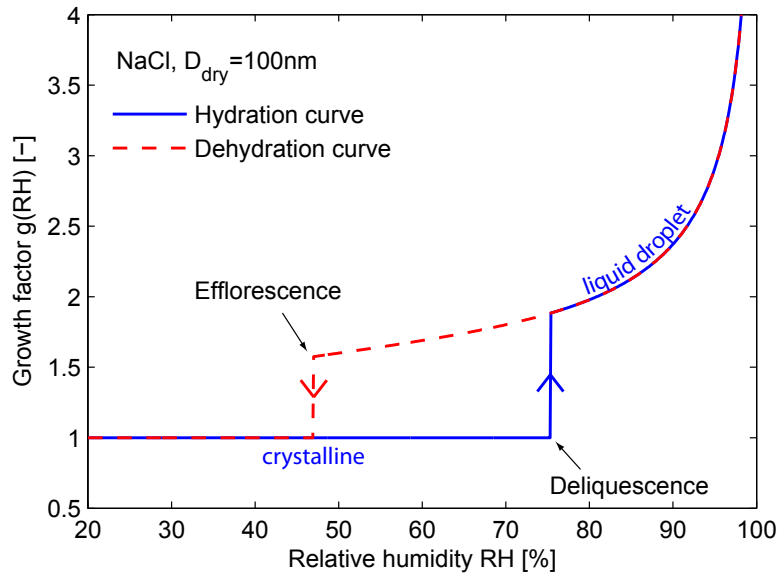


Figure 2.2: The hysteresis curve (hygroscopic growth factor vs. diameter) of a sodium chloride (NaCl) particle ( $D_{\text{dry}}=100$  nm). The  $g(\text{RH})$  has been taken from Topping et al. (2005). Starting from low relative humidity (RH) the particle is crystalline (solid) until it suddenly takes up water at the deliquescence relative humidity (DRH) (for NaCl at 75.3 % RH, Tang, 1996) and the NaCl particle becomes liquid. The liquid droplet takes up water beyond the DRH. Drying the particle (dehydration) leads to a shrinking and a re-crystallization at the efflorescence relative humidity (ERH) at around 46-48 % RH (Tang, 1996) for NaCl.

if the solution contains insoluble impurities (heterogeneous nucleation may take place).

Not all parameters needed to solve the Köhler equation are always known. So a simplified representation of the Köhler equation is often needed to calculate or predict the hygroscopic growth of aerosol particles. Within this work, the  $\kappa$ -Köhler theory, which is based on the work by (Petters and Kreidenweis, 2007, and references therein), has been chosen to parameterize the hygroscopic growth factor  $g(\text{RH})$ . Briefly, Petters and Kreidenweis (2007) use a semi-empirical parameterization for the water activity  $a_w$ :

$$a_w^{-1} = 1 + \kappa \frac{V_{\text{sol}}}{V_w}, \quad (2.8)$$

where  $\kappa$  is the hygroscopicity parameter,  $V_{\text{sol}}$  the volume of the dry particulate matter and  $V_w$  the volume of the water.  $\kappa$  ranges from 0 (non hygroscopic but wettable) to 1.4 (most hygroscopic, value for NaCl) and can be calculated for mixtures by applying a simple volume mixing rule (Stokes and Robinson, 1966). Equation 2.8 can be re-arranged and with Eq. 2.1 the parameterization for  $g(\text{RH})$  follows as:

$$g(a_w) = \left( 1 + \kappa \frac{a_w}{1 - a_w} \right)^{\frac{1}{3}}. \quad (2.9)$$

As known from the Köhler equation (Eq. 2.6), the water activity  $a_w$  can be obtained by dividing the

relative humidity RH (or saturation ratio  $S$ ) by the Kelvin term:

$$a_w = \frac{\text{RH}/100\%}{S_{\text{Kelvin}}} = \frac{\text{RH}/100\%}{\exp\left(\frac{4\sigma_{\text{sol}}M_w}{RT\rho_w D}\right)}. \quad (2.10)$$

If the Kelvin effect is omitted, Eq. 2.9 further simplifies to:

$$g(\text{RH}) = \left(1 + \kappa \frac{\text{RH}/100\%}{1 - \text{RH}/100\%}\right)^{\frac{1}{3}}. \quad (2.11)$$

This simplification is justified for our cases, because the Kelvin term is small for large particles ( $D > 100$  nm), which are important for light scattering.

## 2.2 Atmospheric absorption and scattering of solar radiation

Radiation is attenuated in the atmosphere through scattering and absorption by air molecules, aerosols, cloud and rain droplets, or ice crystals. If an electromagnetic wave hits a particle it will excite the electric charges inside the particle into a higher energetic state. The excited charges may reradiate the energy (scattering) or the radiation may partly be converted into thermal energy (absorption). The scattering process can be divided into elastic and inelastic scattering. For elastic scattering, the incident and outgoing wavelengths are equal, while for inelastic scattering they are different. Raman scattering e.g. used for certain LIDAR (light detection and ranging) applications is an inelastic process, that can only be explained by quantum mechanics. Here, only elastic scattering processes are of interest, because for most of the atmospheric scattering the frequency or wavelength stays unchanged.

The *extinction cross section*  $C_{\text{ext}}$  describes the hypothetical area of a particle normal to the incident light beam that should be intercepted to cause an extinction occurrence. Due to the conservation of energy  $C_{\text{ext}}$  is the sum of the *scattering* and the *absorption cross section*<sup>1</sup>:

$$C_{\text{ext}} = C_{\text{sca}} + C_{\text{abs}}. \quad (2.12)$$

Dividing the extinction cross section by the particle's cross-sectional area  $A$  gives the dimensionless *extinction efficiency*  $Q_{\text{ext}}$  of a particle:

$$Q_{\text{ext}} = \frac{C_{\text{ext}}}{A}, \quad (2.13)$$

where  $Q_{\text{ext}}$  is the sum of the scattering and absorption efficiency ( $Q_{\text{ext}} = Q_{\text{sca}} + Q_{\text{abs}}$ ).

The exponential attenuation of light through a certain medium (here: the atmosphere) can be described by the *Beer-Lambert law*:

$$I_d = I_0 e^{-s \cdot \sigma_{\text{ext}}}, \quad (2.14)$$

<sup>1</sup>All optical properties discussed here are dependent on the wavelength  $\lambda$ , which is omitted in this chapter and only explicitly mentioned when misinterpretation could occur.

where  $I_0$  and  $I_d$  are the intensities of the incident and the transmitted light, and  $s$  the length of the attenuating medium<sup>2</sup>. The coefficient  $\sigma_{\text{ext}}$  is called *extinction coefficient* (in units of  $\text{m}^{-1}$ ), which is the sum of the *scattering* and the *absorption coefficient* ( $\sigma_{\text{ext}} = \sigma_{\text{scat}} + \sigma_{\text{abs}}$ ).

For an atmospheric point of view, the extinction coefficient has to be separated into the extinction (scattering and absorption) caused by molecules or by particulate matter. Since the focus is set on aerosol particles only, we shall call  $\sigma_{\text{ep}}$  the *aerosol extinction coefficient* from now on<sup>3</sup>.

The main parameters that govern the scattering and absorption of light are the particle's size and morphology, the incident wavelength, and the particle's *complex refractive index*  $m$ , which is defined (with respect to air as the surrounding medium) as:

$$m = n + ki, \quad (2.15)$$

where the real part  $n$  denotes the non-absorbing and the imaginary part  $k$  the absorbing property of the particle.  $m$  is defined by the chemical composition of the particle.

In this work, the aerosol particles are assumed to be spherical whose optical parameters can be exactly calculated using Mie theory (see below). Several approaches exist to calculate the light scattering properties of non-spherical particles, like the finite-difference time domain (FDTD) technique or the T-matrix method (see e.g., Liou, 2002; Mishchenko et al., 2000, for an overview of existing methods).

To relate the particle size to the wavelengths of the incident radiation, the *size parameter*  $x$  is defined for spherical particles as follows:

$$x = \frac{\pi D}{\lambda}, \quad (2.16)$$

where  $D$  is the particle diameter and  $\lambda$  the wavelength. If  $x \ll 1$ , so the particle size is small compared to the incident wavelength, the scattering can be described using Rayleigh theory (Sect. 2.2.1). If the particles are much larger in comparison to the incident wavelength ( $x \gg 1$ ) then geometrical optics theory has to be used (which is not discussed here). In the transient regime ( $x \approx 1$ ) Mie theory (Sect. 2.2.2) has to be used.

Another key property is the *aerosol phase function*  $P(\theta)$  (or angular-scattering function) which describes the angular distribution of the scattered light. It is defined (for unpolarized light) as the scattered light intensity  $I(\theta, x, m)$  at a particular scattering (zenith) angle  $\theta$  relative to the incident light beam normalized by the total scattered intensity (Marshall et al., 1995):

$$P(\theta) = \frac{I(\theta, x, m)}{\int_0^\pi I(\theta, x, m) \sin\theta d\theta}. \quad (2.17)$$

Here, the restriction on spherical particles is necessary to remove the azimuthal dependence of  $P$  (otherwise the azimuth angle  $\phi$  has to be included in all angle dependent equations). The phase function is usually normalized to  $4\pi$  or to 1 if the azimuthal dependence is removed ( $2\pi$  cancels out):

<sup>2</sup>The concentration is assumed not to change with  $s$ , otherwise  $\sigma_{\text{ext}}$  has to be replaced by an integral of  $\sigma_{\text{ext}}(s)$  over  $s$ .

<sup>3</sup>The abbreviations "ext, abs, scat" used in most of the textbooks are replaced by "ep, ap, sp" to be consistent with the terminology used throughout this work and the published papers (which is based on the nephelometer terminology by (Anderson and Ogren, 1998).



$$\frac{1}{2} \int_0^\pi P(\theta) \sin \theta d\theta = 1. \quad (2.18)$$

### 2.2.1 Rayleigh theory

Rayleigh theory is used to describe the elastic scattering of spherical particles which are small compared to the wavelength. In the visible spectrum this theory is therefore used to describe the scattering properties of air molecules (and the scattering of sun light is therefore called Rayleigh scattering). The theory assumes that the air molecules are acting as excited Hertzian dipoles. If the incident intensity  $I_0$  is assumed to be unpolarized, the scattered intensity  $I_s$  can be calculated as follows:

$$I_s = \frac{I_0}{\lambda^4} \frac{8\pi^4 \alpha^2}{r^2} (1 + \cos^2 \theta) \quad \text{with} \quad \alpha = \frac{3}{4\pi N} \frac{m^2 - 1}{m^2 + 2}, \quad (2.19)$$

where  $\theta$  is the angle between the incident wave and the observer,  $r$  the distance between particle and observer,  $\lambda$  the wavelength, and  $\alpha$  the so called polarizability (or Lorentz-Lorentz formula) with  $N$  being the particle number density and  $m$  the refractive index. As can be seen in Eq. 2.19, the scattered intensity is inverse proportional to the 4th power of the wavelength, which means that shorter wavelengths are scattered more effectively than longer wavelengths. As a consequence, blue light is scattered more efficiently than red light in the visible spectrum, which explains the blue color of the sky. The angular dependency in Eq. 2.19 can be written more compactly by introducing the non-dimensional scattering phase function  $P(\theta)$  (which is usually normalized to unity):

$$P(\theta) = \frac{3}{4} (1 + \cos^2 \theta). \quad (2.20)$$

The Rayleigh phase function reveals that (unpolarized) light is scattered more into the forward ( $0^\circ$ ) and backward ( $180^\circ$ ) direction, while a minimum occurs in the perpendicular direction ( $90^\circ$ ). In the first panel of Fig. 2.4  $P(\theta)$  is visualized on polar coordinates.

### 2.2.2 Mie theory

For particles that are in the same size range as the incident wavelength ( $x \approx 1$ ), Mie theory has to be used to calculate the scattering and absorption properties. It was established by Gustav Mie in 1908 by solving the Maxwell equations (Mie, 1908)<sup>4</sup>. It is strictly spoken only valid for spherical particles, although numerical approximations exist for non-spherical particles as well. The basic idea of Mie theory is that the incident electromagnetic wave induces multipoles in the particle whose secondary waves can interfere with each other. In the far-field the scattering and absorption properties can be calculated as a function of the scattering angle  $\theta$ , the complex refractive index  $m$ , and the size parameter  $x$ . A detailed derivation and discussion can be found in the corresponding literature (e.g., Mie, 1908; Liou, 2002; Bohren and Huffman, 2004; Van de Hulst, 1981). Here, only a brief summary will be given.

<sup>4</sup>Sometimes it is also called Mie-Debye-Lorenz theory to acknowledge Ludvig Lorenz and Peter Debye who independently worked and developed own (similar) solutions on the theory of light scattering.

The far-field solution is usually expressed in terms of the two scattering functions which have the symmetric form:

$$\begin{aligned} S_1(\theta) &= \sum_{n=1}^{\infty} \frac{2n+1}{n(n+1)} (a_n \pi_n(\cos\theta) + b_n \tau_n(\cos\theta)) \\ S_2(\theta) &= \sum_{n=1}^{\infty} \frac{2n+1}{n(n+1)} (a_n \tau_n(\cos\theta) + b_n \pi_n(\cos\theta)) \end{aligned} \quad (2.21)$$

with

$$\pi_n(\cos\theta) = \frac{P_n^1(\cos\theta)}{\sin\theta}, \quad \tau_n(\cos\theta) = \frac{dP_n^1(\cos\theta)}{d\theta},$$

which can be deduced using the associated Legendre polynomials  $P_n^1(\cos\theta)$  in dependency of the scattering angle  $\theta$ .  $a_n$  and  $b_n$  are called Mie-coefficients and depend on  $x$  and  $m$ . They can be calculated using the Ricatti-Bessel functions  $\psi_n$  and  $\zeta_n$ :

$$\begin{aligned} a_n &= \frac{\psi_n(mx)\psi_n'(x) - \psi_n(x)\psi_n'(mx)}{m\psi_n(mx)\zeta_n'(x) - \zeta_n(x)\psi_n'(mx)} \\ b_n &= \frac{\psi_n(mx)\psi_n'(x) - m\psi_n(x)\psi_n'(mx)}{\psi_n(mx)\zeta_n'(x) - m\zeta_n(x)\psi_n'(mx)}. \end{aligned} \quad (2.22)$$

The scattering and extinction efficiency ( $Q_{sp}$  and  $Q_{ep}$ , see Eq. 2.13) can be calculated via Mie-theory as follows:

$$Q_{sp} = \frac{2}{x^2} \sum_{n=1}^{\infty} (2n+1) (|a_n|^2 + |b_n|^2) \quad (2.23)$$

$$Q_{ep} = \frac{2}{x^2} \sum_{n=1}^{\infty} (2n+1) \text{Re}(a_n + b_n). \quad (2.24)$$

The scattering efficiency  $Q_{sp}$  is seen in Fig. 2.3. As the size parameter increases (or as the diameter increases assuming a fixed wavelength),  $Q_{sp}$  reaches the asymptotic value of 2 in the case of a non-absorbing sphere. If no absorption is assumed (imaginary part of the refractive index is zero) the same would be true for the extinction ( $Q_{sp} = Q_{ep}$ ). This means that the particle removes twice as much radiation through scattering than geometrical optics would predict. The reason is that the light removal from the incident light beam is also caused by diffraction besides reflection and refraction within the particle (Liou, 2002).

The phase function  $P(\theta)$  can be calculated as follows (not normalized yet):

$$P(\theta) = \frac{1}{2} (|S_1(\theta)|^2 + |S_2(\theta)|^2). \quad (2.25)$$

$P(\theta)$  calculated for four different large particles is shown in Fig. 2.4. As the particle increases in size the forward-scattering clearly becomes the dominant factor. This is of importance when it comes to certain measurement techniques, e.g. certain sun- and aureole spectrometer systems use especially

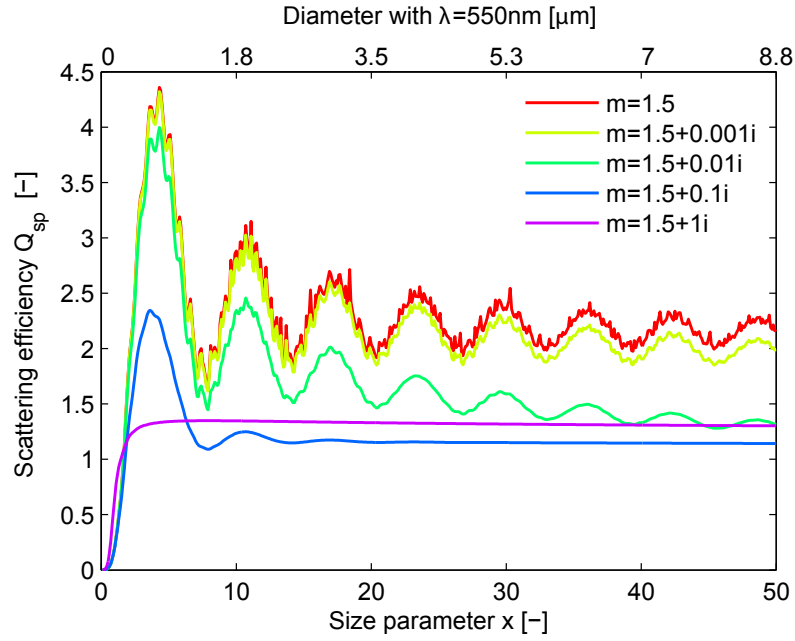


Figure 2.3: The scattering efficiency  $Q_{sp}$  versus the size parameter (lower x-axis) and particle diameter (upper x-axis, if the wavelength  $\lambda=550$  nm is taken) for different refractive indices (see legend).

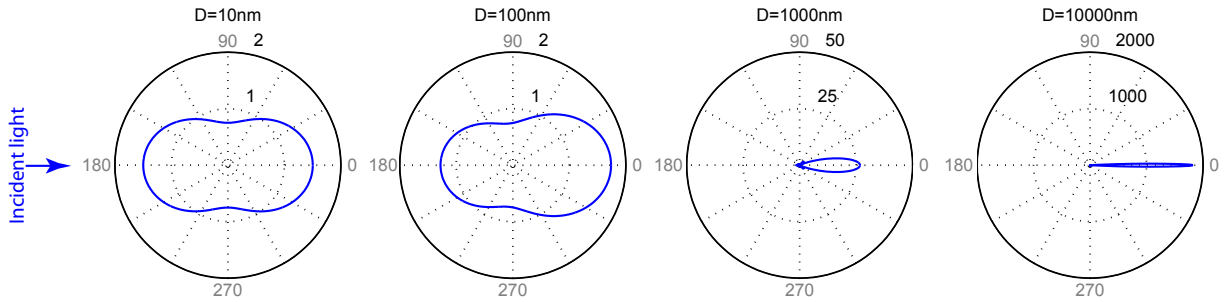


Figure 2.4: Normalized aerosol scattering phase function of four differently sized particles shown in polar coordinates (assuming a refractive index of  $m = 1.54$  and the wavelength of the incident light (entering from the left, see blue arrow) of  $\lambda=550$  nm). For the  $D=10$  nm the phase function is almost identical with the Rayleigh phase function.

the forward scattering region (Zieger et al., 2007) to differentiate aerosol types. Also the nephelometer used here has to be corrected for the missing scattering angles (truncation error correction, Anderson and Ogren 1998, see below). For very small particles (here  $D=10$  nm)  $P(\theta)$  equates to the Rayleigh phase function (Eq. 2.20).

Another important factor is the asymmetry factor  $g$ , which is defined as the intensity-weighted average of the cosine of the scattering angle (Marshall et al., 1995)

$$\begin{aligned}
 g &= \frac{1}{2} \frac{\int_0^\pi \cos(\theta) I(\theta) \sin(\theta) d\theta}{\int_0^\pi I(\theta) \sin(\theta) d\theta} \\
 &= \frac{1}{2} \int_0^\pi \cos(\theta) P(\theta) \sin(\theta) d\theta,
 \end{aligned} \tag{2.26}$$

which can be directly calculated via Mie theory.  $g$  can vary between  $-1$  (everything scattered  $180^\circ$  backward) and  $1$  (everything scattered forward), isotropic scattering has a value of  $g=0$ . It is a fundamental parameter in many radiative transfer codes and can e.g. be derived from in-situ nephelometer measurements of the backscatter ratio  $b$  (e.g., Marshall et al., 1995; Andrews et al., 2006) or from sky radiance measurements using photometers (e.g., Nakajima et al., 1983; Dubovik and King, 2000). The backscatter ratio  $b$  is the fraction of the backscattered light to total scattered light and is defined as follows:

$$b = \frac{\int_{\pi/2}^{\pi} P(\theta) \sin(\theta) d\theta}{\int_0^{\pi} P(\theta) \sin(\theta) d\theta}. \quad (2.27)$$

It can be directly measured using an integrating nephelometer that is equipped with a backscatter shutter (like the one used within this work) and calculated taking the ratio of the backscattering coefficient  $\sigma_{\text{bsp}}$  to the total scattering coefficient  $\sigma_{\text{sp}}$ :

$$b = \frac{\sigma_{\text{bsp}}}{\sigma_{\text{sp}}}. \quad (2.28)$$

As mentioned above, for small size parameters ( $x \rightarrow 0$ ) Mie theory merges to Rayleigh theory, while for very large particles ( $x \gg 1$ ) Mie theory will merge to the geometrical optics. The Mie code used in this work is based on the algorithm given by Bohren and Huffman (2004) (translated by R. Nessler to be used in Matlab).

### 2.2.3 Main aerosol optical properties

Aerosol particles are observed at various size ranges, therefore the aerosol size distribution has to be included when calculating the main optical properties. This is usually done by taking the number size distribution  $dN/dD$ , which will give the total number concentration  $N$  (usually in units  $\text{cm}^{-3}$ ) if integrated over the entire size spectrum.

The aerosol scattering coefficient  $\sigma_{\text{sp}}$  can be calculated as follows:

$$\begin{aligned} \sigma_{\text{sp}} &= \int_{D_{\text{min}}}^{D_{\text{max}}} \pi \left(\frac{D}{2}\right)^2 Q_{\text{scat}}(x, m) \frac{dN}{dD} dD \\ &= \int_{D_{\text{min}}}^{D_{\text{max}}} C_{\text{sp}} \frac{dN}{dD} dD \quad \text{with} \quad C_{\text{sp}} = \pi \left(\frac{D}{2}\right)^2 Q_{\text{sp}}(x, m), \end{aligned} \quad (2.29)$$

where  $D$  is the particle diameter and  $Q_{\text{sp}}$  the scattering efficiency (see Eq. 2.13 and Eq. 2.23).  $C_{\text{sp}}$  is called the *scattering cross section*. The absorption or extinction coefficient ( $\sigma_{\text{ap}}$  and  $\sigma_{\text{ep}}$ ) can be calculated analogously by taking the absorption or the extinction efficiency, respectively.

Integrating the extinction coefficient over a certain distance  $s$  gives the aerosol optical depth<sup>5</sup>  $\tau_{\text{a}}$ :

<sup>5</sup>For most of the atmospheric applications it is useful to relate  $\tau_{\text{a}}$  to the vertical (zenith) direction (sometimes abbreviated with "AOD"). For sun photometer measurement e.g.,  $\tau_{\text{a}}$  is calculated by including the relative air mass factor between the sun and the zenith, see e.g. Eq. 1 in Zieger et al. (2007).

$$\tau_a = \int_{s_1}^{s_2} \sigma_{ep} ds. \quad (2.30)$$

The Ångström formula describes the spectral dependence of  $\tau_a$  by a power law function:

$$\tau_a = \tau_0 \lambda^{-\alpha}, \quad (2.31)$$

where  $\lambda$  is the wavelength,  $\tau_0$  the turbidity coefficient, and  $\alpha$  the Ångström exponent. Equation 2.31 can be formulated analogously for  $\sigma_{sp}$ ,  $\sigma_{ap}$ ,  $\sigma_{ep}$ , or the single scattering albedo  $\omega_0$  (see below). The exponent can be determined by fitting a power law function to the measured spectral aerosol optical depth or by using two discrete wavelengths  $\lambda_1$  and  $\lambda_2$ . Equation 2.31 then becomes:

$$\alpha = -\frac{\log(\tau_a(\lambda_1)/\tau_a(\lambda_2))}{\log(\lambda_1/\lambda_2)}. \quad (2.32)$$

The Ångström exponent is a useful quantity since it is a qualitative indicator of the particle size distribution. For small exponents ( $\alpha < 1$ ) the measured aerosol is dominated by the coarse mode ( $D > 1 \mu\text{m}$ ), whereas for large values ( $\alpha > 2$ ) the size distributions is dominated by the fine mode ( $D < 1 \mu\text{m}$ ). An example is seen in Fig. 2.5, where the  $\alpha$  of the extinction coefficient  $\sigma_{ep}$  (for the wavelengths 450 nm and 550 nm using Eq. 2.32) has been calculated for different single lognormal size distributions (varying the mode diameter  $D_{\text{mod}}$  from 10 nm to 10  $\mu\text{m}$ ; assuming a constant standard deviation and a real part of the refractive index of  $m = 1.5$  and different imaginary parts).  $\alpha$  decreases with increasing particle size. For very small particles,  $\alpha$  reaches 4 (for not too large imaginary parts of the refractive index), the expected wavelength dependency for Rayleigh scattering (see Eq. 2.19). The relationship between  $\alpha$  and size is only valid for non-absorbing aerosols, single mode distributions, and is not well defined for low values of  $\alpha$  (see Fig. 2.5). Nevertheless, it is a first indicator that can be used. In addition, the spectral curvature of  $\tau_a$  or  $\sigma_{ep}$  can be used to gain information on the bimodality of the aerosol size distribution (see Schuster et al., 2006, and references therein).

The *single scattering albedo*  $\omega_0$  is the ratio of the scattering coefficient  $\sigma_{sp}$  to the extinction coefficient  $\sigma_{ep}$ :

$$\omega_0 = \frac{\sigma_{sp}}{\sigma_{sp} + \sigma_{ap}} = \frac{\sigma_{sp}}{\sigma_{ep}}. \quad (2.33)$$

The single scattering albedo can vary from  $\omega_0 = 1$  (extinction is entirely caused by scattering) to  $\omega_0 = 0$  (extinction is entirely caused by absorption). The Ångström exponent  $\alpha_{\omega_0}$  of the single scattering albedo is a useful parameter to gain information on the chemical composition of the measured aerosol. At the Jungfraujoch, for example,  $\alpha_{\omega_0}$  is being used to distinguish long-range transported Saharan dust aerosol from the normal/background aerosol (Collaud Coen et al., 2004).

#### 2.2.4 Modeling the effect of relative humidity on the aerosol optical properties

The change of the size distribution and the refractive index with RH (needed for the Mie calculations) have been calculated with the following procedure.

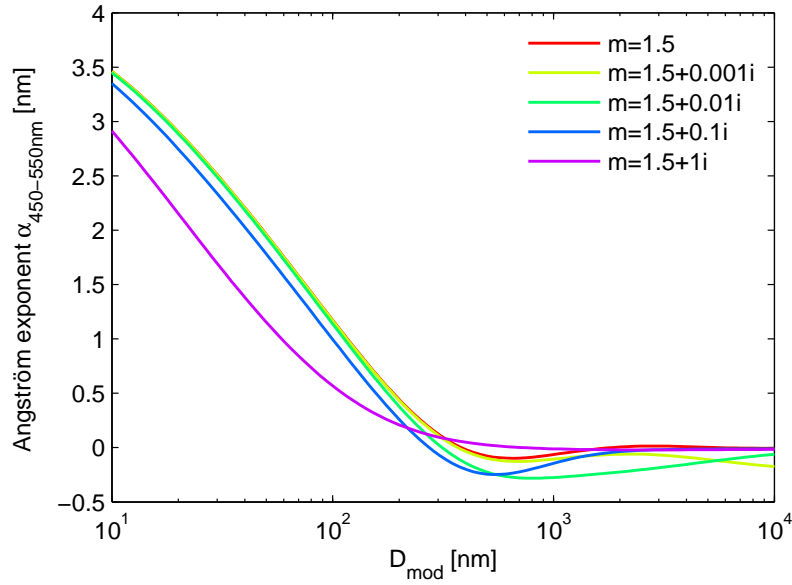


Figure 2.5: The Ångström exponent  $\alpha_{450-550\text{nm}}$  versus the mode diameter of a single lognormal size distribution (assuming a width of  $\sigma=2.0$  and different refractive indexes, see legend).

First, the change of the particle size is determined by multiplying the dry diameter  $D_{\text{dry}}$  by the (dry) size dependent hygroscopic growth factor  $g(\text{RH}, D_{\text{dry}})$ :

$$D_{\text{wet}}(\text{RH}) = g(\text{RH}, D_{\text{dry}})D_{\text{dry}}. \quad (2.34)$$

The number size distribution is then calculated as follows:

$$\frac{d\tilde{N}(D_{\text{wet}})}{d\log D_{\text{wet}}} = \frac{dN(D_{\text{dry}})}{d\log D_{\text{dry}}} \frac{D_{\text{wet}}}{D_{\text{dry}}} \frac{dD_{\text{dry}}}{dD_{\text{wet}}}. \quad (2.35)$$

The number size distribution  $\frac{dN(D_{\text{dry}})}{d\log D_{\text{dry}}}$  can for example be measured by a scanning mobility particle sizer (SMPS).

The change of the dry refractive index is calculated by applying a volume weighting of the dry refractive index  $m_{\text{dry}}$  with the refractive index of water  $m_{\text{H}_2\text{O}}$  (Hale and Querry, 1973):

$$m_{\text{wet}} = \frac{m_{\text{dry}} + m_{\text{H}_2\text{O}}(g(\text{RH})^3 - 1)}{g(\text{RH})^3}. \quad (2.36)$$

For high growth factors and high values of RH, the refractive index of the aerosol droplet converges to the one of water. Although several other mixing rules for the refractive index exist, the volume weighted average was found by Nessler et al. (2005b) to be the most suitable one, since the differences were very small between the different methods and the volume weighting formula was the most simple one to use.

## Chapter 3

# Measured and predicted aerosol light scattering enhancement factors at the high alpine site Jungfraujoch

R. Fierz-Schmidhauser, P. Zieger, M. Gysel, L. Kammermann, P.F. DeCarlo, U. Baltensperger, E. Weingartner

*Laboratory of Atmospheric Chemistry, Paul Scherrer Institut, 5232, Villigen PSI, Switzerland*

*Published in Atmospheric Chemistry and Physics, 10, 2319-2333, doi:10.5194/acp-10-2319-2010, 2010.*

Contribution of P. Zieger: Performance of model calculations, sensitivity study, calculation of refractive index, and general discussion of the obtained results.

### Abstract

Ambient relative humidity (RH) determines the water content of atmospheric aerosol particles and thus has an important influence on the amount of visible light scattered by particles. The RH dependence of the particle light scattering coefficient ( $\sigma_{\text{sp}}$ ) is therefore an important variable for climate forcing calculations. We used a humidification system for a nephelometer which allows for the measurement of  $\sigma_{\text{sp}}$  at a defined RH in the range of 20–95%. In this paper we present measurements of light scattering enhancement factors  $f(\text{RH}) = \sigma_{\text{sp}}(\text{RH}) / \sigma_{\text{sp}}(\text{dry})$  from a 1-month campaign (May 2008) at the high alpine site Jungfraujoch (3580 m a.s.l.), Switzerland. Measurements at the Jungfraujoch are representative for the lower free troposphere above Central Europe. For this aerosol type hardly any information about the  $f(\text{RH})$  is available so far. At this site,  $f(\text{RH}=85\%)$  varied between 1.2 and 3.3. Measured  $f(\text{RH})$  agreed well with  $f(\text{RH})$  calculated with Mie theory using measurements of the size distribution, chemical composition and hygroscopic diameter growth factors as input. Good  $f(\text{RH})$  predictions at  $\text{RH} < 85\%$  were also obtained with a simplified model, which uses the Ångström exponent of  $\sigma_{\text{sp}}(\text{dry})$  as input. RH influences further intensive optical aerosol properties. The backscatter

fraction decreased by about 30% from 0.128 to 0.089, and the single scattering albedo increased on average by 0.05 at 85% RH compared to dry conditions. These changes in  $\sigma_{\text{sp}}$ , backscatter fraction and single scattering albedo have a distinct impact on the radiative forcing of the Jungfraujoch aerosol.

### 3.1 Introduction

Atmospheric aerosols influence the Earth radiation budget by scattering and absorbing light. Further they act as cloud condensation nuclei and therefore influence the radiative properties and the lifetime of clouds. These two effects are called direct and indirect aerosol effect and are estimated to have an anthropogenic radiative forcing of  $-0.5$  and  $-0.7 \text{ Wm}^{-2}$ , compared to  $+2.66 \text{ Wm}^{-2}$  by greenhouse gases (IPCC, 2007). The anthropogenic aerosol forcing uncertainty is substantially larger than that of the greenhouse gases ( $+0.8/-1.5$  vs.  $\pm 0.27 \text{ Wm}^{-2}$ ) (IPCC, 2007). Therefore there is an urgent need to constrain this uncertainty.

To better quantify the direct effect it is important to understand how aerosol light scattering properties are influenced in the atmosphere. At high relative humidity (RH) liquid water comprises a major fraction of the atmospheric aerosol, and therefore the light scattering of aerosols expressed by the scattering coefficient ( $\sigma_{\text{sp}}$ ) depends on RH. The factor that quantifies this dependence is the light scattering enhancement factor  $f(\text{RH}) = \sigma_{\text{sp}}(\text{RH}) / \sigma_{\text{sp}}(\text{dry})$ . To ensure comparability between different  $\sigma_{\text{sp}}$  measurements at GAW (Global Atmosphere Watch) stations, the World Meteorological Organization (WMO) recommends measurements of  $\sigma_{\text{sp}}$  to be below 40% RH (WMO/GAW, 2003), which is considered a dry measurement.

At a fixed RH,  $f(\text{RH})$  depends mainly on the dry particle size distribution and on the particles' hygroscopicity, which is determined by their chemical composition. For a constant chemical composition  $f(\text{RH})$  increases with decreasing particle size (see, e.g. Fierz-Schmidhauser et al., 2010).

Many studies have presented measurements of atmospheric aerosol light scattering enhancement factors  $f(\text{RH})$ , e.g. for biomass burning aerosol (Kotchenruther and Hobbs, 1998; Kim et al., 2006), dust and pollution aerosol (Carrico et al., 2003; Kim et al., 2006), as well as for aerosols at rural (Day and Malm, 2001), continental (Koloutsou-Vakakis et al., 2001; Sheridan et al., 2001) or urban (Yan et al., 2009) sites or close to the sea (Carrico et al., 1998, 2003; Wang et al., 2007). The highest  $f(\text{RH})$  were detected in Gosan, Korea, during measurements of pollution aerosols from China of 2.75 (at 85% RH) and of volcanic aerosols during ACE-Asia of 2.55 (at 82% RH). During ACE-Asia, Carrico et al. (2003) measured a very low  $f(\text{RH})$  of 1.18 (at 82% RH) for dust dominated aerosol. In Brazil, biomass burning aerosol measurements revealed  $f(\text{RH})$  as low as 1.16 at 80% RH (Kotchenruther and Hobbs, 1998).

The aerosol scattering coefficient  $\sigma_{\text{sp}}$  can be measured by an integrating nephelometer. To measure  $\sigma_{\text{sp}}$  at different RH, we built a humidification system for a commercial nephelometer (TSI Inc., model 3563) which allows for the measurement of  $\sigma_{\text{sp}}$  at a defined humidity below 95% RH (Fierz-Schmidhauser et al., 2010). The system is able to measure how hygroscopic properties and hysteresis effects of the atmospheric aerosol influence  $\sigma_{\text{sp}}$ , and it can be continuously and remotely operated with very little maintenance. In May 2008 this humidified nephelometer measured in parallel with a dry nephelometer (RH < 20%) at the high alpine site Jungfraujoch (JFJ). The Jungfraujoch is located at 3580 m a.s.l in the Swiss Alps and is designated a clean continental background station in Central



Europe. JFJ is well suited for the study of background aerosols in climate research (Nyeki et al., 1998). The scattering enhancement at higher RH influences the direct climate forcing by aerosol particles (Charlson et al., 1992; Schwartz, 1996). It is therefore desirable to be able to transform dry  $\sigma_{\text{sp}}$  into ambient  $\sigma_{\text{sp}}$  values. For this purpose we measured the size distribution and the chemical composition of the JFJ aerosol and performed a closure study using a model based on Mie theory, which can calculate the light scattering enhancement factor  $f(\text{RH})$  at different RH. We also compared our model to another model developed by Nessler et al. (2005a).

In this paper we present model calculations of  $f(\text{RH})$  with different model assumptions (constant or variable chemical composition and size distribution) for the month of May 2008. The paper presents the sensitivity of  $f(\text{RH})$  on these two input parameters. The predicted  $f(\text{RH})$  results are compared to the measured  $f(\text{RH})$ . Finally we present the impact of RH on other intensive aerosol properties and the radiative forcing.

## 3.2 Experimental

### 3.2.1 Measurement site

All data presented here were measured at the high alpine research station Jungfraujoch (JFJ, 46° 33' N, 7° 59' E). The measurement campaign took place from 1 to 29 May 2008. The JFJ measurement site lies on an exposed mountain saddle on the north crest of the Bernese Alps, Switzerland, at 3580 m altitude. The JFJ is a Global Atmosphere Watch (GAW) site and aerosol measurements have been performed in this framework since 1995. It is also part of the Swiss National Monitoring Network for Air Pollution (NABEL) and the Federal Office of Meteorology and Climatology (MeteoSwiss). Baltensperger et al. (1997) and Collaud Coen et al. (2007) give more information on the JFJ site and the long-term aerosol measurements performed there. Due to its high elevation the JFJ resides predominantly in the free troposphere (FT) but can be affected by continental and regional pollution sources through vertical transport: During the warmer months injections of more polluted planetary boundary layer (PBL) air occur due to thermal convection. Consequently most extensive aerosol parameters undergo an annual cycle with maxima in the summer months and minima in the winter months (Baltensperger et al., 1991, 1997; Nyeki et al., 1998; Weingartner et al., 1999; Collaud Coen et al., 2007). A diurnal cycle due to mixing of convectively transported PBL aerosol with the air from the free troposphere is superimposed on this seasonal cycle, which often occurs during the spring and summer seasons. This diurnal cycle was clearly present during the first period of this campaign. Throughout the year the station is within clouds about one third of the time (Baltensperger et al., 1998).

### 3.2.2 Instruments

#### Scattering coefficients at dry conditions and at high RH

Since 1995 an integrating nephelometer (TSI Inc., model 3563) has measured the dry scattering coefficients  $\sigma_{\text{sp}}$  and dry backscattering coefficients  $\sigma_{\text{bsp}}$  of total suspended particulate matter (TSP) at

three wavelengths ( $\lambda=450, 550$  and  $700$  nm) at the JFJ. During the campaign in May 2008 the RH in this nephelometer was always below 20% RH. No drying of the air is needed to achieve this low RH, since the temperature difference between the ambient atmosphere and the laboratory is typically more than  $25^\circ\text{C}$ .

We built a novel humidification system for a second integrating nephelometer to measure the RH dependence of  $\sigma_{\text{sp}}$  and  $\sigma_{\text{bsp}}$  at a defined RH in the range of 20–95% RH. The humidification system consists of a humidifier to rise the RH of the aerosol up to 95% RH, followed by a dryer, which dries to aerosol to the desired RH (Fierz-Schmidhauser et al., 2010). This system enables us to measure the hysteresis behavior of deliquescent aerosol particles. The light scattering enhancement factor  $f(\text{RH})$  is defined as the ratio of  $\sigma_{\text{sp}}$  at high and low RH:

$$f(\text{RH}) = \frac{\sigma_{\text{sp}}(\text{RH})}{\sigma_{\text{sp}}(\text{RH} = \text{dry})}. \quad (3.1)$$

The light backscattering enhancement factor,  $f_b(\text{RH})$ , is defined similarly with  $\sigma_{\text{bsp}}$ . During the majority of the measurement period the humidified nephelometer measured at 85% RH ( $\pm 10\%$  RH). During four time periods, humidity cycles of the scattering enhancement, commonly referred to as humidograms, were determined. When both nephelometers measured at dry conditions (RH<40%) (3 May 20:00 LT (local time) to 5 May 10:00 LT) the two instruments agreed well with a slope of 1.03, an intercept of  $5 \times 10^{-7} \text{ m}^{-1}$  and a correlation coefficient of  $R^2=0.982$  (at  $\lambda=550$  nm).  $\sigma_{\text{sp}}$  and  $\sigma_{\text{bsp}}$  were corrected for the truncation error according to Anderson and Ogren (1998). They used the Ångström exponent  $\hat{a}_s$  of the scattering coefficient, which is defined as:

$$\sigma_{\text{sp}} = c \lambda^{-\hat{a}_s}. \quad (3.2)$$

The factor  $c$  (turbidity coefficient) is related to the aerosol concentration and  $\lambda$  is the wavelength of the light. Dividing  $\sigma_{\text{bsp}}$  by  $\sigma_{\text{sp}}$  results in the backscatter fraction  $b$ , which is the percentage of radiation that is scattered back at angles between  $90^\circ$  and  $180^\circ$ .  $b$  increases with decreasing particle size. If the sun is in the zenith,  $b$  is equal to the upscatter fraction  $\beta$ .  $\beta$  is the fraction of light that is scattered by a particle into the upward hemisphere relative to the local horizon, and consequently depends on the zenith angle and the particle size. In this study,  $\beta$  is parameterized from the measured  $b$  using the following equation for the global mean (Wiscombe and Grams, 1976 in Sheridan and Ogren, 1999):

$$\beta = 0.0817 + 1.8495b - 2.9682b^2. \quad (3.3)$$

Often, the actual RH in the nephelometer differed slightly from the target RH of  $\text{RH}_{\text{target}}=85\%$ . Several humidograms measured at different times could be well described with the following empirical relationship:

$$f(\text{RH}) = \left( 1 + a \frac{\text{RH}}{1 - \text{RH}} \right)^{\frac{7}{3}}, \quad (3.4)$$

where  $a$  is the only free parameter. This empirical relationship allows recalculation of  $f(\text{RH})$  to different RH values, assuming that it generally holds. Recalculated  $f(\text{RH})$  at  $\text{RH}_{\text{target}}=85\%$  were determined in this way from  $f(\text{RH})$  measured at  $75\% \leq \text{RH}_{\text{meas}} \leq 95\%$ :

$$\begin{aligned} f_{\text{recalc}}(\text{RH}_{\text{target}}) &= \left( 1 + a_{\text{meas}} \frac{\text{RH}_{\text{target}}}{1 - \text{RH}_{\text{target}}} \right)^{\frac{7}{3}} \\ &= \left( 1 + \left[ f_{\text{meas}}^{\frac{3}{7}} - 1 \right] \frac{1 - \text{RH}_{\text{meas}}}{\text{RH}_{\text{meas}}} \frac{\text{RH}_{\text{target}}}{1 - \text{RH}_{\text{target}}} \right)^{\frac{7}{3}}. \end{aligned} \quad (3.5)$$

Table 3.1: Microphysical properties of selected aerosol compounds used for the model predictions. The imaginary part of the complex refractive index  $n$  was omitted for all components except for black carbon (BC). All values are interpolated to the nephelometer wavelengths. Mean concentrations (and standard deviations) are for the entire measurement period.

$\lambda$	Organics	NH <sub>4</sub> NO <sub>3</sub>	(NH <sub>4</sub> ) <sub>2</sub> SO <sub>4</sub>	NH <sub>4</sub> HSO <sub>4</sub>	H <sub>2</sub> SO <sub>4</sub>	BC
450 nm		1.559 <sup>b</sup>	1.536 <sup>b</sup>		1.438 <sup>d</sup>	1.75+0.46i <sup>e</sup>
$n_i$ 550 nm	1.48 <sup>a,h</sup>	1.556 <sup>b</sup>	1.530 <sup>b</sup>	1.473 <sup>c,h</sup>	1.434 <sup>d</sup>	1.75+0.44i <sup>e</sup>
700 nm		1.553 <sup>b</sup>	1.524 <sup>b</sup>		1.432 <sup>d</sup>	1.75+0.43i <sup>e</sup>
$\rho_i$ (g/cm <sup>3</sup> )	1.4 <sup>f</sup>	1.72 <sup>g</sup>	1.77 <sup>g</sup>	1.78 <sup>g</sup>	1.83 <sup>g</sup>	1.7 <sup>a</sup>
mean conc.	0.703	0.370	0.450	0.097	0.013	0.057
( $\mu\text{g}/\text{m}^3$ ) (std)	(0.808)	(0.638)	(0.611)	(0.111)	(0.027)	(0.054)

<sup>a</sup> Nessler et al. (2005a); <sup>b</sup> Software from Andrew Lacis (from [http://gacp.giss.nasa.gov/data\\_sets/](http://gacp.giss.nasa.gov/data_sets/), last visited on 19 May 2009) based on Toon et al. (1976); Gosse et al. (1997); Tang (1996); <sup>c</sup> Li et al. (2001); <sup>d</sup> Palmer and Williams (1975); <sup>e</sup> Hess et al. (1998); <sup>f</sup> Alfarra et al. (2006); Dinar et al. (2006); <sup>g</sup> Lide (2009); <sup>h</sup> No wavelength dependence assumed.

### Particle number size distributions

A scanning mobility particle sizer (SMPS) measured the dry particle size distribution in the particle mobility diameter range  $12 \text{ nm} < D_p < 562 \text{ nm}$ . This instrument consists of a differential mobility analyzer (DMA) followed by a condensation particle counter (CPC, TSI Inc., model 3772). The SMPS had a closed loop configuration for the sheath and excess air. The volumetric sheath air flow rate was held constant at 5 lpm (liters per minute) by means of a mass flow controller combined with temperature and pressure sensors. The sample flow rate was 1 lpm. In addition, an optical particle counter (OPC, Grimm Dustmonitor 1.108) measured the dry size distribution of the larger particles in the optical diameter range  $0.3 \mu\text{m} < D_p < 25 \mu\text{m}$ . In the OPC the individual particles are classified according to their light scattering behavior, which depends on the particle size, morphology and refractive index. The comparison of the size distribution spectra of the OPC and the SMPS showed that the OPC diameters need to be slightly shifted (multiplication of the diameter by 1.12 on average) to larger sizes to get good agreement. A similar disagreement was found in a different study at the JFJ site by Cozic et al. (2008).

The combined SMPS and OPC data were used as input for the Mie calculation. All diameter corrected data from the OPC were taken, whereas the SMPS data were just used up to  $D_p=340 \text{ nm}$ , to avoid the influence of doubly and triply charged particles for larger diameters. A comparison of the integrated size distribution of the SMPS and OPC to a second CPC, measuring the total number concentration, showed that the SMPS measured  $\sim 20\%$  less than the CPC, if large nucleation events (with high concentrations of particles with  $D_p < 30 \text{ nm}$ ) were excluded for the comparison. The corrected and combined SMPS and OPC data were used as an input for the model calculations (see Sect. 3.2.3).

### Hygroscopic properties

A hygroscopicity tandem differential mobility particle sizer (H-TDMA), based on the instrument presented by Weingartner et al. (2002), was operated to measure the hygroscopic diameter growth factors ( $g$ ), defined as the diameter ratio of high RH and dry conditions. The H-TDMA functions as follows: Particles are dried to  $RH < 10\%$  and brought to charge equilibrium before a first DMA is used to select a dry monodisperse size of the polydisperse aerosol. These particles with a well defined dry diameter then pass through a humidifier before the resulting equilibrium diameters are measured using a second DMA operated at a well defined high RH (typically 90%). The mean growth factor  $g$ , measured at  $RH = 90\% \pm 3\%$ , was obtained from the raw measurement distributions using the TDMAinv inversion algorithm (Gysel et al., 2009). Dry diameters measured in this study were 35, 50, 75, 110, 165 and 265 nm.

### Chemical composition

An Aerodyne High Resolution Time-of-Flight Aerosol Mass Spectrometer (AMS) measured the size resolved aerosol chemical composition of non-refractory submicron aerosol particles. The instrument has been characterized in detail elsewhere (DeCarlo et al., 2006; Canagaratna et al., 2007). Briefly, aerosol is introduced into the instrument via an aerodynamic lens which focuses the aerosol into a tight beam. The particle beam impacts on an inverted conical tungsten vaporizer at  $600^\circ\text{C}$ , where the non-refractory components are flash vaporized. The resulting gas phase plume is ionized by electron ionization at 70 eV. A high mass resolution mass spectrometer (H-TOF, Tofwerk AG, Thun, Switzerland) produces mass spectra which are processed using custom software to give mass concentrations of non-refractory species. At the JFJ the AMS measured with a collection efficiency of 1. This collection efficiency was determined based on intercomparisons of the AMS with both SMPS and dry nephelometer measurements at JFJ. This particular instrument has been deployed at several other locations where intercomparisons with other instruments including other AMS instruments consistently report a collection efficiency of 1 for ambient aerosol. Table 3.1 lists the mean concentrations measured at the JFJ.

### Light absorption coefficient

The aethalometer (AE-31, Magee Scientific) has measured light absorption coefficients ( $\sigma_{\text{ap}}$ ) of TSP at seven wavelengths ( $\lambda = 370, 470, 520, 590, 660, 880, 950 \text{ nm}$ ) at the JFJ since 2001. According to Weingartner et al. (2003)  $\sigma_{\text{ap}}$  was calculated with:

$$\sigma_{\text{ap}} = \frac{A \Delta\text{ATN}}{Q \Delta t} \frac{1}{CR(\text{ATN})}, \quad (3.6)$$

where  $A$  is the filter spot area,  $Q$  the volumetric flow rate and  $\Delta\text{ATN}$  the change in attenuation during the time interval  $\Delta t$ .  $C$  has a value of 2.81 for the JFJ and is a wavelength independent empirical correction factor (Collaud Coen et al., 2010). It corrects for multiple reflections of the light beam at the filter fibers, which enhances the optical path in the filter of the aethalometer.  $R$  corrects for the loading dependent shadowing effect.  $R=1$  is used for the aged aerosol at the JFJ (Weingartner et al.,

2003).

The black carbon (BC) concentration was calculated from  $\sigma_{\text{ap}}$  at 880 nm using an optical absorption cross-section of the manufacturer ( $16.6/C \text{ m}^2/\text{g}=5.91 \text{ m}^2/\text{g}$ ). It is a common practice to use this wavelength for the determination of equivalent BC concentrations since smaller wavelengths may have stronger contributions by other aerosol components (such as organic matter or mineral dust).

The aerosol single scattering albedo  $\omega_0$  describes the relative contribution of scattering to the total light extinction:

$$\omega_0 = \frac{\sigma_{\text{sp}}}{\sigma_{\text{sp}} + \sigma_{\text{ap}}}. \quad (3.7)$$

Since  $\omega_0$  is wavelength dependent  $\sigma_{\text{sp}}$  and  $\sigma_{\text{ap}}$  need to be at the same wavelength. Therefore we transformed  $\sigma_{\text{ap}}$  measured by the aethalometer to the nephelometer wavelengths 450, 550 and 700 nm by using the measured Ångström exponent for the absorption  $\dot{a}_a$  (in analogy to Eq. 3.2).

### 3.2.3 Mie calculations to predict $f(\text{RH})$

#### Using measured physical and chemical properties

We predicted  $f(\text{RH})$  with a model based on Mie theory (Mie, 1908) where the core Mie routine is based on the code of Bohren and Huffman (2004). The particles are assumed to be spherical and homogeneously internally mixed. As input the number size distribution and the complex refractive index  $n$  of the measured aerosol are needed. The SMPS and OPC measured number size distribution; both were combined at 340 nm (see Sect. 3.2.2). The complex refractive index was calculated using the chemical composition measurements of the AMS and the aethalometer. A time resolved mean refractive index was then determined by a volume fraction averaging:

$$n(\lambda) = \sum \frac{mf_i}{\rho_i} n_i(\lambda), \quad (3.8)$$

where  $mf_i$  is the mass fraction,  $\rho_i$  is the density and  $n_i(\lambda)$  is the wavelength dependent complex refractive index of the compound  $i$ . We took the values for  $n_i$  and  $\rho_i$  as listed in Table 3.1.

Hygroscopic growth was accounted for in two alternative ways: either by directly using the size resolved H-TDMA measurements of diameter growth factors or by calculating the hygroscopic growth factor from AMS and aethalometer measurements. The H-TDMA growth factors  $g(\text{RH}=90\%)$  were extrapolated to different RH using Eq. (3) from Gysel et al. (2009), which uses the  $\kappa$ -model introduced by Petters and Kreidenweis (2007). For the wet refractive index a volume weighting between the refractive indices of water and the according dry aerosol was chosen (Hale and Query, 1973).

The AMS plus aethalometer measurements can also be used to calculate the hygroscopic growth factor. For this, we used the individual  $g$  values for the retrieved salts and acids that were derived from Topping et al. (2005). For the organic component, we used a growth factor of 1.2 at  $\text{RH}=85\%$ , which is representative for aged organic aerosol at the JFJ (Sjogren et al., 2008). The BC is believed to be insoluble, i.e.  $g=1$ . An mean growth factor is then calculated from the growth factors of the individual components of the aerosol and their respective volume fractions with the ZSR relation (Stokes and Robinson, 1966).

### Using the Ångström exponent as only directly measured input

Nessler et al. (2005a) proposed a specific algorithm for the JFJ site to adapt dry nephelometer measurements to ambient conditions. They used a coated sphere model also based on Mie theory to calculate  $f(\text{RH})$ . The fine mode was modeled assuming an insoluble core and a homogeneous soluble coating, which absorbs an increasing amount of water with increasing RH. The relative amounts of insoluble and soluble material in the fine mode were derived from experimental chemical composition and hygroscopic growth data. To get a representative range of the JFJ size distributions, Nessler et al. (2005a) combined 15 months of averaged SMPS and OPC data and fitted them with the sum of three log-normal distributions. By varying the geometric standard deviations, median diameters, and coarse mode concentrations within the  $\pm 15\%$  interval of the fitted parameters, they obtained size distributions considered representative for the JFJ aerosol. The coarse mode is considered to be insoluble (no hygroscopic growth), as it is mainly mineral dust which is detected in this size range. The Ångström exponent  $\hat{a}_s$  (see Eq. 3.2), is used as a proxy for the relative contributions of fine and coarse mode particles, and is beside the RH in the nephelometer the only input parameter required to calculate  $f(\text{RH})$ . The parameterization is given for a separate summer and a winter case and is valid in the range of  $-0.25 < \hat{a}_s < 2.75$  and  $0\% < \text{RH} < 90\%$ . Our measurement period lies within the proposed summer case scenario.

## 3.3 Results and discussion

First we give an overview of the measured light scattering enhancement factors  $f(\text{RH})$  in combination with other measurements, then we demonstrate how  $f(\text{RH})$  can be predicted and finally we investigate the impact of RH on further climate relevant intensive properties.

### 3.3.1 Measured $f(\text{RH})$

#### Overview

Figure 3.1 shows an overview of the measured scattering coefficient  $\sigma_{\text{sp}}$  and the light scattering enhancement factor  $f(\text{RH})$  at 85% RH of the campaign in May 2008 at the JFJ. Every data point represents hourly averaged data. All time scales are Central European Summer Time (CEST=UTC+2 h). Figure 3.1a displays the scattering coefficient  $\sigma_{\text{sp}}$  at 550 nm wavelength. The nephelometer measured hourly averaged  $\sigma_{\text{sp}}$  values between 0 and  $1.1 \times 10^{-4} \text{ m}^{-1}$ . The highest scattering signal occurred on 28 May, during a strong Saharan dust event (SDE). The mean  $\sigma_{\text{sp}}$  of the measurement campaign is shown in Table 3.2 (without SDE and for SDE only).  $\sigma_{\text{sp}}$  shows higher values during the first half of the measurement campaign (1 to 16 May) than during the second half (16 to 26 May), until the SDE started. We will treat the time period of the SDE separately (Sect. 3.3.1). We explain the low scattering coefficients of the second half of the measurement campaign by high cloud coverage and precipitation.  $\sigma_{\text{sp}}$  values below  $10^{-6} \text{ m}^{-1}$  for hourly means were included in the calculation of means of  $\sigma_{\text{sp}}$  but not for further data analysis. We highlighted these data points in light green in the curve of  $\sigma_{\text{sp}}$  in Fig. 3.1. For the prediction of  $f(\text{RH})$  (see Sect. 3.3.2)  $\sigma_{\text{sp}}$  values below  $5 \times 10^{-6} \text{ m}^{-1}$  were not used, and

Table 3.2: Scattering coefficient  $\sigma_{\text{sp}}$ , light scattering enhancement factor  $f(\text{RH}=85\%)$ , light backscattering enhancement factor  $f_b(\text{RH}=85\%)$ , backscatter fraction  $b$ , single scattering albedo  $\omega_0$ , Ångström exponent  $\tilde{a}_s$  and hygroscopic growth factor of 265 nm dry particles  $g(D=265 \text{ nm}, \text{RH}=90\%)$  averaged over the whole campaign excluding Saharan dust event (SDE) and averaged exclusively during the SDE.

	Campaign average			
	Excluding SDE		Exclusively SDE	
	<20% RH	85% RH	<20% RH	85% RH
$\sigma_{\text{sp}}(550 \text{ nm}) [\text{m}^{-1}]$	$1.19 \times 10^{-5}$		$2.05 \times 10^{-5}$	
$f(\text{RH}=85\%)$		2.23		1.72
$f_b(\text{RH}=85\%)$		1.60		1.54
$b$	0.128	0.089	0.122	0.101
$\omega_0$	0.907	0.954	0.930	0.960
$\tilde{a}_s$	1.787	0.839	1.671	1.111
$g(D=265 \text{ nm}, \text{RH}=90\%)$		1.522		n.a.

are shown in grey in Fig. 3.1a.

Figure 3.1b presents light scattering enhancement factors  $f(\text{RH}=85\%)$  at 450, 550 and 700 nm wavelength. These data points originate from scattering coefficients that were measured by the humidified nephelometer at a RH between 75 and 95% and were recalculated to RH=85% with Eq. (3.5). During most of the time the instrument measured at 85% RH ( $\pm 10\%$  RH), and  $f(\text{RH}=85\%)$  varied between 1.2 and 3.3 (mean shown in Table 3.2). Daily averaged values of  $f(\text{RH}=85\%)$  were between 1.65 and 2.82, with low values ( $< 2$ ) on 6, 18 and 26 May and values above 2.7 on 10, 12 and 13 May. A back trajectory analysis (FLEXTRA) for the days with  $f(\text{RH}=85\%) > 2.7$  showed that the air masses reaching JFJ often did not pass below 1000 m a.s.l. within the last 7 days. The few times they did it nonetheless was over the Atlantic Ocean. On these days we measured inorganic mass fractions higher than 0.57, largest particle mean diameters and high hygroscopic growth factors ( $g(\text{RH}=90\%) > 1.55$  for particles with a dry diameter of 265 nm). The air masses that reached the JFJ on days with low  $f(\text{RH})$  either passed at less than 1000 m a.s.l. in eastern Europe (6 May), in southwestern and mideastern Europe (19 May), or in northern Africa (26 May). By passing over populated areas the air probably picked up more organic matter which results in a decrease of  $f(\text{RH})$ . This hypothesis can be only confirmed for one day, because of gaps in the AMS measurements on the other days. On 6 May the mean mass fraction of the inorganic compounds was 0.43.

In the beginning of the measurement campaign (1–3 May) the  $f(\text{RH}=85\%, \lambda=700 \text{ nm})$  was lower compared to  $f(\text{RH}=85\%, \lambda=450 \text{ nm})$  while it was larger in the middle of the measurement campaign (11–14 May). This spectral behavior is explainable by a smaller coarse mode fraction and generally smaller particles in the latter case.

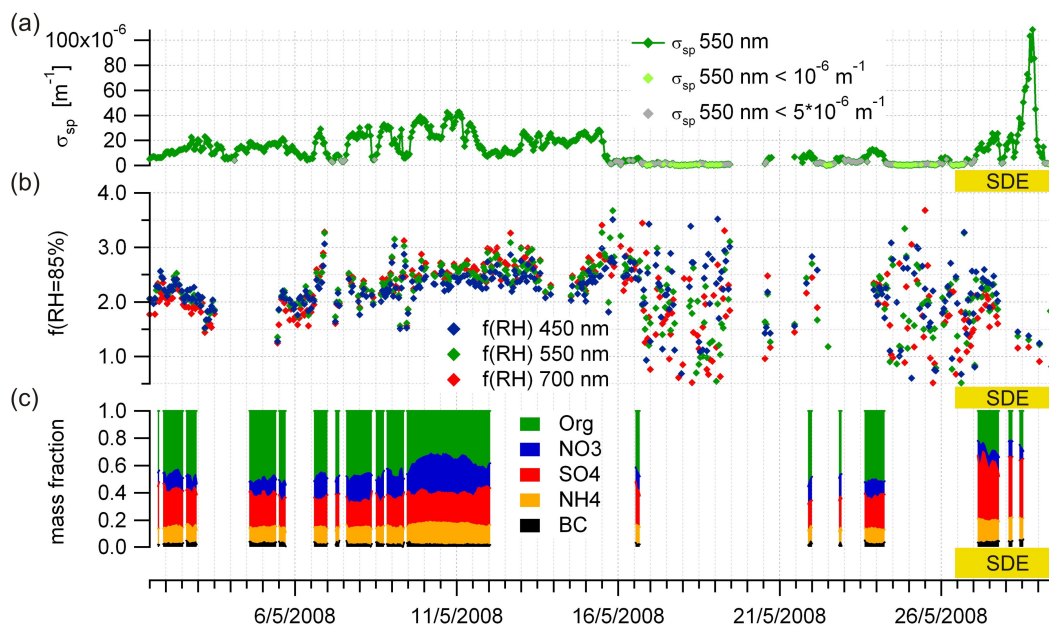


Figure 3.1: Time series of the scattering coefficient ( $\sigma_{sp}$ ) at 550 nm wavelength (a), measured  $f(\text{RH})$  recalculated to  $\text{RH}=85\%$  of three distinct wavelengths (b) and the mass fractions of organics, nitrate, sulfate, ammonium and black carbon (c). SDE indicates the time period, when a Saharan dust event was present. The scattering coefficients shown in light green are below  $10^{-6} \text{ m}^{-1}$ , those shown in grey are below  $5 \times 10^{-6} \text{ m}^{-1}$ .

### Saharan dust event (SDE)

In the end of the measurement campaign a strong Saharan dust event took place (26 May 12:00 LT to 29 May 12:00 LT). During a SDE the aerosol exhibits properties significantly different from the background conditions (Schwikowski et al., 1995; Collaud Coen et al., 2004). Such a SDE event significantly increases the coarse mode mass concentration but it also has an important influence on the accumulation mode. The H-TDMA was not running at this time, but typically shows an external mixture at 250 nm when there is significant influence of dust particles, which was also reported by Sjogren et al. (2008). The  $f(\text{RH}=85\%)$  during the most intensive time of the was the lowest during the whole measurement campaign, with an hourly averaged value of 1.2. Similarly, Carrico et al. (2003) measured in the ACE-Asia campaign during the most dust-dominated period a  $f(\text{RH})$  at 82% of 1.18. Our findings also agree with the ones of Li-Jones et al. (1998), who investigated the  $f(\text{RH})$  of long-range transported Saharan dust.

### Diurnal variations

At the JFJ extensive aerosol properties undergo diurnal variations, which are strongest in spring and summer (Baltensperger et al., 1997; Lugauer et al., 1998; Weingartner et al., 1999). In May 2008 (without SDE)  $\sigma_{sp}$  also varied throughout the day with a maximum in the late afternoon to early evening and a minimum before noon. The maximum was on average 1.5 times higher than the minimum



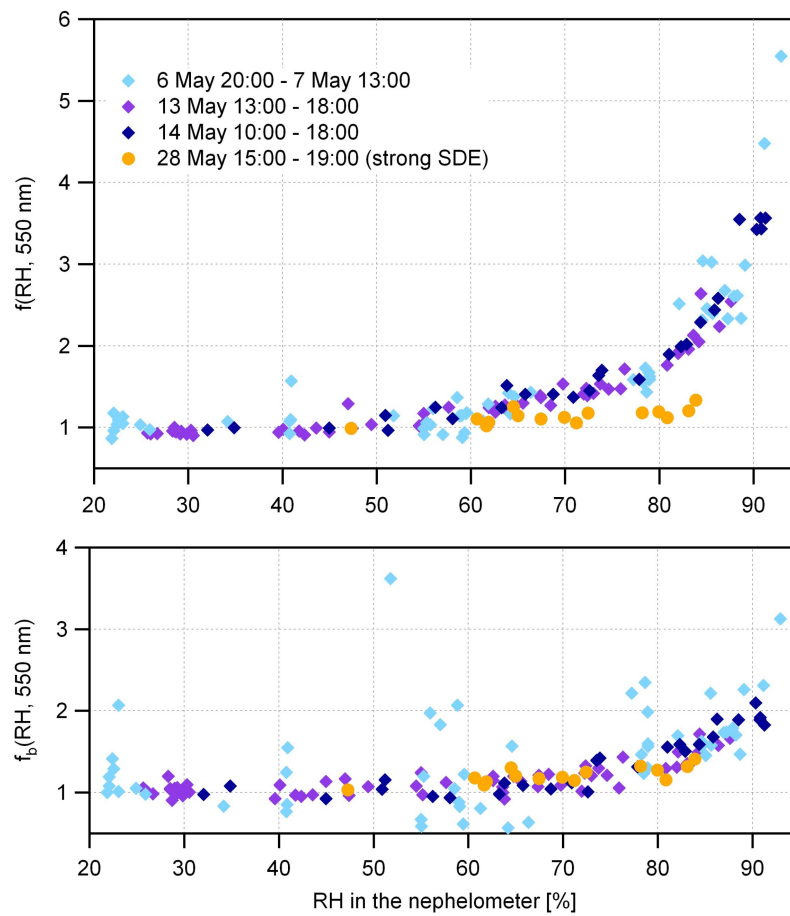


Figure 3.2: Light scattering enhancement factor  $f(\text{RH})$  (top) and light backscattering enhancement factor  $f_b(\text{RH})$  (bottom) at 550 nm wavelength vs. RH at four different time periods when the RH in the humidified nephelometer was cycled (max. 2 cycles per period).

( $9.5 \times 10^{-6} \text{ m}^{-1}$ ). The intensive parameter  $f(\text{RH}=85\%)$  did not experience a clear diurnal pattern in the same time period. A further analysis showed that here  $\sigma_{\text{sp}}$  increased due to an increase in the aerosol load rather than a change in the chemical composition or the size distribution. The time period of 6 to 11 May had long sunshine duration, favoring thermal convection. During this period the diurnal pattern of  $\sigma_{\text{sp}}$  was much more distinct, with the maximum being more than three times higher than the minimum ( $8.5 \times 10^{-6} \text{ m}^{-1}$ ). In this period, averaged  $f(\text{RH})$  values did indeed exhibit a diurnal variation, with the maximum roughly at the same time as  $\sigma_{\text{sp}}$ , suggesting that the chemical composition (or the size distribution) of the aerosol from the PBL was different from the one in the free troposphere. It can, however, be expected that also the reverse diurnal variation is possible, with  $f(\text{RH})$  being minimal when  $\sigma_{\text{sp}}$  shows its maximum.

### Humidograms

During four time periods the RH in the humidified nephelometer was cycled between 20 and 95% RH thus providing  $f(\text{RH})$  over a wide range of RH, also commonly referred to as humidograms. No dis-

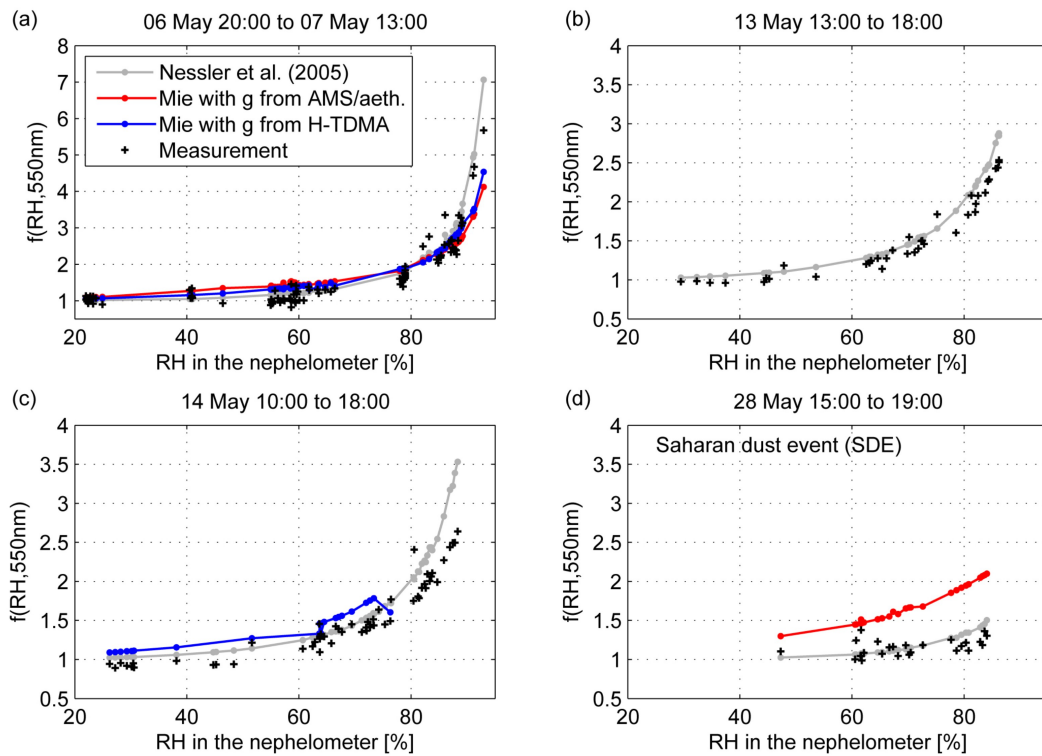


Figure 3.3: Humidograms showing measured (black symbols) and predicted  $f(\text{RH})$  vs. RH in the nephelometer for four example days in May 2008. The grey lines are calculated according to the approach by Nessler et al. (2005a). The red and blue lines are calculated with Mie theory using a combination of size distribution, chemical composition and hygroscopicity data. The latter are inferred either by the H-TDMA (blue lines) or the AMS/aethalometer data (red points). (d) shows a humidogram from the time period of the Saharan dust event (SDE). For 13 and 28 May, no H-TDMA data was available, whereas no AMS/aethalometer data was available on 13 and 14 May.

tinct efflorescence or deliquescence effects were seen, which is in line with previous H-TDMA humidograms recorded at this site (Weingartner et al., 2002; Sjogren et al., 2008). Figure 3.2 presents  $f(\text{RH})$  (top) and  $f_b(\text{RH})$  (bottom) at 550 nm wavelength of four measured humidograms. Each humidogram consists in maximum of two RH cycles, with 10-min means at each RH. The humidograms plotted with the diamond markers (6/7, 13 and 14 May) all have a similar shape and similar magnitude of  $f(\text{RH})$ . On 6 May there is much more variability in the  $f(\text{RH})$  data compared to 13 and 14 May, also seen in Fig. 3.1 for  $\sigma_{\text{sp}}$  data, which is attributed to a lower signal to noise ratio due to a lower aerosol loading. The humidogram in yellow was measured when the Saharan dust event was strongest. The aerosol grows very little with increasing RH, resulting in an  $f(\text{RH})$  at 85% of  $\sim 1.2$ .

There is no significant difference of  $f_b(\text{RH})$  between the SDE and the other days. Smaller particles scatter relatively more light in the backward direction, so when water is added the  $f_b(\text{RH})$  is much smaller than the  $f(\text{RH})$ . During a SDE the particles are larger and grow less and therefore the  $f_b(\text{RH})$  increases by about the same factor as without a SDE.

### 3.3.2 Prediction of $f(\text{RH})$

#### RH dependence

The scattering coefficients were calculated for each measurement point of the humidified nephelometer. The calculated dry and humid scattering coefficients were  $\sim 20\%$  below the measured ones (with a correlation coefficient  $R^2=0.97$  at 550 nm wavelength), which we attribute to a systematic bias in the measured model input parameters. The scattering coefficient at dry conditions depends on the aerosol chemical composition (via the refractive index), on the shape of the aerosol size distribution (or mean size) and on the aerosol concentration. The influence of the refractive index is not large enough to account for the encountered discrepancy of 20%. It is speculated that this discrepancy is mainly caused by a small systematic error in the measurement of the size distribution (i.e., either in the determination of the diameter or number concentration, or a combination of both). Since  $f(\text{RH})$  is not sensitive to the total number concentration and only slightly sensitive to the aerosol size distribution shape (see Sect. 3.3.2), we can neglect the constant difference in the absolute values.

The predicted  $f(\text{RH})$  depends on the aerosol size distribution, on the chemical composition of the aerosol and on the RH in the nephelometer. The chemical composition is used to determine the refractive index and the hygroscopic growth factor  $g$ .  $g$  can be calculated from measurements of the chemical composition by the AMS and the aethalometer or direct measurements with the H-TDMA.

Figure 3.3 presents the same humidograms as in Fig. 3.2 (top) (6/7, 13, 14 and 28 May), along with predicted humidograms. The black points in all four panels represent the measured  $f(\text{RH})$ . The colored points show the  $f(\text{RH})$  predicted by different model approaches (see Sect. 3.2.3). The red points denote  $f(\text{RH})$  predictions based on  $g$  values calculated from the AMS and aethalometer data, whereas the blue lines show  $f(\text{RH})$  predictions from the  $g$  values obtained by the H-TDMA. The grey points were calculated using the approach of Nessler et al. (2005a).

On 6/7 May (Fig. 3.3a) all instruments needed for these predictions were running. All model approaches agree well with the measurements and are similar up to 80% RH. Above 80% RH, the algorithm by Nessler et al. (2005a) overestimates  $f(\text{RH})$ , whereas the Mie calculations based on  $g$  values derived either from H-TDMA or AMS/aethalometer measurements underestimate  $f(\text{RH})$ . Neither AMS/aethalometer nor H-TDMA data are available on 13 May and only partly on 14 May (Fig. 3.3b, c). Predictions available for these days agree quite well with measurements, with the limitation that the algorithm by Nessler et al. (2005a) overestimates  $f(\text{RH})$  above 85% RH. On 28 May (Fig. 3.3d), when the SDE was present, the Mie calculation with  $g$  from the AMS/aethalometer results in a  $f(\text{RH})$  that is quite different from the measured one (no H-TDMA data were available on this day). This is reasonable since Saharan dust contains a large fraction of refractory material (Schwikowski et al., 1995; Collaud Coen et al., 2004; Cozic et al., 2008) which is not detected by the AMS. In addition, the AMS does not measure super-micrometer particles, which are much more abundant during a SDE. The Nessler algorithm predicts  $f(\text{RH})$  quite well during the SDE. As explained above, the only input variable is the Ångström exponent (values in Table 3.2), which is a proxy for the detected size distribution. At low values ( $\hat{a}_s < 1$ ) the aerosol size distribution is dominated by the coarse mode which exhibits much less hygroscopic growth than the accumulation mode.

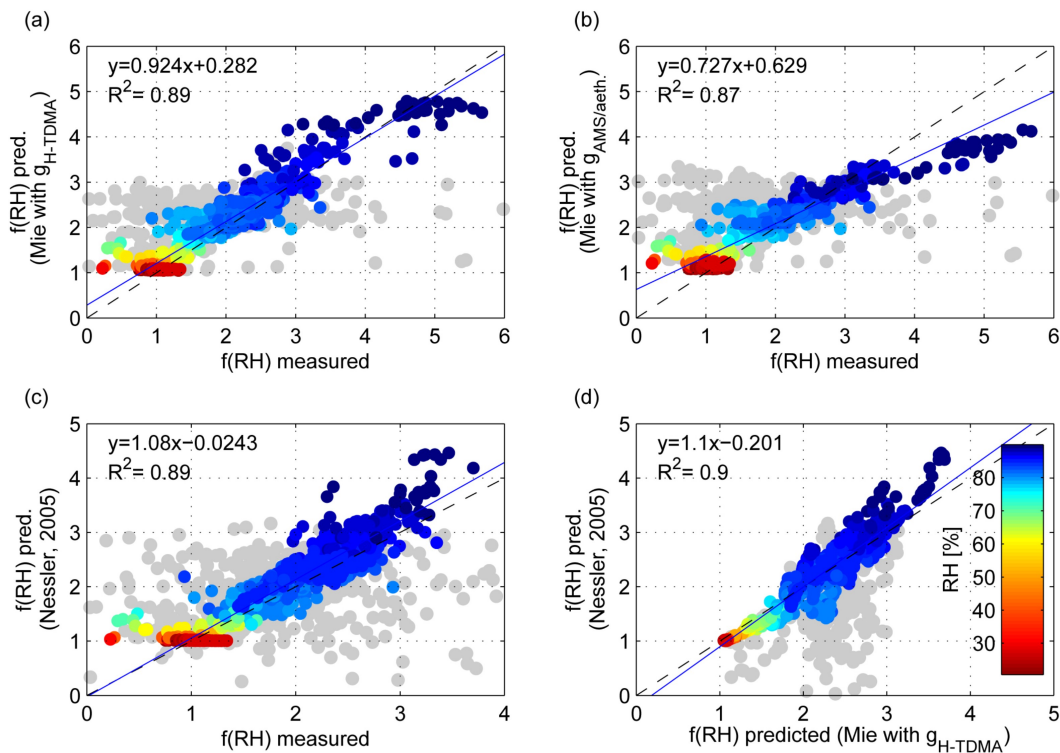


Figure 3.4: Comparison of predicted and measured  $f(\text{RH})$  (6-min means, entire measured RH range, SDE excluded). **(a)** prediction includes size distribution and uses  $g$  from the H-TDMA measurements. **(b)** same as **(a)** but using  $g$  calculated from the AMS/aethalometer data as a proxy for the chemical composition. **(c)** predicted  $f(\text{RH})$  according to Nessler et al. (2005a) vs. measured  $f(\text{RH})$ . **(d)**  $f(\text{RH})$  predicted according to Nessler et al. (2005a) vs.  $f(\text{RH})$  predicted with the method using  $g$  of the H-TDMA. The color code represents the RH in the nephelometer, whereas the grey symbols are data points with  $\sigma_{\text{sp}} < 5 \times 10^{-6} \text{ m}^{-1}$ . The blue solid line represents a non-linear least square regression.

Figure 3.4a and b present the sensitivity of the model predictions to the source of the hygroscopic growth data. The x-axes always show the measured  $f(\text{RH})$ , whereas the y-axes display the predicted  $f(\text{RH})$ , with  $g$  obtained from the H-TDMA (Fig. 3.4a) and from the AMS/aethalometer data (Fig. 3.4b). The colors indicate the RH in the nephelometer. All points in grey are  $f(\text{RH})$  values from scattering coefficients smaller than the threshold of  $5 \times 10^{-6} \text{ m}^{-1}$ . They have a high uncertainty and were therefore not used for the linear regression (blue line) and the correlation coefficient. We excluded all data from the time period of the SDE because of missing H-TDMA data.

By using all measured input parameters we get a good agreement between measured and predicted  $f(\text{RH})$ . However, when  $g$  from the AMS/aethalometer is used instead of  $g$  from the H-TDMA measurements, the predicted  $f(\text{RH})$  is lower than the measured  $f(\text{RH})$  at high RH and higher at low RH. We conclude that we are able to perform a closure of the  $f(\text{RH})$  measurements with our model calculations using a combination of SMPS, OPC, AMS, aethalometer and H-TDMA data.

The same correlation plot but with predictions using the approach by Nessler et al. (2005a) is shown in Fig. 3.4c. The correlation between measurement and prediction is good. At higher RH the Nessler algorithm overestimates  $f(\text{RH})$  slightly. As described above, Nessler et al. (2005a) give 90% RH as

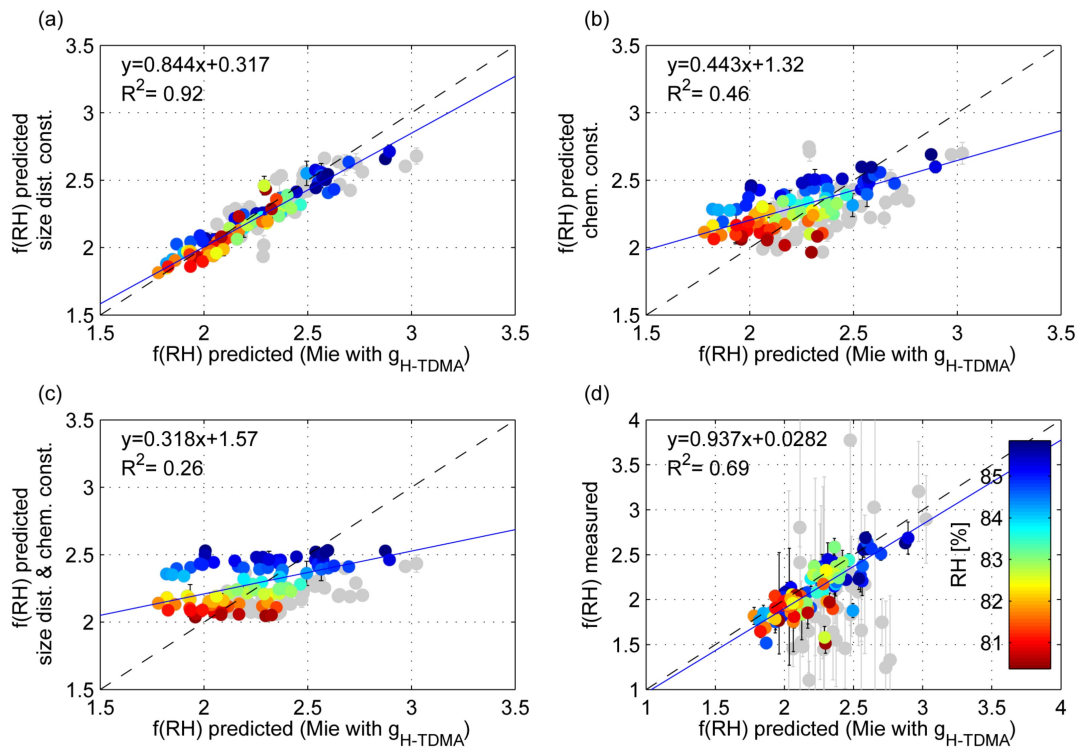


Figure 3.5: Sensitivity analysis of  $f(\text{RH})$  on the chemical composition and size distribution. Hourly means of different predictions vs. the best possible prediction (using size distribution, chemical composition and hygroscopic growth measurements, excluding the SDE) of  $f(\text{RH})$  at  $\text{RH}=80\text{--}86\%$ :  $f(\text{RH})$  predicted with constant size distribution (a), predicted with constant chemical composition (b), and with combined constant size distribution and constant chemical composition (c). (d) shows measured  $f(\text{RH})$  with standard deviation vs. the best possible prediction of  $f(\text{RH})$ . The color code represents the RH in the nephelometer, whereas the grey symbols are data points with  $\sigma_{\text{sp}} < 5 \times 10^{-6} \text{ m}^{-1}$ . The blue solid line represents a non-linear-least-square regression.

an upper limit. In Fig. 3.4d we compare the prediction using  $g$  from the H-TDMA with the model of Nessler. The two models predict similar  $f(\text{RH})$  up to about 85% RH, but at higher RH either the Nessler approach overestimates  $f(\text{RH})$ , or the H-TDMA measurements underestimate  $f(\text{RH})$  with the assumptions made.

### Sensitivity of $f(\text{RH})$ to size distribution shape and chemical composition

To investigate the influence of the size distribution and chemical composition on  $f(\text{RH})$ , we repeated the model predictions by keeping one or both parameters constant. For a constant shape of the size distribution, the monthly mean normalized size distribution was multiplied with the concentration for each data point instead of using the measured size distributions. For a constant chemical composition one mean refractive index and the mean  $g$  from the H-TDMA at the diameter of 265 nm were taken.

For the sensitivity analysis we only considered  $f(\text{RH})$  at RH between 80 and 86% and used hourly

means. The x-axes of all four panels of Fig. 3.5 show the best possible prediction considering measurements of the size distribution, the chemical composition and  $g$ , which is used as a reference case for the simplified predictions. The marker color represents the RH in the nephelometer and the grey symbols represent  $f(\text{RH})$  values with  $\sigma_{\text{sp}}$  below the threshold of  $5 \times 10^{-6} \text{ m}^{-1}$ . Figure 3.5a shows the model prediction using a constant size distribution on the y-axis, which reproduces the reference prediction within  $\pm 8\%$ . This shows that variations of the shape of the number size distributions have very little effect on the variability of  $f(\text{RH})$  at the Jungfrauoch. A major reason for this is that the shape of the accumulation mode size distribution varies little at the JFJ (Weingartner et al., 1999), which was also true for this time period. Figure 3.5b shows the model prediction using constant mean chemical composition. Neglecting the temporal variability of the chemical composition reduces the correlation to the reference case significantly. This demonstrates that the temporal variability of the chemical composition has some influence on the variability of  $f(\text{RH})$ . Nevertheless deviations from the reference case remain smaller than a factor of 1.25, showing that knowing the mean chemical composition is still sufficient for a fair prediction of  $f(\text{RH})$  for this month of measurement, always excluding SDE. The model prediction keeping both chemical composition and size distribution constant has the lowest correlation with the reference case, even though absolute deviations remain similar to the previous simplification.

The effects of changing chemical composition become even more important than shown in the above sensitivity analysis, if SDEs are included. Figure 3.2 clearly shows that  $f(\text{RH})$  drops dramatically if the scattering is dominated by non-hygroscopic dust particles. The fact that knowing the mean chemical composition and typical size distribution of the Jungfrauoch aerosol is sufficient for fair predictions of  $f(\text{RH})$  explains the good performance of Nessler's approach when comparing predictions with measurements across a wide range of RH (see Fig. 3.4c), where changes in RH have the dominant influence on  $f(\text{RH})$ . Furthermore, Nessler's approach is also able to capture SDEs (see Fig. 3.3d) by inferring the relative contributions of hygroscopic fine mode particles and non-hygroscopic coarse mode dust particles from the Ångström exponent, which is a measure of the average size of the aerosol particle population. In contrast, the other two approaches which use AMS and aethalometer or H-TDMA derived growth factors for prediction of  $f(\text{RH})$  are both biased during SDE events because they essentially miss the dust component. The AMS does not measure refractory material such as dust and is limited to the submicron size range. The H-TDMA, which also captures non-hygroscopic dust particles, is limited to particles with diameters below 265 nm. The dominant contribution of dust is found at sizes above 265 nm and therefore the overall contribution of dust is underestimated also with the H-TDMA approach.

### 3.3.3 RH dependence of derived climate relevant properties

#### RH dependence of the backscatter fraction and the single scattering albedo

Beside  $f(\text{RH})$  other intensive properties depend on RH: the Ångström exponent  $\tilde{a}_s$ , the backscatter fraction  $b$  and the single scattering albedo  $\omega_0$ . In this section we will focus on  $b$  and  $\omega_0$ . Figure 3.6 presents frequency distributions of hourly means of  $b$  and  $\omega_0$  at 550 nm wavelength from 1 to 26 May, excluding the last three days of the measurement campaign, when the Saharan dust event was present.

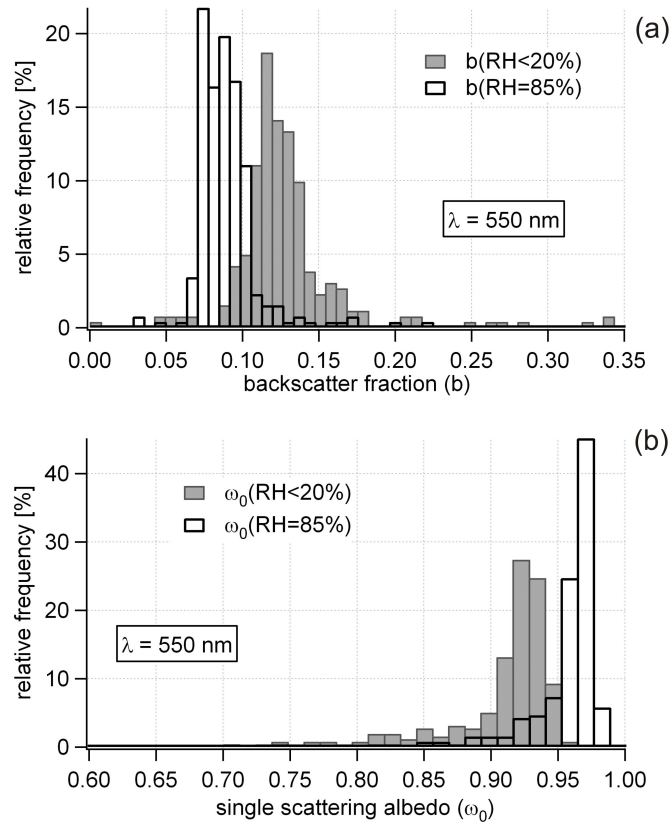


Figure 3.6: Frequency distribution (hourly means) of the backscatter fraction  $b$  (a) and of the single scattering albedo  $\omega_0$  (b) at 85% RH (white) and below 20% RH (grey). The Saharan dust event (SDE) at the end of the campaign as well as data points with  $\sigma_{\text{sp}} < 10^{-6} \text{ m}^{-1}$  were excluded.

Data points with  $\sigma_{\text{sp}} < 10^{-6} \text{ m}^{-1}$  were also omitted.

Figure 3.6a displays the relative frequency of 262 h of measured  $b$  at RH<20% and RH=85%. The  $b(\text{RH}=85\%)$  originates from  $\sigma_{\text{sp}}$  and  $\sigma_{\text{bsp}}$  values at RH between 75 and 95% recalculated to RH=85% using Eq. (3.5). The  $b(\text{RH}<20\%)$  is between 0.08 and 0.18 for 90% of the time, with the mode being at 0.115. The  $b(\text{RH}=85\%)$  is lower (between 0.06 and 0.11 for 90% of the time), since the aerosol particles are larger and hence scatter more in the forward direction. The mean  $b(\text{RH}<20\%)$  and  $b(\text{RH}=85\%)$  are listed in Table 3.2.

Figure 3.6b presents the frequency distribution of  $\omega_0(\text{RH}<20\%)$  and  $\omega_0(\text{RH}=85\%)$ . The latter was determined from  $\sigma_{\text{sp}}$  values recalculated to RH=85% as described above and dry  $\sigma_{\text{ap}}$  values assuming that the absorption does not change with RH (Nessler et al., 2005b). Out of 259 h of measurement  $\omega_0(\text{RH}<20\%)$  was between 0.83 and 0.95 for more than 90% of the time and between 0.91 and 0.94 for more than 50% of the time. In contrast,  $\omega_0(\text{RH}=85\%)$  was below 0.9 for less than 7% of the time, and between 0.96 and 0.98 for about 50% of the time. On average  $\omega_0$  increases by  $\sim 0.05$  due to water uptake (see also Table 3.2).

Since the interest is not only on the two RH ranges shown in Fig. 3.6, we display box plots of  $b$  and  $\omega_0$  for different RH bins in Fig. 3.7. Here we present a subset of the whole dataset where humidograms were measured (totally 51 h of measurements).



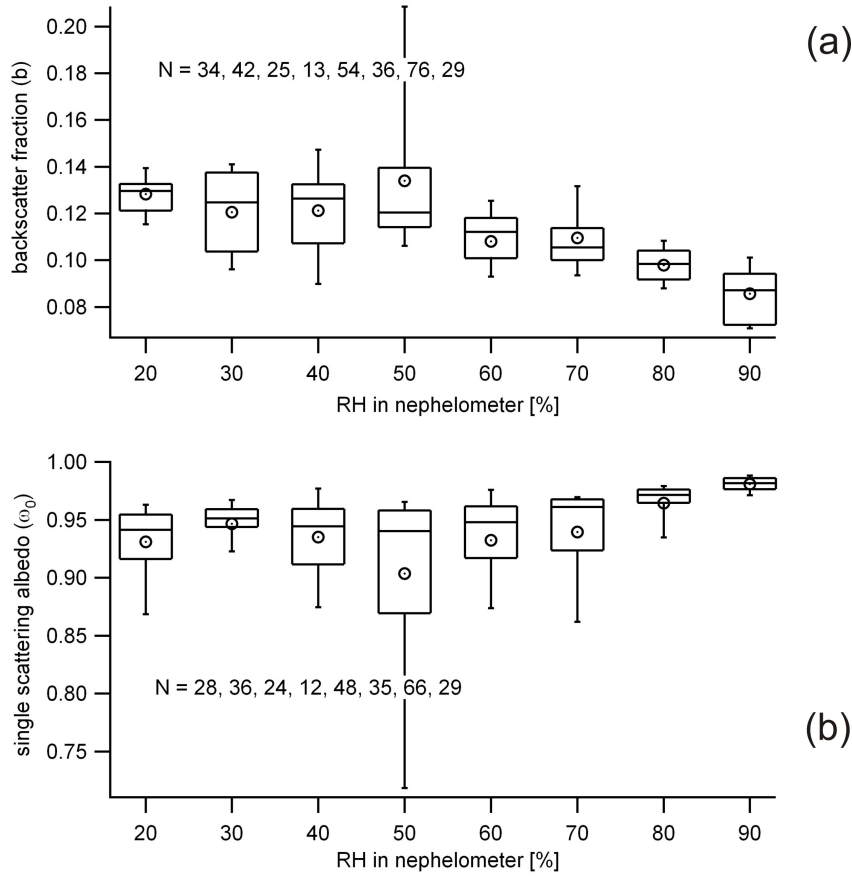


Figure 3.7: Box- and whisker-plot of the backscatter fraction **(a)** and the single scattering albedo **(b)** sorted in bins with a width of 10% RH. Every box contains  $N$  10-min data, measured within  $\pm 5\%$  of the indicated RH. The circles are the mean values, the horizontal lines in the boxes are the medians, the bottom and top limits of the boxes are the 25th and 75th percentiles and the whiskers extend to the 10th and 90th percentiles.

The backscatter fraction  $b$  decreases with increasing RH from about 0.13 at  $20 \pm 5\%$  RH to about 0.09 at  $90 \pm 5\%$  RH. The decrease is not perfectly monotonous, but we assume that this is mainly due to the low number of points measured at 50% RH.  $\omega_0$  shows the opposite behavior above 50% RH, it increases with increasing RH. The observed deviation at 50% RH is again caused by poor statistics which is based on 12 data points. For both  $b(\text{RH}=50\%)$  and  $\omega_0(\text{RH}=50\%)$  a single outlier influences the mean values.

### RH dependence of the radiative forcing

As  $\sigma_{\text{sp}}$ ,  $\omega_0$  and  $b$  are all RH dependent, the radiative forcing  $\Delta F$ , given by the radiative forcing equation by Haywood and Shine (1995), is also RH dependent:

$$\Delta F(\text{RH}) \approx -DS_0 T_{\text{atm}}^2 (1 - A_C) \omega_0(\text{RH}) \beta(\text{RH}) \delta(\text{RH}) \cdot \left\{ (1 - R_S)^2 - \left( \frac{2R_S}{\beta(\text{RH})} \right) \left[ \left( \frac{1}{\omega_0(\text{RH})} \right) - 1 \right] \right\}. \quad (3.9)$$



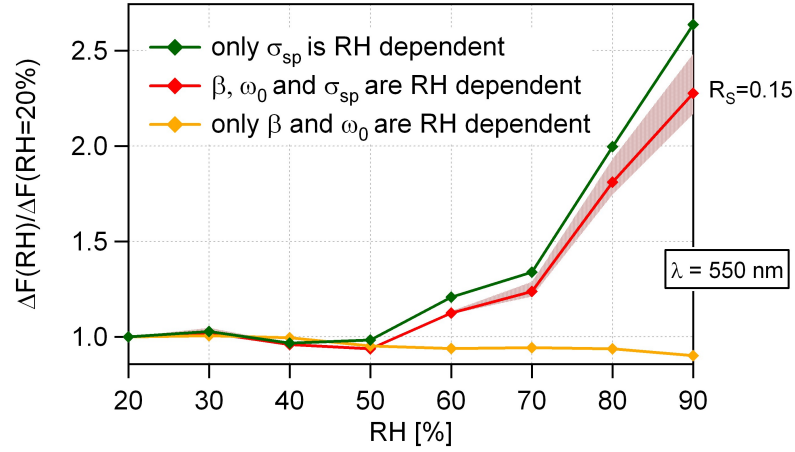


Figure 3.8: Ratio of radiative forcing at a certain RH to radiative forcing at dry conditions (RH=20%) for  $R_S=0.15$ , depending on RH for three different cases where the RH dependence of the following parameters is considered: only  $\sigma_{sp}$  (green curve),  $\sigma_{sp}$ ,  $\omega_0$  and  $\beta$  (red curve), and only  $\omega_0$  and  $\beta$  (yellow curve). The red area shows the  $R_S$  dependence of the red curve ( $0.05 < R_S < 0.25$ ).

The following parameters in the equation are RH independent: fractional daylight  $D$ , solar flux  $S_0$ , atmospheric transmission  $T_{atm}$ , fractional cloud amount  $A_C$ , surface reflectance  $R_S$ . The RH dependent upscatter fraction  $\beta$  was calculated from the backscatter fraction  $b$  with Eq. (3.3). The spectrally weighted aerosol optical depth  $\delta$  depends on RH via  $\sigma_{sp}$  and  $\sigma_{ap}$ . With Eq. (3.7)  $\sigma_{ap}$  can be displaced in the following way:

$$\sigma_{ap}(RH) = \frac{\sigma_{sp}(RH)}{\omega_0(RH)} - \sigma_{sp}(RH), \quad (3.10)$$

which results in an RH dependent aerosol optical depth of:

$$\delta = \int \frac{\sigma_{sp}(RH)}{\omega_0(RH)} dz. \quad (3.11)$$

To investigate the RH dependence of the radiative forcing  $\Delta F$ , we calculate  $\Delta F(RH)/\Delta F(RH=20\%)$  which is now only dependent on  $R_S$ ,  $f(RH)$ ,  $\omega_0$  and  $b$ :

$$\frac{\Delta F(RH)}{\Delta F(RH=20\%)} = \frac{\beta(RH)}{\beta(RH=20\%)} f(RH) \cdot \left\{ \frac{(1-R_S)^2 - \left(\frac{2R_S}{\beta(RH)}\right) \left[\left(\frac{1}{\omega_0(RH)}\right) - 1\right]}{(1-R_S)^2 - \left(\frac{2R_S}{\beta(RH=20\%)}\right) \left[\left(\frac{1}{\omega_0(RH=20\%)}\right) - 1\right]} \right\}. \quad (3.12)$$

$R_S$  is taken as 0.15 (global average, Hummel and Reck, 1979) and the RH dependence of  $\omega_0$  and  $b$  is taken from the parameterization presented above (Fig. 3.7).

Figure 3.8 clearly shows that the radiative forcing increases for  $RH > 50\%$  and is more than twice as high at 90% RH than at 40% RH. Two effects influence this behavior: first and most important is the RH dependence of  $\sigma_{sp}$ , shown as green curve, where  $\omega_0$  and  $b$  are assumed to be RH independent. The total RH dependence of  $\Delta F$  gets slightly smaller, when the RH dependence of  $\omega_0$  and  $b$  is taken into account. The reason for this is that  $b$  decreases with increasing RH.

To be able to transform the radiative forcing from one RH to another we studied the red curve of Fig. 3.8. It tells us that the radiative forcing increases by 24%, 19%, 14%, 11%, if the RH increases from 70% to 75%, 75% to 80%, 80% to 85% and 85% to 90%, respectively.

The radiative forcing due to aerosols does not only depend on the aerosol properties but also on the surface albedo of the ground underneath the aerosol. The last term of Eq. (3.9) in curly brackets determines whether an aerosol layer above a certain surface leads to cooling or warming (Haywood and Shine, 1995). The sensitivity of the red curve on  $R_S$  is shown with the red area, which displays the variability of the red curve with  $R_S$  between 0.25 (upper limit) and 0.05 (lower limit). For the aerosol sampled at the JFJ and so in the free troposphere the critical  $R_S$ , at which this aerosol layer would change from a net cooling to a net warming effect, is at  $R_S=0.51$  for dry conditions and  $R_S=0.61$  at 80% RH. Surface reflectance of this level would be found above snow and ice.

### 3.4 Summary and conclusions

During a month-long measurement campaign at the high alpine site Jungfraujoch we measured light scattering enhancement factors  $f(\text{RH})$  at different RH, but mostly between 80 and 90% RH.  $f(\text{RH}=85\%)$  reached values up to 3.3, whereas the lowest  $f(\text{RH}=85\%)$  values of 1.2 were detected during a Saharan dust event (SDE). The mean  $f(\text{RH}=85\%)$  of the measured free tropospheric aerosol (2.23) is higher than the  $f(\text{RH}=82\%)$  of polluted and clean aerosol in Europe during ACE-2 (1.46 and 1.69, Carrico et al., 2000), but lower than marine aerosol (2.42 at 82% RH, Carrico et al., 2003) or polluted aerosol of East Asia ( $f(\text{RH}=85\%)=2.75$ , Kim et al., 2006). At the JFJ the RH dependence of  $f(\text{RH})$  was similar on three different days, excluding the SDE event, indicating that on these days the aerosol had similar physical and chemical properties in the relevant size range.

Measured  $f(\text{RH})$  were compared to predictions obtained with two different model approaches: the first model uses Mie theory with measured size distributions, chemical composition and a hygroscopicity parameter to calculate  $f(\text{RH})$ . The hygroscopicity parameter  $g$  can be calculated from measurements of the chemical composition by the AMS and the aethalometer or direct measurements from the H-TDMA. The second simplified approach is based on the model of Nessler et al. (2005a), which uses Mie theory and the measured Ångström exponent of the dry scattering coefficient to calculate  $f(\text{RH})$ . Both models reproduce  $f(\text{RH})$  quite well. The Nessler model works fine up to RH values of 85%, whereas at higher RH it overestimates  $f(\text{RH})$ . It also predicts  $f(\text{RH})$  quite well during the SDE. The first model has constraints during the SDE: The AMS does not measure refractory material such as dust and it is limited to the submicron size range. The H-TDMA, which also captures non-hygroscopic dust particles, is limited to particles with diameters below 265 nm. With the first model we additionally performed a sensitivity analysis on the input parameters (chemical composition and size distribution). We found that the variability of the chemical composition has a dominant influence of the variability of  $f(\text{RH})$ , but also a mean size distribution is required to predict  $f(\text{RH})$  well.

The RH influences also other intensive properties than  $f(\text{RH})$ : the backscatter fraction  $b$  and the single scattering albedo  $\omega_0$ .  $b$  gets smaller with increasing RH, due to particle growth and  $\omega_0$  gets closer to 1 with increasing RH, because the influence of the scattering upon the absorption gets more important. By combining all three investigated RH dependent variables  $\omega_0$ ,  $b$  and  $f(\text{RH})$  we can estimate the RH

dependence of the radiative forcing due to aerosols. At 90% RH the radiative forcing is 2.3 times higher than at 20% RH for the conditions found at the JFJ in May 2008.

### **Acknowledgements**

We thank the International Foundation High Altitude Research Stations Jungfrauoch and Gornergrat (HFSJG), which made it possible to carry out the experiments at the High Altitude Research Station at the Jungfrauoch. Financial support for this work was received from the EC projects EUSAAR (European Supersites for Atmospheric Aerosol Research), GEOMON (Global Earth Observation and Monitoring) and EUCAARI (European Integrated Project on Aerosol Cloud Climate Air Quality Interactions), as well as from MeteoSwiss in the framework of the Global Atmosphere Watch program and the Swiss National Science Foundation (grant PZ00P2 121911/1). NILU is acknowledged for providing the FLEX-TRA trajectories ([www.nilu.no/trajectories](http://www.nilu.no/trajectories)) used in this study.



## Chapter 4

# Effects of relative humidity on aerosol light scattering in the Arctic

P. Zieger<sup>1</sup>, R. Fierz-Schmidhauser<sup>1</sup>, M. Gysel<sup>1</sup>, J. Ström<sup>2</sup>, S. Henne<sup>3</sup>, K. E. Yttri<sup>4</sup>, U. Baltensperger<sup>1</sup>, E. Weingartner<sup>1</sup>

<sup>1</sup>Laboratory of Atmospheric Chemistry, Paul Scherrer Institut, 5232, Villigen PSI, Switzerland

<sup>2</sup>Norwegian Polar Institute, Polarmiljøseneteret, 9296 Tromsø, Norway

<sup>3</sup>Empa, Laboratory for Air Pollution and Environmental Technology, Überlandstrasse 129, 8600 Dübendorf, Switzerland

<sup>4</sup>Norwegian Institute for Air Research, Dept. Atmospheric and Climate Research, P.O. Box 100, 2027 Kjeller, Norway

*Published in Atmospheric Chemistry and Physics, 10, 3875-3890, doi:10.5194/acp-10-3875-2010, 2010.*

### Abstract

Aerosol particles experience hygroscopic growth in the ambient atmosphere. Their optical properties – especially the aerosol light scattering – are therefore strongly dependent on the ambient relative humidity (RH). In-situ light scattering measurements of long-term observations are usually performed under dry conditions (RH<30–40%). The knowledge of this RH effect is of eminent importance for climate forcing calculations or for the comparison of remote sensing with in-situ measurements. This study combines measurements and model calculations to describe the RH effect on aerosol light scattering for the first time for aerosol particles present in summer and fall in the high Arctic. For this purpose, a field campaign was carried out from July to October 2008 at the Zeppelin station in Ny-Ålesund, Svalbard. The aerosol light scattering coefficient  $\sigma_{sp}(\lambda)$  was measured at three distinct wavelengths ( $\lambda=450, 550, \text{ and } 700 \text{ nm}$ ) at dry and at various, predefined RH conditions between 20% and 95% with a recently developed humidified nephelometer (WetNeph) and with a second nephelometer measuring at dry conditions with an average RH<10% (DryNeph). In addition, the aerosol size distribution and the aerosol absorption coefficient were measured. The scattering enhancement

factor  $f(\text{RH}, \lambda)$  is the key parameter to describe the RH effect on  $\sigma_{\text{sp}}(\lambda)$  and is defined as the RH dependent  $\sigma_{\text{sp}}(\text{RH}, \lambda)$  divided by the corresponding dry  $\sigma_{\text{sp}}(\text{RH}_{\text{dry}}, \lambda)$ . During our campaign the average  $f(\text{RH}=85\%, \lambda=550 \text{ nm})$  was  $3.24 \pm 0.63$  (mean  $\pm$  standard deviation), and no clear wavelength dependence of  $f(\text{RH}, \lambda)$  was observed. This means that the ambient scattering coefficients at RH=85% were on average about three times higher than the dry measured in-situ scattering coefficients. The RH dependency of the recorded  $f(\text{RH}, \lambda)$  can be well described by an empirical one-parameter equation. We used a simplified method to retrieve an apparent hygroscopic growth factor  $g(\text{RH})$ , defined as the aerosol particle diameter at a certain RH divided by the dry diameter, using the WetNeph, the DryNeph, the aerosol size distribution measurements and Mie theory. With this approach we found, on average,  $g(\text{RH} = 85\%)$  values to be  $1.61 \pm 0.12$  (mean  $\pm$  standard deviation). No clear seasonal shift of  $f(\text{RH}, \lambda)$  was observed during the 3-month period, while aerosol properties (size and chemical composition) clearly changed with time. While the beginning of the campaign was mainly characterized by smaller and less hygroscopic particles, the end was dominated by larger and more hygroscopic particles. This suggests that compensating effects of hygroscopicity and size determined the temporal stability of  $f(\text{RH}, \lambda)$ . During sea salt influenced periods, distinct deliquescence transitions were observed. At the end we present a method on how to transfer the dry in-situ measured aerosol scattering coefficients to ambient values for the aerosol measured during summer and fall at this location.

## 4.1 Introduction

Continuous measurements of aerosol properties in the field, such as the wavelength dependent aerosol light scattering coefficient, are often performed under dry conditions (relative humidity  $\text{RH} < 30\text{--}40\%$  as recommended by WMO/GAW, 2003). These measurements at low RH can differ from the ambient conditions and thus may not be climatically relevant. Since ambient aerosol particles experience hygroscopic growth, their optical properties are strongly dependent on RH. The response of an ambient particle to RH depends mainly on the size and the solubility of the particle. The water pressure above a water droplet containing dissolved material is lowered by the Raoult effect. The size and the fraction of soluble material in an aerosol particle will determine at which supersaturation it will be activated and will become a cloud droplet. The equilibrium size of a droplet was first described by Köhler (1936), who considered the Raoult (solute) and Kelvin (curvature) effect. Quantitative knowledge of this RH effect is of substantial importance when comparing ground based observations with other optical aerosol measurements (e.g. lidar), for the purpose of aerosol correction of satellite retrievals, or in general for climate models.

The growth of an aerosol particle due to water uptake is described by the hygroscopic diameter growth factor  $g(\text{RH})$  which is defined as the particle diameter  $D_{\text{wet}}$  at a certain RH divided by its dry diameter  $D_{\text{dry}}$ :

$$g(\text{RH}) = \frac{D_{\text{wet}}(\text{RH})}{D_{\text{dry}}}. \quad (4.1)$$

The RH dependence of  $g(\text{RH})$  can be parameterized in a good approximation by a one-parameter equation, proposed e.g. by Petters and Kreidenweis (2007):

$$g(a_w) = \left(1 + \kappa \frac{a_w}{1 - a_w}\right)^{\frac{1}{3}}. \quad (4.2)$$

Here,  $a_w$  is the water activity, which can be replaced by the relative humidity RH, if the Kelvin effect is omitted. This is justified in our case, because the Kelvin effect is small for large particles ( $D > 100$  nm), which are relevant to light scattering and absorption. The coefficient  $\kappa$  is a simple measure of the particle's hygroscopicity and captures all solute properties.

The impact of hygroscopic growth on the aerosol light scattering coefficient is usually described by the scattering enhancement factor  $f(\text{RH}, \lambda)$ :

$$f(\text{RH}, \lambda) = \frac{\sigma_{\text{sp}}(\text{RH}, \lambda)}{\sigma_{\text{sp}}(\text{RH}_{\text{dry}}, \lambda)}, \quad (4.3)$$

where the scattering coefficient  $\sigma_{\text{sp}}$  depends on the wavelength  $\lambda$  and the relative humidity RH. Since no clear wavelengths dependence of  $f(\text{RH}, \lambda)$  was found during this study,  $\lambda$  will be omitted for simplicity and the scattering enhancement factor will be written as  $f(\text{RH})$ .

Modeled and measured enhancement factors have been described in previous studies, including maritime (Wang et al., 2007; Carrico et al., 2003), urban (Yan et al., 2009; Fitzgerald et al., 1982), continental (Sheridan et al., 2001), biomass burning (Kotchenruther and Hobbs, 1998) and free tropospheric aerosol (Fierz-Schmidhauser et al., 2010a; Nessler et al., 2005a). This study presents the first experimental data set quantifying the RH effect on aerosol light scattering of an Arctic aerosol.

## 4.2 Experimental

A recently developed humidified nephelometer (WetNeph), an aethalometer, a scanning mobility particle sizer (SMPS) and an optical particle counter (OPC) were operated for three months (15 July–13 October 2008) at the Zeppelin station in Ny-Ålesund, Svalbard. The Zeppelin station (78° 54' N, 11° 53' E) is situated at 475 m a.s.l. on the Zeppelin mountain ridge about 2.3 km south of the settlement Ny-Ålesund, which is located at sea level. The station is part of the Global Atmosphere Watch (GAW) program. Low RH aerosol light scattering measurements have been performed since May 2001 at this station. Detailed information on the GAW measurement program at Ny-Ålesund and Zeppelin mountain can be obtained through the GAW station information system (GAW SIS, <http://gaw.empa.ch/gawsis>). Observations made at the Zeppelin station are in general less affected by local particle production occurring in the surf zone and are assumed to represent boundary layer conditions (Ström et al., 2003). Compared to the stations located at the airport and in the village, the altitude and the distance from the shoreline gives the advantage that the Zeppelin station is less susceptible to the surf and sea spray from breaking waves around the fjord area.

### 4.2.1 Humidified and dry nephelometer

The humidified nephelometer (WetNeph) is described in detail by Fierz-Schmidhauser et al. (2010). Briefly, the aerosol scattering coefficient  $\sigma_{\text{sp}}(\lambda)$  and the back scattering coefficient  $\sigma_{\text{bsp}}(\lambda)$  are measured at three distinct wavelengths ( $\lambda=450, 550, \text{ and } 700$  nm) at defined RH between 20% and 95%. For

this purpose a specifically designed humidification system (consisting of a humidifier and followed by a dryer) brings the initially dry aerosol to a defined RH before its scattering properties are measured by an integrating nephelometer (TSI Inc., Model 3563). The WetNeph was programmed to measure RH cycles. In the first part of the cycle, the dry particles experience elevated RH in the humidifier, after which they are passed through the turned off dryer before their scattering properties are measured in the nephelometer (hydration mode). It should be emphasized that the temperature in the nephelometer's detection cell is  $\sim 1^\circ\text{C}$  higher than in the humidifier, thereby causing a slight RH decrease of approximately 2–6% (see Fig. A1 in Fierz-Schmidhauser et al., 2010) and with that a concurrent shift of the observed deliquescence RH. Deliquescence is known as a sudden uptake of water of an initially dry and solid particle at the defined deliquescence relative humidity (DRH). The deliquescence occurs at the RH where the Gibbs free energy of the wet particle becomes lower than the one of the dry particle. The behavior of dehydrating particles following the upper hysteresis branch of the growth curve is measured by setting the humidifier to its maximum RH ( $\sim 95\%$ ), followed by RH reduction in the dryer and measurement in the nephelometer (dehydration mode). The lowest possible RH in this mode was  $\sim 65\%$ , limited by the capacity of the dryer at the high sample flow of  $16.6\text{ l min}^{-1}$  chosen for this campaign. Particle losses in the humidifier and dryer were characterized in a laboratory study for particle diameters 100–300 nm and found to be less than 5% (Fierz-Schmidhauser et al., 2010).

A second nephelometer (DryNeph, TSI Inc., Model 3563, operated by the Stockholm University – SU) measured the scattering coefficient as a reference in parallel always under dry conditions. The RH inside the DryNeph was always below 20%.

Both nephelometers measured within the scattering angles of  $7^\circ$  to  $170^\circ$ . The scattering coefficients for the complete angle between  $0^\circ$  and  $180^\circ$  were retrieved by correcting the measured values using the scheme proposed by Anderson and Ogren (1998) (truncation error correction).

#### 4.2.2 Measurement of the aerosol size distribution

The aerosol size distribution was measured with a scanning mobility particle sizer (SMPS), which consists of a bipolar particle charger ( $^{85}\text{Kr}$  source), a differential mobility analyzer (DMA) and a condensation particle counter (CPC, TSI Inc., Model 3772). Number size distributions in the diameter range between 14 and 820 nm were recorded with a time resolution of 6 min. A correction accounting for multiply charged particles was applied. However, the data at diameters  $>462$  nm was ignored, because higher moments of the size distribution (such as surface area distribution) are significantly influenced by multiply charged particles with diameters  $>820$  nm.

An optical particle counter (OPC, Model Grimm Dustmonitor 1.108) was used to measure the number size distribution of particles with an optical diameter between 0.3 and  $25\mu\text{m}$  (also at dry conditions). OPC data was recorded with a time resolution of 1 min.

The complete size distribution for diameters between 14 nm and  $25\mu\text{m}$  was obtained by combining the SMPS data at diameters below 462 nm with the OPC data at diameters above 462 nm. No remarkable difference between the two instruments was observed at the merging point, even though the SMPS measures a mobility diameter and the OPC an optical diameter.

The volume fraction of large particles  $V_{\text{OPC}}/V_{\text{tot}}$  is defined as the volume concentration measured by



the OPC ( $D_{\text{dry}} > 462$  nm, after the last SMPS bin) to total volume concentration measured by SMPS and OPC.

### 4.2.3 Measurement of the aerosol light absorption

To determine the absorption properties, an aethalometer (Magee Scientific, Model AE-31) was used. It measures the light attenuation by the aerosol particles (deposited on a filter) at 7 wavelengths ( $\lambda = 370, 470, 520, 590, 660, 880, \text{ and } 950$  nm). The 660-nm channel did not work properly and had to be excluded from the analysis. The light absorption coefficient  $\sigma_{\text{ap}}(\lambda)$  is then derived from the light attenuation (ATN):

$$\sigma_{\text{ap}}(\lambda) = \frac{A}{Q} \frac{\Delta \text{ATN}(\lambda)}{\Delta t} \frac{1}{C \cdot R(\text{ATN}(\lambda))}, \quad (4.4)$$

where  $A$  is the filter spot area,  $Q$  the volumetric flow, and  $\Delta \text{ATN}(\lambda)$  the change of light attenuation during the time interval  $\Delta t$  (Weingartner et al., 2003). The empirical constant  $C$  corrects for multiple scattering in the unloaded filter. Here, a value of  $C = 2.81$  was used, as determined for a remote background aerosol from aethalometer and multi-angle absorption photometer (MAAP) measurements at the high alpine research station Jungfraujoch (JFJ) (Collaud Coen et al., 2010). The wavelength and ATN dependent factor  $R$  corrects for effects caused by the amount of particles deposited on the filter, which decrease the optical path in the filter (also called the shadowing effect).  $R$  was set to be unity, since the contribution of absorption to total light extinction is small (Weingartner et al., 2003), similar to the measurements at the JFJ (Fierz-Schmidhauser et al., 2010a).

The 880-nm channel is used to estimate aerosol equivalent black carbon (BC) concentrations, with the manufacturer's calibration. Aethalometer raw data were recorded with a time resolution of 2 min. The data was later averaged to 1 h values. A comparison of the aethalometer  $\sigma_{\text{ap}}(\lambda = 565 \text{ nm})$  (calculated using Eq. 4.4) with  $\sigma_{\text{ap}}(\lambda = 565 \text{ nm})$  measured by a soot absorption photometer (PSAP) running in parallel showed a good agreement with  $\sim 10\%$  difference and a high correlation ( $R^2 = 0.86$ ). Note, that Eq. 4.11 was used to interpolate the aethalometer values to the PSAP wavelength of  $\lambda = 565$  nm.

### 4.2.4 Aerosol filter sampling and analysis

Aerosol filter samples for the analysis of water soluble calcium ( $\text{Ca}^{2+}$ ), chloride ( $\text{Cl}^-$ ), magnesium ( $\text{Mg}^{2+}$ ), potassium ( $\text{K}^+$ ), sodium ( $\text{Na}^+$ ), sulphate ( $\text{SO}_4^{2-}$ ), nitrate ( $\text{NO}_3^-$ ) and ammonium ( $\text{NH}_4^+$ ) were collected using a three-stage filter pack with a Teflon ( $2 \mu\text{m}$  Zefluor) particle front filter followed by a potassium hydroxide impregnated cellulose filter (Whatman 40) and finally an oxalic acid impregnated cellulose filter (Whatman 40) (EMEP, 1995). In general, the filter pack cannot be used to separate between gas and particle phase in the case of semi-volatile compounds. Thus, for constituents that are subject to volatilization and adsorption processes on the filter, e.g.  $\text{NO}_3^-/\text{HNO}_3$ ,  $\text{NH}_4^+/\text{NH}_3$ ,  $\text{Cl}^-/\text{HCl}$ , only the sum can be determined accurately.  $\text{Ca}^{2+}$ ,  $\text{K}^+$ ,  $\text{Mg}^{2+}$ ,  $\text{Na}^+$ ,  $\text{SO}_4^{2-}$ , however, can be determined from the Teflon filter alone. The filter pack was operated at flow rate of  $16 \text{ l min}^{-1}$  and the sampling time was 24 h (starting time 06:00 UTC).

Prior to ion chromatography analysis, the Zefluor Teflon filters were soaked in Milli-Q water (10 ml)

and subjected to ultrasonic agitation (30 min). The extracts were analyzed with respect to  $\text{Ca}^{2+}$ ,  $\text{K}^+$ ,  $\text{Mg}^{2+}$ ,  $\text{Na}^+$ , and  $\text{NH}_4^+$  on a Dionex 120DX ion chromatograph, using a Dionex cation exchange CS12A column (4 mm×250 mm), and a conductivity detector. The sample was eluted using sulphuric acid at a flow rate of  $1 \text{ ml min}^{-1}$ .  $\text{Cl}^-$ ,  $\text{NO}_3^-$ , and  $\text{SO}_4^{2-}$  were analyzed on a Dionex 120DX ion chromatograph, using a Dionex anion exchange AS9-SC column (4 mm×250 mm), and a conductivity detector. The sample was eluted using carbonate at a flow rate of  $2 \text{ ml min}^{-1}$ .

#### 4.2.5 Comparison of dry nephelometer measurements

A comparison of both nephelometers at low RH (<40%) showed that the DryNeph measured about 28% less than the WetNeph ( $y=1.28x+1.64\times 10^{-7} \text{ m}^{-1}$ ,  $R^2 = 0.98$  for  $\lambda=550 \text{ nm}$ , similar for the other wavelengths). A second comparison between the integrated size distribution measured by SMPS and OPC (same inlet as WetNeph) and a differential mobility particle sizer (DMPS) (same inlet as DryNeph) in the size range of 15 to 750 nm showed that the DMPS also measured 27% less in total number concentration than the SMPS+OPC ( $y=1.27x+2.21 \text{ cm}^{-3}$ ,  $R^2=0.99$ ). The reason for this could be losses in the SU inlet system, due to longer pathways and a lower volumetric flow of  $5 \text{ l min}^{-1}$ . Most of these losses were seen in the accumulation and partly in the coarse mode. These differences were almost constant in time throughout the entire measurement period. Since both DMPS and DryNeph had separate inlet lines but a joint precipitation shelter within the SU inlet system the differences might also be explained by different flow exposition to the SU inlet and/or differences in the inlet characteristics themselves (ill-defined virtual impaction behavior and sedimentation losses for larger particles/hydrometeors). The measured size distribution (SMPS and OPC) and the measured scattering coefficients (WetNeph, when measuring at low RH) were found to agree well within a performed closure study using Mie theory (see Sect. 4.5.5). The high correlation between the two nephelometers and the two size distribution measurements and the temporal stability of the differences suggest that all dry scattering coefficients had to be corrected for the entire period in order to make them comparable to the WetNeph data (e.g. at  $\lambda=550 \text{ nm}$  with  $y=1.28x+1.64\times 10^{-7} \text{ m}^{-1}$  as described above).

#### 4.2.6 Inlet systems

The WetNeph, aethalometer, OPC, and SMPS were all connected to one inlet which had no specific aerosol diameter size cut. The inlet consisted of a vertical pipe which sampled in about 2 m height on the roof of the station (pipe diameter approx. 5 cm, covered on top by a precipitation shelter). The instruments were located in the room directly below the inlet about 1–1.5 m away from the inlet entering the laboratory. The total flow was approx.  $25 \text{ l min}^{-1}$  (WetNeph:  $16.6 \text{ l min}^{-1}$ , SMPS:  $0.3 \text{ l min}^{-1}$ , OPC:  $1.2 \text{ l min}^{-1}$ , aethalometer:  $8 \text{ l min}^{-1}$ ).

The inlets to the routine aerosol instrumentations run by the Stockholm University (DryNeph, CPC, DMPS, and PSAP) do not have an aerosol size characteristic cut off. The inlets consist of a 10 cm diameter carrier shaft with 0.25 inch stainless steel tubing to support the different instruments. The dry nephelometer has its own 0.25 inch inlet with a flow of approx.  $6 \text{ l min}^{-1}$ . The PSAP, CPC, and DMPS share another 0.25 inch inlet with a total flow of approx.  $5.5 \text{ l min}^{-1}$ . The shaft and tubing are covered by a precipitation shelter approx. 25 cm high and are approx. 25 cm in diameter. The low flow

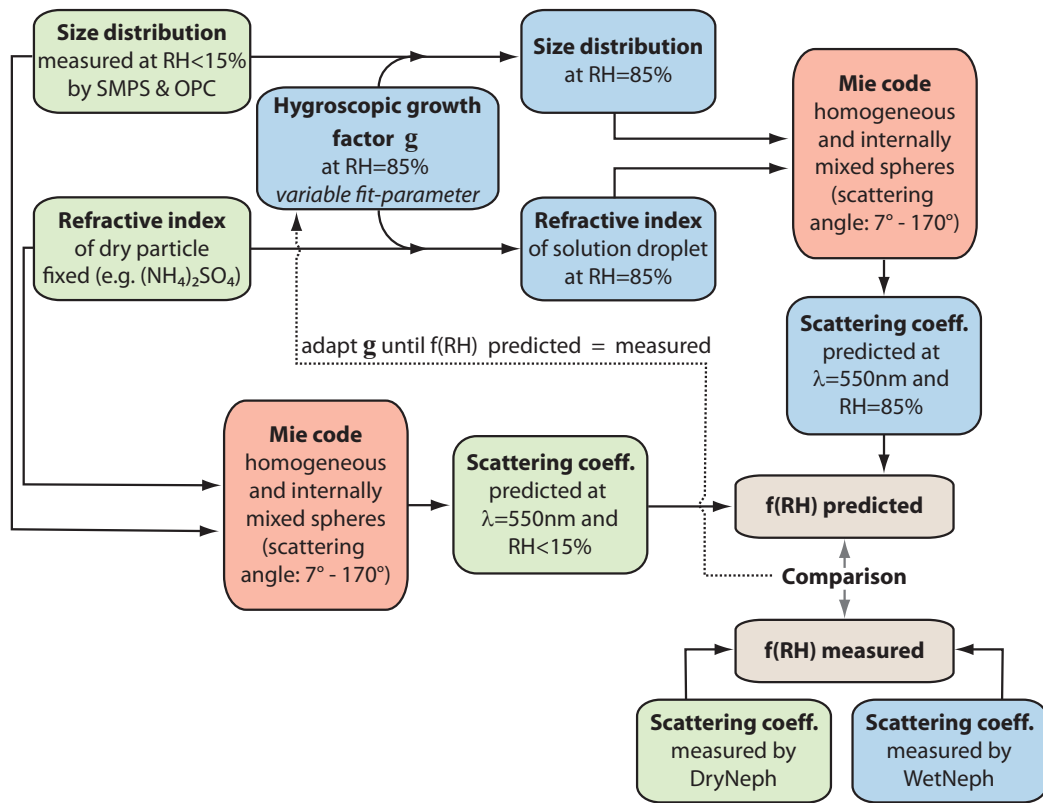


Figure 4.1: Scheme of the growth factor retrieval (backward calculation). See text for details.

rates of around  $5\text{--}10\text{ l min}^{-1}$  will, for the most time, prevent hydrometeors and large aerosol particles to enter the sampling system.

During transport to the instruments, the ambient air sample will equilibrate to room temperature, which is typically much higher than the outside temperature. This often makes the air dryer than 10% RH.

### 4.3 Model description

A computer model based on Mie theory has been developed for the calculation of  $f(\text{RH})$ . It calculates optical properties for polydisperse, internally mixed aerosol particles, which are assumed to be spherical and to have a homogeneous chemical composition. The Mie routine is based on the code of Bohren and Huffman (2004). The aerosol size distribution and the complex refractive index are needed as input parameters. Both input variables change with changing RH due to hygroscopic growth.

The change of the dry number size distribution can be calculated as follows: First, the wet particle diameter  $D_{\text{wet}}$  has to be determined by multiplying  $D_{\text{dry}}$  with  $g(\text{RH})$ :

$$D_{\text{wet}} = g(\text{RH})D_{\text{dry}}. \quad (4.5)$$

Normally,  $g(\text{RH})$  will be a function of  $D_{\text{dry}}$ . Here,  $g(\text{RH})$  is assumed to be independent of the diameter, therefore the wet number size distribution  $dN/d \log D_{\text{wet}}$  will shift to larger diameters.

The complex refractive index of grown particles at high RH is obtained by a volume weighting of the dry refractive index  $m_{\text{dry}}$  with the refractive index of water  $m_{\text{H}_2\text{O}}(\lambda=550 \text{ nm})=1.333$  (Hale and Querry, 1973):

$$m_{\text{wet}} = \frac{m_{\text{dry}} + m_{\text{H}_2\text{O}}(g^3 - 1)}{g^3}. \quad (4.6)$$

In this work, a fixed dry refractive index of  $(\text{NH}_4)_2\text{SO}_4$  (ammonium sulphate)  $m_{\text{dry}}(\lambda=550 \text{ nm})=1.53$  (interpolated from Toon et al., 1976) was used. Neglecting the imaginary part of the refractive index is only possible if no strong absorbing aerosol is found, which is the case for our study. It will be shown in Sect. 4.5 that this is a reasonable assumption.

### 4.3.1 Forward calculation

If the growth factor, the refractive index and the size distribution are known, the scattering properties can be calculated for the dry and the high RH case (using Eqs. 4.1–4.6 and Mie theory).  $f(\text{RH})$  is then determined by Eq. (4.3). These calculations were done for the entire scattering angle (0–180°). The resulting  $f(\text{RH})$  were then compared to the measurements, which were corrected for the nephelometer truncation error (see Sect. 4.2.1). The hygroscopic growth was retrieved via Mie theory (see Sect. 4.3.2) and for comparison assumed to be constant throughout the entire period (see Sect. 4.5.5).

### 4.3.2 Backward calculation – retrieval of the apparent hygroscopic growth factor

Independent measurements of the hygroscopic diameter growth factors (e.g. through measurements of  $g(\text{RH})$  by a hygroscopic tandem differential mobility analyzer) were not available for this study, which makes it impossible to directly calculate or predict the scattering enhancement  $f(\text{RH})$  (as done e.g. by Fierz-Schmidhauser et al., 2010a, for JFJ). However, measured wet and dry scattering coefficient data and the Mie model can be used to infer the hygroscopic growth of the detected aerosol, following the retrieval scheme depicted in Fig. 4.1. For this purpose  $g(\text{RH})$  was varied until the calculated  $f(\text{RH})$  for the measured size distribution matched the measured value within 2%. The dry refractive index was again assumed to be equal to the value of  $(\text{NH}_4)_2\text{SO}_4$ . The retrieval was performed at  $\text{RH}=85\%$  and for  $\lambda=550 \text{ nm}$ .  $g(\text{RH})$  can be transformed to  $\kappa$  using Eq. (4.2) to calculate  $g(\text{RH})$  at additional values of RH.

These calculations were performed in the specific scattering angles of the nephelometer (7–170°), to avoid the truncation error correction. By doing so, the calculated values can be directly compared to the direct measurements. The angular nephelometer illumination sensitivity (Anderson et al., 1996) was also accounted for in the Mie code. Although this retrieval is based on strong simplifications (spherical particles, internal homogeneous mixture, and a fixed dry refractive index for the entire period), it will give useful insights to the apparent physical growth of the measured aerosol.

## 4.4 Simulation of a passive sea salt tracer

A sea salt tracer was simulated for the Zeppelin station by combination of the Lagrangian particle dispersion model (LPDM) FLEXPART (Stohl et al., 2005) and sea salt aerosol sources parameterized

from model wind speeds. In a simplified approach the released sea salt aerosol was treated as a tracer with an e-folding lifetime of 24 h. This analysis gives additional insights concerning the aerosol origin and its composition and is used to support our hypotheses formulated in Sect. 4.5.

#### 4.4.1 Dispersion model

FLEXPART was set up in backwards mode and operated on 3-h global meteorological fields as retrieved from ECMWF analysis and forecasts with a horizontal resolution of  $1^\circ$  by  $1^\circ$  on 91 vertical levels. The output of residence times was stored with a horizontal resolution of  $0.5^\circ$  by  $0.5^\circ$  covering the area north of  $45^\circ$  N and for vertical level tops at 100, 500, 1000, and 3000 m above model ground. The model was initialized every 3 h for the period 15 June to 15 October 2008 and integrated backwards in time for 120 h. 50 000 particles were released in each run at the Zeppelin station at 475 m a.s.l.

#### 4.4.2 Emission calculation

Sea salt sources from open water were calculated following the parametrization given by Gong (2003) based on simulated 10-m wind speeds. Wind speeds were taken from ECMWF analysis and +3 h forecast fields and were available every 3 h with a  $1^\circ$  by  $1^\circ$  horizontal resolution. Sea salt in 3 different size ranges was considered:  $0.01\text{--}10\ \mu\text{m}$ ,  $0.1\text{--}10\ \mu\text{m}$ , and  $1\text{--}10\ \mu\text{m}$ . Emissions from ice covered areas were considered separately according to the parametrization by Yang et al. (2008) and references therein. The fraction of open sea water was obtained from daily sea ice analysis<sup>1</sup>.

The sea salt aerosol number concentrations at the receptor site were calculated by summation of the products of residence times and sea salt over all grid boxes and for each simulated time,  $t$ :

$$S_N(t) = \sum_l \sum_{i,j} \exp\left(\frac{-T_l}{\tau_{ss}}\right) \tau_{i,j,l} \frac{F_{N_{i,j}}}{V_{i,j}}, \quad (4.7)$$

where  $T_l$  is the time before arrival,  $\tau_{ss}$  the life-time of the sea salt tracer,  $\tau$  the residence times in units of s,  $F_N$  the sea salt source (from open water plus ice sheets) in units of  $\text{N}/(\text{m}^2 \text{ s})$  and  $V$  the grid box volume of the lowest FLEXPART output grid (100 m level top). The summation runs over all horizontal grid boxes  $i, j$  and along the integration time  $l$ .

## 4.5 Results

Figure 4.2 shows one day of the recorded data (20 August 2008). The hourly recorded webcam pictures from the Zeppelin station (with view towards the settlement of Ny-Ålesund and the Kongsfjorden) are helpful additional information about the current weather conditions (see Fig. 4.2a, webcam pictures are provided by NILU on their webserver<sup>2</sup>, last checked on 9 December 2009). The beginning of the measurement period was characterized by 24 h of sunlight per day (until mid September when the day-night cycle returned). The RH inside the WetNeph was periodically increased and decreased (see Fig. 4.2b) and the corresponding scattering coefficients measured (blue line in Fig. 4.2c).

<sup>1</sup>[http://cersat.ifremer.fr/data/discovery/by\\_parameter/sea\\_ice/psi\\_ssmi](http://cersat.ifremer.fr/data/discovery/by_parameter/sea_ice/psi_ssmi)

<sup>2</sup><ftp://ftpguest:guest@ftp.npolar.no/In/kim/zepold/ZepplinCam.jpg>

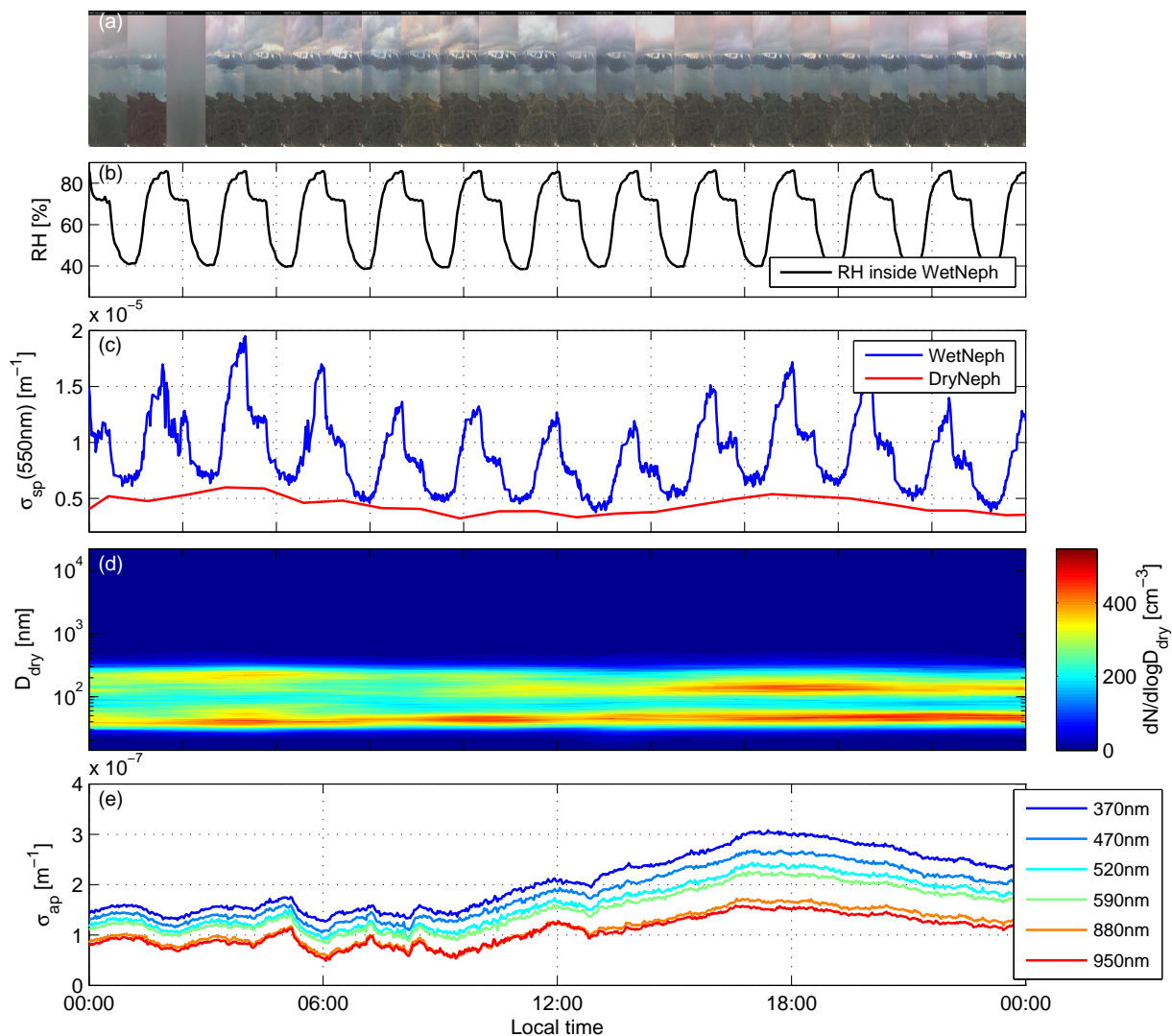


Figure 4.2: Example of the recorded data for 20 August 2008 (local time). **(a)**: Hourly webcam pictures from Zeppelin station. **(b)**: Relative humidity inside the WetNeph. **(c)**: Measured scattering coefficients  $\sigma_{sp}(\lambda=550\text{ nm})$  in the DryNeph (red line, hourly averages) and in the WetNeph (blue line, 2 min values). **(d)**: Number size distribution measured by SMPS and OPC. **(e)**: Absorption coefficient  $\sigma_{ap}$  determined by the aethalometer at different wavelengths (one hour moving mean applied). The 660-nm channel was not working properly and had to be excluded.

The DryNeph measured constantly at dry conditions (red line in Fig. 4.2c) in parallel to the WetNeph. The dry number size distribution was measured by the SMPS and OPC at the same inlet as the WetNeph (see Fig. 4.2d). On 20 August the number size distribution was characterized by two distinct modes at 40 nm and 110 nm. The aerosol absorption coefficients determined by the aethalometer (using Eq. 4.4) are seen in Fig. 4.2e, showing that the absorption coefficients were about two orders of magnitude lower than the scattering coefficients.

An overview of the entire measurement period can be found in Fig. 4.3. The aerosol particle number concentration (blue curve in Fig. 4.3e) shows a temporal decrease towards October, while the total surface area concentration shows no clear increase or decrease (orange curve in Fig. 4.3e). A maximum in

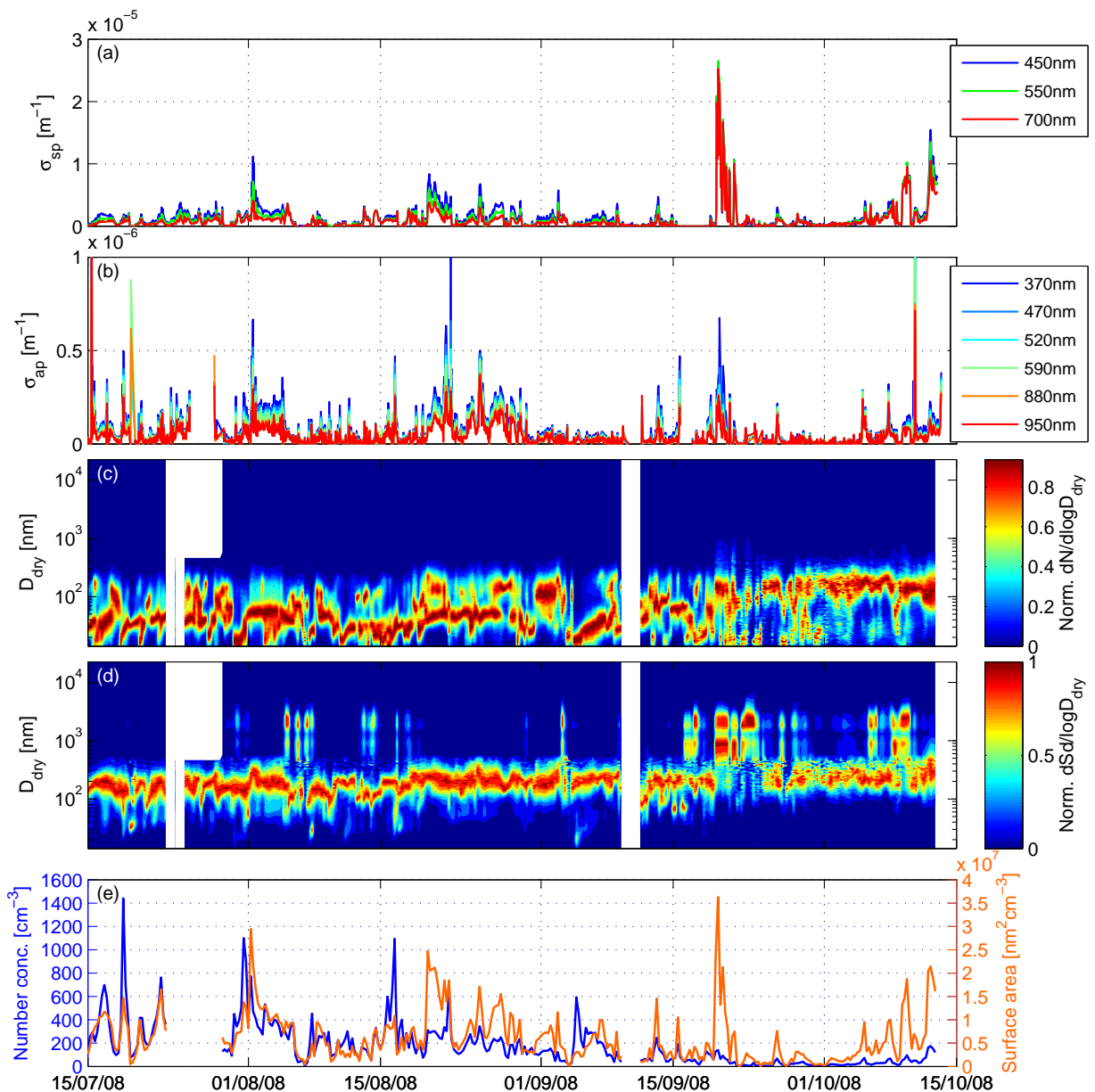


Figure 4.3: Overview of recorded data of the entire campaign. **(a)**: Dry scattering coefficients at 450, 550, and 700 nm (DryNeph, hourly averages). **(b)**: Absorption coefficients at different wavelengths (aethalometer, hourly averages, without 660 nm). **(c)**: Normalized number size distribution (SMPS and OPC, 6 h averages). **(d)**: Normalized surface size distribution measured (SMPS and OPC, 6 h averages). **(e)**: Total number concentration (blue line) and total surface area (orange line) measured by SMPS and OPC (6-h averages).

the aerosol number concentration in the summer has been previously observed by Ström et al. (2003) at the Zeppelin station and also at other Arctic sites, e.g. at Barrow, Alaska by Bodhaine (1989) and Quinn et al. (2002) who mention that the maximum particle concentration in summer in the Arctic could relate to the formation of biogenic sulfur particles. The temporal evolution of the scattering coefficient shows no clear trend, but certain events with elevated values are observed (Fig. 4.3a). These events are probably caused by sea salt particles (larger particles with higher scattering efficiency and

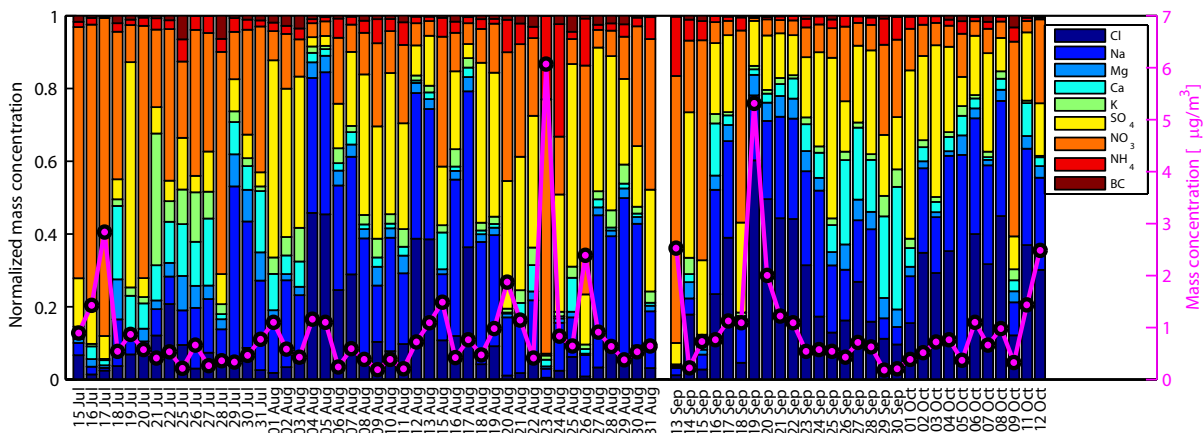


Figure 4.4: Normalized filter measurements of aerosol components (colored bars) and the total mass (magenta line). Shown are only days, where all aerosol components were analyzed completely (exception: 26 and 27 July, where no BC measurements were available, but are assumed to be as low as on the other days). The measurements were performed without a specific size cut (open face sampler).

larger surface area), which is also reflected in a more dominant coarse mode in the surface size distribution during these periods (Fig. 4.3d). Bodhaine (1989) and Quinn et al. (2002) also found for Barrow, Alaska, a minimum in the scattering coefficient in summer and an increase towards fall and winter, attributing this increase to an enhanced sea salt influence. The single scattering albedo  $\omega_0$  is also very high during these sea salt events ( $\omega_0 > 0.98$ ), meaning that the particles are almost pure scatterers (see Sect. 4.5.4). Quinn et al. (2002) found similarly high values of  $\omega_0$  during summer for Barrow, Alaska.

The BC concentrations measured by the aethalometer were on average  $7.2 \text{ ng m}^{-3}$  (90th percentile:  $31 \text{ ng m}^{-3}$ ), which is similar to the findings of Eleftheriadis et al. (2009) who determined a mean value of  $\sim 7 \text{ ng m}^{-3}$  for June to September from 1998 to 2007. The aerosol filter analyses were only available for part of the three month period (see Fig. 4.4). Major sea salt constituents such as  $\text{Na}^+$  and  $\text{Cl}^-$  were always present though they were more dominant during the last third of the campaign and during short periods in between, when the relative mass fraction of non-sea salt  $\text{NO}_3^-$  and  $\text{NH}_4^+$  concurrently decreased. The observations at Zeppelin indicated no clear long range transport of pollution to the measurement site, as can also be confirmed by transport simulations. The FLEXPART backward simulations showed that the air masses reaching the Zeppelin station mainly originated from the Arctic region surrounding Svalbard and the North Atlantic Ocean (see Fig. 4.5). Hence, the measurement period was characterized by maritime and rather clean air masses.

The scattering enhancement factor  $f(\text{RH})$  was calculated using Eq. (4.3). Since no pronounced wavelength dependency of  $f(\text{RH})$  was found, we will focus on the 550 nm wavelength only.

Humidograms of  $f(\text{RH})$ , defined as a plot of  $f(\text{RH})$  vs. RH, were determined as daily median values of  $f(\text{RH})$  (with a 2% RH bin size and synchronized to the aerosol filter sampling intervals). As mentioned above, measurements at  $\text{RH} < 65\%$  are always part of the hydration branch. It was therefore technically not possible to detect any efflorescence at  $\text{RH} < 65\%$ . Measurements above  $\sim 65\%$  RH were done in both the hydration and dehydration mode (see Sect. 4.2.1). Unfortunately, no clear efflorescence was observed at  $\text{RH} > 65\%$ .



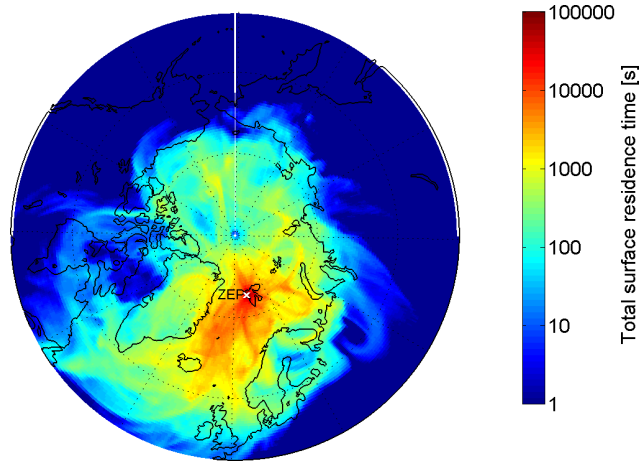


Figure 4.5: Total surface residence time for the Zeppelin station (ZEP, see cross) for the period 15 July to 15 October 2008.

An example humidogram characterized by a smoothly increasing  $f(\text{RH})$  and without a distinct deliquescence transition is seen in Fig. 4.6a (daily average), indicating that the particles were always liquid. A second example humidogram with a distinct increase of  $f(\text{RH})$  at  $\text{RH} \sim 70\%$  is shown in Fig. 4.6b. This increase, known as deliquescence, can be explained by a sudden water uptake of the solid aerosol particle becoming (at least partly) liquid. It has to be repeated that the actual DRH of the aerosol is a few percent higher than what the WetNeph measures due to temperature differences between humidifier and nephelometer (see Sect. 4.2.1).

The temporal evolution of the ambient  $f(\text{RH})$  at  $\text{RH} = 85\%$  is shown in Fig. 4.7d (black points, daily median values between  $84\% < \text{RH} < 86\%$ ). The values measured at  $\text{RH} = 85\%$  are in the range of  $f(\text{RH}) \sim 2\text{--}6$ , which means two- to sixfold increase of the ambient scattering coefficient compared to dry conditions. Campaign average and percentile values of  $f(\text{RH} = 85\%)$  are given in Table 4.1. This can be compared e.g. to values for biomass burning aerosols, where Kotchenruther and Hobbs (1998) measured lower values of  $f(\text{RH} = 80\%, \lambda = 550 \text{ nm}) = 1.01\text{--}1.5$  or to free tropospheric aerosol measured at Jungfraujoch (including Saharan dust events) with values of  $f(\text{RH} = 85\%, \lambda = 550 \text{ nm}) = 1.2\text{--}3.3$  (Fierz-Schmidhauser et al., 2010a). Similarly high values were measured for maritime air by Carrico et al. (2003) with  $f(\text{RH} = 82\%, \lambda = 550 \text{ nm}) = 2.45$ , although at slightly lower RH. Our mean values can be transformed to the RH values used in the previous mentioned studies (using Eq. 4.3):  $f(\text{RH} = 82\%) = 2.89$  and  $f(\text{RH} = 80\%) = 2.71$ .

#### 4.5.1 Parametrization of $f(\text{RH})$

The humidograms of  $f(\text{RH})$  measured at Zeppelin station can be well described using an empirical  $\gamma$ -model, which has also been used in previous studies e.g. by Gasso et al. (2000) and Kotchenruther and Hobbs (1998) and goes back to the work of Kasten (1969):

$$f(\text{RH}) = (1 - \text{RH})^{-\gamma} \quad (4.8)$$

where  $\gamma$  parameterizes the magnitude of the scattering enhancement. Although more advanced multi-parameter equations have been proposed in the literature e.g. by Carrico et al. (2003), it turns out that

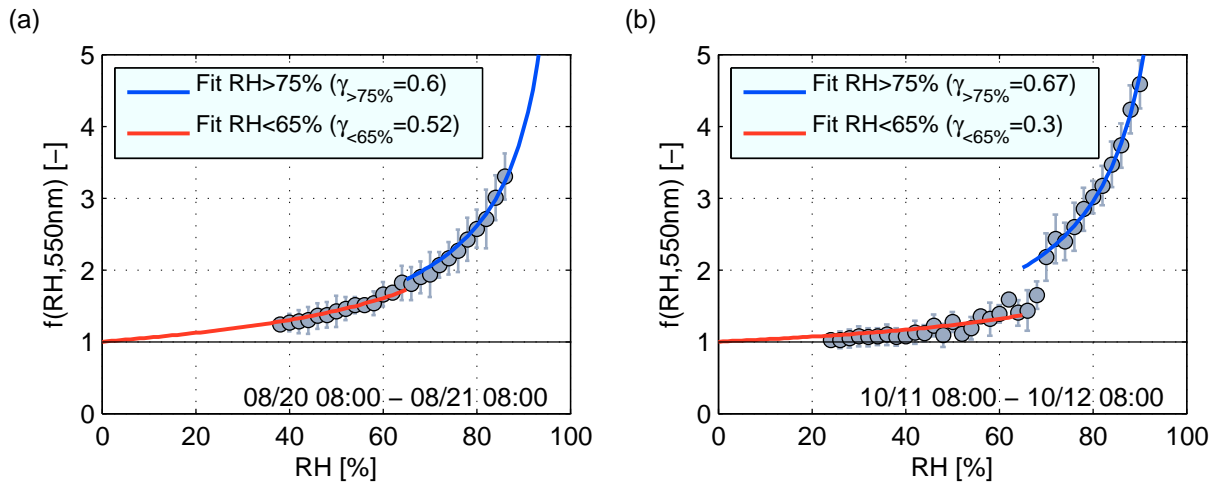


Figure 4.6: Measured humidograms of  $f(\text{RH}, \lambda=550 \text{ nm})$ , given as daily median values, where the error bars denote the standard deviation. **(a)**: Example from 20 August 2008. **(b)**: Example from 11 October 2008. Solid lines are  $\gamma$ -fits for the values with  $\text{RH} > 75\%$  (blue line) and for  $\text{RH} < 65\%$  (red line). The time periods correspond to the filter sampling time (local time).

Table 4.1: Campaign mean, standard deviation (STD), and percentile values of the scattering enhancement factor  $f(\text{RH}=85\%)$ , its fit parameter  $\gamma_{>75\%}$  (both at  $\lambda=550 \text{ nm}$ ), the apparent hygroscopic growth factor  $g(\text{RH}=85\%)$ , and its  $\kappa$  value (both derived via Mie theory as described in Sect. 4.3.2).

	mean	STD	median	10th perc.	90th perc.
$f(\text{RH}=85\%)$	3.24	0.63	3.12	2.54	3.93
$\gamma_{>75\%}$	0.58	0.09	0.57	0.47	0.69
$g(\text{RH}=85\%)$ (Mie)	1.61	0.12	1.60	1.47	1.77
$\kappa$ (Mie)	0.57	0.17	0.55	0.39	0.80

Eq. (4.8) is sufficient to parameterize the behavior of  $f(\text{RH})$  observed in this study.  $f(\text{RH})$  measured at high RH ( $>75\%$ ) and low RH ( $<65\%$ ) were fitted separately to get a criterion for the presence or absence of a deliquescence transition. The time series of the high RH fit parameter  $\gamma_{>75\%}$  is seen in Fig. 4.7a. The error bars denote the 95% confidence level of the fitted parameter and are in general very small, showing that the  $\gamma$ -model works well for the aerosol type measured at the Zeppelin station. Larger error bars are mostly the result of extremely low concentrations, where the noise of the measured scattering coefficients caused a high uncertainty in  $f(\text{RH})$ . It can also be caused by air mass changes during the averaging period of one day. The advantage of using the fit-parameter  $\gamma_{>75\%}$  instead of  $f(\text{RH}=85\%)$  is that measurements taken at different RH can be directly compared, and that  $\gamma_{>75\%}$  describes the humidity dependence of  $f(\text{RH})$  for the entire range  $\text{RH} > 75\%$ . Campaign average and percentile values of  $\gamma_{>75\%}$  can be found in Table 4.1.

### 4.5.2 Deliquescence caused by sea salt

The fit parameters  $\gamma_{>75\%}$  and  $\gamma_{<65\%}$  can be used to check for possible deliquescence transitions. We can define a hysteresis index  $\eta$ :

$$\eta = 1 - \frac{\gamma_{<65\%}}{\gamma_{>75\%}}, \quad (4.9)$$

which describes the magnitude of a deliquescence transition at  $65\% < \text{RH} < 75\%$  within the range of  $\eta=0$  (no deliquescence) and  $\eta=1$  (very distinct deliquescence, i.e. completely undissolved at  $\text{RH} < 75\%$ ). The time series of  $\eta$  is shown in Fig. 4.7b. It can be seen that deliquescence is more often observed during the last third of the campaign (15 September to 15 October 2008). The color code of the circles in Fig. 4.7b denotes the aerosol volume fraction  $V_{\text{OPC}}/V_{\text{tot}}$ , which hereafter will be called volume fraction of large particles. The volume fraction of large particles is most likely dominated by sea salt particles because the observed  $f(\text{RH})$  would be much smaller if it was mineral dust (e.g.  $f(\text{RH}=82\%)=1.69$  measured by Carrico et al., 2003). A high volume fraction of large particles (reddish color in Fig. 4.7b) thus indicates high sea salt influence. High values of  $\eta$  occurred whenever the volume fraction of large particles was high, indicating that the appearance of a distinct deliquescence is linked to the presence of sea salt. The few values of  $\eta < 0$  are not physically reasonable and are caused by possible air mass changes within the averaging time of one day or noisy data at times with extremely low concentrations (especially at the beginning of September). Figure 4.8b shows the scatter plot of  $\eta$  versus the volume fraction of large particles, where the color code denotes the  $\text{Na}^+$ -mass fraction determined from the filter analysis. A positive correlation can be seen between the possibility of a deliquescent transition and the sea salt content. It should be mentioned that organic species in the aerosol chemical composition will most probably lower the magnitude of the deliquescence (Ming and Russell, 2001) as organics will also decrease the hygroscopic growth in general (see Sect. 4.5.3).

The sea salt number concentration derived from the FLEXPART analysis (see Sect. 4.4) also indicates that sea salt is more abundant during the last third of the campaign. The times for which elevated sea salt number concentrations are predicted (see red line in Fig. 4.7c), correspond partly to the times when deliquescence is clearly observed (high  $\eta$  values in Fig. 4.7b). The simplified sea salt tracer analysis only provides qualitative information, while the modeled number concentrations did not match to the SMPS and OPC measurements quantitatively.

### 4.5.3 Compensating effects of size and hygroscopicity

Neither the observed  $f(\text{RH})$  nor the  $\gamma_{>75\%}$  showed a clear seasonal trend (see Fig. 4.7a, d), nor were they positively correlated with the occurrence of sea salt (see Fig. 4.8a), as inferred from the volume fraction of large particles ( $V_{\text{OPC}}/V_{\text{tot}}$ ).

Two hypotheses can be put up for the explanation of these findings:

1. The aerosol properties are constant in time.
2. Compensating effects of different varying aerosol properties cause an almost constant  $f(\text{RH})$ .

The first hypothesis can be excluded given the observed variations of the size distribution, the chemical composition and the influence of sea salt. The temporal evolution of the volume fraction of large

particles ( $V_{\text{OPC}}/V_{\text{tot}}$ ) and the  $\text{Na}^+$ -mass fraction is shown in Fig. 4.7c. The fraction is increasing towards the end of the sampling period, pointing towards a higher sea salt influence. The clear change in the aerosol number and surface area size distribution was already seen in Fig. 4.3. As mentioned above, the aerosol filter analysis showed a clear change in aerosol chemical composition (see Fig. 4.4). The FLEXPART sea salt tracer analysis also showed a possible change in chemical composition, with a higher sea salt probability especially during the second half of September (red line in Fig. 4.7c). This confirms that the aerosol properties did change with time.

How would the optical properties of an aerosol with a constant chemical composition react to a change only in size? This is illustrated by assuming a certain constant hygroscopic growth and refractive index and performing Mie calculations to calculate  $f(\text{RH})$  exemplarily at  $\text{RH}=85\%$  (as described in Sect. 4.3.2) using the measured size distributions as input. The result for assuming a strongly hygroscopic salt (sodium chloride,  $\text{NaCl}$ ), an intermediately hygroscopic salt ( $(\text{NH}_4)_2\text{SO}_4$ ) and for weakly hygroscopic organics is shown in Fig. 4.7d. For  $\text{NaCl}$  and  $(\text{NH}_4)_2\text{SO}_4$  the growth factors were taken from Topping et al. (2005) and the refractive indices from Toon et al. (1976). For the organics, a value of  $g=1.2$  (at  $\text{RH}\approx a_w=85\%$ ) was taken from Sjogren et al. (2008), which is representative of aged organic aerosol in the free troposphere and a corresponding refractive index was taken from Nessler et al. (2005a).  $f(\text{RH})$  of pure  $\text{NaCl}$  would be in general much higher (mean 7.4 at  $\text{RH}=85\%$ , blue points in Fig. 4.7d) than measured. The blue points, assuming pure  $\text{NaCl}$ , clearly illustrate that the increase in particle size during the period after 15 September would lead to distinctly lower  $f(\text{RH})$  if the chemical composition was constant. Assuming pure organics results in much lower  $f(\text{RH})$  (mean 1.6 at  $\text{RH}=85\%$ , green points in Fig. 4.7d). The size effect is also seen though less pronounced.  $f(\text{RH})$  calculated for pure  $(\text{NH}_4)_2\text{SO}_4$  (mean 3.1 at  $\text{RH}=85\%$ , red points in Fig. 4.7d) are in the range of our measurements. The size effect during the period with high volume fraction of large particles is also seen for pure  $(\text{NH}_4)_2\text{SO}_4$ , while the measured  $f(\text{RH})$  decreased only very little (see also Fig. 4.8a).

The compensating effects of changes in size and hygroscopicity (chemical composition) on  $f(\text{RH})$  can be illustrated by performing Mie calculations with a model aerosol consisting of various fractions of a highly hygroscopic inorganic salt ( $\text{NaCl}$ ) and weakly hygroscopic organics. The corresponding growth factors and refractive indices (references see above) were obtained through volume weighting (also known as Zdanovskii-Stokes-Robinson approach). A single log-normal size distribution with varying mode diameter  $D_{\text{mod}}$  and a fixed geometric mean deviation width of 1.8 was chosen as input. Figure 4.9 shows a clear decrease of  $f(\text{RH}=85\%)$  with increasing size when assuming the chemical composition to be constant. It also decreases with increasing organic contribution. This is reasonable, since organic species reduce the hygroscopic growth of sea salt particles significantly (Ming and Russell, 2001). The measured values of  $f(\text{RH}=85\%)$  versus the number mean diameter  $D_{\text{mean}}$  are included in Fig. 4.9. They do not follow the isolines of constant chemical composition but show a rather constant  $f(\text{RH}=85\%)$  with a clear change in particle diameter. Compared to the model calculations they show an increased inorganic contribution (more  $\text{NaCl}$ ) with increasing size, which results in a higher hygroscopic growth. Note that  $D_{\text{mean}}$  (obtained from the measured size distribution by  $D_{\text{mean}}=N^{-1}\int_0^\infty(D_{\text{dry}}dN/d\log D_{\text{dry}})d\log D_{\text{dry}}$ ) is not directly comparable to  $D_{\text{mod}}$  of the log-normal size distribution, but gives the right range for the measured values.

The fact that the measured  $f(\text{RH}=85\%)$  showed no significant change during sea salt periods, with a concurrent increase of mean particle size, implies that also particle hygroscopicity increased during

these periods. Lacking a direct measurement of particle hygroscopicity, the magnitude of hygroscopic growth factors and their trends were estimated using the WetNeph, the DryNeph, and the size distribution measurements (see Sect. 4.3.2 and the retrieval scheme in Fig. 4.1). The index of refraction was assumed to be that of  $(\text{NH}_4)_2\text{SO}_4$  for the entire period, which is a reasonable guess as can be seen in Fig. 4.11 where the dry calculated versus measured values of  $\sigma_{\text{sp}}(\lambda=550 \text{ nm})$  are shown. As mentioned above, neglecting the imaginary part is only possible because no strong absorbing aerosol was found during our period. The slope  $s$  between calculated and measured scattering coefficient (see regression line in Fig. 4.11) would decrease accordingly if an imaginary part was included in the refractive index (e.g. with  $m=1.53+0.001i \rightarrow s=0.91$ , with  $m=1.53+0.01i \rightarrow s=0.82$  or with  $m=1.53+0.1i \rightarrow s=0.56$ ). The growth factor  $g(\text{RH})$  was calculated in 2-h intervals and then averaged to daily values. Figure 4.7e reveals a higher retrieved  $g(\text{RH})$  during sea salt periods especially in the last third of the campaign. This is reasonable because sea salt is amongst the most hygroscopic atmospheric aerosol (Swietlicki et al., 2008). The rest of the measurement period could be dominated by secondary inorganic or organic aerosol, especially during the first half of the campaign, where 24 h of sunlight probably promoted secondary aerosol production. The scatter plot of  $\kappa$  (calculated from  $g(\text{RH})$  at  $\text{RH}=85\%$  using Eq. 4.2) versus  $V_{\text{OPC}}/V_{\text{tot}}$  shows again that the sea salt contribution has an influence on the magnitude of the hygroscopicity (see Fig. 4.8c). Campaign average and percentile values of  $g(\text{RH})$  (and its  $\kappa$  value) are given in Table 4.1.

These findings confirm the hypothesis that compensating effects of hygroscopicity and size determined the temporal stability of  $f(\text{RH}=85\%)$  at Zeppelin station during our campaign. While the beginning of the campaign (July and August) mainly was dominated by smaller and less hygroscopic particles, the end (September and October) was dominated by larger and more hygroscopic particles.

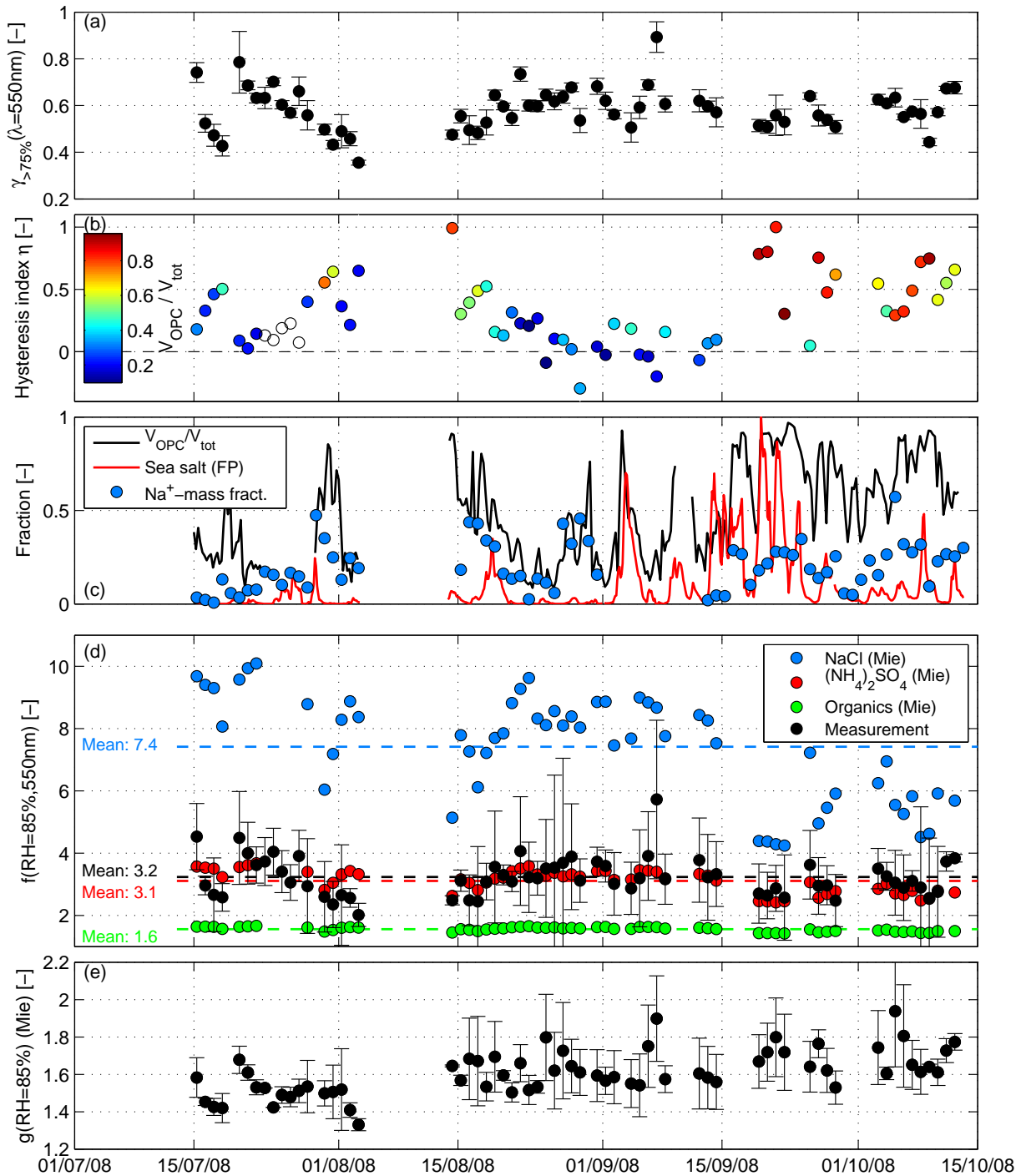


Figure 4.7: **(a)**: Time series of fit-parameter  $\gamma_{>75\%}$ , error bars indicate the 95% confidence level. **(b)**: Hysteresis index  $\eta$ , color code indicates the volume fraction of large particles ( $V_{\text{OPC}}/V_{\text{tot}}$ ). **(c)**: Measured volume fraction of large particles  $V_{\text{OPC}}/V_{\text{tot}}$  (black line), normalized sea salt number concentration for the 1–10 $\mu\text{m}$  particle diameter size range as derived from FLEXPART analysis (red line) and measured  $\text{Na}^+$ -mass fraction (blue points). **(d)**: Calculated  $f(\text{RH}=85\%, \lambda=550\text{nm})$  using the measured size distribution and assuming a constant chemistry (constant hygroscopic growth and complex refractive index) and measurement of  $f(\text{RH}=85\%, \lambda=550\text{nm})$  (black circles, error bars are standard deviation of daily median values). **(e)**: Retrieved growth factor ( $g(\text{RH} = 85\%)$ ). See retrieval scheme in Fig. 4.1. Data is only shown for periods with available WetNeph measurements.

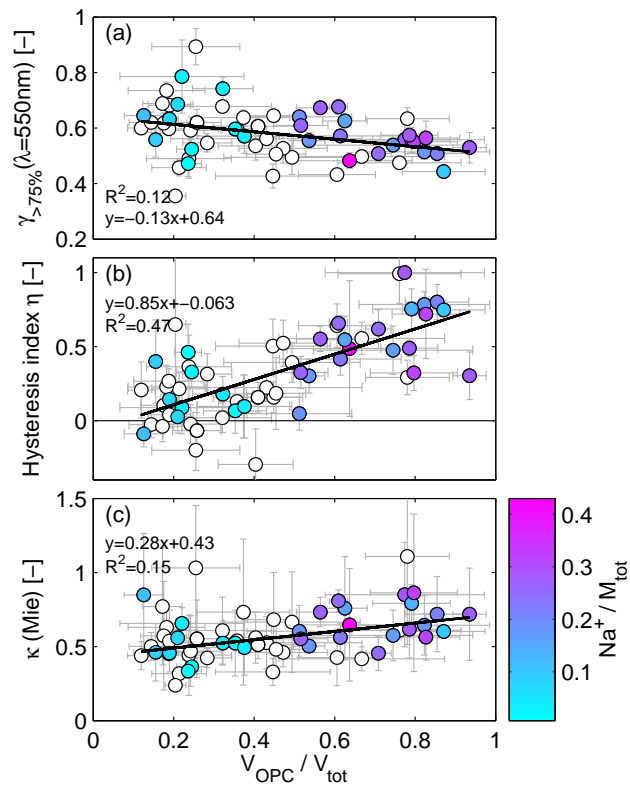


Figure 4.8: **(a)**: Fit-parameter  $\gamma_{>75\%}$  of  $f(\text{RH})$  versus the volume fraction of large particles ( $V_{\text{OPC}}/V_{\text{tot}}$ ). **(b)**: Hysteresis index  $\eta$  versus  $V_{\text{OPC}}/V_{\text{tot}}$ . **(c)**: Retrieved  $\kappa$  (retrieved at  $\text{RH} = 85\%$ ) versus  $V_{\text{OPC}}/V_{\text{tot}}$ . Color code in all panels indicates the  $\text{Na}^+$ -mass fraction determined from filter measurements (only for days where the mole fraction  $0.3 < \text{Na}^+ / \text{Cl}^- < 3$ ). Black lines represent a weighted least-square regression.

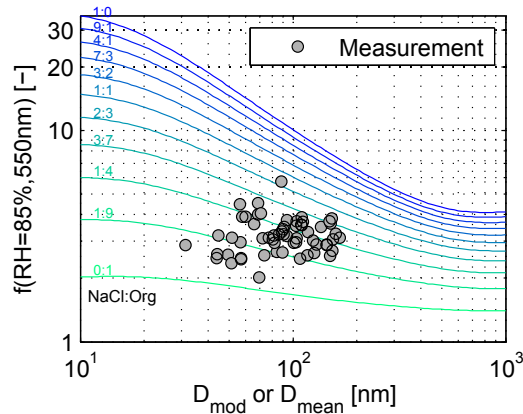


Figure 4.9: Scattering enhancement  $f(\text{RH} = 85\%, \lambda = 550 \text{ nm})$  modeled for various NaCl to organic species volume ratios (colored lines) versus the mode diameter  $D_{\text{mod}}$  of a log-normal size distribution (with a fixed geometric standard deviation of 1.8). The grey points depict the measured values of  $f(\text{RH} = 85\%, \lambda = 550 \text{ nm})$  versus the number mean diameter  $D_{\text{mean}}$  measured by SMPS and OPC (daily averages).

#### 4.5.4 Impact of $f(\text{RH})$ on climate relevant parameters

To demonstrate the impact of  $f(\text{RH})$  on properties which are important to estimate the radiative forcing of aerosol particles, the single scattering albedo  $\omega_0$  was determined from the dry in-situ measurements as well as for the actual ambient RH.  $\omega_0$  gives the fraction of the radiation attenuated by aerosol particles due to scattering. It is defined as the ratio of the aerosol scattering coefficient  $\sigma_{\text{sp}}$  to the total aerosol extinction coefficient, which is the sum of  $\sigma_{\text{sp}}$  and the absorption coefficient  $\sigma_{\text{ap}}$ :

$$\omega_0^{\text{dry}} = \frac{\sigma_{\text{sp}}}{\sigma_{\text{sp}} + \sigma_{\text{ap}}}. \quad (4.10)$$

All variables are dependent on the wavelength  $\lambda$ , which is omitted in Eq. (4.10) for simplicity reasons.  $\omega_0$  is here determined by the (dry) in-situ measurements of  $\sigma_{\text{sp}}$  (DryNeph) and  $\sigma_{\text{ap}}$  (aethalometer, using Eq. 4.4). Since the aethalometer measures at different wavelengths than the nephelometer, the absorption coefficients were recalculated to the wavelengths of the nephelometer using the Ångström law:

$$\sigma_{\text{ap}}(\lambda) = \beta \lambda^{-\alpha}, \quad (4.11)$$

where  $\lambda$  is the wavelength of the aethalometer,  $\beta$  a concentration dependent constant and  $\alpha$  the Ångström exponent. Equation 4.11 was fitted to the averaged spectra of the aethalometer measurement (using all available channels) to retrieve  $\beta$  and  $\alpha$ , which then allowed to calculate the absorption coefficient at the individual nephelometer wavelength.

To retrieve the real ambient value of  $\omega_0$  – from now on called  $\omega_0^{\text{amb}}$  – the daily average of the RH measured outside of the Zeppelin station is used (see Fig. 4.10a, error bars denote the standard deviation). Using the ambient RH, the daily value of  $\gamma_{>75\%}$  (see Fig. 4.7a) and Eq. (4.8) is used to calculate the ambient  $f(\text{RH})$  (see Fig. 4.10b, for  $\lambda=550$  nm). The outliers in Fig. 4.10b with  $f(\text{RH})$  values above 20–30 are on the one hand the result of the large uncertainties in  $\gamma_{>75\%}$  on days which were characterized by extremely low concentrations. On the other hand, values at high RH > 95% have to be treated with care, because small uncertainties in the ambient RH measurement have a strong impact on the determined  $f(\text{RH})$  (e.g.  $f(\text{RH}) \rightarrow \infty$  for  $\text{RH} \rightarrow 100\%$  in Eq. 4.8).

The ambient single scattering albedo  $\omega_0^{\text{amb}}$  is then calculated as followed:

$$\omega_0^{\text{amb}} = \frac{f(\text{RH})\sigma_{\text{sp}}}{f(\text{RH})\sigma_{\text{sp}} + \sigma_{\text{ap}}}. \quad (4.12)$$

The absorption coefficient  $\sigma_{\text{ap}}$  is assumed not to change in a significant way with increasing RH, which is a reasonable assumption for the Arctic aerosol. Nessler et al. (2005b) e.g. showed in a model study the insignificance of the absorption enhancement for an aerosol with high values of  $\omega_0$  (here for the free tropospheric aerosol found at the JFJ).

The dry and ambient values of  $\omega_0$  are seen in Fig. 4.10c (the error bars were calculated by Gaussian error propagation using the standard deviation of RH, assuming a 10% uncertainty of the nephelometer (Anderson et al., 1996), a 20% uncertainty of the aethalometer (M. Collaud, MeteoSwiss, Payerne, personal communication, 2010) and the error of the  $\gamma_{>75\%}$  coefficient, which is the difference of the 95% confidence level). The dry in-situ measured values of  $\omega_0^{\text{dry}}$  are already close to one (mean  $\omega_0^{\text{dry}}=0.95$ , 90th percentile  $\omega_0^{\text{dry}}=0.99$ ), which means that most of the light extinction by aerosol particles is caused



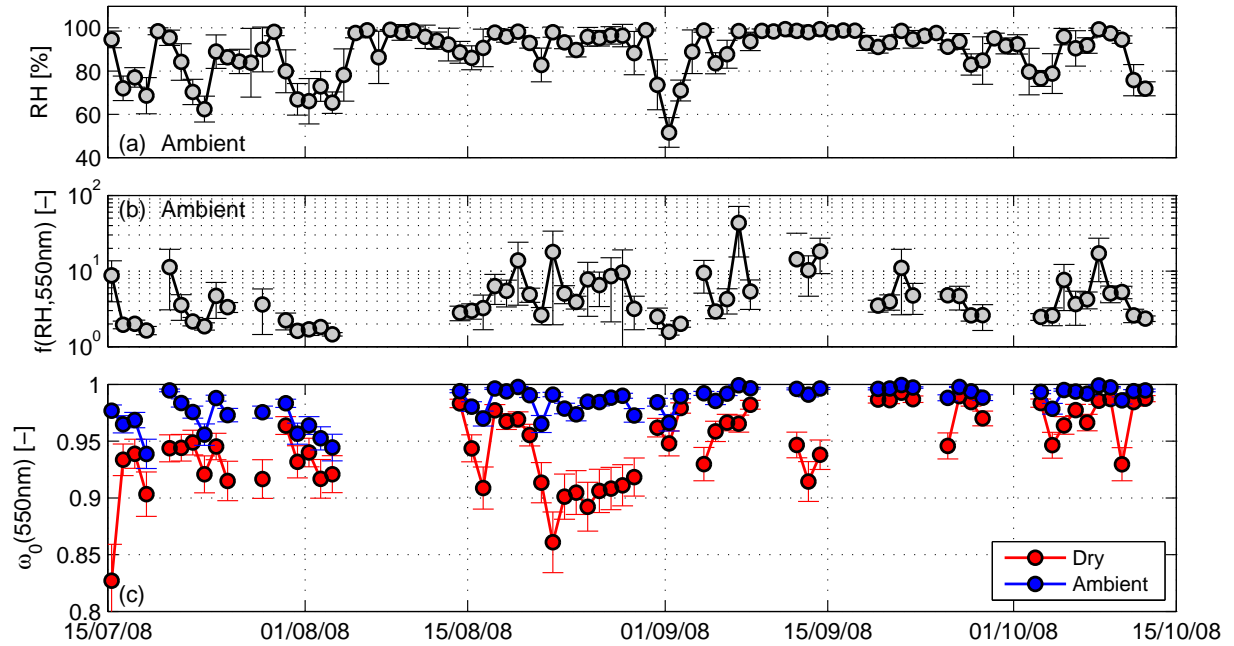


Figure 4.10: Single scattering albedo of the measured dry aerosol and recalculated to ambient conditions. **(a)**: Relative humidity (RH) outside Zeppelin station (error bars denote standard deviation of daily average). **(b)**: Scattering enhancement factor  $f(\text{RH}, \lambda=550 \text{ nm})$  at ambient RH. **(c)**: Single scattering albedo  $\omega_0(\lambda=550 \text{ nm})$  measured at dry conditions (red points) and recalculated to ambient RH (blue points, daily averages, error bars are determined by error propagation).

by scattering. In the high humidity ambient environment, the  $\omega_0^{\text{amb}}$  increases to values even closer to one (mean  $\omega_0^{\text{amb}}=0.98$ , 90th percentile  $\omega_0^{\text{amb}}=0.997$ ). For some days the difference between the dry and the ambient  $\omega_0$  is quite large. Such cases could be important for the critical single scattering albedo (Haywood and Shine, 1995), which is a threshold of  $\omega_0$  that determines whether the radiative forcing will be a negative (cooling) or a positive (warming) one. Over a high albedo surface there are cases where using  $\omega_0^{\text{dry}}$  can cause opposite signs in the radiative forcing than if  $\omega_0^{\text{wet}}$  was used (Randles et al., 2004).

#### 4.5.5 Predicting $f(\text{RH})$

The humidograms in Fig. 4.6 and the time lines in Fig. 4.7 already demonstrated through their relatively high values of  $f(\text{RH})$  the need to correct the dry in-situ measured scattering coefficients. The ambient RH during our investigated time period is characterized by high values (RH mean: 89.0%, 10th percentile: 70.3%, 90th percentile: 99.3%, see Fig. 4.10a), which in addition shows the need to account for hygroscopic growth. Recommendations will be given in this section on how to transform dry measured scattering coefficients to ambient conditions. This is only valid for Arctic aerosol similar to the one found at Zeppelin station during summer and fall.

The model calculations to predict  $f(\text{RH})$  measured by the WetNeph were repeated with modified input parameters. As input, daily averages of the measured dry number size distribution and a constant dry refractive index of  $(\text{NH}_4)_2\text{SO}_4$  were used. The calculations were done for a larger RH range of

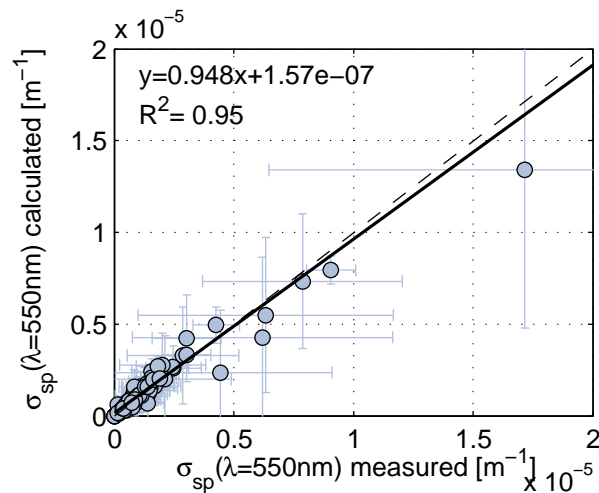


Figure 4.11: Dry calculated versus dry measured scattering coefficients (at  $\lambda=550$  nm) using a refractive index of  $(\text{NH}_4)_2\text{SO}_4$  for the entire campaign and the measured dry size distribution (daily averages, error bars denote standard deviation of the calculated and measured one-hour values). A weighted linear least-square regression is added to the plot (black line).

RH=75–95%. The RH dependency of  $g(\text{RH})$  was accounted for by using the  $\kappa$  model (Eq. 4.2). Different  $\kappa$  values of the hygroscopic growth were used to test the sensitivity of  $f(\text{RH})$  to hygroscopicity. The calculations were performed for  $\kappa=1.11$ , 0.57, and 0.24, corresponding to the maximum, mean and minimum retrieved hygroscopic growth factor, respectively. In addition,  $\kappa$  was parameterized as a function of  $V_{\text{OPC}}/V_{\text{tot}}$ , our proxy for sea salt contribution. Regression of the data shown in Fig. 4.8c gives the linear relationship:

$$\kappa = 0.28 \frac{V_{\text{OPC}}}{V_{\text{tot}}} + 0.43. \quad (4.13)$$

A comparison of the dry calculated scattering coefficients (daily averages) for the entire measurement period showed a good agreement with the measured values (see Fig. 4.11). Therefore, a fixed dry refractive index could be used here. Figure 4.12 shows the result as a histogram of the ratio of predicted to measured  $f(\text{RH})$ . For comparison, the calculations were also done with the exact daily mean  $\kappa$  (see magenta line in Fig. 4.12). Both using the maximum or minimum  $\kappa$  causes a clear over- or under-prediction of  $f(\text{RH})$  by a factor of  $\sim 1.7$  or  $\sim 0.6$ , respectively. Expressing  $\kappa$  as a function of  $V_{\text{OPC}}/V_{\text{tot}}$  generally gives a better performance with the prediction ratios centered around 1. However, just taking the campaign mean  $\kappa \sim 0.57$  is already sufficient, when predicting  $f(\text{RH})$ . Pure  $(\text{NH}_4)_2\text{SO}_4$  has a  $\kappa$  value of 0.48 at RH=85% (Topping et al., 2005), thereby explaining the good agreement between the measurement and the prediction for pure  $(\text{NH}_4)_2\text{SO}_4$  as already shown in Fig. 4.7d.

## 4.6 Conclusions

High scattering enhancement factors  $f(\text{RH}, \lambda=550 \text{ nm})$  (mean  $\pm$  standard deviation =  $3.24 \pm 0.63$  at RH=85%) were observed during summer and fall 2008 at the Zeppelin station in Ny-Ålesund, Svalbard. No clear wavelength dependency of  $f(\text{RH})$  was found. The measured RH dependency of  $f(\text{RH})$  at RH between 75% and 95% can be well described by an empirical one-parameter equation. Filter

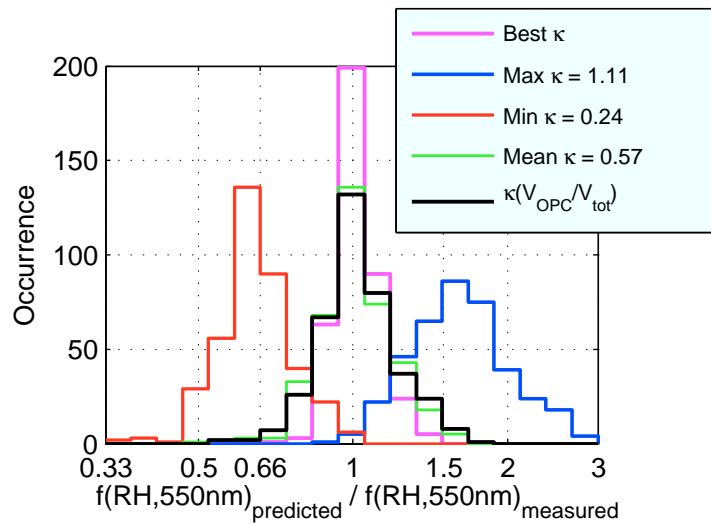


Figure 4.12: Histogram of predicted to measured  $f(\text{RH}, \lambda=550\text{ nm})$  within  $\text{RH}=75\text{--}95\%$  using the minimum ( $\kappa=0.24$ , red line), the maximum ( $\kappa=1.11$ , blue line), and the mean ( $\kappa=0.57$ , green line)  $\kappa$  obtained from the backward calculations as well as  $\kappa$  as a function of the volume fraction of large particles  $V_{\text{OPC}}/V_{\text{tot}}$  (black line). Using the exact daily mean  $\kappa$  derived from the backward calculation is also shown for comparison (magenta line).

measurements and FLEXPART simulations revealed considerable influence from sea salt aerosol during about one third of the time, also reflected in an enhanced volume fraction of large particles. Distinct deliquescence was frequently observed during sea salt influenced periods, while water uptake on the hydration branch was gradual during the other periods. No distinct or even a slightly negative correlation was found between sea salt influence and  $f(\text{RH})$  at  $\text{RH}=85\%$ . This is explained by the fact that equal diameter growth factors translate into smaller  $f(\text{RH})$  at bigger dry sizes. The mean dry size was indeed larger during sea salt influence, and reverse Mie calculations indicate that hygroscopic diameter growth factors were actually slightly higher than during periods without sea salt influence. However, variations of the inferred hygroscopic growth were rather small, such that assuming a constant mean hygroscopicity of  $\kappa=0.57$  for the entire campaign introduces little additional uncertainty in model predictions of  $f(\text{RH})$  based on size distribution data. Although these results were obtained specifically for the Zeppelin station, they might as well be valid for other Arctic areas during summer and fall periods without the clear influence of anthropogenic pollution. In any case it is desirable to perform further measurements during other periods and other places in the Arctic.

It is important to include  $f(\text{RH})$  when deriving aerosol forcing properties like the single scattering albedo  $\omega_0$  at ambient conditions. These results will be used in a future study to compare the in-situ measured scattering coefficients (now brought to ambient conditions) at the height of the Zeppelin station (at 475 m) with lidar measurements, which are regularly performed from the town of Ny-Ålesund located at sea level.

### **Acknowledgements**

We thank Ove Hermansen and Jan Wasseng (Norwegian Institute for Air Research, NILU) and as well Dorothea Schulze and Trond Svenøe (Norwegian Polar Institute) for their support at the Zeppelin station. Thanks to the Stockholm University for performing the continuous aerosol observation at the Zeppelin station and the Swedish Environmental Protection Agency for its funding. We also thank NILU for providing the meteorological data from Zeppelin and the webcam pictures. This work was financially supported by the EC-projects: Global Earth Observation and Monitoring (GEOmon, contract 036677), European Supersites for Atmospheric Aerosol Research (EUSAAR, contract 026140), and the European Centre for Arctic Environmental Research (ARCFAC, contract 026129).

## Chapter 5

# Comparison of ambient aerosol extinction coefficients obtained from in-situ, MAX-DOAS and LIDAR measurements at Cabauw

P. Zieger<sup>1</sup>, E. Weingartner<sup>1</sup>, J. Henzing<sup>2</sup>, M. Moerman<sup>2</sup>, G. de Leeuw<sup>2,3,4</sup>, J. Mikkilä<sup>4</sup>, M. Ehn<sup>4</sup>, T. Petäjä<sup>4</sup>, K. Clémer<sup>5</sup>, M. van Roozendaal<sup>5</sup>, S. Yilmaz<sup>6</sup>, U. Frieß<sup>6</sup>, H. Irie<sup>7</sup>, T. Wagner<sup>8</sup>, R. Shaiganfar<sup>8</sup>, S. Beirle<sup>8</sup>, A. Apituley<sup>9,10</sup>, K. Wilson<sup>9,10</sup>, U. Baltensperger<sup>1</sup>

<sup>1</sup> Paul Scherrer Institut, Laboratory of Atmospheric Chemistry, 5232 Villigen, Switzerland

<sup>2</sup> Netherlands Organization for Applied Scientific Research TNO, Princetonlaan 6, 3508 Utrecht, The Netherlands

<sup>3</sup> Finnish Meteorological Institute, Climate Change Unit, Erik Palmenin Aukio 1, 00101 Helsinki, Finland

<sup>4</sup> University of Helsinki, Department of Physics, Gustaf Hällströmin katu 2, 00014 Helsinki, Finland

<sup>5</sup> Belgium Institute for Space Aeronomy, Ringlaan 3, 1180 Brussels, Belgium

<sup>6</sup> University of Heidelberg, Institute of Environmental Physics, Im Neuenheimer Feld 229, 69120 Heidelberg, Germany

<sup>7</sup> Japan Agency for Marine-Earth Science and Technology, Research Institute for Global Change, Yokohama, Japan

<sup>8</sup> Max-Planck-Institute for Chemistry, Joh.-Joachim-Becher-Weg 27, 5512 Mainz, Germany

<sup>9</sup> National Institute for Public Health and the Environment RIVM, 3721 Bilthoven, The Netherlands

<sup>10</sup> Royal Netherlands Meteorological Institute KNMI, 3730 AE De Bilt, The Netherlands

Published in *Atmospheric Chemistry and Physics*, 11, 2603-2624, doi:10.5194/acp-11-2603-2011, 2011.

## Abstract

In the field, aerosol in-situ measurements are often performed under dry conditions (relative humidity  $RH < 30\text{--}40\%$ ). Since ambient aerosol particles experience hygroscopic growth at enhanced RH, their microphysical and optical properties – especially the aerosol light scattering – are also strongly dependent on RH. The knowledge of this RH effect is of crucial importance for climate forcing calculations or for the comparison of remote sensing with in-situ measurements. Here, we will present results from a four-month campaign which took place in summer 2009 in Cabauw, The Netherlands. The aerosol scattering coefficient  $\sigma_{sp}(\lambda)$  was measured dry and at various, predefined RH conditions between 20 and 95% with a humidified nephelometer. The scattering enhancement factor  $f(RH, \lambda)$  is the key parameter to describe the effect of RH on  $\sigma_{sp}(\lambda)$  and is defined as  $\sigma_{sp}(RH, \lambda)$  measured at a certain RH divided by the dry  $\sigma_{sp}(\text{dry}, \lambda)$ . The measurement of  $f(RH, \lambda)$  together with the dry absorption measurement (assumed not to change with RH) allows the determination of the actual extinction coefficient  $\sigma_{ep}(RH, \lambda)$  at ambient RH. In addition, a wide range of other aerosol properties were measured in parallel. The measurements were used to characterize the effects of RH on the aerosol optical properties. A closure study showed the consistency of the aerosol in-situ measurements. Due to the large variability of air mass origin (and thus aerosol composition) a simple parameterization of  $f(RH, \lambda)$  could not be established. If  $f(RH, \lambda)$  needs to be predicted, the chemical composition and size distribution need to be known. Measurements of four MAX-DOAS (multi-axis differential optical absorption spectroscopy) instruments were used to retrieve vertical profiles of  $\sigma_{ep}(\lambda)$ . The values of the lowest layer were compared to the in-situ values after conversion of the latter ones to ambient RH. The comparison showed a good correlation of  $R^2 = 0.62\text{--}0.78$ , but the extinction coefficients from MAX-DOAS were a factor of 1.5–3.4 larger than the in-situ values. Best agreement is achieved for a few cases characterized by low aerosol optical depths and low planetary boundary layer heights. Differences were shown to be dependent on the applied MAX-DOAS retrieval algorithm. The comparison of the in-situ extinction data to a Raman LIDAR (light detection and ranging) showed a good correlation and higher values measured by the LIDAR ( $R^2 = 0.82\text{--}0.85$ , slope of 1.69–1.76) if the Raman retrieved profile was used to extrapolate the directly measured extinction coefficient to the ground. The comparison improved if only nighttime measurements were used in the comparison ( $R^2 = 0.96$ , slope of 1.12).

## 5.1 Introduction

Atmospheric aerosol particles change in size due to water uptake which is determined by their chemical composition and the ambient relative humidity (RH). As a result their optical properties – especially the aerosol light scattering – also strongly depend on RH. Therefore, long-term measurements of aerosol physical and optical properties are generally recommended at dry conditions in order to keep measurements comparable (e.g.  $RH < 30\text{--}40\%$  as recommended by WMO/GAW, 2003). However, for the comparison of such ground-based measurements with other optical aerosol measurements (e.g. LIDAR, MAX-DOAS or satellite retrieval), for the purpose of aerosol correction of satellite retrievals, or for the use in climate models, accurate knowledge of the RH effect is very important.

The size and the solubility of a particle determine the response of an ambient particle to changes in

RH. The water vapor pressure above a water droplet containing dissolved material is lowered by the Raoult effect. The equilibrium size of a droplet was first described by Köhler (1936), who considered the Kelvin (curvature) and Raoult (solute) effect. The growth of an aerosol particle due to water uptake is described by the hygroscopic growth factor  $g(\text{RH})$  which is defined as the particle diameter  $D_{\text{wet}}$  at a certain RH divided by its dry diameter  $D_{\text{dry}}$ :

$$g(\text{RH}) = \frac{D_{\text{wet}}(\text{RH})}{D_{\text{dry}}}. \quad (5.1)$$

The RH dependence of  $g(\text{RH})$  can be parameterized in a good approximation by a one-parameter equation, proposed e.g. by Petters and Kreidenweis (2007):

$$g(a_w) = \left(1 + \kappa \frac{a_w}{1 - a_w}\right)^{\frac{1}{3}}. \quad (5.2)$$

Here,  $a_w$  is the water activity, which can be replaced by the relative humidity RH, if the Kelvin effect is negligible, as for particles with sizes more relevant for light scattering and absorption, i.e. with  $D_{\text{wet}} > 100$  nm. The coefficient  $\kappa$  is a simple measure of the particle's hygroscopicity and captures all solute properties (Raoult effect). The impact of hygroscopic growth on the aerosol light scattering coefficient is usually described by the scattering enhancement factor  $f(\text{RH}, \lambda)$ :

$$f(\text{RH}, \lambda) = \frac{\sigma_{\text{sp}}(\text{RH}, \lambda)}{\sigma_{\text{sp}}(\text{dry}, \lambda)}, \quad (5.3)$$

where the scattering coefficient  $\sigma_{\text{sp}}$  depends on the wavelength  $\lambda$  and the relative humidity RH. In the following we will discuss the characteristics of the scattering enhancement factor for  $\lambda = 550$  nm. Since no clear wavelength dependency was found during our measurement period (in the range of 450–700 nm), we will omit  $\lambda$  for simplicity and refer to the scattering enhancement factor as  $f(\text{RH})$ .

Measured and modeled enhancement factors have been described in several previous studies, including studies on urban (Yan et al., 2009; Fitzgerald et al., 1982), continental (Sheridan et al., 2001), biomass burning (Kotchenruther and Hobbs, 1998), maritime (Fierz-Schmidhauser et al., 2010b; Wang et al., 2007; Carrico et al., 2003), free tropospheric (Fierz-Schmidhauser et al., 2010a; Nessler et al., 2005a) or Arctic aerosol (Zieger et al., 2010).

The comparison of remote sensing measurements to in-situ values of the aerosol extinction coefficient for validation purposes has been performed in several studies. Lidar measurements have been compared to nephelometer measurements, but almost always with dry nephelometer data using model assumptions or literature values of  $f(\text{RH})$  (Ferrare et al., 1998; Voss et al., 2001) and only rarely using a humidified nephelometer (Morgan et al., 2010). The MAX-DOAS technique for aerosol retrieval is novel and only few comparisons have been made with in-situ data. The first comparison of the extinction coefficient (measured at Ghuangzhou, China) with a single MAX-DOAS instrument (similar retrieval as for the instrument by the Max-Planck-Institute for Chemistry (MPI), see below) to nephelometer data was made by Li et al. (2010) using a single parameterization from a different station (60 km further away) to calculate the ambient aerosol extinction coefficients from the dry nephelometer data. In addition, they only used ground based RH measurements and differences between indoor and ambient RH and temperature conditions were not accounted for.

In this study, the RH dependency of the aerosol extinction coefficient was examined using direct measurements of aerosol optical properties as a function of RH taken during a four months' campaign at Cabauw, The Netherlands. The data were compared in an optical closure study with Mie-calculations, which relied on the aerosol number size distribution corrected to a specific RH using hygroscopicity measurements. As a proof of concept, the in-situ measurements of the aerosol extinction coefficient were compared to remote sensing data from MAX-DOAS and LIDAR measurements. The vertical profiles of the aerosol extinction coefficient obtained from MAX-DOAS and their comparison to LIDAR measurements are discussed in an upcoming publication (Frieß et al., 2011).

## 5.2 The Cabauw site and the CINDI campaign

A field campaign was carried out from 8 June to 6 October 2009 at the Cabauw Experimental Site for Atmospheric Research (CESAR, located at 51.97° N, 4.93° E) in The Netherlands. The site is located approximately 33 km north-east of the city of Rotterdam and 30 km south-west of Utrecht. CESAR is a facility dedicated to the observation and characterization of the state of the atmosphere, its radiative properties and interaction with land surface, for the study of physical processes, climate monitoring and validation studies (Russchenberg et al., 2005). A large set of continuous in-situ and remote sensing equipment is installed at the site. A 213 m high mast equipped with various meteorological sensors (like temperature, dew point, wind direction, wind speed, etc.) is the main feature of the CESAR site. The continuous aerosol measurements are contributing to the EUSAAR (European Supersites for Atmospheric Aerosol Research) project (Philippin et al., 2009) with associated quality control, site audits, and reporting.

During 16 June and 24 July 2009 our measurements were part of the CINDI campaign (Cabauw Intercomparison Campaign of Nitrogen Dioxide measuring Instruments) where the main goal was to compare different remote sensing and in-situ techniques measuring  $\text{NO}_2$ . Besides  $\text{NO}_2$ , other atmospheric gases and aerosols were measured and intercompared. For more details see Roscoe et al. (2010) and Pitters et al. (2011).

## 5.3 Experimental

Various physical aerosol properties have been measured during the four-month period. The following section describes the main experimental techniques used in this work. In the first part (Sect. 5.3.1) the main in-situ instruments used to characterize the effects of RH on the aerosol extinction coefficient will be described. The results of the in-situ measurements are later compared to two different atmospheric profiling techniques: First to MAX-DOAS measurements (Sect. 5.3.2) and in a next step to LIDAR measurements (Sect. 5.3.3). This comparison is carried out only for the lowest ground layer.



### 5.3.1 In-situ measurements

#### Inlet system

Air is sampled at a height of 60 m at the Cabauw tower. The inlet system consists of four parts: (a) PM<sub>10</sub> size selective inlets (4 PM<sub>10</sub> heads), (b) a Nafion drying system that dries aerosol to or below 40% RH, (c) a 60-m stainless steel pipe, and (d) a manifold that splits the flow to the suite of instruments. The manifold and the in-situ instruments are all located at the basement of the tower. The in-situ measurements used in this paper are those from the nephelometer, the multi-angle absorption photometer (MAAP), the aethalometer, the scanning mobility particle sizer (SMPS) and aerodynamic particle sizer (APS), all of which are described below. These instruments sampled their flow from the manifold using separate pumps to adjust the required flow for proper operation of the instruments.

The total flow sustained in the 60-m inlet pipe was 60 lpm, for optimal operation of the PM<sub>10</sub> inlets. Whenever an instrument was added or removed, the flows to the other instruments were checked and adjusted when needed. Although attempts have been made to characterize the losses, they were not conclusive in an experimental sense. In general the losses in similar inlet pipes can be calculated by theory (e.g., Birmili et al., 2007). Losses through diffusion (for smaller particles with  $D < 0.1 \mu\text{m}$ ) and sedimentation (for larger particles with  $D > 2 \mu\text{m}$ ) are expected to be below 10–20%. Since the main contribution to the extinction in the visible nephelometer wavelength will be in the size range between 0.1 and 1  $\mu\text{m}$ , the effect of particle losses on the dry extinction coefficient is assumed to be smaller than 10–20%. Additional losses are expected due to the use of a Nafion dryer but there is no quantitative information for the specific dryer used in Cabauw.

#### Humidified and dry nephelometer

A recently developed humidified nephelometer (WetNeph) was installed for four months next to the continuously running aerosol in-situ instruments. The WetNeph is described in detail by Fierz-Schmidhauser et al. (2010). Briefly, the aerosol scattering coefficient  $\sigma_{\text{sp}}(\lambda)$  and the back scattering coefficient  $\sigma_{\text{bsp}}(\lambda)$  are measured at three wavelengths ( $\lambda = 450, 550, \text{ and } 700 \text{ nm}$ ) at defined RH between 20% and 95%. For this purpose a specifically designed single-stream humidification system (consisting of a humidifier followed by a dryer) brings the initially dry aerosol (the aerosol is already dried at the main inlet) to a defined RH before its scattering properties are measured by an integrating nephelometer (TSI Inc., Model 3563).

The WetNeph was programmed to measure RH cycles. In the first part of the cycle, the dry particles experience elevated RH in the humidifier, after which they are passed through the turned off dryer before their scattering properties are measured in the nephelometer (hydration mode). It is noted that the temperature in the nephelometer's detection cell is  $\sim 1^\circ\text{C}$  higher than in the humidifier, thereby causing a slight RH decrease of approximately 2–6% (see Fig. A1 in Fierz-Schmidhauser et al., 2010) and with that a concurrent shift of the observed deliquescence RH. Deliquescence is described as a sudden uptake of water of an initially dry and solid particle at the defined deliquescence relative humidity. Inorganic salts (for instance ammonium sulfate or sodium chloride) exhibit a distinct deliquescence. Organic constituents of mixed atmospheric aerosols can suppress the deliquescence of

inorganic salts (Sjogren et al., 2007). The behavior of dehydrating particles following the upper hysteresis branch of the growth curve is measured by setting the humidifier to its maximum RH (~95%), followed by RH reduction in the dryer and measurement in the nephelometer (dehydration mode). The lowest possible RH in this mode was ~55%, limited by the capacity of the dryer at the high sample flow of  $101 \text{ min}^{-1}$  chosen for this campaign. The RH inside the nephelometer cell is monitored by a HygroClip (Rotronic), which was calibrated before and after the campaign with standard salt solutions, and in addition by a dew point mirror (Edge Tech, Model 2000, Dewprime DF). More technical details can be found in Fierz-Schmidhauser et al. (2010).

A second nephelometer (DryNeph, TSI Inc., Model 3563, operated by TNO) was used in parallel to measure the scattering coefficient under dry conditions as a reference. The RH inside the DryNeph was always below 30% (campaign mean RH = 17.7%).

Both nephelometers measured within the scattering angles of  $7^\circ$  to  $170^\circ$ . The scattering coefficients for the complete angle between  $0^\circ$  and  $180^\circ$  were retrieved by correcting the measured values using the scheme proposed by Anderson et al. (1996) (truncation error correction) which also accounts for non-idealities of the light source in the nephelometer.

Both nephelometers were calibrated (with particle-free air and  $\text{CO}_2$ ) and compared directly (WetNeph without humidifier system). In addition, the scattering coefficients at dry conditions ( $\text{RH}_{\text{WetNeph}} < 40\%$ ) were compared for the entire campaign. From these measurements it was found that the WetNeph scattering coefficients at dry conditions were slightly higher than the ones of the DryNeph (for 450 nm:  $\sigma_{\text{WetNeph}} = 1.07\sigma_{\text{DryNeph}} + 8.7 \times 10^{-7} \text{ m}^{-1}$ ,  $R^2 = 0.99$ ; for 550 nm:  $\sigma_{\text{WetNeph}} = 1.06\sigma_{\text{DryNeph}} + 6.7 \times 10^{-7} \text{ m}^{-1}$ ,  $R^2 = 0.97$ ; for 700 nm:  $\sigma_{\text{WetNeph}} = 1.03\sigma_{\text{DryNeph}} + 4.5 \times 10^{-7} \text{ m}^{-1}$ ,  $R^2 = 0.94$ ), which was caused by differences in the absolute calibration of the nephelometer (WetNeph nephelometer measured higher scattering coefficients) and losses in the humidifier (~ 5%, see Fierz-Schmidhauser et al. 2010). The WetNeph measurements were therefore corrected accordingly.

### Measurement of the aerosol absorption coefficient

A multi-angle absorption photometer (MAAP) and an aethalometer were used to quantify the aerosol absorption properties.

The MAAP (Thermo Scientific Inc., Model 5012, operated by TNO) measures the light attenuation and light scattered back from aerosol particles which are deposited on a filter. The measurement is performed at  $\lambda = 637 \text{ nm}$  (which differs from the manufacturer's value of 670 nm, Müller et al., 2011). A radiative transfer scheme is applied to retrieve the fraction of light absorbed by the deposited aerosol (Petzold and Schönlinner, 2004). The aerosol absorption coefficient  $\sigma_{\text{ap}}$  is obtained by multiplying the measured black carbon (BC) mass concentration with the instrumental set value of the mass absorption cross section of  $6.6 \text{ m}^2 \text{ g}^{-1}$ .

In addition, an aethalometer (Magee Scientific, Model AE-31, operated by RIVM) was used which measures the light attenuation by the aerosol particles (also deposited on a filter) at 7 wavelengths ( $\lambda = 370, 470, 520, 590, 660, 880, \text{ and } 950 \text{ nm}$ ). The aerosol absorption coefficient  $\sigma_{\text{ap}}(\lambda)$  is then derived from

the light attenuation:

$$\sigma_{\text{ap}}(\lambda) = \frac{A}{Q} \frac{\Delta \text{ATN}(\lambda)}{\Delta t} \frac{1}{C \cdot R(\text{ATN}(\lambda))}, \quad (5.4)$$

where  $A$  is the filter spot area,  $Q$  the volumetric flow, and  $\Delta \text{ATN}(\lambda)$  the change of light attenuation during the time interval  $\Delta t$  (Weingartner et al., 2003). The empirical constant  $C$  corrects for multiple scattering in the unloaded filter. Here, a value of  $C = 4.09$  was used (Collaud Coen et al., 2010). The wavelength and ATN dependent factor  $R$  corrects for effects caused by the amount of particles deposited on the filter, which decrease the optical path in the filter (also called the shadowing effect).  $R$  was set to unity as the single scattering albedo  $\omega_0$  (defined as the ratio of scattering to extinction coefficient) is larger than 0.8 most of the time (Weingartner et al., 2003).

Since the aethalometer measures at various wavelengths, the absorption Ångström exponent  $\alpha_{\text{ap}}$  can be derived:

$$\sigma_{\text{ap}}(\lambda) = \epsilon \lambda^{-\alpha_{\text{ap}}}, \quad (5.5)$$

where  $\lambda$  is the wavelength of the aethalometer and  $\epsilon$  a concentration dependent constant.

Using the measured  $\alpha_{\text{ap}}$  of the aethalometer and the measured value of  $\sigma_{\text{ap}}(637 \text{ nm})$  from the MAA, the absorption coefficient for a different wavelength  $\lambda$  was calculated as follows:

$$\sigma_{\text{ap}}(\lambda) = \sigma_{\text{ap}}(637 \text{ nm}) \left( \frac{\lambda}{637 \text{ nm}} \right)^{-\alpha_{\text{ap}}}. \quad (5.6)$$

### Measurement of the aerosol size distribution

A scanning mobility particle sizer (SMPS) and an aerodynamic particle sizer (APS) were used to measure the aerosol size distribution for dry diameters between approximately 10 nm and 5  $\mu\text{m}$  (both operated by TNO).

The SMPS (a modified TSI Inc., Model 3034) consists of a bipolar particle charger, a differential mobility analyzer (DMA) and a condensation particle counter (CPC). Particles are charged before they are classified in the DMA according to their electrical mobility diameter and are counted by the CPC. A correction for multiple charged particles was applied. Number size distributions in the diameter range between approximately 10 and 520 nm were recorded with a time resolution of 5 min.

The APS (TSI Inc., Model 3321) measures the particle size distribution between aerodynamic diameters of approximately 0.5 and 20  $\mu\text{m}$ . However, in Cabauw, particles larger than approximately 5  $\mu\text{m}$  are not sampled through the inlet system due to the  $\text{PM}_{10}$  size cut at the inlet and the drying thereafter, which results in a reduction in size. One distribution is recorded each minute.

The overlap between the SMPS and APS showed to be good for most of the cases. Small differences seen in the transition of the volume size distribution were caused by variations in density and shape influencing the APS sizing. However, they were found to be negligible for our purposes, since the scattering coefficient is dominated by contributions from the fine mode ( $D_p < 500 \text{ nm}$ , measured by the SMPS). The measured volume size distributions could be well fitted using a three modal lognormal size distribution equation.

Table 5.1: Overview of the main MAX-DOAS technical and inversion properties.

	BIRA <sup>a</sup>	IUPHD <sup>b</sup>	JAMSTEC <sup>c</sup>	MPI <sup>d</sup>
Wavelength	400–700 nm	290–790 nm	223–558 nm	310–461 nm
Spectral resolution (FWHM)	0.95 nm	0.5–0.6 nm	0.7 nm	0.5–0.9 nm
Field of view	0.8°	0.9°	<1°	1.2°
O <sub>4</sub> bands used	477 nm	477 nm <sup>e</sup>	477 nm <sup>f</sup>	360 nm
Scaling factor	0.75	0.8	0.8	0.83
Elevation angles (°)	1, 2, 4, 5, 8, 10, 15, 30, 90	2, 4, 8, 15, 30, 90	2, 4, 8, 15, 30, 90 <sup>g</sup>	2, 4, 6, 8, 10, 15, 30, 90
Inversion scheme	Optimal estimation	Optimal estimation	Optimal estimation	Least squares
Time resolution	15 min	15 min	30 min	10 min
	1 elevation sequence	2–3 elevation sequences	1 elevation sequence	1 elevation sequence
Radiative transfer model	LIDORT v3.3 <sup>h</sup>	SCIATRAN <sup>i</sup>	MCARaTS <sup>j</sup>	McARTim <sup>k</sup>
Aerosol optical properties	AERONET <sup>l</sup> , in-situ	OPAC <sup>m</sup>	$\omega_0$ : 0.95, AP: 0.65 <sup>n</sup>	$\omega_0$ : 0.95, AP: 0.68
Time period used	19.6.–21.7.	23.6.–26.9.	19.6.–24.7.	22.6.–14.7.
Vertical discretization	200 m	200 m	1 km	20–5000 m

<sup>a</sup> Clémer et al. (2010); <sup>b</sup> Frieß et al. (2006); <sup>c</sup> Irie et al. (2008, 2009); <sup>d</sup> Li et al. (2010); Wagner et al. (2011); <sup>e</sup>  $\sigma_{ep}$  is retrieved at 450 nm due to specifications of the radiative transfer model and the employed OPAC database (Hess et al., 1998); <sup>f</sup> The retrieved  $\sigma_{ep}$  is for 476 nm, which is the O<sub>4</sub> cross-section-weighted mean wavelength over the fitting window used. <sup>g</sup> from 08.06.–21.06. 3° was used instead of 2°; <sup>h</sup> Spurr (2008); <sup>i</sup> Rozanov et al. (2001); <sup>j</sup> Iwabuchi (2006); <sup>k</sup> Deutschmann and Wagner (2008); <sup>l</sup> Holben et al. (1998); <sup>m</sup> Calculated for an assumed mixture of water soluble and soot particles with a number mixing ratio of 0.46 and 0.54, respectively (Hess et al., 1998); <sup>n</sup>  $\omega_0$ : single scattering albedo, AP: asymmetry parameter;

### Measurement of the hygroscopic growth factor

Hygroscopic particles are able to grow in size by absorbing water vapor even at sub-saturated conditions. A simple way to describe the hygroscopicity of a particle is via the diameter growth factor  $g(\text{RH})$  as defined in Eq. (5.1). This property can be measured directly with a hygroscopicity tandem differential mobility analyzer (H-TDMA, Liu et al., 1978). The aerosol sample is first dried in the H-TDMA, and then charged with a bipolar charger. Subsequently a dry size class of particles,  $D_{\text{dry}}$ , is selected using a DMA (Winklmayr et al., 1991). At Cabauw, the H-TDMA of the University of Helsinki (modified version of the instrument presented by Ehn et al., 2007) was set up to measure  $D_{\text{dry}}$  of 35, 50, 75, 110, and 165 nm. Then the monodisperse particles are exposed to controlled relative humidity (90%) and temperature. The wet aerosol goes through the second DMA, which scans a size range covering possible growths factors from 0.7 to 2.5. A corresponding concentration for each size fraction is monitored with a CPC. A humidified size distribution for a certain  $D_{\text{dry}}$  is then obtained. The growth factors in this study were determined within  $\pm 0.05$ , which is typical for a well-maintained TDMA system (Swietlicki et al., 2008).

In a complex location such as Cabauw, with several different aerosol sources, the particles are typically externally mixed. This is reflected in the hygroscopic growth factor spectrum by a widened distribution, or even by clearly separated growth modes, for a given particle size. The piecewise linear method of the TDMAinv Toolkit (Gysel et al., 2009) was used to retrieve the growth factor distributions. Although many different sources can contribute to the aerosol population, typically one of the sources dominated. Therefore, simply using the average growth factor for each distribution is sufficient to describe the temporal variation of the growth of the accumulation mode particles at 90% RH. In this

work only the data at the largest dry size, 165 nm, was utilized as the larger particles contribute to the optical properties the most (Sundström et al., 2009).

### 5.3.2 MAX-DOAS measurements

Multi-axis differential optical absorption spectroscopy (MAX-DOAS) is a technique to derive profiles of atmospheric gases and aerosols using spectral radiation measurements under different (mostly slant) elevation angles (Hönninger and Platt, 2002; Leser et al., 2003; Van Roozendael et al., 2003; Wittrock et al., 2004; Hönninger et al., 2004; Wagner et al., 2004; Sinreich et al., 2005; Heckel et al., 2005; Frieß et al., 2006; Irie et al., 2008).

For the retrieval of aerosol extinction profiles, usually the atmospheric absorption of the oxygen collision-induced dimer ( $O_2-O_2$  or  $O_4$ ) is analyzed. Since the atmospheric  $O_2$  concentration is almost constant, changes in the observed absorption can be attributed to changes in the atmospheric radiative transfer, e.g. caused by the influence of aerosol scattering and absorption (Wagner et al., 2004; Frieß et al., 2006). By comparison with a forward model which describes the effects of aerosols on the MAX-DOAS measurements, aerosol properties can be inverted from the measured  $O_4$  absorption. Usually MAX-DOAS aerosol retrieval consists of two steps: first, the  $O_4$  optical depth is retrieved from the measured spectra using the DOAS technique (Platt and Stutz, 2008). In a second step, the aerosol properties are inverted by comparing the measured  $O_4$  optical depths to those simulated by a radiative transfer model. As was shown by Frieß et al. (2006) and Clémer et al. (2010), dependent on the wavelength and atmospheric visibility, typically 1–3 independent pieces of information on the aerosol extinction profile can be obtained from MAX-DOAS  $O_4$  observations. It is noted that usually for some of the aerosol optical properties (e.g. the single scattering albedo or the asymmetry parameter) either fixed values are assumed or information from independent measurements (e.g. sun photometers or in-situ measurements) is used.

In this study MAX-DOAS aerosol retrievals from four groups are included: the Belgium Institute for Space Aeronomy (BIRA), the Institute for Environmental Physics of the University of Heidelberg (IUPHD), the Japan Agency for Marine-Earth Science and Technology, Research Institute for Global Change (JAMSTEC), and the Max-Planck-Institute for Chemistry (MPI). All groups use similar retrieval schemes for the spectral analysis of the  $O_4$  absorption (first step); further details of the spectral analysis can be found in Roscoe et al. (2010). For the inversion of the aerosol properties by comparison with radiative transfer simulations (second step) two different approaches are used. BIRA, IUPHD, and JAMSTEC apply the optimal estimation method (Rodgers, 2000), which yields height-resolved profiles of the aerosol extinction coefficient. MPI uses a more simplified approach following the technique of Li et al. (2010): the aerosol extinction profile is described by only two parameters (the total aerosol optical depth and the aerosol layer height) which are determined by fitting the measured  $O_4$  optical depths to the radiative transfer simulations using a least squares method (the aerosol extinction is assumed to be constant within the aerosol layer).

The properties of the different MAX-DOAS measurements and the specific settings of the aerosol inversion schemes are summarized in Table 5.1. Note that most groups analyze the  $O_4$  absorption band at 477 nm which is close to the wavelengths of the in-situ aerosol measurements. Because of the lim-

ited spectral range of the instrument, MPI uses the O<sub>4</sub> band at 360 nm. It should also be noted that some uncertainty with respect to the absolute value of the O<sub>4</sub> absorption cross section exists (Wagner et al., 2009; Cl  mer et al., 2010), and all groups apply a correction factor to the retrieved O<sub>4</sub> absorption ranging between 0.75 and 0.83, see Table 5.1. Additional information on the individual retrievals can be found in a comparison exercise of the spectral analyses during the CINDI campaign (Roscoe et al., 2010) and in a MAX-DOAS aerosol comparison paper by Frie   et al. (2011).

### 5.3.3 Lidar measurements

The LIDAR CAELI (CESAR Water Vapour, Aerosol and Cloud Lidar; Apituley et al., 2009) is a high-performance, multi-wavelength Raman LIDAR, capable of providing round-the-clock measurements. The instrument is part of the European Aerosol Research Lidar Network (EARLINET), and provides profiles of volume backscatter and extinction coefficients of aerosol particles, the depolarization ratio, and water-vapor-to-dry-air mixing ratio. A high-power Nd:YAG laser transmits pulses at 355, 532, and 1064 nm. Because a large telescope is essentially blind for LIDAR signals from close to the instrument, a second, small telescope is needed to cover the near range, in particular for measurements in the planetary boundary layer. The LIDAR echoes at the elastic and Raman scattered wavelengths are relayed to the photo detectors through optical fibers. The LIDAR returned signals strongly depend on the range  $h$  and decrease with  $h^2$ . Multiplication with  $h^2$  thus removes the range dependence. In this way, the range-corrected signals for the vertically pointing ground-based LIDAR are obtained. Range-corrected signals at 1064 nm are dominated by particle backscatter and are therefore well-suited to display aerosol layering structure and dynamics and to detect the presence of clouds (see e.g. Fig. 5.7a).

Raman LIDAR instruments can retrieve aerosol extinction profiles using a single LIDAR signal at a nitrogen Raman scattered wavelength (here: 387 nm), with just the help of an atmospheric density profile (e.g. a radio sonde or an atmospheric model) (Ansmann et al., 1992). However, two major problems occur when extinction needs to be calculated at daytime and close to the ground:

1. Raman signals are relatively weak and often dominated by the daylight background, and
2. the geometry of the LIDAR instrument, the so-called overlap-function, dictates a minimum distance beyond which unbiased extinction values can be derived.

For CAELI, the Raman signals at 387 nm are strong enough for daytime performance up to a few km altitude, however, trustworthy extinction profiles start between 500 and 1000 m above ground.

To work around the overlap problem for this study, extinction profiles were calculated via the Raman aerosol backscatter profiles down to about 60 m above ground. This was achieved by calculating the Raman aerosol backscatter profile from the ratio of the N<sub>2</sub> Raman signal and the elastic (normal) LIDAR signal (Ansmann et al., 1992). Because both of these signals are affected in the same way by the overlap function, for a well-aligned LIDAR system, it does not affect their ratio. For CAELI, correct alignment could be verified using methods described by Freudenthaler (2008).

For a given measurement, the Raman backscatter ( $\beta$ ) and extinction ( $\sigma_{\text{ep}}$ ) profiles are calculated.

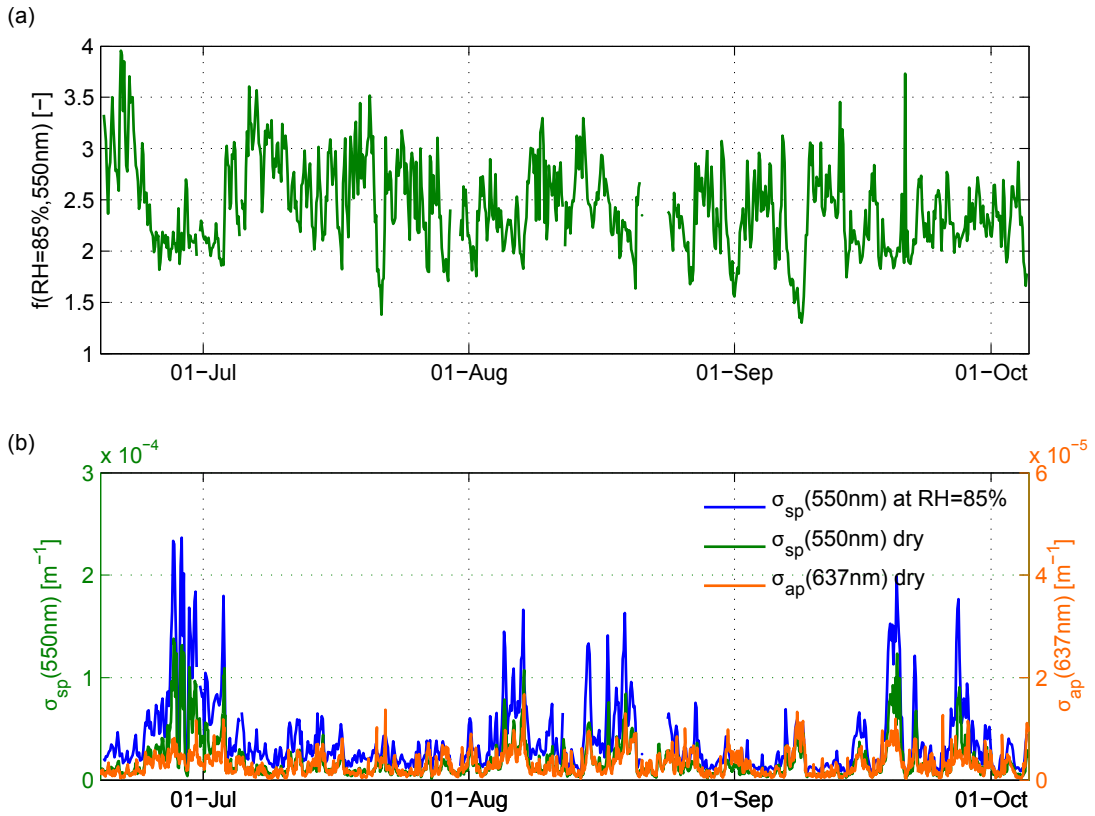


Figure 5.1: Panel (a) Time series of the scattering enhancement factor  $f(\text{RH} = 85\%, 550 \text{ nm})$  measured at Cabauw, The Netherlands, over the period from mid June to the beginning of October 2009. Panel (b) Scattering coefficient at  $\lambda = 550 \text{ nm}$  at  $\text{RH} = 85\%$  (blue line) and at dry conditions (green line) measured by the humidified nephelometer (WetNeph) and reference nephelometer (DryNeph). The absorption coefficient at  $\lambda = 637 \text{ nm}$  (orange line) was measured by the multi-angle absorption photometer (MAAP) at dry conditions.

From these profiles the LIDAR ratio LR is determined:

$$\text{LR}(h) = \frac{\sigma_{\text{ep}}(h)}{\beta(h)} \quad (5.7)$$

where  $h$  denotes the height above the ground.

The LIDAR ratio is only valid beyond the minimum overlap height where both  $\sigma_{\text{ep}}$  and  $\beta$  are valid. However, it can be argued that within well-mixed states of the boundary layer, LR should be fairly constant, since it is representative for a particular type of aerosol and only RH can be a significant factor determining the LR (Salemink et al., 1984; Ackermann, 1998). So by assuming an effective LR,  $\text{LR}'$ , the backscatter profile at lower altitudes can be converted to an extinction profile using  $\text{LR}'$  as a conversion factor in Eq. (5.7). By varying  $\text{LR}'$  over a range of values and comparing to in-situ measurements, it can be determined whether the values obtained in this way are consistent.

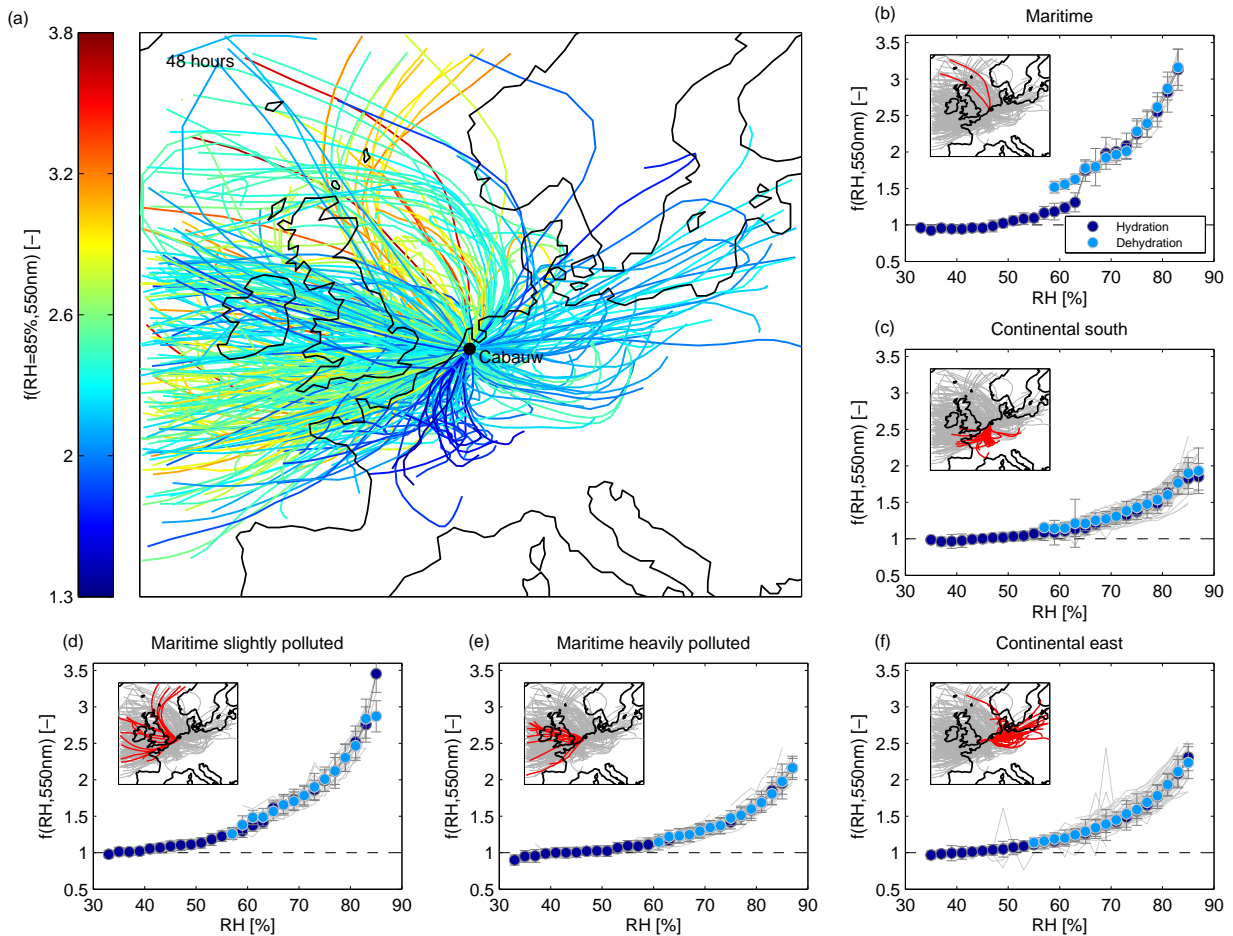


Figure 5.2: Panel (a) FLEXTRA trajectories (48h backward calculation) of air parcels arriving at Cabauw. The trajectories are color coded with the mean aerosol scattering enhancement  $f(RH = 85\%, 550\text{nm})$  measured at the site. Panels (b)–(f) Example humidograms classified by the origin of the air masses. Dark blue circles denote averages of  $f(RH)$  for the hydration branch of the humidogram, while light blue circles are averages of the dehydration branch (2% RH bins). Underlined in grey are the individual humidograms of each trajectory. Error bars denote the standard deviation.

## 5.4 Results

The results of the in-situ measurements are presented in the first Sects. 5.4.1 to 5.4.3. First, the results of the WetNeph analysis and the factors influencing  $f(RH)$  at Cabauw are discussed in Sects. 5.4.1 and 5.4.2. A closure study using different aerosol in-situ measurements is shown in Sect. 5.4.3. The prediction of  $f(RH)$  without explicit WetNeph measurements at Cabauw is also discussed in Sect. 5.4.3. The ambient aerosol extinction coefficient is compared to MAX-DOAS and LIDAR measurements in Sect. 5.4.4.



### 5.4.1 WetNeph analysis

During the four-month campaign the WetNeph and DryNeph were running continuously without any major interruptions (except for a 70-h break at the end of August). The WetNeph was set up to measure humidograms for most of the time, except for two 7- and 11-day long periods in July and August, where the relative humidity was set on a constant value of approximately 82–85%. This was done to further investigate diurnal cycles. Due to the large variation of air masses, no explicit diurnal cycles were found. The humidograms were parameterized with an empirical equation, which has been used in previous studies (Clarke et al., 2002; Carrico et al., 2003) and has been found to best describe the individual branches (hydration, dehydration separately):

$$f(\text{RH}) = a(1 - \text{RH})^{-\gamma}, \quad (5.8)$$

where  $a$  and  $\gamma$  are two independent curve fit parameters ( $a$  is the intercept at  $\text{RH} = 0\%$  and  $\gamma$  parameterizes the magnitude of the scattering enhancement). The humidograms were averaged (3-h mean values for 2% wide RH-bins) and fitted with Eq. (5.8) for  $\text{RH} > 70\%$ . No differences were found at these high RH values between the hydration and dehydration branch). During the periods when the WetNeph was operated in a constant RH mode Eq. (5.8) was used with a campaign mean value for  $a = 0.7$  (upper branch only).

Figure 5.1a shows the temporal evolution of  $f(\text{RH})$  for  $\text{RH} = 85\%$  for the entire campaign period. The values varied between mid June and the beginning of October between approximately 1.3 and 3.9 (10th percentile = 1.93, 90th percentile = 2.9). The corresponding measured dry and wet (at  $\text{RH} = 85\%$ ) scattering coefficients (at 550 nm) and dry absorption coefficients (at 637 nm) are shown in Fig. 5.1b. The main contribution to the ambient extinction coefficient (= scattering plus absorption coefficient) is the scattering coefficient, since the absorption coefficient is about an order of magnitude lower than the scattering coefficient.

The distinct periods of lowered and elevated  $f(\text{RH})$  values (see Fig. 5.1a) were correlated with the origin of the air masses as revealed from 48-h air-mass back trajectories which were calculated using the FLEXTRA trajectory model (Stohl et al., 1995; Stohl and Seibert, 1998) and ECMWF (European Centre for Medium Range Weather Forecasts) meteorological data (trajectories are provided by NILU at [www.nilu.no/trajectories](http://www.nilu.no/trajectories)). The result is shown in Fig. 5.2a where the back trajectories are color coded by the  $f(\text{RH} = 85\%)$  measured at Cabauw. In general, the  $f(\text{RH} = 85\%)$  is lower in air masses originating from the continent and urban regions (like Rotterdam or Ruhr area), probably reflecting the presence of aerosol particles with lower hygroscopicity resulting from anthropogenic emissions and lower sea salt content. Air masses that were transported over the North Atlantic Ocean or the North Sea prior to their arrival in Cabauw likely contain more sea salt leading to higher hygroscopic growth and therefore to higher values of  $f(\text{RH} = 85\%)$ . Mixtures of both extremes are frequently observed, for example air parcels that have their origin over the Atlantic Ocean and are passing over heavy industrialized areas (like the Rotterdam area or southern Great Britain) where the addition of anthropogenic pollution leads to lower hygroscopicity.

Examples of typical humidograms measured at Cabauw are shown in Fig. 5.2b–f. These averaged humidograms are sorted according to the origin of the air masses arriving at the site. A typical maritime case is presented in Fig. 5.2b (selection criteria used: direction of arriving air parcel between

$45^\circ < \theta < 315^\circ$ ,  $f(\text{RH} = 85\%, 550 \text{ nm}) > 3.5$ , average of 4 humidograms). This humidogram shows a sudden increase of  $f(\text{RH})$  at  $\sim 65\%$  RH (deliquescence) during the hydration mode (increase of RH, dark blue circles). During the dehydration mode (humidifier constantly at high RH and dryer on, light blue circles), the deliquescence RH is passed and  $f(\text{RH})$  decreases until  $\text{RH} \approx 58\%$ . This is not the crystallization RH, which unfortunately can not be measured with our set-up, due to temperature and flow conditions inside the WetNeph (see Sect. 5.3.1). The distinct hysteresis behavior indicates that an almost pure maritime aerosol consisting mainly of inorganic salts – e.g. NaCl – was detected here. Figure 5.2d and e are two further examples of air masses having a maritime origin, although they show no clear deliquescence behavior. The maritime slightly polluted case (Fig. 5.2d; with  $225^\circ < \theta < 315^\circ$  and  $f(\text{RH} = 85\%, 550 \text{ nm}) > 3$ , average of 31 humidograms) reveals a similarly high magnitude of  $f(\text{RH})$  as the clean maritime case (Fig. 5.2b), but without deliquescence, while the maritime heavily polluted case is characterized by much lower values of  $f(\text{RH})$  (Fig. 5.2e; with  $225^\circ < \theta < 315^\circ$  and  $f(\text{RH} = 85\%, 550 \text{ nm}) < 2$ , average of 25 humidograms). This is probably caused by additional pollution and/or a higher fraction of organics, which suppresses the deliquescence and/or reduces the hygroscopic growth of the particles (Ming and Russell, 2001). Figure 5.2c and f show two examples of air masses having a continental origin (continental south:  $135^\circ < \theta < 225^\circ$  and  $f(\text{RH} = 85\%, 550 \text{ nm}) < 2$ , average of 48 humidograms; continental east:  $60^\circ < \theta < 135^\circ$ , average of 75 humidograms). Both humidograms show a smooth increase of  $f(\text{RH})$  without a distinct deliquescence behavior. This means that the particles are liquid over a broad RH range. The continental south air masses (Fig. 5.2c) show the lowest values of  $f(\text{RH})$  of  $\sim 1.9$  at  $\text{RH} = 85\%$ . These air parcels originated from northern France, Belgium and The Netherlands south of Cabauw. It is emphasized that these are examples of selected air masses only. A simple and generalized categorization using the air mass trajectories could not be established due to the high variability of size and composition and the short measurement period. For a better statistical analysis a longer time period of at least a year would be desirable.

#### 5.4.2 Factors influencing $f(\text{RH})$ at Cabauw

What determines the magnitude of  $f(\text{RH})$  and what other parameters can be used as proxies to estimate  $f(\text{RH})$ ? To answer these questions, the main in-situ aerosol parameters available during our measurement period were cross-correlated. The result is presented in Fig. 5.3, which shows the coefficient of determination  $R^2$  (squared correlation coefficient) of  $f(\text{RH} = 85\%)$  versus each parameter (the positive or negative sign shows the algebraic sign of the correlation coefficient). The strongest correlation ( $R^2 = 0.72$ ) of  $f(\text{RH} = 85\%)$  exists with the hygroscopic growth factor  $g(\text{RH}, 165 \text{ nm})$  measured by the H-TDMA for the dry diameter of 165 nm. The chemical composition of the particle at this rather large diameter is the main factor that determines its ability to grow. This value seems to be the best proxy measured independently that can be used to estimate  $f(\text{RH})$ . It will be shown later that together with the measured size distribution and Mie theory this factor can be used to get an estimate of  $f(\text{RH})$ .

The BC volume fraction  $V_{\text{BC}}/V_{\text{tot}}$  (assuming a density of  $2.1 \text{ g cm}^{-3}$ ) shows only a weak (negative) correlation with  $f(\text{RH})$ . Also the coarse mode volume fraction  $V_{\text{APS}}/V_{\text{tot}}$  is only weakly (positively) correlated to  $f(\text{RH})$ . These rather low correlations to  $f(\text{RH})$  are accompanied by significant correlations of both  $V_{\text{BC}}/V_{\text{tot}}$  and  $V_{\text{APS}}/V_{\text{tot}}$  to  $g(\text{RH})$ . The positive correlation can be explained by the fact that a

larger coarse mode volume fraction is an indicator for the presence of sea salt, which exhibits a higher hygroscopic growth (therefore positively correlated). Increased BC fractions on the other hand are an indicator for anthropogenic pollution with a reduced hygroscopic growth, causing a negative correlation because high amounts of BC in the aerosol reduce its ability for hygroscopic growth (Weingartner et al., 1997).

The mean diameter  $D_{\text{mean}} = N^{-1} \int_0^{\infty} (D_{\text{dry}} dN / d \log D_{\text{dry}}) d \log D_{\text{dry}}$  measured by the APS (representative for the coarse mode) and by the SMPS and APS (representative for the entire size distribution) show similar values of  $R^2$  as the coarse mode fraction if compared to  $f(\text{RH})$ . Both coarse mode proxies ( $V_{\text{APS}}/V_{\text{tot}}$  and  $D_{\text{APS}}$ ) are more highly correlated to  $g(\text{RH})$  than to  $f(\text{RH})$ , because  $f(\text{RH})$  is a measure for the entire size distribution (where the hygroscopic properties may change with size) while  $g(\text{RH})$  is representative for only one dry diameter. This may also point towards effects of non-linearity in the Mie-scattering, where both size and chemical composition are input parameters. If the chemical composition (hygroscopic growth and refractive index) is assumed to be constant for a given wavelength,  $f(\text{RH})$  will decrease with increasing particle size. This can be compensated if the size changes concurrently with its hygroscopicity. A similar effect was e.g. observed and modeled for Arctic aerosol (see Fig. 9 in Zieger et al. 2010), where smaller but less hygroscopic particles had a similar magnitude of  $f(\text{RH})$  compared to larger but more hygroscopic particles (in that case the coarse mode was also dominated by hygroscopic sea salt).

The scattering Ångström exponent  $\alpha_{\text{sp}}$  (retrieved similar to Eq. (5.5) but using  $\sigma_{\text{sp}}$  instead of  $\sigma_{\text{ap}}$ ) of the dry and wet (at  $\text{RH} = 85\%$ ) scattering coefficient show no correlation with  $f(\text{RH})$ .  $\alpha_{\text{sp}}$  is commonly used as a proxy for the mean size (as can be seen in the clear anticorrelation between  $\alpha_{\text{sp}}$  and the coarse mode volume fraction  $V_{\text{APS}}/V_{\text{tot}}$ ). This implies that they can not be used as a simple proxy for  $f(\text{RH})$ , as for example it has been proposed and verified for the typical aerosol found at the high alpine site Jungfraujoch (JFJ) (Nessler et al., 2005a; Fierz-Schmidhauser et al., 2010a). The reason for this is the occasional presence of a hygroscopic coarse mode (sea salt) at Cabauw (and most probably for all measurement sites with maritime influence), whereas at the JFJ a coarse mode is mainly composed of mineral dust with very low hygroscopicity. Neither the dry backscattering coefficient  $b_{\text{dry}}$  (measured by the nephelometer) nor the dry single scattering albedo  $\omega_{0,\text{dry}}$  (e.g. measured by the nephelometer, the MAAP and/or the aethalometer) are suitable proxies. The Ångström exponent of the scattering enhancement factor  $\alpha_{f(\text{RH})}$  shows no significant correlation to any in-situ parameters.

### 5.4.3 Closure study

To check for consistency within the aerosol in-situ measurements a closure study using Mie theory was performed. The main goal was to reproduce the WetNeph measurements using independent measurements of the hygroscopic growth factor (H-TDMA), the aerosol size distribution (SMPS and APS), the aerosol absorption (MAAP and aethalometer), and scattering properties (DryNeph). The Mie-based model is described in detail in Zieger et al. (2010). The focus was set on the period 4 July to 18 July 2009, because during this period all instruments were operating successfully (for the other periods the SMPS did not measure). Independent measurements of the chemical composition were not available for this study, but are needed to calculate the complex refractive index used in the Mie calculations. Therefore, an inversion of the dry scattering and absorption coefficients using the mea-

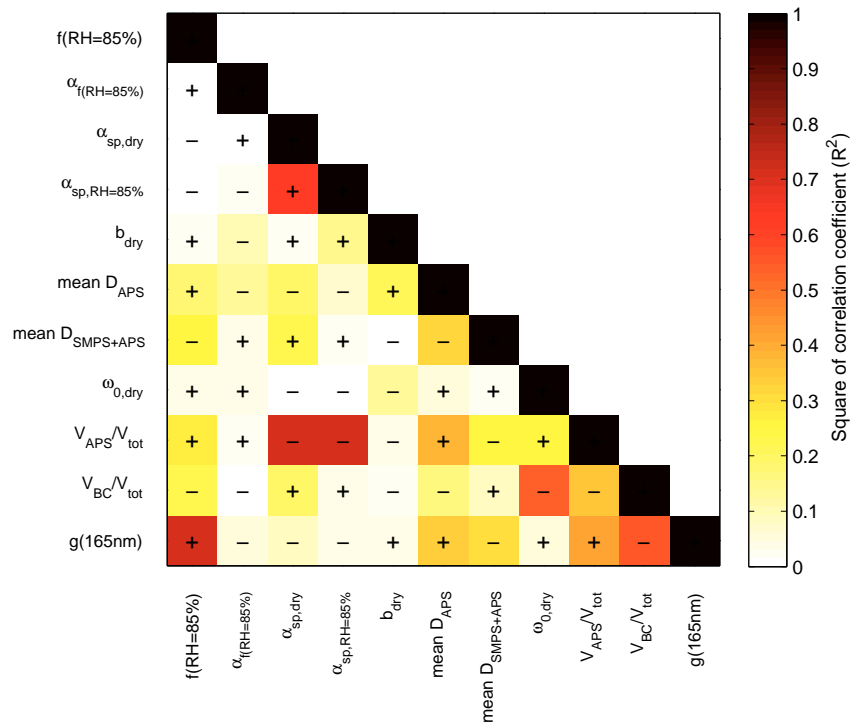


Figure 5.3: Correlation plot of all intensive aerosol parameters measured in-situ at the Cabauw tower.  $f(\text{RH} = 85\%, 550 \text{ nm})$ : scattering enhancement factor;  $\alpha_{f(\text{RH})}$ : Ångström exponent of  $f(\text{RH} = 85\%, 550 \text{ nm})$ ;  $\alpha_{\text{sp,dry}}$ : Ångström exponent of scattering coefficient at low RH;  $\alpha_{\text{sp,RH}=85\%}$ : Ångström exponent of scattering coefficient at  $\text{RH} = 85\%$ ;  $b_{\text{dry}}$ : backscatter fraction (at  $\lambda = 550 \text{ nm}$ ) at low RH;  $D_{\text{APS}}$ : mean (dry) diameter of APS size distribution measurement;  $D_{\text{SMPS}}$ : mean (dry) diameter of SMPS size distribution measurement;  $\omega_{0,\text{dry}}$ : single scattering albedo at low RH (at  $\lambda = 550 \text{ nm}$ );  $V_{\text{APS}}/V_{\text{tot}}$ : coarse mode fraction measured by APS and SMPS;  $V_{\text{BC}}/V_{\text{tot}}$ : black carbon volume fraction measured by MAA, SMPS, and APS;  $g(\text{RH} = 90\%, 165 \text{ nm})$ : hygroscopic growth factor measured at the dry diameter  $d_0 = 165 \text{ nm}$  and at  $\text{RH} = 90\%$  by the H-TDMA. Plus and minus signs indicate the slope of the regression line.

sured size distribution and Mie theory was done (assuming a  $50 \times 50$  field of real and imaginary parts of the refractive index). With this inversion only a mean refractive index (representative for the entire aerosol size distribution) can be derived. This procedure is not a critical issue for the WetNeph closure itself because the closure will be done for a high RH (here, at 85%) as an example, where the particle's refractive index will be close to that of water.

The retrieval of the refractive index showed additionally that the imaginary part anticorrelates well with the hygroscopic growth factor which is measured independently by the H-TDMA ( $R^2 = 0.51$ , see Fig. 5.4). This shows that less hygroscopic particles at Cabauw are also characterized by an enhanced absorption, which indicates the presence of black carbon. A functional description (e.g. polynomial fit) can not be established due to the clear and strong presence of organic matter at Cabauw (Morgan et al., 2010), which is expected to lower the hygroscopic growth while having a minor influence on the refractive index (negligible imaginary part of the refractive index compared to BC, Nessler et al. 2005a). Therefore, an extrapolation to  $g = 1$  in order to estimate the imaginary part of BC can not be made

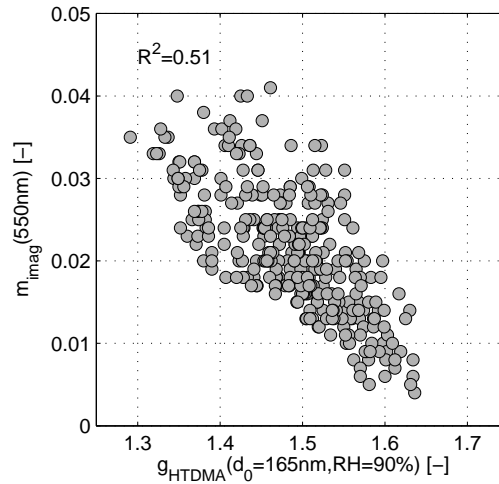


Figure 5.4: Retrieved imaginary part of the complex refractive index versus the hygroscopic growth factor measured by the H-TDMA (at  $d_0 = 165$  nm and  $\text{RH} = 90\%$ ).

without assumptions. The imaginary part versus the BC volume fraction showed a very good correlation ( $R^2 = 0.96$ ,  $m_i = 0.68 V_{\text{BC}} / V_{\text{tot}} - 0.0013$  at 550 nm); an extrapolation to  $V_{\text{BC}} / V_{\text{tot}} \rightarrow 1$  would lead to an imaginary part of pure BC of  $\sim 0.7$ , which is in accordance with literature values (see e.g., Bond and Bergstrom, 2006). The good correlation is not surprising since the imaginary part was retrieved using the BC measurements from the MAAP in conjunction with the size distribution and nephelometer measurements.

The hygroscopic growth factor  $g(\text{RH})$  is measured by the H-TDMA at the dry diameters of 35, 50, 75, 110, and 165 nm. Since the H-TDMA measured at a constant  $\text{RH} = 90\%$ , the value of  $g(\text{RH})$  for different  $\text{RH}$  was calculated using Eq. (5.2), where instead of the water activity  $a_w$  the relative humidity  $\text{RH}$  is used. The largest diameter is the most important one for the determination of the optical properties. The change of the size distribution at  $\text{RH} = 85\%$  was calculated assuming that particles larger than 165 nm have the same hygroscopic growth as the 165-nm-particles. The result for the wet scattering coefficient  $\sigma_{\text{sp}}(\text{RH} = 85\%)$  is presented in Fig. 5.5a (the results are shown for  $\lambda = 550$  nm and are similar for the other nephelometer wavelengths). For the linear regression a bivariate weighted fit according to York et al. (2004) as described in Cantrell (2008) with the assumption of a 10% error in the measured (Anderson et al., 1996) and calculated scattering coefficients has been used. This method includes the uncertainties of both the  $x$  and  $y$  variables and allows the calculation of the uncertainties of the retrieved slope and intercept. The high correlation coefficient and the good linear relationship are clear indicators that the aerosol in-situ measurements are consistent with each other (at least for the investigated period). The slightly lower values of the calculated  $\sigma_{\text{sp}}(\text{RH} = 85\%)$  can be explained by the fact that the H-TDMA measures only rather small particles and misses the coarse mode which might include large hygroscopic particles such as sea salt. This is also seen in the applied color code. While the H-TDMA measures particles with low hygroscopicity (e.g.  $g < 1.3$ , blue points) the measured values of  $\sigma_{\text{sp}}(\text{RH} = 85\%)$  are larger than the calculated ones. One reason could be the presence of a mixture containing a polluted fine mode (e.g. soot) and a coarse mode consisting of sea salt, which can not be measured with the H-TDMA. The calculated  $f(\text{RH} = 85\%)$  using the measured  $g(\text{RH})$  of the H-TDMA is therefore lower than that derived from the measurements (see Fig. 5.5b).

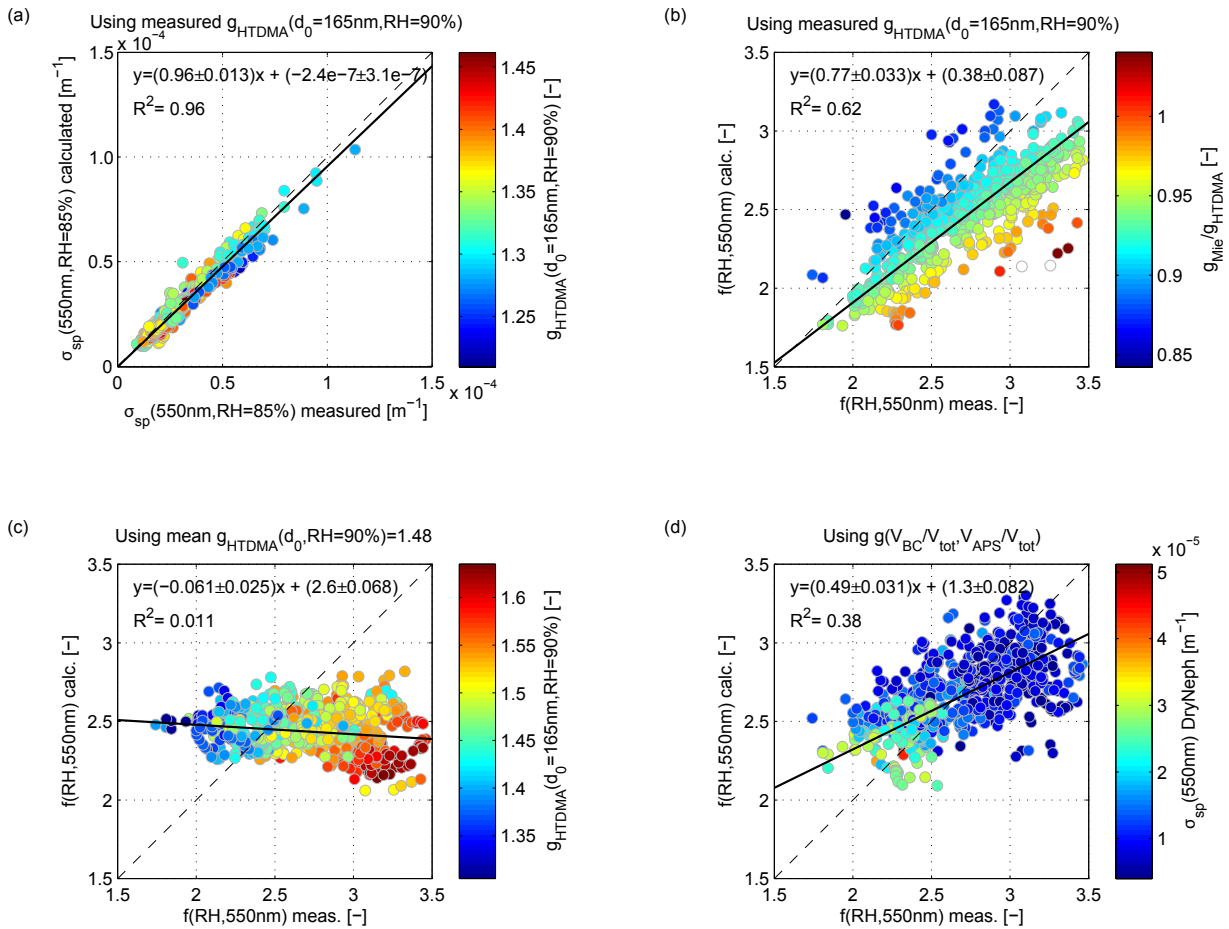


Figure 5.5: Panel (a) Scattering coefficient  $\sigma_{sp}$  calculated vs. measured using the hygroscopic growth factor measured by the H-TDMA. Panel (b)–(d) Scattering enhancement factor  $f(\text{RH} = 85\%, 550 \text{ nm})$  calculated vs. measured values. Panel (b) The measured hygroscopic growth factor of the H-TDMA (dry diameter  $d_0 = 165 \text{ nm}$ ) has been used for the calculation, the color code denotes the ratio of  $g_{\text{Mie}}/g_{\text{HTDMA}}$ . Panel (c) A fixed value of  $g(d_0 \text{ RH} = 90\%) = 1.48$  (mean for that period) has been used for the calculation. Panel (d) An empirical relation of  $g(V_{\text{BC}}/V_{\text{tot}}, V_{\text{APS}}/V_{\text{tot}})$  has been used for the calculation of  $f(\text{RH})$ . All values are shown at RH = 85%. The solid black line represents a bivariate linear regression including weights (with calculated uncertainty of slope and intercept). The 1:1-line is shown as a dashed line.

Keeping the dry refractive index at a fixed value does not significantly change the agreement within this closure study. Despite the fact that the number size distribution dominates the magnitude of the calculated dry scattering coefficient the variation of the dry refractive index still has an influence. Taking e.g.  $m = 1.5291 + 0.024i$  at 550 nm (used in Fierz-Schmidhauser et al. (2010b) for polluted air at Mace Head, Ireland) gives  $y = (1.0 \pm 0.014)x + (2.2 \times 10^{-7} \pm 2.4 \times 10^{-7})\text{m}^{-1}$  and  $R^2 = 0.94$  for the comparison of the wet scattering coefficients to the calculated values (analog to Fig. 5.5a). For the comparison of the measured and calculated  $f(\text{RH})$  using the growth factor of the H-TDMA (analog to Fig. 5.5b) gives a slightly lower agreement  $y = (0.64 \pm 0.029)x + (0.57 \pm 0.078)$  and  $R^2 = 0.61$ .

To further demonstrate the effect of the limited size range of the H-TDMA measurements for the clo-

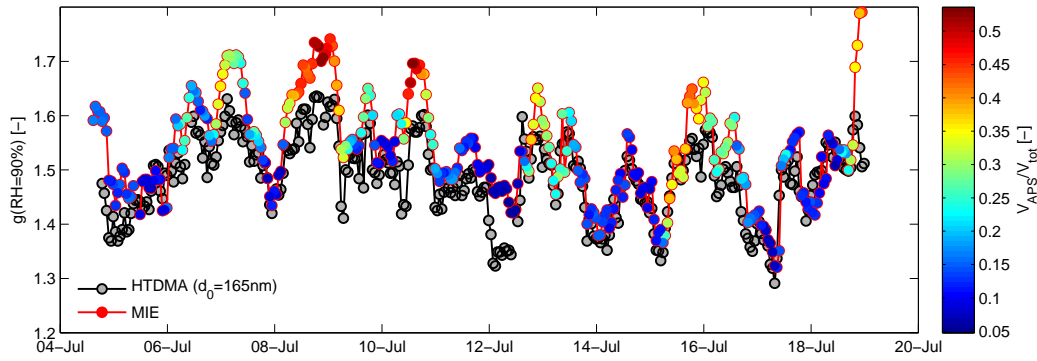


Figure 5.6: Time series of the hygroscopic growth factor measured by the H-TDMA (black line) and retrieved from WetNeph, DryNeph, SMPS, APS measurements and Mie theory (red line). The color code denotes the coarse mode volume fraction measured by the APS and SMPS.

sure study, the hygroscopic growth factor was derived via Mie theory from the WetNeph, DryNeph and size distribution measurements (for more details see Zieger et al. 2010). The results are presented in Fig. 5.6 together with the hygroscopic growth factors measured with the H-TDMA (both at  $\text{RH} = 90\%$ ). While the correlation between both methods is quite good ( $R^2 = 0.71$ ) and the agreement is good for certain periods, the WetNeph based  $g_{\text{Mie}}(\text{RH})$  is generally slightly higher ( $g_{\text{Mie}}(\text{RH}) = 1.3g_{\text{HTDMA}}(\text{RH}) - 0.4$  derived by an orthogonal linear regression), but there are certain periods where the differences increase substantially. These are most probably episodes with enhanced sea salt influence, as can be seen by an enlarged coarse mode measured by the APS and SMPS (see color code in Fig. 5.6).

The calculations were repeated using a fixed hygroscopic growth factor of  $g(d_0, \text{RH} = 90\%) = 1.48$  (mean campaign value for 165 nm) to demonstrate the effect of assuming a constant hygroscopic growth. The result is depicted in Fig. 5.5c. The calculated  $f(\text{RH})$  values are clearly lower than the measured values of  $f(\text{RH})$ . The color code shows the  $g(\text{RH})$  measured by the H-TDMA, which is high for the underestimated and low for the overestimated values of  $f(\text{RH})$ .

If  $f(\text{RH})$  needs to be predicted, the chemical composition (especially the coarse mode composition) needs to be known. Fierz-Schmidhauser et al. (2010a) and Nessler et al. (2005a) used one mean growth factor to successfully predict  $f(\text{RH})$  at the JFJ, but they were in a comfortable position that the aerosol coarse mode consisted only of non-hygroscopic mineral dust.

The question arises whether other continuously measured aerosol properties can be used as a proxy to estimate  $f(\text{RH})$  or  $g(\text{RH})$ .  $f(\text{RH})$  correlates poorly with other in-situ measured parameters as already shown in Fig. 5.3, but clearly correlates with  $g(\text{RH})$ .  $g(\text{RH})$  on the other hand correlates well with the coarse mode and black carbon volume fraction. An empirical equation was retrieved from the available measurements

$$g(\text{RH} = 85\%) = b_1 + b_2 V_{\text{BC}}/V_{\text{tot}} + b_3 V_{\text{APS}}/V_{\text{tot}} + b_4 V_{\text{APS}}/V_{\text{tot}} \cdot V_{\text{BC}}/V_{\text{tot}} \quad (5.9)$$

with  $b_1 = 1.38$ ,  $b_2 = -1.64$ ,  $b_3 = 0.35$ , and  $b_4 = -1.77$  and found to be the best suitable equation. The result of the  $f(\text{RH})$  calculation using Eq. 5.9 for  $g(\text{RH})$  compared to the measurements is presented in

Fig. 5.5d. Although the variation is quite large, an improvement compared to the constant chemistry assumption is clearly seen. Nevertheless, these examples demonstrate the need for a full chemical analysis and measured size distribution to predict  $f(\text{RH})$  if no humidified nephelometer (or at least H-TDMA) measurements are available.

#### 5.4.4 Comparison to remote sensing data

The WetNeph measurements allow the determination of the ambient extinction coefficient, assuming that the absorption coefficient does not change with RH. This assumption can be made, because the scattering is the dominant part of the extinction (median  $\omega_0 = 0.81$ , 10th percentile  $\omega_0 = 0.70$ , 90th percentile  $\omega_0 = 0.89$  at dry conditions for the entire campaign) and model studies for free tropospheric aerosol (although with a higher  $\omega_0$ ) show that the effect of RH on the absorption coefficient (with respect to the extinction) is negligible (Nessler et al., 2005b). The extinction is then calculated as follows:

$$\sigma_{\text{ep}}(\text{RH}) = c_p (f(\text{RH})\sigma_{\text{sp}} + \sigma_{\text{ap}}). \quad (5.10)$$

$\sigma_{\text{sp}}$  and  $\sigma_{\text{ap}}$  are measured by the DryNeph and the MAAP and aethalometer under dry conditions.  $c_p$  is a correction factor for pressure and temperature differences (see below). All optical measurements were inter- or extrapolated to the relevant wavelength using the Ångström law (Eq. (5.5), with  $\sigma_{\text{ep}}$ ).  $\alpha_{\text{ap}}=0.84$  was assumed for periods without aethalometer measurements which represents the mean value measured until the 6th of July by the aethalometer at the site. The assumption of a constant value of  $\alpha_{\text{ap}}$  is justified in our case due to the low variation of the measured value (10th percentile: 0.71, 90th percentile: 0.98) and due to the negligible impact of  $\alpha_{\text{ap}}$  on the ambient extinction coefficient where the scattering is the clearly dominant part (e.g. taking 1 or 1.5 as a fixed value for  $\alpha_{\text{ap}}$  would increase the ambient extinction coefficient only by a factor of 1.002 or 1.01, respectively).  $f(\text{RH})$  was interpolated assuming a linear relationship. Time periods with  $\text{RH}>95\%$  were ignored, due to the uncertainty in the parameterization of  $f(\text{RH})$  at very high RH values (e.g.  $f(\text{RH}) \rightarrow \infty$  for  $\text{RH} \rightarrow 100\%$ ).  $c_p = p(h)T_0/p_0T(h)$  accounts for pressure and temperature differences inside ( $p_0$ ,  $T_0$ ) and outside ( $p(h)$ ,  $T(h)$ ) the nephelometer. For the calculation of  $p(h)$  the barometric formula was used, where  $h$  is the height of the RH measurement. This is mainly of importance for the comparison to the MPI measurements where the measured extinction coefficient is a mean value for a varying layer height (20–5000 m). At the Cabauw tower, the temperature and dew point (from which the RH can be derived via the Magnus formula) are continuously measured at 10, 20, 40, 80, 140, and 200 m. For the MPI comparison the temperature and RH profiles were taken from the operational weather forecast model COSMO (based on assimilated data, see <http://www.cosmo-model.org/>). It was assumed that the aerosol type and concentration are constant with altitude and only RH is changing. Only the retrievals at the lowest height level of the remote sensing instruments were compared to in-situ measurements.



Table 5.2: Results of an orthogonal linear regression (using weights) between ambient in-situ and MAX-DOAS extinction coefficients for the time periods given in Table 5.1. Values in parenthesis are for time periods when all four MAX-DOAS instruments were measuring in parallel.

	BIRA with Cimel	BIRA with in-situ	IUPHD	JAMSTEC	MPI
Slope	3.4 (2.9)	2.7 (2.4)	2.9 (2.2)	3.4 (2.6)	1.5 (1.2)
Error slope	0.06 (0.08)	0.04 (0.06)	0.05 (0.06)	0.06 (0.09)	0.08 (0.2)
Intercept	$-1.6 \times 10^{-5}$ ( $-2.4 \times 10^{-5}$ )	$-8.2 \times 10^{-6}$ ( $-1.3 \times 10^{-5}$ )	$-1.2 \times 10^{-5}$ ( $1.2 \times 10^{-5}$ )	$-2.9 \times 10^{-6}$ ( $1.4 \times 10^{-5}$ )	$4.6 \times 10^{-5}$ ( $4.3 \times 10^{-5}$ )
Error intercept	$2 \times 10^{-6}$ ( $3 \times 10^{-6}$ )	$1 \times 10^{-6}$ ( $2 \times 10^{-6}$ )	$2 \times 10^{-6}$ ( $4 \times 10^{-6}$ )	$2 \times 10^{-6}$ ( $3 \times 10^{-6}$ )	$8 \times 10^{-6}$ ( $2 \times 10^{-5}$ )
No. of points	404 (124)	362 (132)	830 (177)	629 (96)	642 (194)
$R^2$	0.78 (0.79)	0.81 (0.83)	0.66 (0.76)	0.74 (0.75)	0.62 (0.72)

## MAX-DOAS

For comparison with the in-situ measurements, aerosol extinction coefficient from the lowermost layer of the MAX-DOAS profiles from BIRA, IUPHD and JAMSTEC are used. BIRA and IUPHD retrievals use a layer thickness of 200 m, whereas from the JAMSTEC retrieval with a layer height of 1 km, an extinction coefficient representative for the lowermost 200 m has been estimated by assuming an exponentially decreasing extinction profile. In the MPI retrieval a mean aerosol extinction coefficient in the boundary layer is estimated by retrieving the layer height and the aerosol optical thickness. The  $f(\text{RH})$  value was calculated for each available RH measurements of the tower (for MPI taken from the COSMO model), and a mean value was then calculated using Eq. (5.10). For the correction factor  $c_p$ , the pressure was taken from ground based measurements (and taking the barometric height formula for the height dependency) and the temperature was measured next to the RH sensors (for MPI again the COSMO data was used). It should be pointed out that the comparison of the lowest MAX-DOAS extinction coefficient with in-situ measurements is of special interest since the MAX-DOAS retrieval has its highest sensitivity at the ground (Frieß et al., 2006) while LIDAR measurements are usually challenged with the overlap problem at low altitudes. In a recent study (Li et al., 2010), good agreement was found between aerosol extinction coefficients retrieved from MAX-DOAS and surface in-situ measurements. MAX-DOAS aerosol extinction coefficient profiles have only been compared in very few studies with other independent profiling techniques. Irie et al. (2008, 2009) made comparisons between lower-tropospheric vertical profiles retrieved from the JAMSTEC MAX-DOAS and coincident LIDAR observations at Tsukuba, Japan. They found reasonable agreement for layers of 0–1 and 1–2 km to within 30% and 60%, respectively, for most cases. However, these very few studies also show the need for further independent validation studies like the one presented here.

In Fig. 5.7 an example measurement of 24 June 2009 is seen. This day was characterized by almost entirely cloud free conditions in the morning and was classified as one of the golden days during CINDI (Roscoe et al., 2010). This is also reflected in the LIDAR measurement (Fig. 5.7a), which showed the appearance of cirrus clouds at around 10:00 a.m. and low level clouds at around 11:30 a.m. The agreement between MAX-DOAS and in-situ is good during the forenoon, which was characterized by high ambient RH values, which were decreasing until noon (see color code of ambient in-situ values in Fig. 5.7b–e); concurrently the extinction was decreasing within all measurements. From approximately 10:30 a.m. (12:00 p.m. for IUPHD) the MAX-DOAS and ambient in-situ values of  $\sigma_{\text{ep}}$  were diverging. This was coincident with an increase of the planetary boundary layer height and the ap-

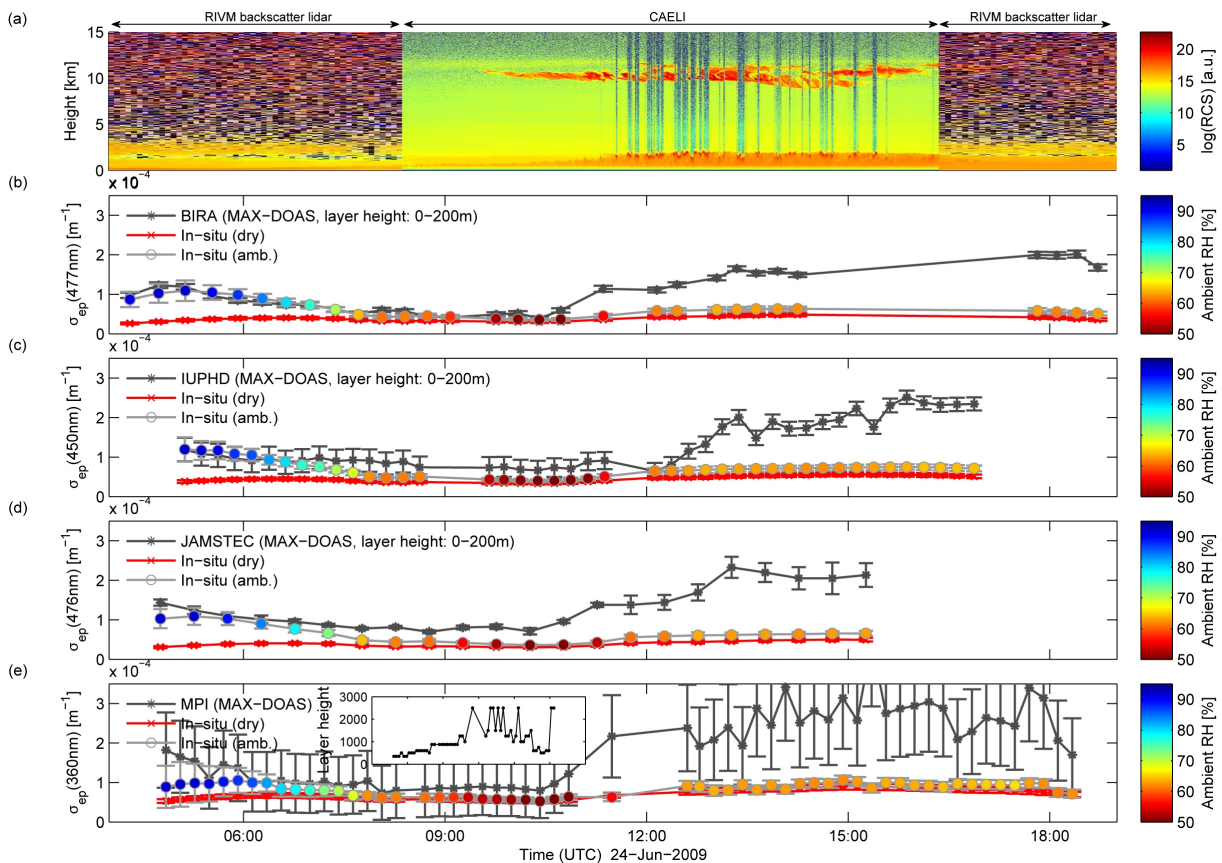


Figure 5.7: Example day 24 June 2009 (golden day). Panel (a) Range corrected signal (RCS) at 1064 nm measured by the RIVM backscatter and the CAELI LIDAR. Panels (b)–(e) Time series of the aerosol extinction coefficient retrieved by MAX-DOAS instruments (black line) compared to in-situ measurements (red line: dry in-situ extinction coefficient, grey line: ambient value at the RH denoted in the color coded dots).

pearance of low level clouds (see LIDAR measurement in Fig. 5.7a), while the surface values of RH (between 0–200 m) stayed below 70%. The comparison of the aerosol optical depth (AOD), which is the integral of  $\sigma_{\text{ep}}$  over the vertical column, retrieved by the MAX-DOAS and measured by a Cimel sun photometer showed good agreement during the entire day, although this is just a columnar value being compared and gives no information on the true profile shape (further details in Frieß et al., 2011).

Figures 5.8 and 5.9 display the comparison of the entire data set, for the time periods given in Table 5.1. All MAX-DOAS instruments detect generally a higher extinction coefficient than the in-situ measurements. The slope of the applied bivariate linear regression (Cantrell, 2008; York et al., 2004) varies from 2.9 (IUPHD), 3.4 (JAMSTEC) to 3.4 (BIRA, with sun photometer (Cimel) used as input values). The MPI MAX-DOAS shows a lower slope (1.5), but has to be treated with care since the retrieval height varied and RH profiles were taken from a re-analyzed weather model (COSMO). All comparisons are well correlated ( $R^2 = 0.62$  to  $0.78$ ). An overview of the coefficients retrieved from the orthogonal linear fit and the correlation is found in Table 5.2. Slope and  $R^2$  improve slightly if only identical time periods (when all four MAX-DOAS instruments were measuring at the same time) are being compared, although the number of comparable points is largely reduced (see Table 5.2). A distinct number of points show a

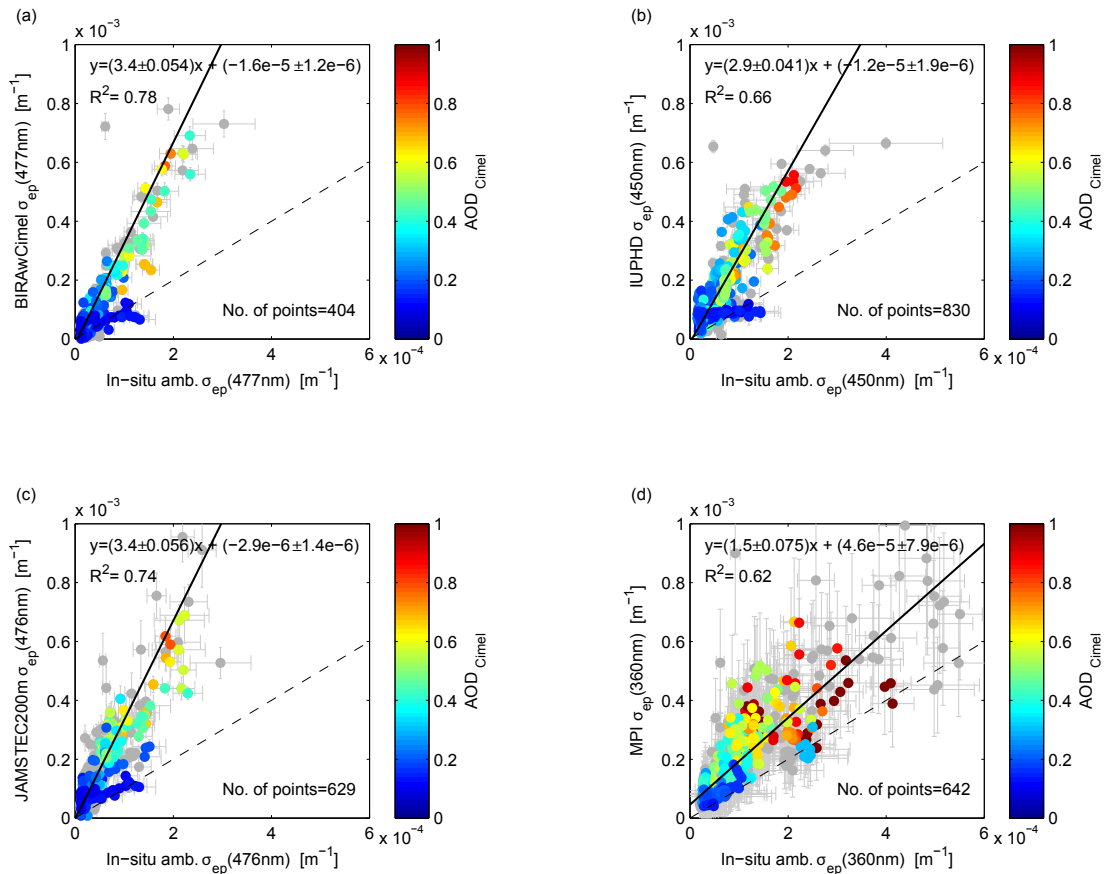


Figure 5.8: Ambient extinction coefficient retrieved by MAX-DOAS vs. in-situ measurements brought to ambient conditions. The color code denotes the AOD measured by the Cimel sun photometer (AOD interpolated in accordance with the appropriate wavelength; grey points are times with no sun photometer measurements). The solid black line represents a bivariate linear regression including weights (with calculated uncertainty of slope and intercept). The dashed line is the 1:1-line.

good agreement and are located on the 1:1-line. The color code in Fig. 5.8 reveals that these are times with a low aerosol optical depth (data from the AERONET sun photometer measurement, level 2.0). Figure 5.9 shows the same comparison, but with the planetary boundary layer (PBL) height as color code. The PBL height is measured by a ceilometer (Vaisala, Model LD-40; for details concerning the algorithm see De Haij et al., 2007, 2010). The points with better agreement show a low PBL height.

Figure 5.10 illustrates the comparison of the MPI measurement, where the layer height is kept variable during the retrieval. The agreement improves with decreasing layer height despite the assumptions that had to be made (well mixed aerosol layer, same aerosol type, RH from COSMO).

The error bars of the ambient in-situ extinction coefficient in Figs. 5.7–5.10 were derived from Gaussian error propagation assuming a 10% uncertainty of the nephelometer (Anderson et al., 1996) and a 12% uncertainty of the MAAP (Petzold and Schönlinner, 2004).

For the BIRA and IUPHD retrieval the error bars represent the sum of the noise and smoothing error. Forward model errors were not considered here (Rodgers, 2000; Frieß et al., 2006; Clémer et al., 2010). For the JAMSTEC retrieval the errors have been quantified by the retrieval covariance matrix, which is

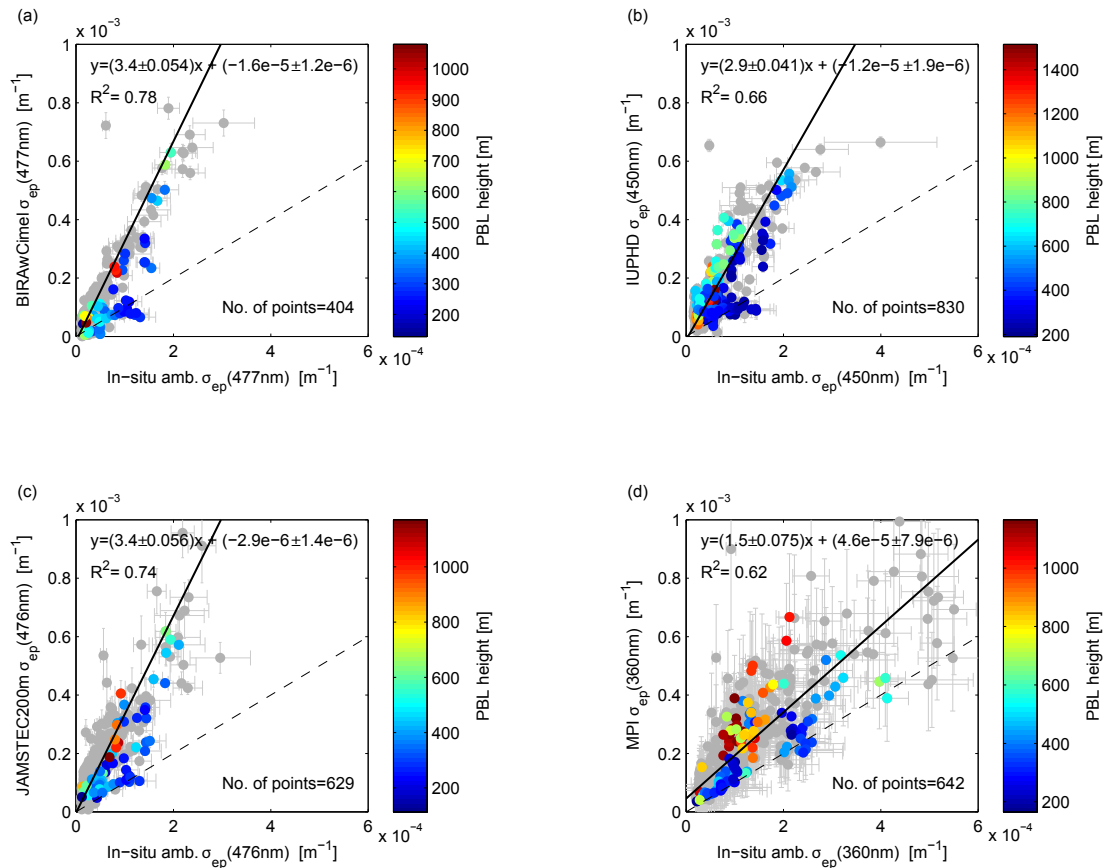


Figure 5.9: Same as Fig. 5.8, but here the color code denotes the planetary boundary layer height measured by the ceilometer (grey points: no quality assured PBL data available).

defined to represent the sum of the smoothing error and the retrieval noise error (Rodgers, 2000). For the MPI retrieval so far no full error assessment was implemented, and the errors were assumed to be  $0.25\sigma_{ep} + 0.05 \times 10^{-3} \text{ m}^{-1}$ .

As already mentioned, BIRA uses the values of the asymmetry factor and the single scattering albedo inverted from sun photometer measurements in their standard retrieval. The comparison improves if in-situ measurements (at ambient conditions) of the asymmetry factor and the single scattering albedo are taken as input parameters (see Table 5.2). This however can be caused by the large uncertainty of the single scattering albedo and the asymmetry factor retrieved from AERONET at low AOD.

The following hypotheses concerning the disagreement are being made. On the in-situ side:

- Particle losses due to impaction or diffusion in the inlet system
- Underestimation of the measured extinction due to the  $\text{PM}_{10}$  size cut
- Parameterization of  $f(\text{RH})$  (Eq. (8), large errors for  $\text{RH} > 90\%$ )

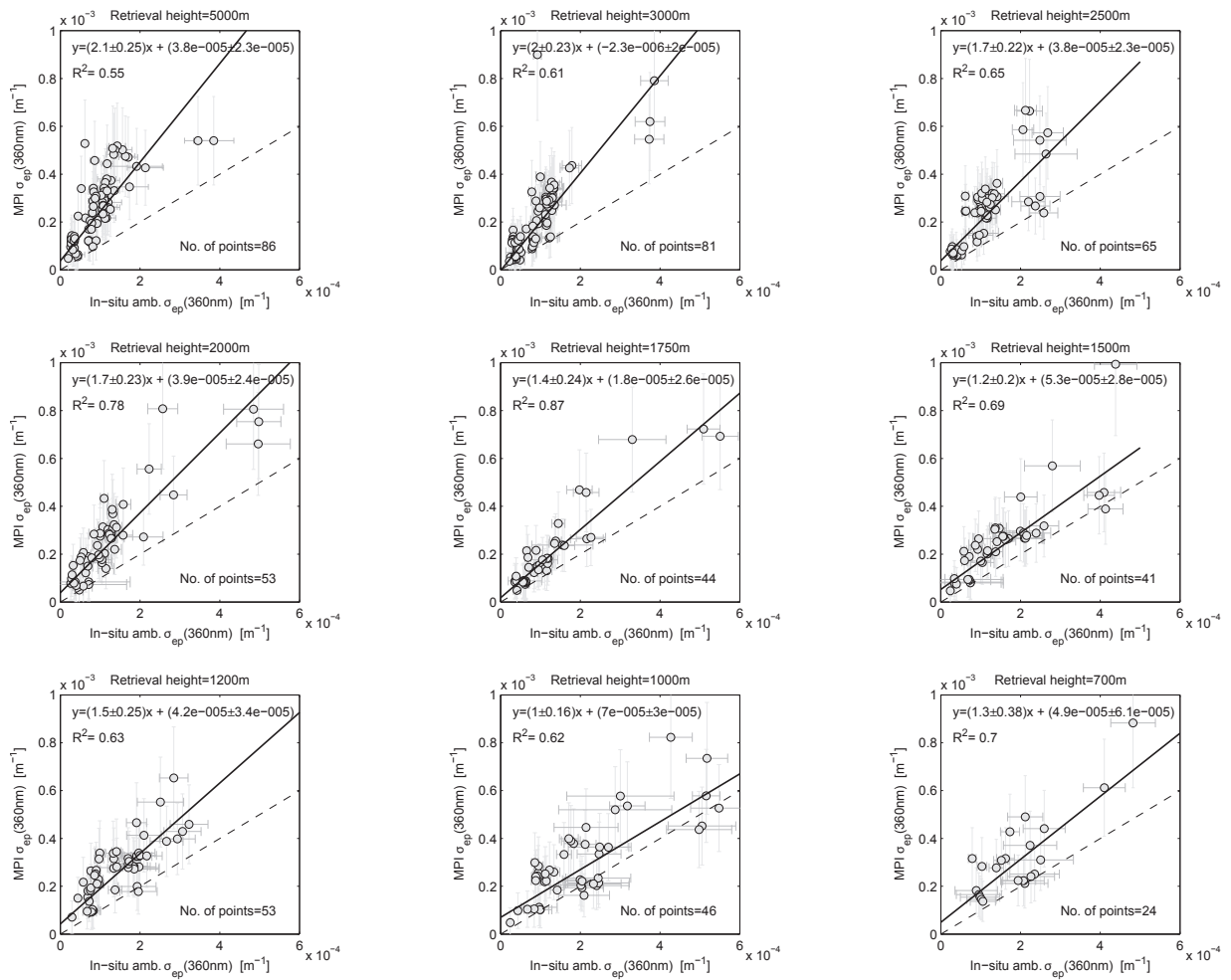


Figure 5.10: Ambient extinction coefficient measured by the MPI MAX-DOAS instrument, where the layer height is kept variable during the MAX-DOAS retrieval vs. in-situ. The aerosol type is assumed to be constant within the layer (for the calculation of the in-situ  $\sigma_{ep}$ , only the RH changes with height). The RH profiles are taken from assimilated COSMO data. Solid line represents a bivariate linear regression including weights (with calculated uncertainty of slope and intercept), dashed line is the 1:1-line.

On the MAX-DOAS side:

- BIRA, JAMSTEC, IUPHD: systematic overestimation of the lowest level (0–200 m). The most probable explanation for this finding is that due to the limited vertical resolution of the retrievals, the presence of aerosol at higher altitudes (>200 m) might result in an overestimation of the lowest level of  $\sigma_{ep}$ . In addition, in the case of an uplifted aerosol layer with a strong vertical gradient near the surface, the vertical resolution of about 250 m near the surface will be insufficient and result in an overestimation of the surface value.
- Influence of the horizontal aerosol gradient, which might exhibit large variation
- Influence of clouds

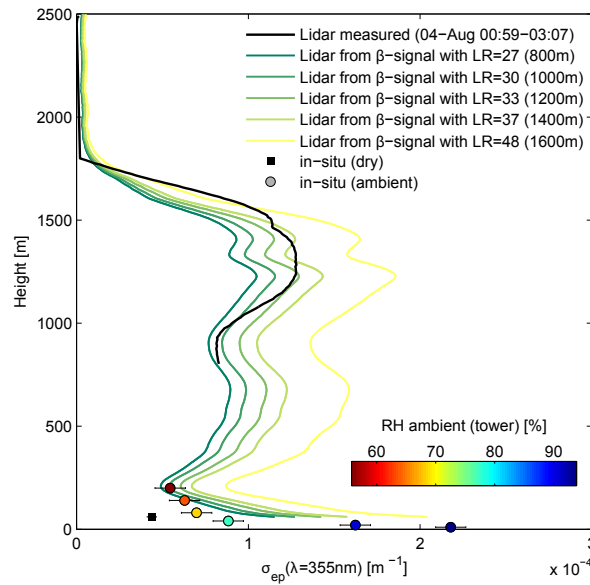


Figure 5.11: Lidar and in-situ measurements of the aerosol extinction coefficient  $\sigma_{ep}$  at  $\lambda = 355$  nm (4 August 2009, 00:59–03:07). Black line: Direct LIDAR measurement of  $\sigma_{ep}$ ; Colored lines:  $\sigma_{ep}$  calculated from the backscatter signal using measured LIDAR ratios (LR) obtained from mean values of different height levels ( $\pm 100$  m); black square:  $\sigma_{ep}$  measured in-situ at dry conditions; colored circles:  $\sigma_{ep}$  brought to ambient conditions (color code denotes the ambient RH measured at the tower, error bars are retrieved via Gaussian error propagation).

The influence of clouds was tested by comparing only data points for which AERONET AOD measurements (level 2.0) were available (other time periods were excluded in the AERONET data processing due to the presence of clouds). No clear improvement could be observed; therefore the influence of clouds is believed not to be the main cause for this disagreement.

The smaller slope of the regression line for the MPI measurements could indicate that the coarser resolution with more simplified assumptions is a more robust retrieval. It should, however, also be noted that the scatter and the y-axis intercept for the MPI retrieval is larger than for the other retrievals.

The comparison was also tested against other parameters like the ambient RH (to check the validity of the  $f(\text{RH})$  parameterization), the aerosol mean diameter (to check for dependencies concerning the size dependent losses), the wind direction, and the single scattering albedo (to check for aerosol type dependencies). No clear dependency was found. With this and with the favorable results from the closure study in mind (Sect. 5.4.3), we assume that the in-situ measurements are not the main reason for the disagreement and only a certain percentage (possibly  $<10\text{--}30\%$ ) can be explained through errors in the in-situ data.

## LIDAR

Due to the long averaging times, only 22 profiles (within the period 23 June–20 September, averaging time  $1.85 \pm 0.5$  h (mean  $\pm$  standard deviation)) of the aerosol extinction coefficient measured by the CAELI LIDAR could be compared to the in-situ measurements. The aerosol extinction coeffi-

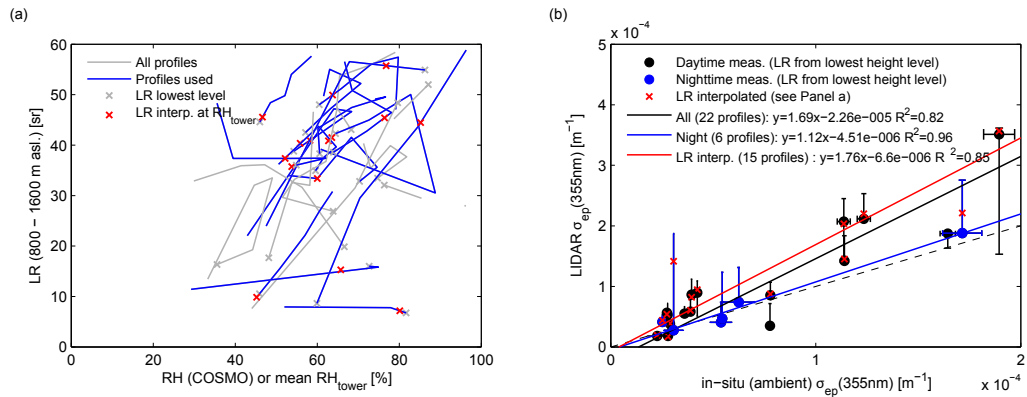


Figure 5.12: Panel (a): The LIDAR ratio LR measured in 200-m altitude intervals between 700 and 1700 m versus the RH in the individual layer (taken from COSMO). Grey crosses denote the LR of the lowest layer, red crosses show the interpolated LR for the RH measured at the ground (mean 60–200 m). The profiles used to retrieve the interpolated value are shown in blue. Grey are all profiles (where no interpolation was possible or where no WetNeph measurements were available). Panel (b): Comparison of the extinction coefficient  $\sigma_{ep}$  at the ground retrieved from LIDAR vs. the in-situ values (mean for 60–200 m). Circular points denote the mean value if the LR from the lowest level is taken (black daytime measurements; blue nighttime measurements). Red crosses show the mean value if the LR interpolated to the ground RH is taken (see Panel a). The y-error bars give the range of the retrieved  $\sigma_{ep}$  taking the measured minima and maxima LR of the upper layer. The x-error bars give the calculated error in the ambient in-situ measurement. The solid lines represent linear orthogonal regressions (see legend).

cient (at 355 nm) can be measured directly using the Raman channel above approximately 750 m. The backscatter signal, retrieved using the Raman method, starts at approximately 60 m and can be used to extrapolate the direct measurement of  $\sigma_{ep}$  if an appropriate LIDAR ratio LR (Eq. 5.7) is assumed. Instead of an educated guess, the measured LR of the upper layers between 700 and 1700 m was determined (mean values for 200 m thick levels) and multiplied with the backscatter signal.

An example day is presented in Fig. 5.11. The extinction is directly measured above  $\sim 750$  m (black line). The LR of the upper layers increase with height from LR = 37 to LR = 48 (due to changing RH and/or aerosol type changes or lower signal to noise ratio). These values are used to calculate  $\sigma_{ep}$  by multiplying the backscatter signal with the LR. The in-situ values at dry (black square) and at ambient conditions at the RH measurement of the tower (color coded circles) are also shown. The large RH gradient results in a strong increase of  $\sigma_{ep}$  concurrently determined indirectly from both the in-situ aerosol measurements and the LIDAR measurements.

The LR values are within the range as e.g. modeled by Ackermann (1998) for marine (LR =  $\sim 10$ –25 between RH = 0–99%) or continental aerosol (LR =  $\sim 40$ –70 between RH = 0–99%) or as observed by Müller et al. (2007) for urban haze in central Europe (LR =  $58 \pm 12$ ). As mentioned above, the LR depends besides the aerosol composition also strongly on the RH. To illustrate the effect of RH on the LR measured here, the LR of the individual layer versus the layer RH is shown in Fig. 5.12a. The RH-profiles were taken from a re-analyzed weather model (COSMO). One can observe that for most of the cases the LR



increases with increasing RH, similar to the model results of Ackermann 1998 or the measurements of Salemink et al. (1984). Of course, also the aerosol type might change with altitude which can not be excluded here.

The LR of the lowest possible height level was multiplied with the mean backscatter coefficient measured between (~60–200m) to retrieve a mean extinction coefficient for the ground (see Eq. 5.7). In addition, the individual retrieved LR-RH-relationships (see Fig. 5.12a) were used to calculate (interpolate) the LR for the mean RH measured at the ground. With this method only 15 profiles could be compared since the no extrapolation was performed. The result is shown in Fig. 5.12b. The error bars denote the range of the retrieved extinction coefficient taking the maximum and minimum value of the measured LR to calculate  $\sigma_{ep}$  at the ground.

Orthogonal linear regressions (without weights) revealed that the LIDAR retrieved  $\sigma_{ep}$  were about ~1.7–1.8 higher compared to the ambient in-situ values. There is no large difference if the LR interpolated to the ground RH (instead of the LR from the lowest layer) is being used, which indicates that the LR of the lowest level has been a good estimate for the LR at the ground (at least for most of the cases). Both sets of  $\sigma_{ep}$  are well correlated to the ambient in-situ values ( $R^2 = 0.82$ – $0.96$ ). Night-time measurements showed to have a better agreement (slope 1.12,  $R^2 = 0.96$ ) compared to daytime measurements, which might be due to lower noise in the LIDAR measurements during nighttime. However, this improvement has to be treated with care since only 6 profiles were measured during nighttime.

## 5.5 Conclusions

In this study, the influence of water uptake on the aerosol extinction coefficient was investigated during a 4-month campaign at the Cabauw field station (The Netherlands) using direct measurements of aerosol optical and micro-physical properties. While the scattering coefficient was measured as a function of RH, the absorption coefficient was measured dry and assumed not to change with RH. The scattering enhancement factor  $f(\text{RH})$  was found to be highly variable ( $f(\text{RH})$  varied between ~1.4 and 3.8 at  $\text{RH} = 85\%$ ) and dependent on the air mass origin. Continental aerosol showed a lower scattering enhancement possibly due to anthropogenic pollution and lower sea salt content. Hysteresis was observed only during some very few events, when the air masses arrived directly from the oceans. The best quantity to estimate  $f(\text{RH})$  from other continuous in-situ measurements was found to be the hygroscopic growth factor measured e.g. by a H-TDMA. The use of the scattering Ångström exponent did not correlate well with  $f(\text{RH})$  due to the large variability in the chemical composition. This makes a simple prediction of  $f(\text{RH})$  at Cabauw, in contrast to other sites (e.g. Jungfraujoch), quite difficult. Here, continuous measurements of  $f(\text{RH})$  and/or better chemical composition measurements would be desirable to better relate dry measured values to the ambient ones. A closure study, which relied on the measured size distribution and the hygroscopic growth, showed the consistency of the aerosol in-situ measurements. The imaginary part of the retrieved complex refractive index was found to correlate well with the hygroscopic growth factor of the HTDMA, which means that more absorbing particles grow less. As a proof of concept, the in-situ measurements were compared with remote sensing data from MAX-DOAS and LIDAR measurements. A good correlation was found be-



tween in-situ and MAX-DOAS measurements. For certain cases (low AOD and low PBL height) good agreement was found, but for most of the time MAX-DOAS retrieved a  $\sim 1.5$ – $3.4$  higher extinction coefficient. Differences could have been caused by e.g. particle losses in the inlet system (all remote-sensing instruments were measuring generally higher extinction) or by the fact that the limited vertical resolution of the MAX-DOAS retrieval overestimated the extinction in the lowest layer when lofted layers were present. In addition, the MAX-DOAS retrieval could have been influenced by the horizontal aerosol gradient, which could have exhibited large variations. The smaller slope of the regression line for the MPI measurements could indicate that the coarser resolution with more simplified assumptions is a more robust MAX-DOAS aerosol retrieval. Lidar and in-situ comparison found to be in better agreement, although the direct measurement of the ambient extinction coefficient started from an altitude above 750 m. Extrapolation with the backscatter signal showed a good correlation ( $R^2 = 0.82 - 0.85$ ) and a higher extinction compared to in-situ (slope of 1.69-1.76), which improved (slope of 1.12,  $R^2 = 0.96$ ) if only nighttime measurements were compared.

### Acknowledgements

We thank Jacques Warmer and the staff of KNMI at the CESAR site for providing an excellent service during our campaign. We thank the CINDI local organization team at KNMI, in particular Ankie Piters, Mark Kroon, and Jennifer Hains, for facilitating this very successful campaign. We gratefully acknowledge Henk Klein-Baltink (KNMI) for providing the ceilometer data. We also gratefully acknowledge the easy access of the meteorological data used in this work via <http://www.cesar-observatory.nl>. We thank Rahel Fierz (PSI) for valuable discussions. Many thanks to Michel Tinquely (PSI) for helping out with the COSMO data, which was provided by the Swiss Federal Office of Meteorology and Climatology (MeteoSwiss). NILU and especially Ann Mari Fjæraa are gratefully acknowledged for providing the air mass trajectories. Many thanks to A. Rozanov from the Institute of Environmental Physics, University of Bremen, for providing the SCIATRAN radiative transfer model to IUPHD. Hitoshi Irie thanks H. Takashima, Y. Kanaya, and PREDE, Co., Ltd for their technical assistance in developing and operating the MAX-DOAS instrument. Observation by JAMSTEC was supported by the Japan EOS Promotion Program of the Ministry of Education, Culture, Sports, Science and Technology (MEXT), and by the Global Environment Research Fund (S-7) of the Japanese Ministry of the Environment. Katrijn Clémer (BIRA-IASB) was financially supported by the AGACC project (contract SD/AT/10A) funded by the Belgian Federal Science Policy Office. This work was financially supported by the ESA Climate Change Initiative Aerosol\_cci (ESRIN/Contract No. 4000101545/10/I-AM) and by the EC-projects Global Earth Observation and Monitoring (GEOmon, contract 036677) and European Supersites for Atmospheric Aerosol Research (EUSAAR, contract 026140).



## Chapter 6

# Comparison and conclusions

This chapter summarizes and compares the results obtained from the three European sites: Jungfraujoch in the Swiss Alps (Chapt. 3), Ny-Ålesund in the high Arctic (Chapt. 4), and Cabauw in the Netherlands (Chapt. 5). First, in Sect. 6.1, the measurements and model studies will be compared. Section 6.2 focuses on the comparison of the recorded data to a widely used aerosol optical database. The chapter will end with general conclusions (Sect. 6.3) and an outlook (Sect. 6.4).

### 6.1 Scattering enhancement at three European sites

The effects of relative humidity (RH) on the aerosol light scattering have been investigated at three European sites that were selected based on the prevailing aerosol type. At the high alpine site Jungfraujoch (JFJ), located in the Swiss Alps at 3580 m (a.s.l.) altitude, mainly free tropospheric air masses were sampled in May 2008, which were interrupted by transport events from the European atmospheric boundary layer (Henne et al., 2010) and occasionally even by long-range transported Saharan dust. Henne et al. (2010) characterized the JFJ site as being *mainly remote*. At the Zeppelin station in Ny-Ålesund (NYA), Spitsbergen, typical Arctic aerosol was measured from July to October 2008. This period was characterized by very low particle concentrations and distinct sea salt transports to the station, which is located at an altitude of 475 m (a.s.l.). Very clean conditions dominated here since no local sources or long-range transport phenomena of pollutants (known as Arctic haze) were observed during this time of the year. In contrast to the sites JFJ and NYA, the Cabauw site (CAB) is located in a rural area between the cities of Utrecht and Rotterdam, the Netherlands, and is therefore influenced by transported pollution from the European continent, by local sources as well as by the marine environment. Henne et al. (2010) categorized the CAB site as *agglomeration* which is characterized by large pollution burdens. During the measurement period between June and October 2009 the aerosol at CAB showed a high variability in composition.

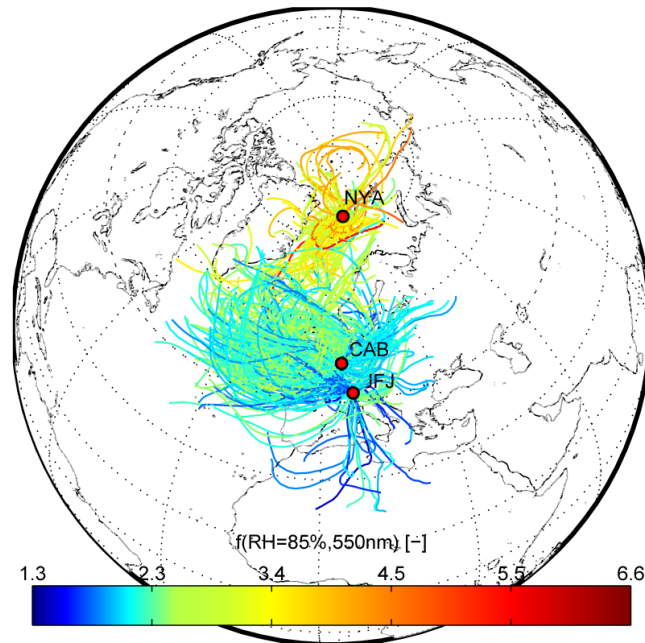


Figure 6.1: FLEXTRA trajectories (72-h backward calculations, time resolution 6 hours) for the three investigated sites: Jungfraujoch (JFJ), Ny-Ålesund (NYA), and Cabauw (CAB). The trajectories are color coded with the mean scattering enhancement  $f(\text{RH}=85\%, 550\text{nm})$  measured at the site. Trajectories where no WetNeph measurements were available are not shown. Note that the field campaigns were carried out during different time periods (see Tab. 6.1).

### 6.1.1 Measurements

The measured scattering enhancement factor  $f(\text{RH})$  showed individual characteristics significant for each of the three sites<sup>1</sup>. Figure 6.1 shows FLEXTRA trajectories (Stohl et al., 1995; Stohl and Seibert, 1998) for each site color coded by the  $f(\text{RH}=85\%)$  value measured at the time of the air parcel arriving at the site<sup>2</sup>. Only periods with available WetNeph measurements are shown. For JFJ, Fig. 6.1 reveals that the air masses were mainly originating from central Europe but also had their origin in the North African regions. These air masses transported mineral dust particles as well up to JFJ. Since mineral dust shows low hygroscopic growth, their  $f(\text{RH}=85\%)$  values are low compared to other air masses. At CAB, air masses with low  $f(\text{RH}=85\%)$  values mainly had their origin in the industrialized areas of e.g. the Ruhr area, Northern France, Southern Britain, the Netherlands, and Belgium.  $f(\text{RH}=85\%)$  was elevated at CAB when the air masses originated from the Atlantic Ocean or the Northern Sea and contained hygroscopic sea salt. However, only few clear sea salt events were observed at CAB e.g. showing hysteresis behavior as one would expect from pure inorganic salts like NaCl. As an extreme, the NYA site showed the largest  $f(\text{RH}=85\%)$  compared to the other sites which could range up to values of 6.6. The main catchment area at NYA was the open oceans and ice shields of the Arctic, bringing e.g. clean sea salt to the site. Selected humidograms recorded at the three sites will be shown later in Sect. 6.2.

<sup>1</sup>As for the other chapters,  $f(\text{RH})$  is discussed for the 550 nm wavelength exemplarily, the explicit reference is omitted from now on for simplicity reasons since no clear wavelength dependency was observed at the three sites for the standard nephelometer wavelengths (450, 550, and 700 nm).

<sup>2</sup>The trajectories were provided by the Norwegian Institute for Air Research (NILU) at [www.nilu.no/trajectories](http://www.nilu.no/trajectories).

### 6.1.2 Closure studies

One goal of this thesis was to calculate and predict the scattering enhancement using auxiliary measurements, like size distribution, hygroscopic growth, and chemical composition and applying Mie calculations. The first task was to check for consistency within the in-situ measurements, so called closure studies, and in a next step to search for other independently measured parameters that can be used to predict  $f(\text{RH})$ . If the auxiliary aerosol measurements are operated on a continuous basis e.g. within a monitoring program, they can possibly be used to predict  $f(\text{RH})$  without explicit RH-dependent optical measurements using e.g. a humidified nephelometer. Unfortunately, the suite of aerosol instruments available was not identical within the three field campaigns. An overview of the main measurements and campaign time frames can be found in Tab. 6.1. The optical parameters (scattering coefficient at defined RH and at dry conditions as well as the absorption coefficient) were almost completely measured at all sites, while the applied aerosol in-situ techniques varied from site to site. At JFJ, the most comprehensive set of instruments were operated. In particular, the bulk aerosol chemical composition was determined with an aerosol mass spectrometer (AMS). The AMS measurements were used to calculate (a) the hygroscopic growth factor (in addition to the direct measurement of the hygroscopic tandem differential mobility analyzer (H-TDMA)) and (b) the refractive index which is needed as an input parameter for the Mie calculations. At NYA, the chemical composition was only partly determined by filter measurements (which were limited to inorganic substances). Also the hygroscopic growth factor was not measured directly using e.g. a H-TDMA, instead it was retrieved by Mie theory through an inverse calculation using the measured size distribution, the optical measurements, and an assumption on the refractive index. At CAB, no chemical measurements at all were available during the observation period, but a H-TDMA was partly deployed. For the closure studies, the scanning mobility particle sizer (SMPS) is probably the most important instrument since it measures in the optically relevant size range the particle number concentration usually up to  $\sim 550$  nm with a high precision. It was in operation at all three sites (unfortunately at CAB only for two weeks within the four month's campaign).

Figure 6.2 summarizes the results of the obtained closure studies by comparing the predicted and measured values of  $f(\text{RH})$  at  $\text{RH}=85\%$ . First, Fig. 6.2a shows the probability density function (PDF) of the observed  $f(\text{RH}=85\%)$  for the three sites. As mentioned above, the closure studies at JFJ and CAB could only be performed for specific time periods that differed from the entire WetNeph measurement period (the dashed lines show the PDF of the entire period, while the solid lines are representative for the closure periods). Panels (a) to (c) in Fig. 6.2 show the PDF of the ratio of the predicted to measured value of  $f(\text{RH}=85\%)$  for the three sites.

At JFJ, the best closure was achieved, if the measured size distribution, the chemical composition (refractive index) and the hygroscopic growth factor (AMS or H-TDMA) were used in the Mie model. The slightly higher predicted values were probably due to calibration issues of the RH sensor inside the WetNeph. Keeping the chemical composition constant (refractive index and hygroscopic growth) or the size distribution shape constant still delivered reasonable prediction results, showing that a mean chemical composition is sufficient to predict  $f(\text{RH})$  (see Sect. 3.3.2 for more details). This result is in accordance with findings of Jurányi et al. (2010) who showed that for a prediction of the cloud condensation nuclei (CCN) number concentration, using measured size distribution and hygroscopicity

Table 6.1: Overview of the used instrumentation for the three investigated sites.

Parameter	Employed instrument	Jungfraujoch (JFJ) <sup>a</sup>	Ny-Ålesund (NYA) <sup>b</sup>	Cabauw (CAB) <sup>c</sup>
Scattering coefficient	Humidified nephelometer (WetNeph)	x	x	x
	Nephelometer (DryNeph)	x	x	x
Light absorption coefficient	Aethalometer	x	x	x <sup>d</sup>
	Multi-angle absorption photometer (MAAP)	x	-	x
Aerosol size distribution	Scanning mobility particle sizer (SMPS)	x	x	x <sup>d</sup>
	Optical particle counter (OPC)	x	x	-
	Aerodynamic particle sizer (APS)	-	-	x
Hygroscopic growth	Hygroscopic tandem differential mobility analyzer (H-TDMA)	x <sup>d</sup>	-	x <sup>d</sup>
Chemical composition	Aerosol mass spectrometer (AMS)	x	-	-
	Filter measurements	-	x	-
Time period (days)		May 08 (31)	Jul.-Oct. 08 (91)	Jun.-Oct. 09 (120)

<sup>a</sup> 46.55°N, 7.98°E, 3580 m a.s.l.; <sup>b</sup> 78.92°N, 11.94°E, 475 m a.s.l. <sup>c</sup> 51.97°N, 4.93°E, 1 m a.s.l. (inlet height 60 m a.s.l.); <sup>d</sup> Only partly available

measurements (H-TDMA), a mean chemical composition is sufficient. Nessler et al. (2005a) proposed a very simplified scheme to predict  $f(\text{RH})$  for the summer and winter periods separately, using the measured Ångström exponent of the dry scattering coefficient. It was shown that it captures the magnitude and the curvature of the  $f(\text{RH})$  measured during the campaign, but often showed a systematic overestimation. This model benefits from the fact that the aerosol coarse mode at JFJ consists mainly of non-hygroscopic mineral dust which is characterized by low Ångström exponents, in contrast to the other two sites where the coarse mode was mainly attributed to sea salt. A slightly broader distribution of the PDF of the predicted to measured value of  $f(\text{RH}=85\%)$  is observed due to the simplifications in the Nessler et al. (2005a) model (see orange curve in Fig. 6.2b). However, a full seasonal validation of the model by Nessler et al. (2005a) would be desirable.

At NYA, the measured values of  $f(\text{RH}=85\%)$  were in general higher compared to the other sites (see Fig. 6.1 and Fig. 6.2a). The full chemical composition and the hygroscopic growth were not measured directly. Nevertheless, the hygroscopic growth was retrieved from the measured size distribution, and the absorption and scattering properties using again Mie theory. As described in Sect. 4.5.5 and summarized in Fig. 6.2c, also a mean hygroscopicity (using a growth factor of  $g(\text{RH}=85\%)=1.6$ ) is sufficient to predict  $f(\text{RH}=85\%)$  at NYA, although with a higher uncertainty compared to JFJ.

For CAB, the situation is more complex, because the aerosol origin showed larger fluctuations. Besides the continental and urban influence, the close by marine environment also contributed to the aerosol composition. As described in Sect. 5.4.3, the measured hygroscopic growth factor is limited to smaller size ranges since the largest dry diameter of the deployed H-TDMA was 165 nm. The larger particles in the coarse mode were therefore missed by the H-TDMA. Since the coarse mode can be influenced by highly hygroscopic sea salt particles, the ratio of predicted to measured values of  $f(\text{RH}=85\%)$  in Fig. 6.2d (blue curve) using the growth factor  $g(\text{RH})$  of the H-TDMA is shifted towards an underestimation of the predicted  $f(\text{RH}=85\%)$ . A proposed parameterization of  $g(\text{RH})$  using the coarse mode volume fraction and black carbon (BC) volume fraction improved the agreement to the measured val-

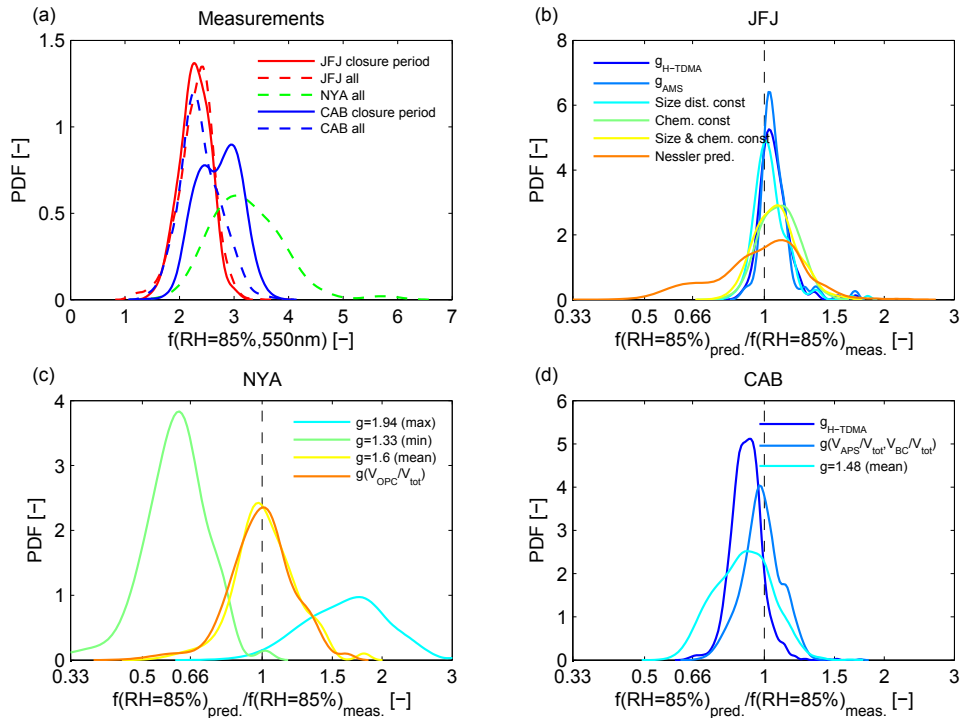


Figure 6.2: Panel (a): Probability density function (PDF) of the measured scattering enhancement  $f(\text{RH}=85\%, 550\text{nm})$  at the three investigated sites Jungfraujoch (JFJ), Ny-Ålesund (NYA), and Cabauw (CAB). The dashed lines are the result for the (shorter) time periods used for the closure studies. Panel (b) - (d): PDF of predicted to measured  $f(\text{RH}=85\%, 550\text{nm})$  of the individual closure studies, which all had their own characteristic settings.

ues. Assuming a constant value of  $g(\text{RH})$ , which can be done for JFJ and NYA, is not sufficient at CAB as can be seen in Fig. 6.2d (green curve).

In summary, both size and chemical composition mattered when determining  $f(\text{RH})$ , which is schematically depicted in Fig. 6.2. For the aerosol discussed here, the relative contributions of the accumulation to the coarse mode and the specific chemical composition were important. At JFJ, the coarse mode was most probably attributed to long-range transported non-hygroscopic mineral dust, whereas at NYA and CAB it was also dominated by hygroscopic sea salt. Sea salt was not observed at JFJ which also explains the absence of hysteresis effects. The accumulation mode was dominated either by low hygroscopic organic substances, non-hygroscopic BC, or by hygroscopic inorganic salts. The interaction between size and hygroscopicity can lead to compensation effects for  $f(\text{RH})$ , as observed at NYA, where smaller and less hygroscopic particles had the same magnitude of  $f(\text{RH})$  as larger and more hygroscopic particles (see Sect. 4.5.3).

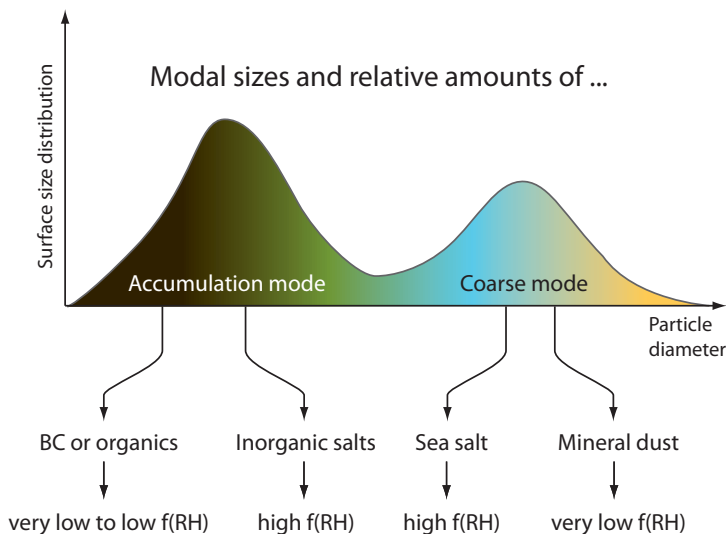


Figure 6.3: Schematic overview on the factors influencing the scattering enhancement  $f(\text{RH})$ . The size and the relative contributions of the different modes with its distinct chemical composition (governing the hygroscopic growth and refractive index) are all influencing  $f(\text{RH})$ . This does also include compensating effects of size and chemical composition.

## 6.2 Comparison to OPAC

The measured scattering enhancement factors have been compared to the database OPAC (optical properties of aerosol and clouds) by Hess et al. (1998). OPAC is a popular database on aerosol and cloud optical properties, which is widely used in the scientific community<sup>3</sup> since it provides a comprehensive set of microphysical and optical data of aerosols and clouds. The data is stored as components (see Tab. 6.2 for the aerosol components) that are meant to be representative for a certain origin (Hess et al., 1998). All components represent average conditions and the authors clearly state that the given values may not be necessarily valid for actual conditions. Nevertheless, a comparison of the measurements performed here to OPAC is a needed scientific task as a first step to improve future versions of OPAC.

The main OPAC aerosol components will be briefly described here. The *water-soluble* component combines all aerosol particles that originate from gas to particle conversion (including various kinds of sulfates, nitrates, and also organic substances), while the *insoluble* component describes soil particles which also contain organic compounds, but do not experience hygroscopic growth. The *soot* component describes the absorbing black carbon. The chain-like structure is neglected here, since the Mie calculations are performed for spherical particles only (i.e. on the primary soot particles which explains the small size and the corresponding high number concentrations in Tab. 6.2). The *sea salt* components are given for the accumulation and the coarse mode separately and both are dependent on RH. To describe desert originated aerosols, different *mineral* components are provided. A special *mineral-transported* component is used to describe long-range transported mineral dust. The *sulfate*

<sup>3</sup> *ISI Web of Knowledge* lists over 640 citations (last accessed on 21 February 2011). OPAC has been used e.g. in the radiative transfer calculations of the MAX-DOAS retrieval from the University of Heidelberg (see Sect. 5.3.2) or in Zieger et al. (2007) to predict an instruments signal output for typical aerosol types.



Table 6.2: Main size and optical parameters of OPAC components according to Hess et al. (1998). The size parameters of a lognormal distribution and the refractive index (at  $\lambda = 550$  nm) are given at RH=0%, while the hygroscopic growth factor is given here at RH=90%.

Component	Standard deviation $\sigma$	Mode (dry) $D_{\text{modN}}$ (nm)	Refractive index at $\lambda = 550$ nm (dry)	Hygroscopic growth factor $g(\text{RH}=90\%)$
Insoluble	2.51	942	1.53 + 0.008i	1
Water-soluble	2.24	42.4	1.53 + 0.006i	1.64
Soot	2.00	23.6	1.75 + 0.44i	1
Sea salt (acc. mode)	2.03	418	1.50 + 0i	2.38
Sea salt (coa. mode)	2.03	3500	1.50 + 0i	2.39
Mineral (nuc. mode)	1.95	140	1.53 + 0.0055i	1
Mineral (acc. mode)	2.00	780	1.53 + 0.0055i	1
Mineral (coa. mode)	2.15	3800	1.53 + 0.0055i	1
Mineral-transported	2.20	1000	1.53 + 0.0055i	1
Sulfate droplets	2.03	139	1.43 + 0i	1.94

component is mainly used to describe the highly sulfate containing Antarctic aerosol and is also used to model the stratospheric background aerosol. Also this component is able to take up water and therefore depends on RH.

Besides the wavelength dependent refractive index, the number size distribution of each component is provided as a lognormal size distribution:

$$\frac{dN_i(r)}{d\log D} = \frac{N_i}{\sqrt{2\pi} \log \sigma_i} \exp \left[ -\frac{1}{2} \left( \frac{\log D - \log D_{\text{mod},i}}{\log \sigma_i} \right)^2 \right], \quad (6.1)$$

where  $D$  is the diameter,  $D_{\text{mod},i}$  the mode diameter,  $N_i$  the total particle number density, and  $\sigma_i$  the width (or standard deviation) of the distribution of component  $i$ . The size parameters and refractive indexes are provided for eight different RH's (0%, 50%, 70%, 80%, 90%, 95%, 98%, and 99%) for the RH-dependent components (see hygroscopic growth factor in Tab. 6.2).

The OPAC components can be externally mixed (using the number mixing ratio of each component) to aerosol types. Hess et al. (1998) propose aerosol types (ready mixtures) as examples that are typically found in the atmosphere (see Tab. 6.3).

The strength of OPAC is the option to individually compose aerosol types (using the number mixing ratio, as mentioned above). Therefore, our measurements will also be compared to individually mixed aerosol types besides the aerosol examples that are proposed in OPAC (see Tab. 6.3). These mixtures were calculated when full size distribution measurements were available at the same time. The number mixing ratio  $n_i$  for each component was calculated as follows:

$$n_i = \frac{N_i}{N_{\text{tot}}} = \left( \int_{D_{i,\text{min}}}^{D_{i,\text{max}}} \frac{dN(D)}{d\log D} d\log D \right) / N_{\text{tot}}, \quad (6.2)$$

where  $N_i$  is the number concentration between  $D_{i,\text{min}}$  and  $D_{i,\text{max}}$ , which is determined by taking the

Table 6.3: Composition of typical aerosol types according to Hess et al. (1998).

Aerosol type	Component	Number density $N_i$ (cm <sup>-3</sup> )	Number mixing ratio $n_i$
Continental clean	water-soluble	2600	1.0
	insoluble	0.15	$0.577 \cdot 10^{-4}$
Continental average	water-soluble	7000	0.458
	insoluble	0.4	$0.261 \cdot 10^{-4}$
	soot	8300	0.542
Continental polluted	water-soluble	15700	0.314
	insoluble	0.6	$0.12 \cdot 10^{-4}$
	soot	34300	0.686
Urban	water-soluble	28000	0.177
	insoluble	1.5	$0.949 \cdot 10^{-5}$
	soot	130000	0.823
Desert	water-soluble	2000	0.87
	mineral (nuc.)	269.5	0.117
	mineral (acc.)	30.5	$0.133 \cdot 10^{-1}$
	mineral (coa.)	0.142	$0.617 \cdot 10^{-4}$
Maritime clean	water-soluble	1500	0.987
	sea salt (acc.)	20	$0.132 \cdot 10^{-1}$
	sea salt (coa.)	$3.2 \cdot 10^{-3}$	$0.211 \cdot 10^{-5}$
Maritime polluted	water-soluble	3800	0.422
	sea salt (acc.)	20	$0.222 \cdot 10^{-2}$
	sea salt (coa.)	$3.2 \cdot 10^{-3}$	$0.356 \cdot 10^{-6}$
	soot	5180	0.576
Maritime tropical	water-soluble	590	0.983
	sea salt (acc.)	10	$0.167 \cdot 10^{-1}$
	sea salt (coa.)	$1.3 \cdot 10^{-3}$	$0.217 \cdot 10^{-5}$
Arctic	water-soluble	1300	0.197
	insoluble	0.01	$0.152 \cdot 10^{-5}$
	sea salt (acc.)	1.9	$0.288 \cdot 10^{-3}$
	soot	5300	0.803
Antarctic	sulfate	42.9	0.998
	sea salt (acc.)	$0.47 \cdot 10^{-1}$	$0.109 \cdot 10^{-2}$
	mineral (trans.)	$0.53 \cdot 10^{-2}$	$0.123 \cdot 10^{-3}$

middle value of  $D$  between the individual mode diameters of two neighboring components, and  $N_{\text{tot}}$  is the total number concentration. For a mixture of *water-soluble* and *sea salt (acc. mode)* components for example, the size distribution would be integrated from 0 to 187.8 nm to calculate the apparent number concentration of the *water-soluble* component and from 187.8 nm to the end of the measured distribution for the number concentration of the *sea salt (acc. mode)* component (see Tab. 6.2 for the mode diameters of the two components). For CAB, the mixture was composed taking the *soot*, the *water-soluble*, and the two *sea salt* components. For NYA, the *water-soluble* and the two *sea salt* components were chosen, while for JFJ only the *water-soluble* and the *mineral-transported* components

were taken for the calculation of  $f(\text{RH})$ .

Figure 6.4 shows example humidograms recorded at the three sites (gray points) compared to the OPAC example aerosol types, which would have been expected to be observed at the specific site. The individually mixed OPAC result is shown (called *OPAC mix* in Fig. 6.4) for time periods when corresponding size distribution measurements were available. For the same periods, the result of the Mie model calculations has been added (magenta line in Fig. 6.4), which used the measured (or for NYA retrieved)  $\kappa$ -value and the measured size distribution as input. The  $\kappa$ -equation is based on the work of Petters and Kreidenweis (2007) and represents a one-parameter approximation to describe the RH dependence of the hygroscopic growth factor  $g(\text{RH})$ :

$$g(\text{RH}) = \frac{D(\text{RH})}{D_{\text{dry}}} = \left( 1 + \kappa \frac{\text{RH}/100\%}{1 - \text{RH}/100\%} \right)^{\frac{1}{3}}, \quad (6.3)$$

where  $D(\text{RH})$  is the particle diameter at a certain RH,  $D_{\text{dry}}$  the dry diameter, and  $\kappa$  the one parameter that describes the magnitude of the hygroscopic growth. More details can be found in Sect. 2.1.

In general, Fig. 6.4 reveals that the calculated values using the OPAC input data, which are only given for eight discrete RH values, are clearly higher than the measured values of  $f(\text{RH})$  for all three sites, except for the Saharan dust event at JFJ, which is well described by OPAC (see Fig. 6.4i). OPAC is not capable to describe hysteresis effects like observed for clean maritime air (see Fig. 6.4a and Fig. 6.4g) and only refers to the liquid state (same as for the  $\kappa$ -equation).

The shape also significantly differs from the measurements, especially for low and medium values of RH. Taking the measured number size distribution and re-mixed OPAC components does not improve the agreement significantly, except for the CAB maritime slightly polluted case (Fig. 6.4d). The calculated  $f(\text{RH})$  curve using the measured (or retrieved)  $\kappa$ -value seems to perform well, indicating that the  $\kappa$ -equation (Eq. 6.3) is suitable to describe the curvature of  $f(\text{RH})$  in combination with Mie calculations.

The overestimation by OPAC is most probably caused by:

- (a) the fixed size distribution modes
- (b) the implemented hygroscopic growth
- (c) the used refractive index

of the individual components. The influence of the refractive index can not be checked due to missing chemical composition measurements, while the influence of the implemented size distributions and the hygroscopic growth can be tested against the measurements where available (see below).

The mode diameters  $D_{\text{modN}}$  of the OPAC components are given in Tab. 6.2. The *water-soluble* and *soot* components are the two main components to describe the fine mode in OPAC besides the *sea salt (acc. mode)*. The OPAC aerosol type surface size distributions are compared to the measured ones in Fig. 6.5a-f. The number size distributions have been transferred to (normalized) surface size distributions, since they are a better representation for the optically relevant size ranges. For the proposed aerosol type examples, the surface size distributions are mainly shifted to smaller diameters and are

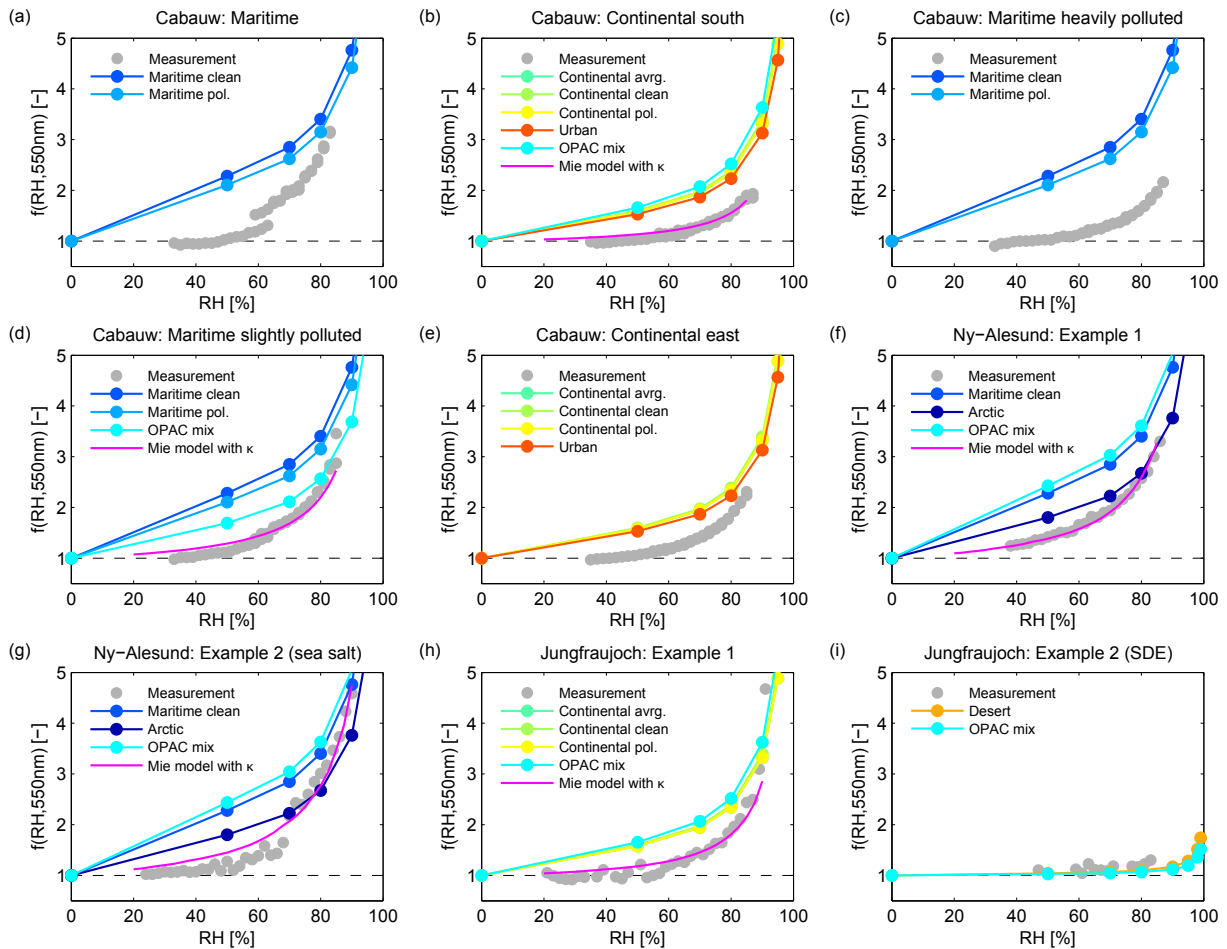


Figure 6.4: Example humidograms from the three investigated sites (gray bullets) compared to OPAC aerosol examples given in Hess et al. (1998) (colored bullet lines). Panel (a) - (e): Averaged humidograms measured at Cabauw; Panel (f) - (g): Two typical humidograms measured at Ny-Ålesund; Panel (h) - (i): Averaged humidograms measured at Jungfraujoch (SDE: Saharan dust event). The cyan bullets (OPAC mix) denote the OPAC result if the individual OPAC components are weighted with the measured size distribution. The magenta line shows the calculated humidogram using the measured size distribution, the (partially) measured chemical composition, the hygroscopicity parameter  $\kappa$  and applying Mie calculations if the measurements were available (see text for details).

also characterized by larger mode widths compared to the measured distributions. The concentration (or particle surface) is as well different to the measurements. Mixing the components according to the measured number size distribution (using Eq. 6.2, as described above) does not improve the comparison, since the fixed distribution modes and widths make an accurate mixing difficult (see magenta line in Fig. 6.5a-f).

The hygroscopic growth factor  $g(\text{RH})$  in OPAC is based on the work of Hänel and Zank (1979) and is shown in Fig. 6.6 for the four RH-dependent OPAC components. In addition, Fig. 6.6 shows the  $g(\text{RH})$  calculated using the  $\kappa$ -equation (see Eq. 6.3). For the *sea salt* components  $g(\text{RH}=90\%)=2.1$  was taken from Swietlicki et al. (2008) for highly hygroscopic marine aerosol. For the *water-soluble* component a mean value of  $g(\text{RH}=90\%)=1.48$  measured by the H-TDMA during the Cabauw campaign

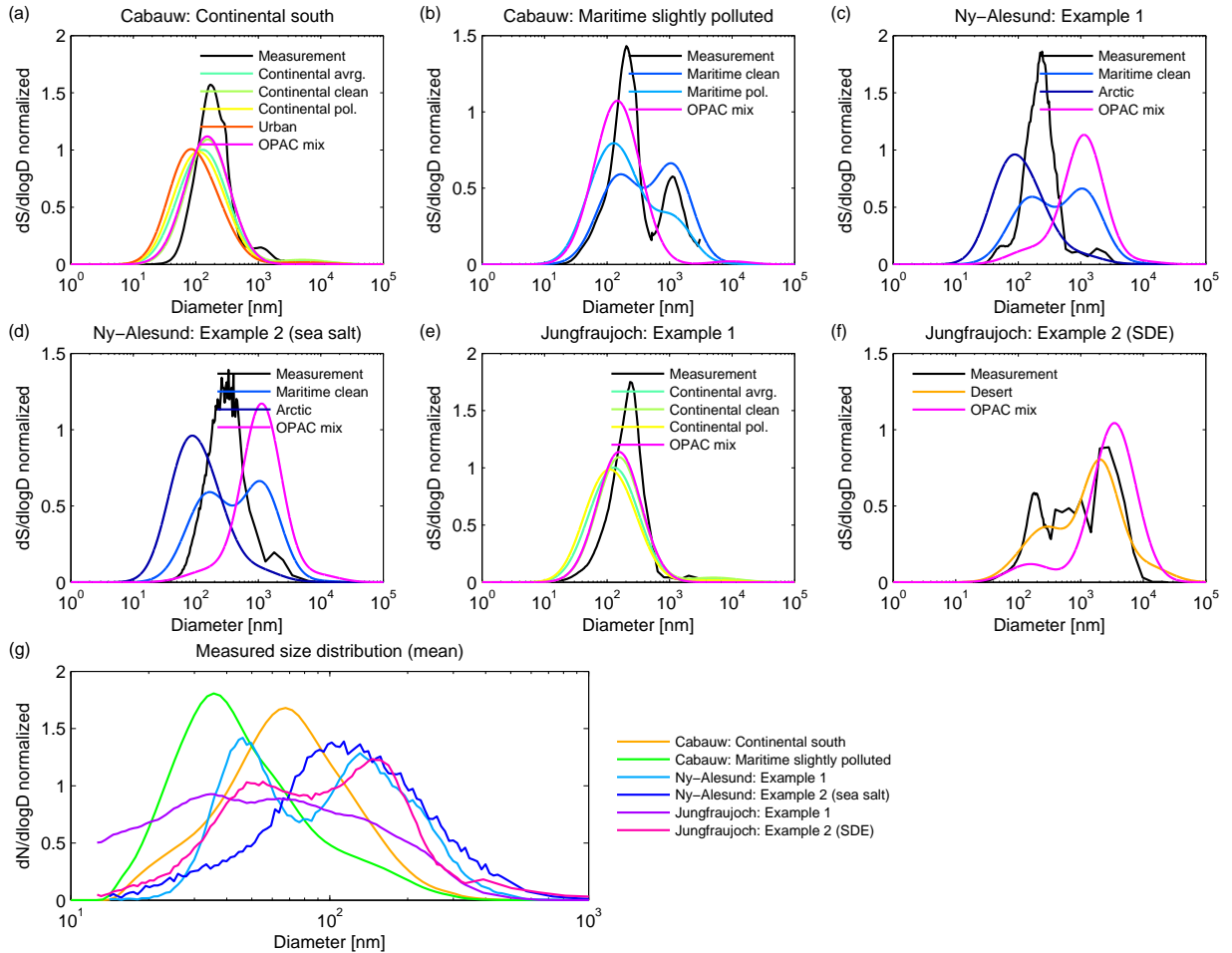


Figure 6.5: Panel (a) - (f): Normalized surface size distributions measured (black line) during the humidogram times as shown in Fig. 6.4, normalized surface size distributions from the OPAC aerosol type examples (colored lines), and the OPAC size distributions if the individual components are weighted with the measured number size distribution (magenta line). Note that the OPAC components have a fixed mode diameter and therefore the OPAC individually mixed size distributions do not match the measured distribution in all cases. Panel (g): Measured mean number size distribution.

was taken, while for the *sulfate droplets*  $g(\text{RH}=90\%) = 2.05$  was taken from Topping et al. (2005). The implemented hygroscopic growth in OPAC is not in correspondence with the course of  $g(\text{RH})$  if the  $\kappa$ -equation is taken into account. Especially for low RH ( $< 80\%$ ) the OPAC values are clearly above the  $\kappa$ -curve, while for higher RH the agreement seems to be better. As shown in the example humidograms (see Fig. 6.4), the  $\kappa$ -equation is a good approximation to describe the hygroscopic growth in terms of  $f(\text{RH})$  at different RH in combination with the measured size distribution, an appropriate refractive index, and Mie theory.

To further investigate the influence of the hygroscopic growth as implemented in OPAC, the hygroscopic growth of the *water-soluble* and *sea salt (acc. and coarse mode)* was modified and tested against measurements. For the modification part, the hygroscopic growth of the *water-soluble* and the *sea salt (acc. and coarse mode)* components was changed. The mean  $g(\text{RH}=90\%)=1.48$  measured during CAB campaign at 165 nm was taken for the *water-soluble* component, and  $g(\text{RH}=90\%)=2.1$  was taken for

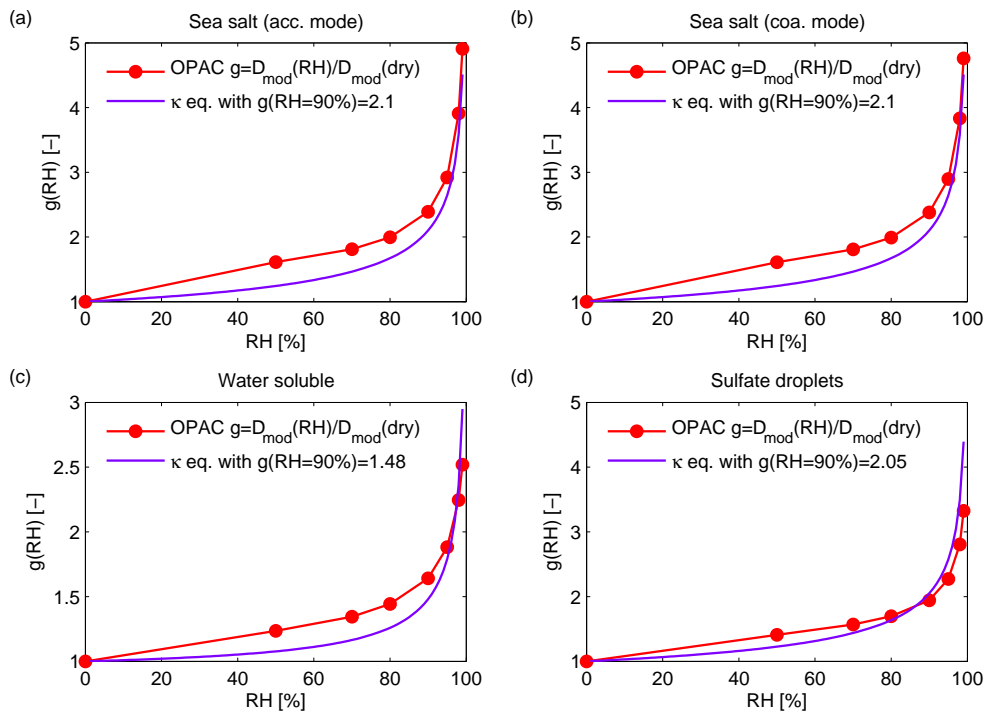


Figure 6.6: Hygroscopic growth factor  $g(\text{RH})$  as implemented for the four hygroscopic OPAC components. Panel (a): Sea salt (accumulation mode), Panel (b): Sea salt (coarse mode), Panel (c): Water-soluble, and Panel (d): Sulfate droplets (used to model Antarctic and stratospheric background aerosol). The mode diameter (red curve) growth factors used for the individual lognormal size distributions are shown. The violet curve denotes the hygroscopic growth factor as calculated using literature values of  $g(\text{RH})$  and the  $\kappa$ -equation (see text for details).

the two *sea salt* components from Swietlicki et al. (2008). Again, the  $\kappa$ -equation was taken to calculate  $g(\text{RH})$  at different RH values (see violet curve in Fig. 6.6a-c for the applied growth factors). The time period of the closure study during the CAB campaign was chosen (4 - 18 July 2009), which is considered to be the most complete time series covering a wide range of different aerosol types, ranging from continental to maritime aerosol types. The number mixing ratios (or number concentrations) of both modes were again calculated using Eq. 6.2. The *soot*, *water-soluble*, and *sea salt (acc. mode and coarse mode)* components were found to be the most dominant components during the CAB period of the closure study.

Taking the original components *soot*, *water-soluble*, and *sea salt (acc. and coarse mode)*, OPAC overestimates  $f(\text{RH})$  especially for the low and medium RH values, as already seen in the example humidograms in Fig. 6.4 and as shown in Fig. 6.7a, where the ratio of calculated to measured value is seen for the above mentioned closure period at CAB. It improves towards higher RH, but the ratio is still above 1 at 90% RH. Modifying the *water-soluble* and *sea salt (acc. and coarse mode)* components leads to an improved agreement between calculated and observed  $f(\text{RH})$  (see Fig. 6.7b). The remaining discrepancy is probably caused by the fixed distribution modes and in general by the simplification of the aerosol at CAB when assuming only four main components.

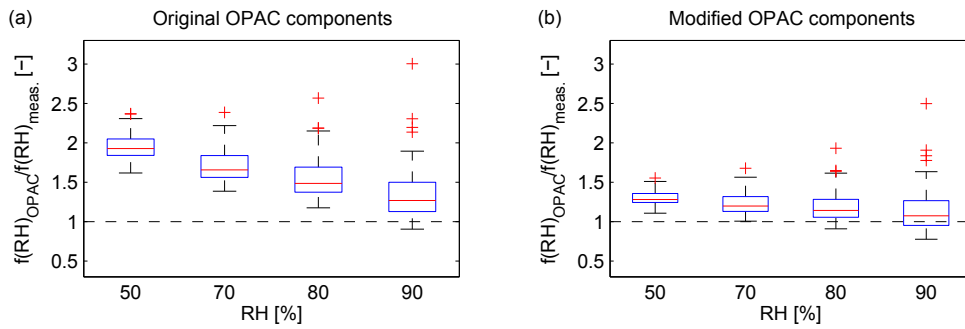


Figure 6.7: Box plots of the ratio of calculated to measured  $f(\text{RH})$  (at 550 nm) for the RH values of 50, 70, 80, and 90% (OPAC values and range of measurements) for Cabauw (4 - 18 July 2009). The central red mark is the median, the edges of the box are the 25th and 75th percentiles, the error bars show the extent to the most extreme data points that are not considered as outliers, while the outliers are plotted individually (red crosses). Panel (a):  $f(\text{RH})$  calculated using the original OPAC components weighted with the measured size distribution. Panel (b):  $f(\text{RH})$  calculated using the modified OPAC components (changed hygroscopic growth) weighted with the measured size distribution.

### 6.3 Conclusions

The effect of hygroscopic growth on aerosol light scattering has been investigated at various European measurement sites using measurements and model calculations. Each site has been chosen to be representative for a certain aerosol type. The increase in variability and complexity in aerosol composition increased from remote sites to urban and continental sites, and therefore the number of known parameters needed to predict of  $f(\text{RH})$  increased concurrently. Free tropospheric aerosol found e.g. at the JFJ can be simply parameterized using the Ångström exponent (Nessler et al., 2005b). This rather simplistic approach can only be made at this site due to that fact that increased coarse mode fractions (low Ångström exponents) at the JFJ will most likely be a proxy for more mineral dust with reduced hygroscopicity and therefore result in a lower  $f(\text{RH})$ . For the other sites, an enlarged coarse mode points to an enlarged sea salt contribution, which in contrast to mineral dust is highly hygroscopic. Therefore, a simple proxy like the Ångström exponent as a proxy for size can not be used alone to predict  $f(\text{RH})$ . Instead, information on the full size distribution is needed. For example, for the Arctic aerosol found in summer and fall in NYA a single hygroscopicity ( $\kappa$ -value) and measured size distribution together with a Mie model were found to be sufficient to calculate the ambient value of the scattering coefficient. The high variability of aerosol composition and size at CAB made a precise prediction of the scattering enhancement difficult. Here, only measurements of the full size distribution and the full chemical composition will make a good prediction of  $f(\text{RH})$  possible, if no explicit humidified nephelometer measurements are available. The knowledge of the RH effect is for example important to perform validation studies for different aerosol measurement techniques. At CAB, for example, the measurements allowed a comprehensive comparison study of ambient extinction coefficient measured in-situ, by MAX-DOAS (multi-axis differential optical absorption spectroscopy) and by LIDAR (light detection and ranging) technique.

## 6.4 Outlook

### Long-term field measurements

The results analyzed and discussed here were based on intensive field campaigns at three European sites. Due to the limitations in time and instrumental set-ups, it would be desirable to perform longer intensive field campaigns, using e.g. a humidified nephelometer and the standard aerosol optical measurements besides a full physical and chemical analysis of the aerosol. Suitable locations should include sites where the variety of aerosol types would be large but also well defined (such that it is possible to use other proxies to differentiate between the encountered aerosol types).

### Aerosol optical closure studies

Within this work, one focus was set on so called *closure studies*. These studies are needed to understand and improve the understanding of the physical principles behind an observation. Often different kinds of techniques can be applied to access a certain quantity. For example, the aerosol extinction coefficient, which may be needed in radiative transfer calculations, can be accessed by different remote sensing techniques (such as MAX-DOAS or LIDAR observations on satellites or aircrafts) and also by in-situ instruments (e.g. with a nephelometer and an aethalometer). As shown for Cabauw (CAB) (Chapt. 5), all instrumentations have their limitations and do not always deliver agreeing results. Inspired by the discrepancies found at CAB, a new field campaign was initiated in summer 2010. Within the CLACE 2010 campaign (Cloud and Aerosol Characterization Experiment) different kinds of in-situ and remote sensing techniques were deployed at the Jungfraujoch (JFJ) and at the Kleine Scheidegg (KLS), which is located about 1500 m below the JFJ station. The aerosol scattering coefficient was again measured dry and at predefined RH conditions with the humidified nephelometer (WetNeph) together with other continuously running aerosol measurements at the JFJ. In addition, a MAX-DOAS retrieved aerosol extinction profiles. At the KLS, a variety of remote sensing instruments were installed (which also helped to overcome the overlap problem as encountered at CAB). A scanning backscatter LIDAR measured the aerosol backscatter signal together with a ceilometer at 355 nm and 1064 nm, respectively. In addition, two sun and aureole spectrometer systems FUBISS-ASA1 and ASA2 (Asseng et al., 2004; Zieger et al., 2007) measured, among other parameters, the aerosol optical depth and the slope of the phase function in the forward scattering region (aureole index) at various wavelengths in the visible and near-infrared spectrum (see Fig. 6.8 for an overview of the set-up). This kind of set-up allows a detailed validation of different kinds of measurement techniques (and are called optical closure study). Especially for the novel MAX-DOAS technique a thorough validation of the aerosol profiles is of eminent importance and will help to improve the quality of aerosol profiling in the future.

### Validation of satellite data

Another important task is the validation of satellite data on aerosol optical properties, like the Ångström exponent or the asymmetry parameter, using ground based in-situ data, which are re-calculated to



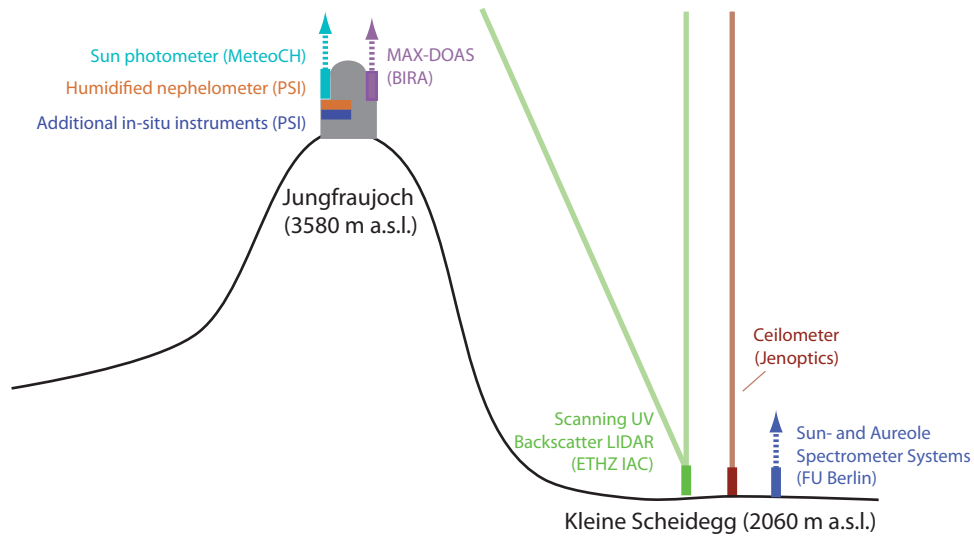


Figure 6.8: Set-up for the optical closure study during the CLACE 2010 campaign at Jungfrauoch and Kleine Scheidegg in the Swiss Alps.

represent ambient conditions. Here, our results will be used (in combination with information on the vertical aerosol profile) for *ground-truthing* of satellite measurements within the aerosol working group of the Climate Change Initiative program (CCI) initiated by the European Space Agency (ESA)<sup>4</sup>. Within this task, first comparisons between the Ångström exponent and the single scattering albedo of in-situ and AERNOET sun photometer measurements (Holben et al., 1998; Dubovik and King, 2000) have been made. The comparison of a columnar measurement to a single-point measurement is of course a difficult task, where certain assumptions, e.g. about the planetary boundary layer height and the mixing state, have to be made. However, first results have clearly revealed the need to correct the dry in-situ measurements for the RH-effect to improve the agreement (S. Kinne, pers. comm., 2011).

### Towards a new OPAC database

As shown for the OPAC database (Optical Properties of Aerosols and Clouds by Hess et al., 1998), the original implementation of the hygroscopic growth and the used size distribution should be revised. This could be done by using new long-term in-situ data sets of the hygroscopic growth or size distribution, e.g. by taking recent long-term H-TDMA (see e.g., Swietlicki et al., 2008, and references therein) or SMPS (Asmi et al., 2011) data recorded within the EUSAAR project (Philippin et al., 2009).

### Improving global circulation models

Besides further measurements, improvements, or validations of measurement techniques, the implementation and validation of the obtained results in aerosol models is needed to better constrain our understanding on the climate impact of aerosol particles (Ghan and Schwartz, 2007). Global circulation models (GCMs) are used to study long-term past and future climate changes. For an analysis of aerosol-climate interactions using a GCM the knowledge of the aerosol size distribution, the chemical

<sup>4</sup>see <http://www.esa-aerosol-cci.org/>

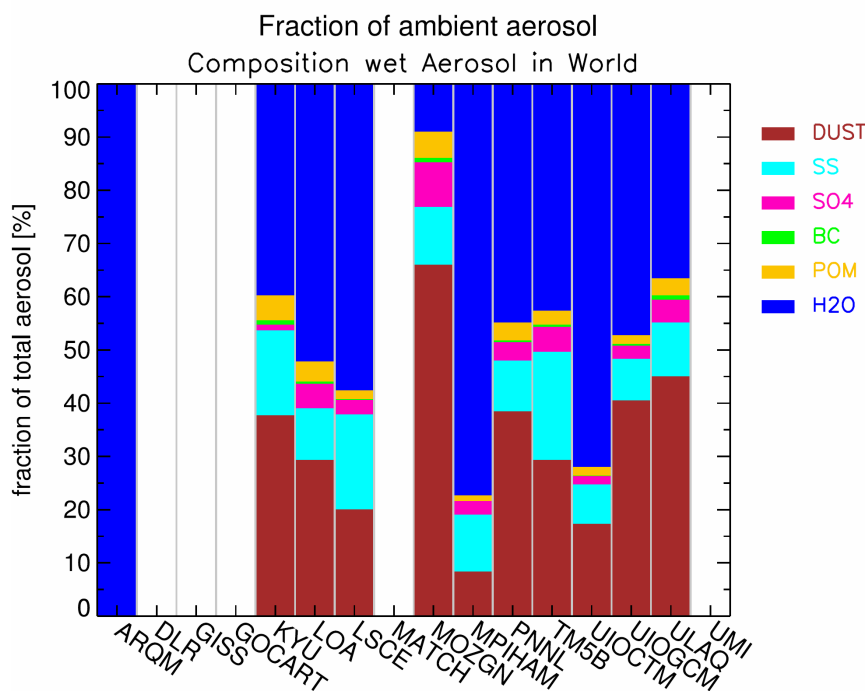


Figure 6.9: Global, annual average composition of ambient aerosol (DUST: mineral dust, SS: sea salt, SO<sub>4</sub>: sulfate, BC: black carbon, POM: particulate organic matter, H<sub>2</sub>O: water) in relation to total ambient aerosol mass as calculated from different global aerosol models. The model abbreviations can be found in Textor et al. (2006), where this figure is taken from.

composition, the mixing state, and various atmospheric processes (including feedback processes) is needed (Stier et al., 2005). Due to the complexity of the microphysics involved, the aerosol modules inside GCMs depend on (often highly simplified) parameterizations of the different aerosol processes. Besides a correct and computationally efficient implementation of the individual aerosol physical and chemical schemes, the global aerosol emissions (Textor et al., 2007) and the meteorological fields determined by the models (Liu et al., 2007) are responsible for differences between global aerosol model simulations (see e.g., Grant et al., 1999; Textor et al., 2006; Kinne et al., 2006, and references therein). The specific parameterization of the water uptake is one contributor (besides many others) that causes uncertainties between different models. Within the comprehensive global aerosol model comparison performed by Textor et al. (2006) the fractional contribution of water to the total aerosol mass as a global average was compared between the participating models. A high scatter of results was found between the different global aerosol models as can be seen in Fig. 6.9 (not all participating models delivered full component specific mass ratios and therefore were excluded in this figure). It has to be clearly stated that the differences are not caused by the hygroscopic growth parameterization alone, it is rather a superposition of different effects like the estimated aerosol composition and the amount (especially of sea salt) or the relative humidity computed by the model. A precise implementation of the hygroscopicity effect will at the end help to improve the estimation of the radiative forcing of aerosol by GCM simulations (Schulz et al., 2006). It is interesting to note that some global aerosol models compared in Textor et al. (2006) used the rather old parameterizations of Hänel (1976) and Hess et al. (1998) (see OPAC comparison above). Recent models have meanwhile started to use the

---

$\kappa$ -parameterization of Petters and Kreidenweis (2007) to describe the hygroscopic growth (O'Donnell et al., 2011, for secondary organic aerosol).

A direct comparison of the findings obtained here is definitely challenging but urgently required. Due to the coarse spatial and temporal resolution of GCMs or even smaller gridded regional climate models, a comparison would have to be established by comparing typical air masses with the average humidograms found for certain aerosol types and would also include a thorough analysis of other microphysical parameters.



# List of abbreviations

AERONET	Aerosol Robotic Network
AMS	Aerosol Mass Spectrometer
AOD	Aerosol Optical Depth
APS	Aerodynamic Particle Sizer
ATN	Attenuation
BC	Black Carbon
BIRA	Belgium Institute for Space Aeronomy
CAB	Cabauw
CAELI	CESAR Water Vapour Aerosol and Cloud Lidar
CCI	Climate Change Initiative
CCN	Cloud Condensation Nuclei
CESAR	Cabauw Experimental Site for Atmospheric Research
CFC	Chlorofluorocarbon
CINDI	Cabauw Intercomparison Campaign of Nitrogen Dioxide measuring Instruments
CLACE	Cloud and Aerosol Characterization Experiment
COSMO	Consortium for Small-scale Modeling
CPS	Condensation Particle Counter
DMA	Differential Mobility Analyzer
DMPS	Differential Mobility Particle Sizer
EARLINET	European Aerosol Research Lidar Network
ESA	European Space Agency
EUCAARI	European Integrated Project on Aerosol Cloud Climate Air Quality Interactions
EUSAAR	European Supersites for Atmospheric Aerosol Research
ETHZ	Swiss Federal Institute of Technology Zurich
FDTD	Finite-Difference Time Domain
FLEXTRA	Flexible Trajectories
FT	Free Troposphere
FUB	Free University Berlin
FUBISS-ASA	Free University Berlin Integrated Spectrographic System Aureole and Sun Adapter
GAW	Global Atmosphere Watch
GCM	Global Circulation Models
GEOMON	Global Earth Observation and Monitoring
H-TDMA	Hygroscopicity Tandem Differential Mobility Analyzer

IAC	Institute for Atmospheric and Climate Science
IPCC	Intergovernmental Panel on Climate Change
IUPHD	Institute for Environmental Physics of the University of Heidelberg
JAMSTEC	Japan Agency for Marine-Earth Science and Technology
JFJ	Jungfraujoch
LIDAR	Light Detection And Ranging
LPDM	Lagrangian Particle Dispersion Model
LR	Lidar Ratio
MAAP	Multi-Angle Absorption Photometer
MAX-DOAS	Multi-Axis Differential Absorption Spectroscopy
MPI	Max-Planck-Institute (here: for Chemistry)
NABEL	Swiss National Monitoring Network for Air Pollution
NYA	Ny-Ålesund
OPAC	Optical Properties of Aerosols and Clouds
OPC	Optical Particle Counter
PDF	Probability Density Function
PBL	Planetary Boundary Layer
PSAP	Particle Soot Absorption Photometer
PSI	Paul Scherrer Institut
RH	Relative Humidity
SDE	Saharan Dust Event
SMPS	Scanning Mobility Particle Sizer
TNO	Netherlands Organisation for Applied Scientific Research
VOC	Volatile Organic Compounds
WetNeph	Humidified Nephelometer
WMO	World Meteorological Organization
ZSR	Zdanovskii-Stokes-Robinson

# Bibliography

- Ackermann J., The extinction-to-backscatter ratio of tropospheric aerosol: A numerical study, *Journal of Atmospheric and Oceanic Technology*, 15(4), 1043–1050, 1998.
- Alfarra M., Paulsen D., Gysel M., Garforth A., Dommen J., Prévôt A., Worsnop D., Baltensperger U., and Coe H., A mass spectrometric study of secondary organic aerosols formed from the photooxidation of anthropogenic and biogenic precursors in a reaction chamber, *Atmospheric Chemistry and Physics*, 6(12), 5279–5293, doi:10.5194/acp-6-5279-2006, 2006.
- Anderson T., Covert D., Marshall S., Laucks M., Charlson R., Waggoner A., Ogren J., Caldow R., Holm R., Quant E., Sem G., Wiedensohler A., Ahlquist N., and Bates T., Performance characteristics of a high-sensitivity, three-wavelength, total scatter/backscatter nephelometer, *Journal of Atmospheric and Oceanic Technology*, 13(5), 967–986, 1996.
- Anderson T. and Ogren J., Determining aerosol radiative properties using the TSI 3563 integrating nephelometer, *Aerosol Science and Technology*, 29, 57–69, 1998.
- Andrews E., Sheridan P., Fiebig M., McComiskey A., Ogren J., Arnott P., Covert D., Elleman R., Gasparini R., Collins D., Jonsson H., Schmid B., and Wang J., Comparison of methods for deriving aerosol asymmetry parameter, *Journal of Geophysical Research (Atmospheres)*, 111, D05S04, doi:10.1029/2004JD005734, 2006.
- Ansmann A., Wandinger U., Riebesell M., Weitkamp C., and Michaelis W., Independent measurement of extinction and backscatter profiles in cirrus clouds by using a combined Raman elastic-backscatter lidar, *Applied Optics*, 31(33), 7113–7131, doi:10.1364/AO.31.007113, 1992.
- Apituley A., Wilson K., Potma C., Volten H., and de Graaf M., Performance assessment and application of CAELI – a high-performance Raman lidar for diurnal profiling of water vapour, aerosols and clouds, in *Proceedings of the 8th International Symposium on Tropospheric Profiling, 19–23 Oct. 2009, Delft, the Netherlands*, 2009.
- Asmi A., Wiedensohler A., Laj P., Fjaeraa A., Sellegri K., Birmili W., Weingartner E., Baltensperger U., Zdimal V., Zikova N., Putaud J., Marinoni A., Tunved P., Hansson H., Fiebig M., Kivekäs N., Lihavainen H., Asmi E., Ulevicius V., Aalto P.P., Swietlicki E., Kristensson A., Mihalopoulos N., Kalivitis N., Kalapov I., Kiss G., de Leeuw G., Henzing B., Harrison R., Beddows D., O’Dowd C., Jennings S., Flentje H., Weinhold K., Meinhardt F., Ries L., and Kulmala M., Number size distributions and seasonality of submicron particles in Europe 2008–2009, *Atmospheric Chemistry and Physics*, 11(11), 5505–5538, doi:10.5194/acp-11-5505-2011, 2011.

- Asseng H., Ruhtz T., and Fischer J., Sun and aureole spectrometer for airborne measurements to derive aerosol optical properties, *Applied Optics*, 43(10), 2146–2155, doi:10.1364/AO.43.002146, 2004.
- Baltensperger U., Gäggeler H., Jost D., Emmenegger M., and Nägeli W., Continuous background aerosol monitoring with the epiphaniometer, *Atmospheric Environment. Part A. General Topics*, 25(3-4), 629–634, doi:10.1016/0960-1686(91)90060-K, 1991.
- Baltensperger U., Gäggeler H., Jost D., Lugauer M., Schwikowski M., Weingartner E., and Seibert P., Aerosol climatology at the high-alpine site Jungfraujoch, Switzerland, *Journal of Geophysical Research (Atmospheres)*, 102(D16), 19707–19715, doi:10.1029/97JD00928, 1997.
- Baltensperger U., Schwikowski M., Jost D., Nyeki S., Gäggeler H., and Poulida O., Scavenging of atmospheric constituents in mixed phase clouds at the high-alpine site Jungfraujoch Part I: Basic concept and aerosol scavenging by clouds, *Atmospheric Environment*, 32(23), 3975–3983, 1998.
- Birmili W., Stopfkuchen K., Hermann M., Wiedensohler A., and Heintzenberg J., Particle penetration through a 300 m inlet pipe for sampling atmospheric aerosols from a tall meteorological tower, *Aerosol Science and Technology*, 41(9), 811–817, 2007.
- Bodhaine B., Barrow surface aerosol: 1976-1986, *Atmospheric Environment*, 23(11), 2357–2369, 1989.
- Bohren C. and Huffman D., *Absorption and Scattering of Light by Small Particles*, Wiley-VCH, 2004.
- Bond T. and Bergstrom R., Light absorption by carbonaceous particles: An investigative review, *Aerosol Science and Technology*, 40(1), 27–67, 2006.
- Brimblecombe P., *The Big Smoke: A History of Air Pollution in London Since Medieval Times*, Routledge Kegan & Paul, 1987.
- Canagaratna M., Jayne J., Jimenez J., Allan J., Alfarra M., Zhang Q., Onasch T., Drewnick F., Coe H., Middlebrook A., Delia A., Williams L., Trimborn A., Northway M., DeCarlo P., Kolb C., Davidovits P., and Worsnop D., Chemical and microphysical characterization of ambient aerosols with the aerodyne aerosol mass spectrometer, *Mass Spectrometry Reviews*, 26(2), 185–222, 2007.
- Cantrell C., Technical Note: Review of methods for linear least-squares fitting of data and application to atmospheric chemistry problems, *Atmospheric Chemistry and Physics*, 8(17), 5477–5487, 2008.
- Carrico C., Kus P., Rood M., Quinn P., and Bates T., Mixtures of pollution, dust, sea salt, and volcanic aerosol during ACE-Asia: Radiative properties as a function of relative humidity, *Journal of Geophysical Research (Atmospheres)*, 108(D23), 8650, doi:10.1029/2003JD003405, 2003.
- Carrico C., Rood M., and Ogren J., Aerosol light scattering properties at Cape Grim, Tasmania, during the first Aerosol Characterization Experiment (ACE 1), *Journal of Geophysical Research (Atmospheres)*, 103(D13), 16565–16574, doi:10.1029/98JD00685, 1998.
- Carrico C., Rood M., Ogren J., Neusüß C., Wiedensohler A., and Heintzenberg J., Aerosol optical properties at Sagres, Portugal, during ACE-2, *Tellus B*, 52(2), 694–715, doi:10.1034/j.1600-0889.2000.00049.x, 2000.



- Charlson R., Atmospheric visibility related to aerosol mass concentration: A review, *Environmental Science & Technology*, 3(10), 913–918, doi:10.1021/es60033a002, 1969.
- Charlson R., Langner J., Rodhe H., Leovy C., and Warren S., Perturbation of the northern hemisphere radiative balance by backscattering from anthropogenic sulfate aerosols, *Tellus A*, 43(4), 152–163, 1991.
- Charlson R., Schwartz S., Hales J., Cess R., Coakley Jr J., Hansen J., and Hofmann D., Climate forcing by anthropogenic aerosols, *Science*, 255(5043), 423–430, 1992.
- Chin M., Kahn R., and Schwartz S., *CCSP 2009: Atmospheric Aerosol Properties and Climate Impacts, A Report by the U.S. Climate Change Science Program and the Subcommittee on Global Change Research.*, DIANE Publishing, National Aeronautics and Space Administration, Washington, D.C., USA., 2009.
- Clarke A., Howell S., Quinn P., Bates T., Ogren J., Andrews E., Jefferson A., Massling A., Mayol-Bracero O., Maring H., et al., INDOEX aerosol: A comparison and summary of chemical, microphysical, and optical properties observed from land, ship, and aircraft, *Journal of Geophysical Research (Atmospheres)*, 107, doi:803310.1029/2001JD000572, 2002.
- Clémer K., Van Roozendaal M., Fayt C., Hendrick F., Hermans C., Pinardi G., Spurr R., Wang P., and De Mazière M., Multiple wavelength retrieval of tropospheric aerosol optical properties from MAXDOAS measurements in Beijing, *Atmospheric Measurement Techniques*, 3(4), 863–878, doi: 10.5194/amt-3-863-2010, 2010.
- Collaud Coen M., Weingartner E., Apituley A., Ceburnis D., Fierz-Schmidhauser R., Flentje H., Henning J., Jennings S., Moerman M., Petzold A., Schmid O., and Baltensperger U., Minimizing light absorption measurement artifacts of the Aethalometer: Evaluation of five correction algorithms, *Atmospheric Measurement Techniques*, 3(2), 457–474, doi:10.5194/amt-3-457-2010, 2010.
- Collaud Coen M., Weingartner E., Nyeki S., Cozic J., Henning S., Verheggen B., Gehrig R., and Baltensperger U., Long-term trend analysis of aerosol variables at the high-alpine site Jungfraujoch, *Journal of Geophysical Research (Atmospheres)*, 112, D13213, doi:10.1029/2006JD007995, 2007.
- Collaud Coen M., Weingartner E., Schaub D., Hueglin C., Corrigan C., Henning S., Schwikowski M., and Baltensperger U., Saharan dust events at the Jungfraujoch: Detection by wavelength dependence of the single scattering albedo and first climatology analysis, *Atmospheric Chemistry and Physics*, 4(11/12), 2465–2480, doi:10.5194/acp-4-2465-2004, 2004.
- Cozic J., Verheggen B., Weingartner E., Crosier J., Bower K., Flynn M., Coe H., Henning S., Steinbacher M., Henne S., Collaud Coen M., Petzold A., and Baltensperger U., Chemical composition of free tropospheric aerosol for PM<sub>1</sub> and coarse mode at the high alpine site Jungfraujoch, *Atmospheric Chemistry and Physics*, 8(2), 407–423, 2008.
- Day D. and Malm W., Aerosol light scattering measurements as a function of relative humidity: A comparison between measurements made at three different sites, *Atmospheric Environment*, 35(30), 5169–5176, 2001.

- De Haij M., Baltink H., and Wauben W., *Continuous mixing layer height determination using the LD-40 ceilometer: A feasibility study*, Koninklijk Nederlands Meteorologisch Instituut, PO Box 201, 3730 AE De Bilt, The Netherlands, 2007.
- De Haij M., Wauben W., Klein Baltink H., and Apituley A., Determination of the mixing layer height by a ceilometer, *Proceedings of the 8th International Symposium on Tropospheric Profiling*, 2010.
- DeCarlo P., Kimmel J., Trimborn A., Northway M., Jayne J., Aiken A., Gonin M., Fuhrer K., Horvath T., Docherty K., Worsnop D.R., and Jimenez J., Field-deployable, high-resolution, time-of-flight aerosol mass spectrometer, *Analytical Chemistry*, 78(24), 8281–8289, 2006.
- Deutschmann T. and Wagner T., *TRACY-II Users manual*, 2008.
- Dinar E., Mentel T., and Rudich Y., The density of humic acids and humic like substances (HULIS) from fresh and aged wood burning and pollution aerosol particles, *Atmospheric Chemistry and Physics*, 6(12), 5213–5224, doi:10.5194/acp-6-5213-2006, 2006.
- Dockery D., Pope C., Xu X., Spengler J., Ware J., Fay M., Ferris B., and Speizer F., An association between air pollution and mortality in six US cities, *New England Journal of Medicine*, 329(24), 1753, 1993.
- Dubovik O. and King M., A flexible inversion algorithm for retrieval of aerosol optical properties from Sun and sky radiance measurements, *Journal of Geophysical Research (Atmospheres)*, 105(D16), 20673–20695, 2000.
- Ehn M., Petäjä T., Aufmhoff H., Aalto P., Hämeri K., Arnold F., Laaksonen A., and Kulmala M., Hygroscopic properties of ultrafine aerosol particles in the boreal forest: Diurnal variation, solubility and the influence of sulfuric acid, *Atmospheric Chemistry and Physics*, 7(1), 211–222, doi: 10.5194/acp-7-211-2007, 2007.
- Eleftheriadis K., Vratolis S., and Nyeki S., Aerosol black carbon in the European Arctic: Measurements at Zeppelin station, Ny-Ålesund, Svalbard from 1998–2007, *Geophysical Research Letters*, 36, L02809, doi:10.1029/2008GL035741, 2009.
- EMEP, Manual for sampling and chemical analysis, EMEP/CCC Report 1/95, Last rev. 2006, Technical report, Norwegian Institute for Air Research, Kjeller, Norway, 1995.
- Ferrare R., Melfi S., Whiteman D., Evans K., and Leifer R., Raman lidar measurements of aerosol extinction and backscattering 1. Methods and comparisons, *Journal of Geophysical Research (Atmospheres)*, 103(D16), 19663–19672, doi:10.1029/98JD01646, 1998.
- Fierz R., Enhancement of the light scattering coefficient of atmospheric aerosol particles by water uptake, ETH Diss. Nr. 18784, Eidgenössische Technische Hochschule Zürich, doi:10.3929/ethz-a-006113754, 2010.
- Fierz-Schmidhauser R., Zieger P., Wehrle G., Jefferson A., Ogren J., Baltensperger U., and Weingartner E., Measurement of relative humidity dependent light scattering of aerosols, *Atmospheric Measurement Techniques*, 3(1), 39–50, doi:10.5194/amt-3-39-2010, 2010.

- Fierz-Schmidhauser R., Zieger P., Gysel M., Kammermann L., DeCarlo P., Baltensperger U., and Weingartner E., Measured and predicted aerosol light scattering enhancement factors at the high alpine site Jungfraujoch, *Atmospheric Chemistry and Physics*, 10(5), 2319–2333, doi:10.5194/acp-10-2319-2010, 2010a.
- Fierz-Schmidhauser R., Zieger P., Vaishya A., Monahan C., Bialek J., O’Dowd C.D., Jennings S.G., Baltensperger U., and Weingartner E., Light scattering enhancement factors in the marine boundary layer (Mace Head, Ireland), *Journal of Geophysical Research (Atmospheres)*, 115, D20204, doi:10.1029/2009jd013755, 2010b.
- Fitzgerald J., Hoppel W., and Vietti M., The size and scattering coefficient of urban aerosol particles at Washington, DC as a function of relative humidity, *Journal of Atmospheric Sciences*, 39, 1838–1852, 1982.
- Freudenthaler V., The telecover test: A quality assurance tool for the optical part of a lidar system, *Proceedings ILRC24, Boulder, Colorado*, 2008.
- Frieß U., Clémer K., Irie H., Vlemmix T., Wagner T., Wittrock F., Yilmaz S., Zieger P., and Apituley A., Intercomparison of MAX-DOAS aerosol profile retrieval algorithms during the CINDI campaign, *Atmospheric Measurement Techniques (in preparation)*, 2011.
- Frieß U., Monks P., Remedios J., Rozanov A., Sinreich R., Wagner T., and Platt U., MAX-DOAS O<sub>4</sub> measurements: A new technique to derive information on atmospheric aerosols: 2. Modeling studies, *Journal of Geophysical Research (Atmospheres)*, 111, D14203, doi:10.1029/2005JD006618, 2006.
- Gasso S., Hegg D., Covert D., Collins D., Noone K., Öström E., Schmid B., Russell P., Livingston J., Durkee P., and Jonsson H., Influence of humidity on the aerosol scattering coefficient and its effect on the upwelling radiance during ACE-2, *Tellus B*, 52(2), 546–567, 2000.
- Ghan S. and Schwartz S., Aerosol properties and processes, *Bulletin of the American Meteorological Society*, 88, 1059–1083, 2007.
- Gong S., A parameterization of sea-salt aerosol source function for sub-and super-micron particles, *Global Biogeochemical Cycles*, 17(4), 1097, doi:10.1029/2003GB002079, 2003.
- Gosse S., Wang M., Labrie D., and Chylek P., Imaginary part of the refractive index of sulfates and nitrates in the 0.7–2.6- $\mu\text{m}$  spectral region, *Applied Optics*, 36(16), 3622–3634, 1997.
- Grant K., Chuang C., Grossman A., and Penner J., Modeling the spectral optical properties of ammonium sulfate and biomass burning aerosols: Parameterization of relative humidity effects and model results, *Atmospheric Environment*, 33(17), 2603–2620, 1999.
- Gysel M., McFiggans G., and Coe H., Inversion of tandem differential mobility analyser (TDMA) measurements, *Journal of Aerosol Science*, 40(2), 134–151, doi:10.1016/j.jaerosci.2008.07.013, 2009.
- Hale G. and Query M., Optical constants of water in the 200-nm to 200- $\mu\text{m}$  wavelength region, *Applied Optics*, 12(3), 555–563, doi:10.1364/AO.12.000555, 1973.

- Hänel G., The properties of atmospheric aerosol particles as functions of the relative humidity at thermodynamic equilibrium with the surrounding moist air, *Advances in Geophysics*, 19(1), 73–188, 1976.
- Hänel G. and Zank B., Aerosol size and relative humidity: Water uptake by mixtures of salts, *Tellus*, 31(6), 478–486, doi:10.1111/j.2153-3490.1979.tb00929.x, 1979.
- Haywood J. and Shine K., The effect of anthropogenic sulfate and soot aerosol on the clear sky planetary radiation budget, *Geophysical Research Letters*, 22(5), 603–606, doi:10.1029/95GL00075, 1995.
- Haywood J. and Shine K., Multi-spectral calculations of the direct radiative forcing of tropospheric sulphate and soot aerosols using a column model, *Quarterly Journal of the Royal Meteorological Society*, 123(543), 1907–1930, 1997.
- Heckel A., Richter A., Tarsu T., Wittrock F., Hak C., Pundt I., Junkermann W., and Burrows J., MAX-DOAS measurements of formaldehyde in the Po-Valley, *Atmospheric Chemistry and Physics*, 5(4), 909–918, doi:10.5194/acp-5-909-2005, 2005.
- Heintzenberg J., Raes F., and Schwartz S., *Atmospheric Chemistry in a Changing World: An Integration and Synthesis of a Decade of Tropospheric Chemistry Research: The International Global Atmospheric Chemistry Project of the International Geosphere-Biosphere Programme, Chapter 4: Tropospheric Aerosols*, Springer Verlag, 2003.
- Henne S., Brunner D., Folini D., Solberg S., Klausen J., and Buchmann B., Assessment of parameters describing representativeness of air quality in-situ measurement sites, *Atmospheric Chemistry and Physics*, 10(8), 3561–3581, doi:10.5194/acp-10-3561-2010, 2010.
- Hess M., Koepke P., and Schult I., Optical properties of aerosols and clouds: The software package OPAC, *Bulletin of the American Meteorological Society*, 79(5), 831–844, 1998.
- Holben B., Eck T., Slutsker I., Tanre D., Buis J., Setzer A., Vermote E., Reagan J., Kaufman Y., Nakajima T., Lavenu F., Jankowiak I., and Smirnov A., AERONET - A federated instrument network and data archive for aerosol characterization, *Remote Sensing of Environment*, 66, 1–6, 1998.
- Hönninger G. and Platt U., Observations of BrO and its vertical distribution during surface ozone depletion at Alert, *Atmospheric Environment*, 36(15-16), 2481–2489, 2002.
- Hönninger G., von Friedeburg C., and Platt U., Multi axis differential optical absorption spectroscopy (MAX-DOAS), *Atmospheric Chemistry and Physics*, 4(1), 231–254, doi:10.5194/acp-4-231-2004, 2004.
- Hummel J. and Reck R., A global surface albedo model, *Journal of Applied Meteorology*, 18(3), 239–253, 1979.
- IPCC, *Climate Change 2007: The Physical Science Basis. Contribution of Working Group I to the Fourth Assessment Report of the Intergovernmental Panel on Climate Change*, Cambridge University Press, 2007.

- Irie H., Kanaya Y., Akimoto H., Iwabuchi H., Shimizu A., and Aoki K., First retrieval of tropospheric aerosol profiles using MAX-DOAS and comparison with lidar and sky radiometer measurements, *Atmospheric Chemistry and Physics*, 8(2), 341–350, doi:10.5194/acp-8-341-2008, 2008.
- Irie H., Kanaya Y., Akimoto H., Iwabuchi H., Shimizu A., and Aoki K., Dual-wavelength aerosol vertical profile measurements by MAX-DOAS at Tsukuba, Japan, *Atmospheric Chemistry and Physics*, 9(8), 2741–2749, doi:10.5194/acp-9-2741-2009, 2009.
- Iwabuchi H., Efficient Monte Carlo methods for radiative transfer modeling, *Journal of the Atmospheric Sciences*, 63(9), 2324–2339, 2006.
- Jurányi Z., Gysel M., Weingartner E., DeCarlo P., Kammermann L., and Baltensperger U., Measured and modelled cloud condensation nuclei number concentration at the high alpine site Jungfraujoch, *Atmospheric Chemistry and Physics*, 10(16), 7891–7906, doi:10.5194/acp-10-7891-2010, 2010.
- Kasten F., Visibility forecast in the phase of pre-condensation, *Tellus*, 21(5), 631–635, 1969.
- Kim J., Yoon S., Jefferson A., and Kim S., Aerosol hygroscopic properties during Asian dust, pollution, and biomass burning episodes at Gosan, Korea in April 2001, *Atmospheric Environment*, 40(8), 1550–1560, 2006.
- Kinne S., Schulz M., Textor C., Guibert S., Balkanski Y., Bauer S., Berntsen T., Berglen T., Boucher O., Chin M., Collins W., Dentener F., Diehl T., Easter R., Feichter J., Fillmore D., Ghan S., Ginoux P., Gong S., Grini A., Hendricks J., Herzog M., Horowitz L., Isaksen I., Iversen T., Kirkevåg A., Kloster S., Koch D., Kristjansson J.E., Krol M., Lauer A., Lamarque J.F., Lesins G., Liu X., Lohmann U., Montanaro V., Myhre G., Penner J., Pitari G., Reddy S., Seland Ø., Stier P., Takemura T., and Tie X., An AeroCom initial assessment - optical properties in aerosol component modules of global models, *Atmospheric Chemistry and Physics*, 6(7), 1815–1834, doi:10.5194/acp-6-1815-2006, 2006.
- Köhler H., The nucleus in and the growth of hygroscopic droplets, *Transactions of the Faraday Society*, 32, 1152–1161, 1936.
- Koloutsou-Vakakis S., Carrico C., Kus P., Rood M., Li Z., Shrestha R., Ogren J., Chow J., and Watson J., Aerosol properties at a midlatitude Northern Hemisphere continental site, *Journal of Geophysical Research (Atmospheres)*, 106(D3), 3019–3032, doi:10.1029/2000JD900126, 2001.
- Kotchenruther R. and Hobbs P., Humidification factors of aerosols from biomass burning in Brazil, *Journal of Geophysical Research (Atmospheres)*, 103(D24), 32081–32089, doi:10.1029/98JD00340, 1998.
- Laden F., Schwartz J., Speizer F., and Dockery D., Reduction in fine particulate air pollution and mortality: Extended follow-up of the Harvard Six Cities study, *American Journal of Respiratory and Critical Care Medicine*, 173, 667–672, 2006.
- Leser H., Hönninger G., and Platt U., MAX-DOAS measurements of BrO and NO<sub>2</sub> in the marine boundary layer, *Geophysical Research Letters*, 30(10), 1537, doi:10.1029/2002GL015811, 2003.
- Li J., Wong J., Dobbie J., and Chylek P., Parameterization of the optical properties of sulfate aerosols, *Journal of the Atmospheric Sciences*, 58(2), 193–209, 2001.

- Li X., Brauers T., Shao M., Garland R.M., Wagner T., Deutschmann T., and Wahner A., MAX-DOAS measurements in southern China: Retrieval of aerosol extinctions and validation using ground-based in-situ data, *Atmospheric Chemistry and Physics*, 10(5), 2079–2089, doi:10.5194/acp-10-2079-2010, 2010.
- Li-Jones X., Maring H., and Prospero J., Effect of relative humidity on light scattering by mineral dust aerosol as measured in the marine boundary layer over the tropical Atlantic Ocean, *Journal of Geophysical Research (Atmospheres)*, 103(D23), 31113–31121, doi:10.1029/98JD01800, 1998.
- Lide D., *Handbook of Chemistry and Physics*, CRC Press/Taylor and Francis, Boca Raon, FL, 89th edition, 2009.
- Liou K., *An Introduction to Atmospheric Radiation - Second Edition*, volume 84 of *International Geophysics Series*, Academic Press, 2002.
- Liu B., Pui D., Whitby K., Kittelson D., Kousaka Y., and McKenzie R., Aerosol mobility chromatograph – new detector for sulfuric-acid aerosols, *Atmospheric Environment*, 12(1-3), 99–104, 1978.
- Liu X., Penner J., Das B., Bergmann D., Rodriguez J., Strahan S., Wang M., and Feng Y., Uncertainties in global aerosol simulations: Assessment using three meteorological data sets, *Journal of Geophysical Research*, 112(D11), D11212, doi:10.1029/2006JD008216, 2007.
- Lohmann U. and Feichter J., Global indirect aerosol effects: A review, *Atmospheric Chemistry and Physics*, 5(3), 715–737, doi:10.5194/acp-5-715-2005, 2005.
- Lugauer M., Baltensperger U., Furger M., Gäggeler H., Jost D., Schwikowski M., and Wanner H., Aerosol transport to the high Alpine sites Jungfrauoch (3454 m asl) and Colle Gnifetti (4452 m asl), *Tellus B*, 50(1), 76–92, 1998.
- Malm W., Sisler J., Huffman D., Eldred R., and Cahill T., Spatial and seasonal trends in particle concentration and optical extinction in the United States, *Journal of Geophysical Research (Atmospheres)*, 99(D1), 1347–1370, doi:10.1029/93JD02916, 1994.
- Marshall S., Covert D., and Charlson R., Relationship between asymmetry parameter and hemispheric backscatter ratio: Implications for climate forcing by aerosols, *Applied Optics*, 34(27), 6306–6311, 1995.
- Mie G., Beiträge zur Optik trüber Medien, speziell kolloidalen Metallösungen, *Annalen der Physik*, 25(3), 377–445, 1908.
- Ming Y. and Russell L., Predicted hygroscopic growth of sea salt aerosol, *Journal of Geophysical Research (Atmospheres)*, 106, 28259–28274, doi:10.1029/2001JD000454, 2001.
- Mishchenko M., Hovenier J., and Travis L., *Light Scattering by Nonspherical Particles: Theory, Measurements, and Applications*, Academic Press, 2000.
- Morgan W., Allan J., Bower K., Esselborn M., Harris B., Henzing J., Highwood E.J., Kiendler-Scharr A., McMeeking G., Mensah A., Northway M., Osborne S., Williams P. and Krejci R., and Coe H., Enhancement of the aerosol direct radiative effect by semi-volatile aerosol components: Airborne

- measurements in North-Western Europe, *Atmospheric Chemistry and Physics*, 10(17), 8151–8171, doi:10.5194/acp-10-8151-2010, 2010.
- Müller D., Ansmann A., Mattis I., Tesche M., Wandinger U., Althausen D., and Pisani G., Aerosol-type-dependent lidar ratios observed with Raman lidar, *Journal of Geophysical Research (Atmospheres)*, 112(D16), D16202, doi:10.1029/2006JD008292, 2007.
- Müller T., Henzing J., de Leeuw G., Wiedensohler A., Alastuey A., Angelov H., Bizjak M., Collaud Coen M., Engström J., Gruening C., Hillamo R., Hoffer A., Imre K., Ivanow P., Jennings G., Sun J.Y., Kalivitis N., Karlsson H., Komppula M., Laj P., Li S.M., Lunder C., Marinoni A., Martins dos Santos S., Mörner M., Nowak A., Ogren J., Petzold A., Pichon J., Rodriguez S., Sharma S., Sheridan P., Teinilä K., Tuch T., Viana M., Virkkula A., Weingartner E., Wilhelm R., and Wang Y., Characterization and intercomparison of aerosol absorption photometers: Result of two intercomparison workshops, *Atmospheric Measurement Techniques*, 4(2), 245–268, doi:10.5194/amt-4-245-2011, 2011.
- Nakajima T., Tanaka M., and Yamauchi T., Retrieval of the optical properties of aerosols from aureole and extinction data, *Applied Optics*, 22, 2951–2959, 1983.
- Nessler R., Weingartner E., and Baltensperger U., Adaptation of dry nephelometer measurements to ambient conditions at the Jungfraujoch, *Environmental Science and Technology*, 39(7), 2219–2228, doi:10.1021/es035450g, 2005a.
- Nessler R., Weingartner E., and Baltensperger U., Effect of humidity on aerosol light absorption and its implications for extinction and the single scattering albedo illustrated for a site in the lower free troposphere, *Journal of Aerosol Science*, 36, 958–972, doi:10.1016/j.jaerosci.2004.11.012, 2005b.
- Nyeki S., Li F., Weingartner E., Streit N., Colbeck I., Gäggeler H., and Baltensperger U., The background aerosol size distribution in the free troposphere: An analysis of the annual cycle at a high-alpine site, *Journal of Geophysical Research (Atmospheres)*, 103(D24), 31749–31761, doi:10.1029/1998JD200029, 1998.
- O'Donnell D., Tsigaridis K., and Feichter J., Estimating the influence of the secondary organic aerosols on present climate using ECHAM5-HAM, *Atmospheric Chemistry and Physics Discussions*, 11(1), 2407–2472, doi:10.5194/acpd-11-2407-2011, 2011.
- Palmer K. and Williams D., Optical constants of sulfuric acid; application to the clouds of Venus?, *Applied Optics*, 14(1), 208–219, 1975.
- Petters M. and Kreidenweis S., A single parameter representation of hygroscopic growth and cloud condensation nucleus activity, *Atmospheric Chemistry and Physics*, 7(8), 1961–1971, doi:10.5194/acp-7-1961-2007, 2007.
- Petzold A. and Schönlinner M., Multi-angle absorption photometry—a new method for the measurement of aerosol light absorption and atmospheric black carbon, *Journal of Aerosol Science*, 35(4), 421–441, 2004.

- Philippin S., Laj P., Putaud J., Wiedensohler A., Leeuw G., Fjaeraa A., Platt U., Baltensperger U., and Fiebig M., EUSAAR - An unprecedented network of aerosol observation in Europe, *Eurozoru Kenkyu*, 24(2), 78–83, 2009.
- Piters A., Hains J., Boersma F., Kroon M., Wittrock F., and van Roozendaal M., The Cabauw Inter-comparison campaign for Nitrogen Dioxide Measuring Instruments (CINDI), June/July 2009, The Netherlands, *Atmospheric Measurement Techniques (in preparation)*, 2011.
- Platt U. and Stutz J., *Differential Optical Absorption Spectroscopy: Principles and Applications*, Springer Verlag, 2008.
- Pope III C., Burnett R., Thun M., Calle E., Krewski D., Ito K., and Thurston G., Lung cancer, cardiopulmonary mortality, and long-term exposure to fine particulate air pollution, *Journal of the American Medical Association*, 287(9), 1132–1141, 2002.
- Pope III C. and Dockery D., Health effects of fine particulate air pollution: Lines that connect, *Journal of the Air & Waste Management Association*, 56(6), 709–742, 2006.
- Pruppacher H. and Klett J., *Microphysics of Clouds and Precipitation*, Springer, 2010.
- Quinn P., Miller T., Bates T., Ogren J., Andrews E., and Shaw G., A 3-year record of simultaneously measured aerosol chemical and optical properties at Barrow, Alaska, *Journal of Geophysical Research (Atmospheres)*, 107(D11), 4130, doi:10.1029/2001JD001248, 2002.
- Ramanathan V., Crutzen P., Kiehl J., and Rosenfeld D., Aerosols, climate and the hydrological cycle, *Science*, 294, 2119–2124, 2001.
- Ramaswamy V., Boucher O., Haigh J., Hauglustaine D., and Haywood J., *Radiative Forcing of Climate Change*, Cambridge University Press, Cambridge, United Kingdom and New York, NY, USA, 2001.
- Randles C., Russell L., and Ramaswamy V., Hygroscopic and optical properties of organic sea salt aerosol and consequences for climate forcing, *Geophysical Research Letters*, 31, L16108, doi:10.1029/2004GL020628, 2004.
- Remer L., Kaufman Y., Tanré D., Mattoo S., Chu D., Martins J., Li R., Ichoku C., Levy R., Kleidman R., Eck T., Vermote E., and Holben B., The MODIS aerosol algorithm, products, and validation, *Journal of the Atmospheric Sciences*, 62(4), 947–973, doi:10.1175/JAS3385.1, 2005.
- Rodgers C., *Inverse Methods for Atmospheric Sounding: Theory and Practice (Series on Atmospheric Oceanic and Planetary Physics)*, volume 30, World Scientific Publishing Company, 2000.
- Roscoe H., Van Roozendaal M., Fayt C., du Piesanie A., Abuhassan N., Adams C., Akrami M., Cede A., Chong J., Clémer K., Friess U., Gil Ojeda M., Goutail F., Graves R., Griesfeller A., Grossmann K., Hemerijckx G., Hendrick F., Herman J., Hermans C., Irie H., Johnston P.V., Kanaya Y., Kreher K., Leigh R., Merlaud A., Mount G., Navarro M., Oetjen H., Pazmino A., Perez-Camacho M., Peters E., Pinardi G., Puenteadura O., Richter A., Schönhardt A., Shaiganfar R., Spinei E., Strong K., Takashima H., Vlemmix T., Vrekoussis M., Wagner T., Wittrock F., Yela M., Yilmaz S., Boersma F., Hains J., Kroon



- M., Pipers A., and Kim Y., Intercomparison of slant column measurements of NO<sub>2</sub> and O<sub>4</sub> by MAX-DOAS and zenith-sky UV and visible spectrometers, *Atmospheric Measurement Techniques*, 3(6), 1629–1646, doi:10.5194/amt-3-1629-2010, 2010.
- Rozanov A., Rozanov V., and Burrows J., A numerical radiative transfer model for a spherical planetary atmosphere: Combined differential-integral approach involving the Picard iterative approximation, *Journal of Quantitative Spectroscopy and Radiative Transfer*, 69(4), 491–512, 2001.
- Russchenberg H., Bosveld F., Swart D., ten Brink H., de Leeuw G., Uijlenhoet R., Arbesser-Rastburg B., van der Marel H., Ligthart L., Boers R., and Apituley A., Ground-based atmospheric remote sensing in The Netherlands: European outlook, *IEICE Transactions on Communications*, 88(6), 2252–2258, doi:10.1093/ietcom/e88-b.6.2252, 2005.
- Salemink H., Schotanus P., and Bergwerff J., Quantitative lidar at 532 nm for vertical extinction profiles and the effect of relative humidity, *Applied Physics B: Lasers and Optics*, 34(4), 187–189, 1984.
- Schulz M., Textor C., Kinne S., Balkanski Y., Bauer S., Berntsen T., Berglen T., Boucher O., Dentener F., Guibert S., Isaksen I., Iversen T., Koch D., Kirkevåg A., Liu X., Montanaro V., Myhre G., Penner J., Pitari G., Reddy S., Seland Ø., Stier P., and Takemura T., Radiative forcing by aerosols as derived from the AeroCom present-day and pre-industrial simulations, *Atmospheric Chemistry and Physics*, 6(12), 5225–5246, doi:10.5194/acp-6-5225-2006, 2006.
- Schuster G., Dubovik O., and Holben B., Angstrom exponent and bimodal aerosol size distributions, *Journal of Geophysical Research (Atmospheres)*, 111, D07207, doi:10.1029/2005JD006328, 2006.
- Schwartz S., The Whitehouse Effect—Shortwave radiative forcing of climate by anthropogenic aerosols: An overview, *Journal of Aerosol Science*, 27(3), 359–382, 1996.
- Schwikowski M., Seibert P., Baltensperger U., and Gäggeler H., A study of an outstanding Saharan dust event at the high-alpine site Jungfrauoch, Switzerland, *Atmospheric Environment*, 29(15), 1829–1842, 1995.
- Seinfeld J. and Pandis S., *Atmospheric Chemistry and Physics: From Air Pollution to Climate Change*, John Wiley and Sons, Inc., Hoboken, New Jersey, 2006.
- Sheridan P., Delene D., and Ogren J., Four years of continuous surface aerosol measurements from the Department of Energy's Atmospheric Radiation measurement Program Southern Great Plains Cloud and Radiation Testbed site, *Journal of Geophysical Research (Atmospheres)*, 106(D18), 20735–20747, 2001.
- Sheridan P. and Ogren J., Observations of the vertical and regional variability of aerosol optical properties over central and eastern North America, *Journal of Geophysical Research (Atmospheres)*, 104(D14), 16793–16805, doi:10.1029/1999JD900241, 1999.
- Sinreich R., Frieß U., Wagner T., and Platt U., Multi-axis differential optical absorption spectroscopy (MAX-DOAS) of gas and aerosol distributions, *Faraday Discussions*, 130, 153–164, 2005.

- Sjogren S., Gysel M., Weingartner E., Alfarra M., Duplissy J., Cozic J., Crosier J., Coe H., and Baltensperger U., Hygroscopicity of the submicrometer aerosol at the high-alpine site Jungfraujoch, 3580 m a.s.l., Switzerland, *Atmospheric Chemistry and Physics*, 8(18), 5715–5729, doi:10.5194/acp-8-5715-2008, 2008.
- Sjogren S., Gysel M., Weingartner E., Baltensperger U., Cubison M., Coe H., Zardini A., Marcolli C., Krieger U., and Peter T., Hygroscopic growth and water uptake kinetics of two-phase aerosol particles consisting of ammonium sulfate, adipic and humic acid mixtures, *Journal of Aerosol Science*, 38(2), 157–171, 2007.
- Spurr R., LIDORT and VLIDORT: Linearized pseudo-spherical scalar and vector discrete ordinate radiative transfer models for use in remote sensing retrieval problems, *Light Scattering Reviews* 3, pages 229–275, 2008.
- Stier P., Feichter J., Kinne S., Kloster S., Vignati E., Wilson J., Ganzeveld L., Tegen I., Werner M., Balkanski Y., Schulz M., Boucher O., Minikin A., and Petzold A., The aerosol-climate model ECHAM5-HAM, *Atmospheric Chemistry and Physics*, 5(4), 1125–1156, doi:10.5194/acp-5-1125-2005, 2005.
- Stohl A., Forster C., Frank A., Seibert P., and Wotawa G., Technical note: The Lagrangian particle dispersion model FLEXPART version 6.2, *Atmospheric Chemistry and Physics*, 5(9), 2461–2474, doi:10.5194/acp-5-2461-2005, 2005.
- Stohl A. and Seibert P., Accuracy of trajectories as determined from the conservation of meteorological tracers, *Quarterly Journal of the Royal Meteorological Society*, 124(549), 1465–1484, 1998.
- Stohl A., Wotawa G., Seibert P., and Kromp-Kolb H., Interpolation errors in wind fields as a function of spatial and temporal resolution and their impact on different types of kinematic trajectories, *Journal of Applied Meteorology*, 34(10), 2149–2165, 1995.
- Stokes R. and Robinson R., Interactions in aqueous nonelectrolyte solutions. I. Solute-solvent equilibria, *The Journal of Physical Chemistry*, 70(7), 2126–2131, 1966.
- Ström J., Umegård J., Tørseth K., Tunved P., Hansson H., Holmén K., Wismann V., Herber A., and König-Langlo G., One year of particle size distribution and aerosol chemical composition measurements at the Zeppelin Station, Svalbard, March 2000-March 2001, *Physics and Chemistry of the Earth*, 28(28–32), 1181–1190, 2003.
- Sundström A., Nousiainen T., and Petäjä T., On the quantitative low-level aerosol measurements using ceilometer-type lidar, *Journal of Atmospheric and Oceanic Technology*, 26(11), 2340–2352, doi:10.1175/2009JTECHA1252.1, 2009.
- Swietlicki E., Hansson H., Hämeri K., Svenningsson B., Massling A., McFiggans G., McMurry P., Petäjä T., Tunved P., Gysel M., Topping D., Weingartner E., Baltensperger U., Rissler J., Wiedensohler A., and Kulmala M., Hygroscopic properties of submicrometer atmospheric aerosol particles measured with H-TDMA instruments in various environments - a review, *Tellus B*, 60(3), 432–469, 2008.
- Tang I., Chemical and size effects of hygroscopic aerosols on light scattering coefficients, *Journal of Geophysical Research (Atmospheres)*, 101(D14), 19245–19250, doi:10.1029/96JD03003, 1996.

- Textor C., Schulz M., Guibert S., Kinne S., Balkanski Y., Bauer S., Berntsen T., Berglen T., Boucher O., Chin M., Dentener F., Diehl T., Easter R., Feichter H., Fillmore D., Ghan S., Ginoux P., Gong S., Grini A., Hendricks J., Horowitz L., Huang P., Isaksen I., Iversen I., Kloster S., Koch D., Kirkevåg A., Kristjansson J.E., Krol M., Lauer A., Lamarque J., Liu X., Montanaro V., Myhre G., Penner J., Pitari G., Reddy S., Seland Ø., Stier P., Takemura T., and Tie X., Analysis and quantification of the diversities of aerosol life cycles within AeroCom, *Atmospheric Chemistry and Physics*, 6(7), 1777–1813, doi: 10.5194/acp-6-1777-2006, 2006.
- Textor C., Schulz M., Guibert S., Kinne S., Balkanski Y., Bauer S., Berntsen T., Berglen T., Boucher O., Chin M., Dentener F., Diehl T., Feichter J., Fillmore D., Ginoux P., Gong S., Grini A., Hendricks J., Horowitz L., Huang P., Isaksen I., Iversen T., Kloster S., Koch D., Kirkevåg A., Kristjansson J., Krol M., Lauer A., Lamarque J., Liu X., Montanaro V., Myhre G., Penner J.E., Pitari G., Reddy M.S., Seland Ø., Stier P., Takemura T., and Tie X., The effect of harmonized emissions on aerosol properties in global models – an AeroCom experiment, *Atmospheric Chemistry and Physics*, 7(17), 4489–4501, doi:10.5194/acp-7-4489-2007, 2007.
- Toon O., Pollack J., and Khare B., The optical constants of several atmospheric aerosol species: Ammonium sulfate, aluminum oxide, and sodium chloride, *Journal of Geophysical Research (Atmospheres)*, 81(33), 5733–5748, doi:10.1029/JC081i033p05733, 1976.
- Topping D., McFiggans G., and Coe H., A curved multi-component aerosol hygroscopicity model framework: Part 2 – Including organic compounds, *Atmospheric Chemistry and Physics*, 5(5), 1223–1242, doi:10.5194/acp-5-1223-2005, 2005.
- Twomey S., Influence of pollution on shortwave albedo of clouds, *Journal of the Atmospheric Sciences*, 34(7), 1149–1152, 1977.
- Van de Hulst H., *Light Scattering by Small Particles (Structure of Matter Series)*, Dover, New York, 1981.
- Van Roozendaal M., Fayt C., Post P., Hermans C., and Lambert J.C., *Retrieval of BrO and NO<sub>2</sub> from UV-Visible Observations*, Springer-Verlag, 2003.
- Voss K., Welton E., Quinn P., Frouin R., Miller M., and Reynolds R., Aerosol optical depth measurements during the Aerosols99 experiment, *Journal of Geophysical Research (Atmospheres)*, 106(D18), 20821–20831, doi:10.1029/2000JD900783, 2001.
- Wagner T., Beirle S., Brauers T., Deutschmann T., Frieß U., Hak C., Halla J., Heue K., Junkermann W., Li X., Platt U., and Pundt-Gruber I., Inversion of tropospheric profiles of aerosol extinction and HCHO and NO<sub>2</sub> mixing ratios from MAX-DOAS observations in Milano during the summer of 2003 and comparison with independent data sets, *Atmospheric Measurement Techniques Discussions*, 4(3), 3891–3964, doi:10.5194/amtd-4-3891-2011, 2011.
- Wagner T., Deutschmann T., and Platt U., Determination of aerosol properties from MAX-DOAS observations of the Ring effect, *Atmospheric Measurement Techniques*, 2(2), 495–512, doi:10.5194/amt-2-495-2009, 2009.

- Wagner T., Dix B., von Friedeburg C., Frieß U., Sanghavi S., Sinreich R., and Platt U., MAX-DOAS O<sub>4</sub> measurements: A new technique to derive information on atmospheric aerosols: Principles and information content, *Journal of Geophysical Research (Atmospheres)*, 109, D22205, doi: 10.1029/2004JD004904, 2004.
- Wang W., Rood M., Carrico C., Covert D., Quinn P., and Bates T., Aerosol optical properties along the northeast coast of North America during the New England Air Quality Study–Intercontinental Transport and Chemical Transformation 2004 campaign and the influence of aerosol composition, *Journal of Geophysical Research (Atmospheres)*, 112(D10), D10S23, doi:10.1029/2006JD007579, 2007.
- Weingartner E., Burtscher H., and Baltensperger U., Hygroscopic properties of carbon and diesel soot particles, *Atmospheric Environment*, 31(15), 2311–2327, 1997.
- Weingartner E., Gysel M., and Baltensperger U., Hygroscopicity of aerosol particles at low temperatures. 1. New low-temperature H-TDMA instrument: Setup and first applications, *Environmental Science and Technology*, 36(1), 55–62, 2002.
- Weingartner E., Nyeki S., and Baltensperger U., Seasonal and diurnal variation of aerosol size distributions ( $10 < D < 750$  nm) at a high-alpine site (Jungfraujoch 3580 m asl), *Journal of Geophysical Research (Atmospheres)*, 104(D21), 26809–26820, doi:10.1029/1999JD900170, 1999.
- Weingartner E., Saathoff H., Schnaiter M., Streit N., Bitnar B., and Baltensperger U., Absorption of light by soot particles: Determination of the absorption coefficient by means of Aethalometers, *Journal of Aerosol Science*, 34, 1445–1465, 2003.
- Whitby K. and Cantrell B., Fine particles, in *International Conference on Environmental Sensing and Assessment, Las Vegas, NV, Institute of Electrical and Electronic Engineers*, 1976.
- Winklmayr W., Reischl G., Lindner A., and Berner A., A new electromobility spectrometer for the measurement of aerosol size distributions in the size range from 1 to 1000 nm, *Journal of Aerosol Science*, 22(3), 289–296, doi:10.1016/S0021-8502(05)80007-2, 1991.
- Wiscombe W. and Grams G., The backscattered fraction in two-stream approximations, *Journal of the Atmospheric Sciences*, 33(12), 2440–2451, 1976.
- Wittrock F., Oetjen H., Richter A., Fietkau S., Medeke T., Rozanov A., and Burrows J.P., MAX-DOAS measurements of atmospheric trace gases in Ny-Ålesund - Radiative transfer studies and their application, *Atmospheric Chemistry and Physics*, 4(4), 955–966, doi:10.5194/acp-4-955-2004, 2004.
- WMO/GAW, *Aerosol Measurement Procedures Guidelines and Recommendations, Report No. 153*, World Meteorological Organization, Geneva, Switzerland, 2003.
- Yan P., Pan X., Tang J., Zhou X., Zhang R., and Zeng L., Hygroscopic growth of aerosol scattering coefficient: A comparative analysis between urban and suburban sites at winter in Beijing, *Particuology*, 7, 52–60, 2009.
- Yang X., Pyle J., and Cox R., Sea salt aerosol production and bromine release: Role of snow on sea ice, *Geophysical Research Letters*, 35, L16815, doi:10.1029/2008GL034536, 2008.

- York D., Evensen N., Martínez M., and Delgado J., Unified equations for the slope, intercept, and standard errors of the best straight line, *American Journal of Physics*, 72, 367–375, 2004.
- Zieger P., Fierz-Schmidhauser R., Gysel M., Ström J., Henne S., Yttri K., Baltensperger U., and Weingartner E., Effects of relative humidity on aerosol light scattering in the Arctic, *Atmospheric Chemistry and Physics*, 10(8), 3875–3890, doi:10.5194/acp-10-3875-2010, 2010.
- Zieger P., Ruhtz T., Preusker R., and Fischer J., Dual-aureole and sun spectrometer system for airborne measurements of aerosol optical properties, *Applied Optics*, 46(35), 8542–8552, doi:10.1364/AO.46.008542, 2007.
- Zieger P., Weingartner E., Henzing J., Moerman M., de Leeuw G., Mikkilä J., Ehn M., Petäjä T., Clémer K., van Roozendaal M., Yilmaz S., Frieß U., Irie H., Wagner T., Shaiganfar R., Beirle S., Apituley A., Wilson K., and Baltensperger U., Comparison of ambient aerosol extinction coefficients obtained from in-situ, MAX-DOAS and LIDAR measurements at Cabauw, *Atmospheric Chemistry and Physics*, 11(6), 2603–2624, doi:10.5194/acp-11-2603-2011, 2011.



# Acknowledgements

This work would not have been possible without the help and support of many people, to whom I have to express my deepest gratitude.

I would especially like to thank ...

- ... Thomas Peter for being my doctoral father and for all the helpful and good discussions we had.
- ... Ernest Weingartner and Urs Baltensperger for accepting me as their PhD student and for the many thrilling scientific insights they gave me within the last years! I have enjoyed the very professional and productive atmosphere in the Laboratory of Atmospheric Chemistry. The pleasant atmosphere (especially in Ernest's group) regularly confirmed my decision to carry out my PhD work abroad.
- ... Gerrit de Leeuw for agreeing to be my co-examiner and the discussion we had during the GEOmon meetings. I have enjoyed my work within the GEOmon community which helped me from the beginning on to see my work in a broader context.
- ... Rahel, for starting to introduce me to Swiss customs, for the all discussions we had and for being my friendly office-mate.
- ... Nicolas and Martin, for the fruitful discussions we had and for the help you gave me.
- ... all the former and current PhD students at the LAC! Here, I have to especially thank Torsten, Zsofi, Lukas, Francesco, Arnaud, Peter B., Peter M., Julie, Emanuel, Dani, Iakovos, Marie, Kathrin, Jonathan, Axel ... and of course Agi! Without all of you, my PhD time wouldn't stay in such a good memory. Thank you for the numerous trekking and biking trips!
- ... all the other cool PSI'ler whom I've got to know during my last years.
- ... the LAC-backbone: René, Günther, Michel R., Hannes, Michel T., and of course Doris! Without her the LAC wouldn't have run as smoothly as it did.
- ... all my co-authors of the Ny-Ålesund, Cabauw, and Jungfrauoch projects. It was really a pleasure to work together with all of you!
- ... to all my friends and family! Especial thanks to the people from Zürich that I have got to know within the last years. You know who you are and you should know, that I feel fortunate to have met you!





# Curriculum vitae

## Paul Christoph Zieger

**Date of birth:** 29 September 1978

**Place of birth:** Leipzig, Germany

**Citizenship:** German

## Education

2007-2011 Ph.D. student at the Laboratory of Atmospheric Chemistry, Paul Scherrer Institut (PSI), Villigen, Switzerland and the Swiss Federal Institute of Technology (ETH), Zurich, Switzerland

2007 Diploma in Physics (with distinction)

Diploma thesis: *Development of an airborne spectrometer system for the remote sensing of aerosol optical properties*

2000-2006 Freie Universität Berlin, Germany, Study of Physics

2002-2003 Universidad de Granada, Spain, Study of Physics

1991-1998 Georg-Büchner-Oberschule (Grammar school), Berlin, Germany

1992-1993 Madison Junior High School and Naperville Central High School, Naperville, U.S.A.

1986-1991 Annedore-Leber-Grundschule (Elementary school), Berlin, Germany

## Publications

Bukowiecki, N., **Zieger, P.**, Weingartner, E., Jurányi, Z., Gysel, M., Neining, B., Schneider, B., Hueglin, C., Ulrich, A., Wichser, A., Henne, S., Brunner, D., Kaegi, R., Schwikowski, M., Tobler, L., Wienhold, F., Engel, I., Buchmann, B., Peter, T., and Baltensperger, U., Ground-based and airborne in-situ measurements of the Eyjafjallajökull volcanic aerosol plume in Switzerland in spring 2010, *Atmospheric Chemistry and Physics Discussions*, 11, 12949-13002, doi:10.5194/acpd-11-12949-2011, 2011.

**Zieger, P.**, Weingartner, E., Henzing, J., Moerman, M., de Leeuw, G., Mikkilä, J., Ehn, M., Petäjä, T., Clémer, K., van Roozendaal, M., Yilmaz, S., Frieß, U., Irie, H., Wagner, T., Shaiganfar, R., Beirle, S., Apituley, A., Wilson, K., and Baltensperger, U., Comparison of ambient aerosol extinction coefficients obtained from in-situ, MAX-DOAS and LIDAR measurements at Cabauw, *Atmospheric Chemistry and Physics*, 11, 2603-2624, doi:10.5194/acp-11-2603-2011, 2011.

**Zieger, P.**, Fierz-Schmidhauser, R., Gysel, M., Ström, J., Henne, S., Yttri, K.E., Baltensperger, U., and Weingartner, E., Effects of relative humidity on aerosol light scattering in the Arctic, *Atmospheric Chemistry and Physics*, 10, 3875-3890, 2010.

Fierz-Schmidhauser, R., **Zieger, P.**, Gysel, M., Kammermann, L., DeCarlo, P.F., Baltensperger, U., and Weingartner, E., Measured and predicted aerosol light scattering enhancement factors at the high alpine site Jungfraujoch, *Atmospheric Chemistry and Physics*, 10, 2319-2333, 2010.

Fierz-Schmidhauser, R., **Zieger, P.**, Vaishya, A., Monahan, C., Bialek, J., O'Dowd, C.D., Jennings, S.G., Baltensperger, U., and Weingartner, E.: Light scattering enhancement factors in the marine boundary layer (Mace Head, Ireland), *Journal of Geophysical Research (Atmospheres)*, 115, D20204, doi:10.1029/2009JD013755, 2010.

Fierz-Schmidhauser, R., **Zieger, P.**, Wehrle, G., Jefferson, A., Ogren, J.A., Baltensperger, U., and Weingartner, E., Measurement of relative humidity dependent light scattering of aerosols, *Atmospheric Measurement Techniques*, 3, 39-50, 2010.

**Zieger, P.**, Ruhtz, T., Preusker, R., and Fischer, J., Dual-aureole and sun spectrometer system for airborne measurements of aerosol optical properties, *Applied Optics*, 46, 8542-8552, 2007.

Zurich, March 30, 2011



